TAMPEREEN TEKNILLINEN YLIOPISTO
TAMPERE UNIVERSITY OF TECHNOLOGY

Grégory Dominique Dubus

From Plain Visualisation to Vibration Sensing: Using a Camera to Control the Flexibilities in the ITER Remote Handling Equipment

Julkaisu 1250 • Publication 1250

Tampere 2014

Tampereen teknillinen yliopisto. Julkaisu 1250
Tampere University of Technology. Publication 1250

Grégory Dominique Dubus

From Plain Visualisation to Vibration Sensing: Using a Camera to Control the Flexibilities in the ITER Remote Handling Equipment

Thesis for the degree of Doctor of Science in Technology to be presented with due permission for public examination and criticism in Konetalo Building, Auditorium K1702, at Tampere University of Technology, on the 10th of October 2014, at 12 noon.

Tampereen teknillinen yliopisto - Tampere University of Technology
Tampere 2014

Pre-Examiners

Dr. Héctor Montes Franceschi
Department of Automatic Control
Institute of Industrial Automation
Spanish National Research Council - CSIC
Spain

Prof. Dr. Huapeng Wu
Laboratory of Intelligent Machines
LUT Mechanical Engineering
Faculty of Technology
Lappeenranta University of Technology
Finland

Opponents

Dr. Héctor Montes Franceschi
Department of Automatic Control
Institute of Industrial Automation
Spanish National Research Council - CSIC
Spain

Prof. Dr. Juha Röning
Department of Computer Science and Engineering
Faculty of Information Technology and Electrical Engineering
University of Oulu
Finland

Custos

Prof. Dr. Jouni Mattila
Department of Intelligent Hydraulics and Automation
Faculty of Engineering Sciences
Tampere University of Technology
Finland

ISBN 978-952-15-3374-7 (printed)
ISBN 978-952-15-3375-4 (PDF)
ISSN 1459-2045

ABSTRACT

TAMPERE UNIVERSITY OF TECHNOLOGY

Grégory Dominique DUBUS: From plain visualisation to vibration sensing: using a camera to control the flexibilities in the ITER remote handling equipment;

Thesis for the degree of Doctor of Science in Technology, 168 pages, 25 pages of references;

Keywords: thermonuclear fusion, fusion reactors, ITER, remote handling, heavy loads handling, flexible manipulators, vibration suppression, vision-based control, KLT algorithm, sinusoidal regression, change detection algorithm, image capture delay.

Thermonuclear fusion is expected to play a key role in the energy market during the second half of this century, reaching 20% of the electricity generation by 2100. For many years, fusion scientists and engineers have been developing the various technologies required to build nuclear power stations allowing a sustained fusion reaction. To the maximum possible extent, maintenance operations in fusion reactors are performed manually by qualified workers in full accordance with the "as low as reasonably achievable" (ALARA) principle. However, the option of hands-on maintenance becomes impractical, difficult or simply impossible in many circumstances, such as high biological dose rates. In this case, maintenance tasks will be performed with remote handling (RH) techniques.

The International Thermonuclear Experimental Reactor ITER, to be commissioned in southern France around 2025, will be the first fusion experiment producing more power from fusion than energy necessary to heat the plasma. Its main objective is "to demonstrate the scientific and technological feasibility of fusion power for peaceful purposes". However ITER represents an unequalled challenge in terms of RH system design, since it will be much more demanding and complex than any other remote maintenance system previously designed.

The introduction of man-in-the-loop capabilities in the robotic systems designed for ITER maintenance would provide useful assistance during inspection, i.e. by providing the operator the ability and flexibility to locate and examine unplanned targets, or during handling operations, i.e. by making peg-in-hole tasks easier. Unfortunately, most transmission technologies able to withstand the very specific and extreme environmental conditions existing inside a fusion reactor are based on gears, screws, cables and chains, which make the whole system very flexible and subject to vibrations. This effect is further increased as structural parts of the maintenance equipment are generally lightweight and slender structures due to the size and the arduous accessibility to the reactor.

Several methodologies aiming at avoiding or limiting the effects of vibrations on RH system performance have been investigated over the past decade. These methods often rely on the use of vibration sensors such as accelerometers. However, reviewing market shows that there is no commercial off-the-shelf (COTS) accelerometer that meets the very specific requirements for vibration sensing in the ITER in-vessel RH equipment (resilience to high total integrated dose, high sensitivity). The customisation and qualification of existing products or investigation of new concepts might be considered. However, these options would inevitably involve high development costs.

While an extensive amount of work has been published on the modelling and control of flexible manipulators in the 1980s and 1990s, the possibility to use vision devices to stabilise an oscillating robotic arm has only been considered very recently and this promising solution has not been discussed at length. In parallel, recent developments on machine vision systems in nuclear environment have been very encouraging. Although they do not deal directly with vibration sensing, they open up new prospects in the use of radiation-tolerant cameras.

This thesis aims to demonstrate that vibration control of remote maintenance equipment operating in harsh environments such as ITER can be achieved without considering any extra sensor besides the embarked rad-hardened cameras that will inevitably be used to provide real-time visual feedback to the operators. In other words it is proposed to consider the radiation-tolerant vision devices as full sensors providing quantitative data that can be processed by the control scheme and not only as plain video feedback providing qualitative information. The work conducted within the present thesis has confirmed that methods based on the tracking of visual features from an unknown environment are effective candidates for the real-time control of vibrations. Oscillations induced at the end effector are estimated by exploiting a simple physical model of the manipulator. Using a camera mounted in an eye-in-hand configuration, this model is adjusted using direct measurement of the tip oscillations with respect to the static environment.

The primary contribution of this thesis consists of implementing a markerless tracker to determine the velocity of a tip-mounted camera in an untrimmed environment in order to stabilise an oscillating long-reach robotic arm. In particular, this method implies modifying an existing online interaction matrix estimator to make it self-adjustable and deriving a multimode dynamic model of a flexible rotating beam. An innovative vision-based method using sinusoidal regression to sense low-frequency oscillations is also proposed and tested. Finally, the problem of online estimation of the image capture delay for visual servoing applications with high dynamics is addressed and an original approach based on the concept of cross-correlation is presented and experimentally validated.

DISCLAIMER

The work leading to this thesis was performed as part of the PREFIT (Preparing Remote Handling Engineers for ITER) programme, funded by the European Commission under the European Fusion Training Scheme (EFTS). The views and opinions expressed herein are the sole responsibility of the author and do not necessarily reflect those of the European Commission.

ACKNOWLEDGEMENTS

To Prof. Jouni Mattila, from the Department of Intelligent Hydraulics and Automation (Tampere University of Technology), for his unfailing guidance and encouragement throughout the preparation of this thesis.

To Dr. Héctor Montes Franceschi and Prof. Huapeng Wu, respectively from the Centre for Automation and Robotics (CSIC-UPM, Spanish National Research Council) and the Laboratory of Intelligent Machines (Lappeenranta University of Technology), for acting as pre-examiners and providing constructive comments that helped improve this thesis.

To Dr. Alan Rolfe, from Oxford Technologies Ltd., for setting up the PREFIT programme and sharing through it his enthusiasm and unequalled experience in the field of remote handling.

To Yvan Measson and Olivier David, from the Commissariat à l'Energie Atomique et aux Energies Alternatives, for making my first professional experience a memorable one, for initiating me to hard-core robotics and for planting the seed in me of pursuing a doctoral degree.

To Dr. Carlo Damiani, from Fusion for Energy, for giving me the opportunity to grow professionally among the nuclear fusion community and for allowing me to complete this thesis.

To Karoliina Salminen, Teemu Kekäläinen, Ryan King, Dr. Robin Shuff and Dr. Jean-Baptiste Izard, for taking part in PREFIT as my fellow researchers and for the great memories we shared together during these few years.

To Mélanie, my wife, for giving birth to two beautiful daughters—Louise and Sophie—in half the time I needed to write this thesis and for looking after them during its finalisation.

TABLE OF CONTENTS

LIST OF SYMBOLS

Unbold symbols denote scalars, bold symbols denote vectors and matrices.

Greek symbols

α,β,γ,δ	Unknowns of the linear regression form obtained by integrations
α_c	Image aspect ratio
α_i,β_i	Coefficients of the forcing function f_i
$\boldsymbol{\alpha}$	$p \times 1$ vector whose components are the α_i
$\boldsymbol{\beta}$	$p \times 1$ vector whose components are the β_i
Γ_a^-,Γ_a^+	Thresholds determining an abrupt change
Γ_g^-,Γ_g^+	Thresholds determining a gradual change
$\boldsymbol{\Gamma_2}$	Noise repartition matrix
δ_{ij}	Kronecker delta
$\boldsymbol{\delta}$	Vector of link and rotor positions
Δ	Time delay
$\boldsymbol{\epsilon}$	General tracking error between measured and desired output values
$\boldsymbol{\zeta}$	Matrix of damping ratio
η	Time-varying amplitude
η_i	i^{th} time-dependent function in the modal base
θ_i	Position of the i^{th} link
$\delta\theta_i$	Deflection at the i^{th} joint
$\boldsymbol{\theta}$	Vector of the n link positions
$\boldsymbol{\theta_d}$	Link coordinates reference
$\bar{\boldsymbol{\theta}}$	Quasi-static estimate of the link position
$\boldsymbol{\delta\theta}$	Vector of the n flexible joint deflections
λ	Dimensionless wave number
Λ	Influence function of an M-estimator
μ	Material mass density per unit length
ν	Inverse of the square of the frequency ω
$\boldsymbol{\xi}$	Vector of visual features
$\boldsymbol{\xi^*}$	Vector of desired values for the visual features
$\dot{\boldsymbol{\xi}}_{\boldsymbol{high}}$	High dynamics component of the features velocity $\dot{\boldsymbol{\xi}}$
$\dot{\boldsymbol{\xi}}_{\boldsymbol{low}}$	Low dynamics component of the features velocity $\dot{\boldsymbol{\xi}}$
$\boldsymbol{\delta\xi}$	Frame to frame displacement of the image features
$\widehat{\boldsymbol{\delta\xi}}_{\boldsymbol{high}}$	Estimated vibration in the image
κ	Rotary mass moment of inertia per unit length of the shaft
ρ	Material mass density per unit volume
υ	Normalised change rate of the monitored signal
$\boldsymbol{\upsilon_c}$	Instantaneous linear velocity of the origin of the camera frame
ϱ	Forgetting factor of the interaction matrix estimator
σ	Temporal standard deviation

σ_*	Standard deviation after change of the signal
σ_i	Standard deviation of the sequence $\{y_i\}_{i\geq 1}$
Σ	Abbreviated writing for $\sum\limits_{i=1}^{N}$
τ	Exponential time constant
τ_c	Constant refresh rate
τ_i	Measured torque at the i^{th} joint
τ_s	Varying refresh rate
$\boldsymbol{\tau}$	Vector of the n joint input torques
$\boldsymbol{\tau_0}$	Constant torque vector balancing gravity
$\boldsymbol{\tau_J}$	Elastic torque transmitted through the joints
$\boldsymbol{\tau_{ext}}$	Contact torques
$\boldsymbol{\tau_{J,d}}$	Elastic torque reference
$\boldsymbol{\delta\tau}$	Deviations of $\boldsymbol{\tau}$ from its static value
ϕ	Torsional deflection angle
φ	Shear modulus of the material
$\boldsymbol{\omega_c}$	Instantaneous angular velocity of the origin of the camera frame
ω_d	Damped natural frequency
ω_e	Estimated value of the vibration fundamental frequency
ω_i	i^{th} natural frequency
${}^{\boldsymbol{\mathcal{R}i}}\boldsymbol{\omega_{Ri}}$	Angular velocity of the i^{th} rotor body in the motor frame of the i^{th} link

Latin symbols

a,b,c	Parameters of the sinusoidal function f
a_1,a_2,a_3,a_4	Constant coefficients of the mode shape function
$\boldsymbol{a}$	Camera intrinsic parameters
$\boldsymbol{A}$,$\boldsymbol{A_1}$,$\boldsymbol{A_2}$	Process matrices
$\boldsymbol{A_c}$,$\boldsymbol{B_c}$,$\boldsymbol{C_c}$	State-space representation matrices for the system to control
$\boldsymbol{A_k}$	Process matrix of discrete state-space representations
$\mathcal{A}_i$	Amplitude of the i^{th} eigenfunction
$\boldsymbol{\mathcal{A}}$	$1 \times p$ vector whose components are the $\mathcal{A}_i$
b_1,b_2	Constant coefficients of the time-varying amplitude function
B	Statistical variance change detection test
$\boldsymbol{B}$	Rotor inertia matrix
$\boldsymbol{B_1}$	Input matrix
c_i	Abbreviated writing for $\cos(k_i L)$
cch_i	Abbreviated writing for $\cos(k_i L)\, ch(k_i L)$
ch_i	Abbreviated writing for $\cosh(k_i L)$
c_u, c_v	2D coordinates of the image center
$\boldsymbol{c}$,$\boldsymbol{c_1}$,$\boldsymbol{c_2}$	Vectors of centrifugal and Coriolis torques
C_1,C_2	Arbitrary constants of integration

$\boldsymbol{C}$,$\boldsymbol{C_1}$,$\boldsymbol{C_2}$	Output matrices
$\boldsymbol{C_k}$	Output matrix of discrete state-space representations
$\boldsymbol{C_s^*}$	Output matrix of a discrete state-space representation at $s = k - \Delta N$
$\mathcal{C}_{xy}(n)$	Cross-correlation between signals $x(n)$ and $y(n)$
$\mathcal{C}_{yx}^{old}(n)$	Cross-correlation computed prior to the last reception of visual data
$\mathcal{C}_{yx}^{new}(n)$	Cross-correlation computed from the latest visual data
$\mathcal{C}_{zz}(n)$	Auto-correlation of signals $z(n)$
$\boldsymbol{\mathcal{C}}$	Controllability matrix
$\boldsymbol{\mathcal{C}_{cc}}$	Matrix of factorised Coriolis and centrifugal terms
$\boldsymbol{\mathcal{C}_r}$,$\boldsymbol{\mathcal{C}_f}$	Centrifugal and Coriolis torques and forces vectors
$\boldsymbol{d}$	Displacement vector between two images
$\boldsymbol{D}$	Deformation matrix between two images
$\boldsymbol{e}$	Vector of the m deflections variables
$\boldsymbol{e_0}$	Static deflection for a given joint position
$\boldsymbol{\delta e}$	Deviations of $\boldsymbol{e}$ from its static value
E	Young's modulus of the beam material
$f(t)$	Sinusoidal function to be identified
$f(x,t)$	Forcing function
f_c	Camera focal length
f_i	i^{th} forcing function in the modal base
$F(t)$	First antiderivative of $f(t)$
$\boldsymbol{F}$	Vector of forces/torques acting from the environment on the robot
$\boldsymbol{F_q}$	Matrix of viscous coefficients on the link side
$\boldsymbol{F_\theta}$	Matrix of viscous coefficients on the motor side
$\mathcal{F}_i$	Working force at the i^{th} link
g	Standard acceleration of gravity
$g(x)$	Change of variable function
gr_i	Reduction ratio (or gear ratio) at the i^{th} joint
$\boldsymbol{g}$	Gravity vector
$\boldsymbol{g_r}$,$\boldsymbol{g_f}$	Gravitational terms vectors
$G(t)$	Second antiderivative of $f(t)$
h	Adjustment parameter of the M-estimators
H_0,H_1	Hypotheses tested for variance change detection
$\boldsymbol{H}$	Decoupling matrix of the system
i,j	Indexes
I	Cross-sectional area moment of inertia
$\boldsymbol{I}$	Identity matrix
$^{\boldsymbol{\mathcal{R}i}}\boldsymbol{I_{Ri}}$	Inertia matrix of the i^{th} rotor in the i^{th} motor frame
J_x	Polar area moment of inertia about the neutral axis of the beam
$\boldsymbol{J_e}$	Jacobian matrix of the end-point wrt the deflection variables
$\boldsymbol{J_\xi}$	Feature Jacobian matrix

$\boldsymbol{J_\theta}$	Jacobian matrix of the end-point wrt the articular positions
$\boldsymbol{J_\theta^+}$	Moore-Penrose pseudoinverse of the Jacobian matrix
$\boldsymbol{J_{Rij}}$	j^{th} column of the Jacobian relating $\dot{\boldsymbol{\theta}}$ to the velocity of the i^{th} rotor
$\mathcal{J}$	Cost function
k	Wave number
k_n	Adjusting factor of the sliding window size
$k_{0,i}$,...,$k_{3,i}$	Diagonal elements of the matrices $\boldsymbol{k_0}$,...,$\boldsymbol{k_3}$
$\boldsymbol{k_0}$,...,$\boldsymbol{k_3}$	Diagonal gain matrices defining a tracked trajectory
K_D	Derivative gain of a PID controller
K_i	Stiffness of the i^{th} joint
K_P	Proportional gain of a PID controller
$\boldsymbol{K}$	Stiffness matrix
$\boldsymbol{K_s}$	Submatrix of the stiffness matrix
$\boldsymbol{K_k}$	Discrete Kalman gain matrix
$\mathcal{K}$	$\mathcal{K}$ operator
$\boldsymbol{L_1}$,$\boldsymbol{L_2}$	LQR controller gains
$\boldsymbol{L_\xi}$	Interaction matrix related to $\boldsymbol{\xi}$
$\boldsymbol{L_\xi^+}$	Moore-Penrose pseudoinverse of the interaction matrix
$\widehat{\boldsymbol{L_\xi^+}}$	Approximation of the interaction matrix pseudoinverse
$\mathcal{L}$	System Lagrangian
$\mathcal{L}_i$	Link frame of the i^{th} link
m	Number of deflections variables
m_{Li}	Mass of the i^{th} link
m_{Ri}	Mass of the i^{th} drive
$\boldsymbol{m}$	Set of image measurements
M	Beam bending moment
M_c	Matrix of camera motions
M_p	Payload mass, or tip mass
$\boldsymbol{M}$	Inertia matrix
$\boldsymbol{M_L}$	Link inertia matrix
$\boldsymbol{M_R}$	Rotor mass matrix
$\boldsymbol{M_{ff}}$	Mass matrix for flexible coordinates in flexible equations
$\boldsymbol{M_{fr}}$	Mass matrix for rigid coordinates in flexible equations
$\boldsymbol{M_{rf}}$	Mass matrix for flexible coordinates in rigid equations
$\boldsymbol{M_{rr}}$	Mass matrix for rigid coordinates in rigid equations
M_ξ	Matrix of feature motions
$\mathcal{M}$	$\mathcal{M}$ operator
n	Number of joints/links of the considered robot
n_0	Delay between signal $z(n)$ and signal $y(n)$
n_c	Current timestamp
n_i	Initial timestamp

N	Size of the considered sliding window
N_c	Number of independent camera motions
N_{min}	Minimum size of the considered sliding window
N_{max}	Maximum size of the considered sliding window
ΔN	Indeterminate number of delayed samples
$\boldsymbol{\mathcal{O}}$	Observability matrix
$\boldsymbol{P}$	Covariance matrix
$\boldsymbol{P_k^+}$	A posteriori error covariance matrix in Kalman filter
$\boldsymbol{P_k^-}$	A priori error covariance matrix in Kalman filter
$\mathcal{P}$	Second-order polynomial depending on a, b, c, ω, C_1 and C_2
q_i	Drive position of the i^{th} joint
q_{mi}	Drive position of the i^{th} joint before reduction
$\boldsymbol{q}$	Vector of the n rotor positions
$\boldsymbol{q_d}$	Motor variables reference
$\boldsymbol{q_m}$	Vector of the n drive positions before reduction
$\boldsymbol{Q}$,$\boldsymbol{Q_1}$,$\boldsymbol{Q_2}$	Process noises covariance matrices
$\boldsymbol{Q_{LQR}}$,$\boldsymbol{R_{LQR}}$	Penalty matrices for the LQR controller
r	Number of tracked visual features
$\boldsymbol{R}$,$\boldsymbol{R_1}$,$\boldsymbol{R_2}$	Measurement noises covariance matrices
$\boldsymbol{R^*}$	Delayed measurement noises covariance matrices
$\mathcal{R}_i$	Motor frame of the i^{th} link
$\boldsymbol{\mathcal{R}}$	Vector of external and other non-conservative forces
s_i	Abbreviated writing for $\sin(k_iL)$
sch_i	Abbreviated writing for $\sin(k_iL)\, ch(k_iL)$
sh_i	Abbreviated writing for $\sinh(k_iL)$
S	Cross section of the beam
$\boldsymbol{S}$	Matrix of inertial couplings between rotors and links
t	Time variable
t_i	Time data received from the features tracker
T	Twisting moment
$\boldsymbol{{}^cT_n}$	Transformation matrix between end-effector and camera frame
$\mathcal{T}$	System kinetic energy
$\mathcal{T}_{link}$	System kinetic energy due to the links
$\mathcal{T}_{rotor}$	System kinetic energy due to the rotors
u	Beam axial deflection
$\boldsymbol{u}$	New input of the feedback linearised system
$\boldsymbol{U}$	Torque repartition matrix
$\mathcal{U}$	System potential energy
$\mathcal{U}_{elast}$	System elastic energy
$\mathcal{U}_{grav}$	System potential energy due to gravity
$\mathcal{U}_{grav,link}$	Potential energy due to gravity acting on the links

$\mathcal{U}_{grav,motor}$	Potential energy due to gravity acting on the drives
v	Transverse displacement of a beam neutral surface
v_0	Static deflection along x for a given joint position
v_{Ri}	Linear velocity of the centre of mass of the i^{th} rotor
δv	Deviation of v from its static value
$\boldsymbol{v}$,$\boldsymbol{v_1}$,$\boldsymbol{v_2}$	Measurement noises
$\boldsymbol{v_c}$	Spatial velocity of the camera
$\boldsymbol{v_k}$	Measurement noise of discrete state-space representations
$\boldsymbol{v_k}^*$	Delayed measurement noise of a discrete state-space representation
w	Deflection variable associated to the homogeneous system
$\boldsymbol{w}$,$\boldsymbol{w_1}$,$\boldsymbol{w_2}$	Process noises
$\boldsymbol{w_k}$	Process noise of discrete state-space representations
W	Mode shape
W_i	i^{th} mode shape corresponding to the natural frequency ω_i
$\boldsymbol{W}$	Weighting matrix of the interaction matrix estimator
x,y	Orthogonal coordinates in the beam base or the image base
$x(n), y(n), z(n)$	Periodic signals of period N_s
x_u, x_v	2D coordinates of a point expressed in pixel units
$\boldsymbol{x}$,$\boldsymbol{x_1}$,$\boldsymbol{x_2}$	State vectors of state-space representations
$\boldsymbol{x_k}$	State vector of discrete time state-space representations
$\hat{\boldsymbol{x}}_{\boldsymbol{k}}^{+}$	A posteriori state estimate in Kalman filter
$\hat{\boldsymbol{x}}_{\boldsymbol{k}}^{-}$	A priori state estimate in Kalman filter
X, Y, Z	3D coordinates of an interest point
$\boldsymbol{X}$	Vector of 3D coordinates (X, Y, Z) of an interest point
y_i	Displacement data received from the features tracker
$\overline{y}_i$	Mean of the sequence $\{y_i\}_{i\geq 1}$
$\boldsymbol{y_c}$	Controlled output vector of the whole system
$\boldsymbol{y_d}$	Desired output values of the whole system
Y_i	i^{th} normalised eigenfunction
$\boldsymbol{Y}$	Matrix to be determined in the Riccati equation
$\boldsymbol{z}$,$\boldsymbol{z_1}$,$\boldsymbol{z_2}$	Output vectors of state-space representations
$\boldsymbol{z_k}$	Output vector of discrete state-space representations
$\boldsymbol{z_k^*}$	Delayed output vector of a discrete state-space representation

LIST OF ACRONYMS

AIA	Articulated Inspection Arm
ALARA	as low as reasonably achievable
ARMA	autoregressive moving-average (model)
BLS	blockwise least squares
BRHS	Blanket Remote Handling System
CAD	computer-aided design
CCD	charge-coupled device
CCFE	Culham Centre for Fusion Energy
CEA	Commissariat à l'Energie Atomique et aux Energies Alternatives
CID	charge-integration device
CMM	cassette multi-functional mover
CMOS	complementary metal-oxide semiconductor
CODAC	Control, Data Access and Communication
COTS	commercial off-the-shelf
CPRHS	Cask and Plug Remote Handling System
CPU	central processing unit
CSA	Canadian Space Agency
CTM	cassette toroidal mover
CTS	cask transfer system
DAM	Direction des Applications Militaires (CEA)
DEMO	demonstration fusion power plant
DOF	degree of freedom
DRHS	Divertor Remote Handling System
DTP2	Divertor Test Platform 2
EDM	enhanced disturbance map
EFDA	European Fusion Development Agreement
ELM	edge localised mode
ENEA	Agenzia nazionale per le nuove tecnologie, l'energia e lo sviluppo economico sostenibile
ESA	European Space Agency
F4E	Fusion for Energy
FBG	fibre Bragg grating
FDD	Fast Deployment Device
FEA / FEM	finite element analysis / finite element method
FIR	finite impulse response
FMSM	flexible master-slave manipulator
FPGA	field-programmable gate array
FS	frequency shaping
GPU	graphics processing unit
HC / HCRHS	Hot Cell / Hot Cell Remote Handling System
HMI	human-machine interface

HSV	hue saturation value
IBVS	image-based visual servoing
ICRH	Ion Cyclotron Resonant Heating
IFMIF	International Fusion Materials Irradiation Facility
IIR	infinite impulse response
IPP	Max-Planck-Institut für PlasmaPhysik
IRFM	Institut de Recherche sur la Fusion Magnétique (CEA)
ISS	International Space Station
ITER	International Thermonuclear Experimental Reactor
IVT	in-vessel transporter
IVVS	In-Vessel Viewing System
JADA	Japan Domestic Agency for ITER
JAERI	Japan Atomic Energy Research Institute
JAXA	Japan Aerospace Exploration Agency
JEMRMS	Japanese Experiment Module Remote Manipulator System
JET	Joint European Torus
JT-60	Japan Torus 60
K-DEMO	Korean demonstration fusion power plant
KLT	Kanade-Lucas-Tomasi (feature tracker)
LED	light-emitting diode
LEM	lumped-elements method
LIST	Laboratoire d'Intégration de Systèmes et des Technologies (CEA)
LMJ	Laser Megajoule
LQ	linear quadratic
LQ-E/-G/-R	linear quadratic estimator / Gaussian / regulator
LS	least-square
LTR	loop transfer recovery
LWR	light water reactor
MAD	median absolute deviation
MEF	momentum exchange feedback
MEMS	microelectronic mechanical system
MIMO	multiple-input multiple-output (system)
MLE	maximum likelihood estimator
MPD	Multi-Purpose Deployer
MRAC	model reference adaptive control
MSM	master-slave manipulator
NASA	National Aeronautics and Space Administration
NB	Neutral Beam
NBRHS	Neutral Beam Remote Handling System
NDT	non-destructive testing
NIF	National Ignition Facility
ODE	ordinary differential equation
OS	operating system

PBVS	position-based visual servoing
PCP	primary closure plate
PD	proportional-derivative (controller)
PDE	partial differential equation
RGB	red, green, blue
RGB-D	red, green, blue - distance
RH	remote handling
RHCS	Remote Handling Supervisory Control System
RLS	recursive least squares
RMFS	rigid master–flexible slave
ROViR	Remote Operation and Virtual Reality centre
SCK-CEN	StudieCentrum voor Kernenergie - Centre d'étude de l'Energie Nucléaire
SIFT	scale-invariant feature transform
SIMO	single-input multiple-output (system)
SMC	sliding-mode control
SMCPE	sliding mode control with perturbation estimation
SNA-ZV	specified negative amplitude zero-vibration (shaper)
SPDM	Special Purpose Dexterous Manipulator
SRMS	Space Shuttle Remote Manipulator System
SSRMS	Space Station Remote Manipulator System
STS-2	Space Transportation System 2
TAO	téléopération assistée par ordinateur (computer-aided teleoperation)
TFR	Tokamak de Fontenay-aux-Roses
TFTR	Tokamak Fusion Test Reactor
TMM	transfer matrix method
TUT	Tampere University of Technology
UDP	user datagram protocol
UTFUS	Unità Tecnica Fusione (ENEA)
VS	visual servoing
VTT	Valtion Teknillinen Tutkimuskeskus, Technical Research Centre of Finland
VV	vacuum vessel
WEC	World Energy Council
WEST	Tungsten (W) Environment in Steady-state Tokamak
ZV	zero-vibration (shaper)
ZVD	zero-vibration and derivative (shaper)
ZVDD	zero-vibration derivative derivative (shaper)

LIST OF CORRECTIONS FROM PRINTED VERSION

This electronic version contains minor changes and corrections from the printed version:

- **p.X:** typo corrected ($\boldsymbol{L}_{\boldsymbol{\xi}}^{+}$ is the Moore-Penrose pseudoinverse of the interaction matrix);
- **p.X:** symbol $\boldsymbol{J}_{\boldsymbol{\theta}}^{+}$ added (Moore-Penrose pseudoinverse of the Jacobian matrix);
- **p.51:** paragraph break inserted before third paragraph of section 1.2.2;
- **p.117:** invariability of $\boldsymbol{A}_{\boldsymbol{k}}$ made explicit ($\boldsymbol{A}_{\boldsymbol{k}} = \boldsymbol{A}$) and Kalman filter equations (3.21–3.25) re-written accordingly;
- **p.119:** modified Kalman filter equation (3.29) corrected ($\boldsymbol{x}_{\boldsymbol{k}}^{-} \rightarrow \hat{\boldsymbol{x}}_{\boldsymbol{k}}^{-}$);
- **pp.122–123:** interaction matrix estimator equations (3.34 and 3.36) corrected (Moore-Penrose pseudoinverse $\boldsymbol{J}_{\boldsymbol{\theta}}^{+}$ initially omitted); and
- **p.123:** Equation (3.35) corrected ($\boldsymbol{J}_{\boldsymbol{e}} \rightarrow \boldsymbol{J}_{\boldsymbol{\theta}}$).

1. INTRODUCTION

1.1 Context of the study

1.1.1 The challenges of tomorrow's energy market

Population growth and steadily rising standards of living, especially in developing countries, will keep demand for energy growing substantially for years to come. The World Energy Council (WEC) recently stated [1] that the global demand for primary energy is expected to increase between 27% ("Symphony" scenario) and 61% ("Jazz" scenario) by 2050. Beyond 2050, several scenarios diverge. Part of that divergence will depend on technological developments, industrial strategies, policy choices and consumer choices. The more pessimistic scenarios predict an energy production peak around 2100 followed by an overall energy shortfall (see Fig. 1.1).

A single energy source will probably not be able to fulfil that increasing demand. On the contrary, energy security and sustainability for everyone will be achieved through a mix of power sources. Therefore, all energy options must be kept open to ensure responses that are as environmentally and economically appropriate as possible. Thermonuclear fusion is one of these options. At present, more than 80% of the energy consumed globally comes from fossil fuels. However, high CO_2 emissions and decreasing coal, gas and oil reserves call for a transition towards other forms of energy. The future energy supply may include fossil fuels, renewables, nuclear fission and nuclear fusion.

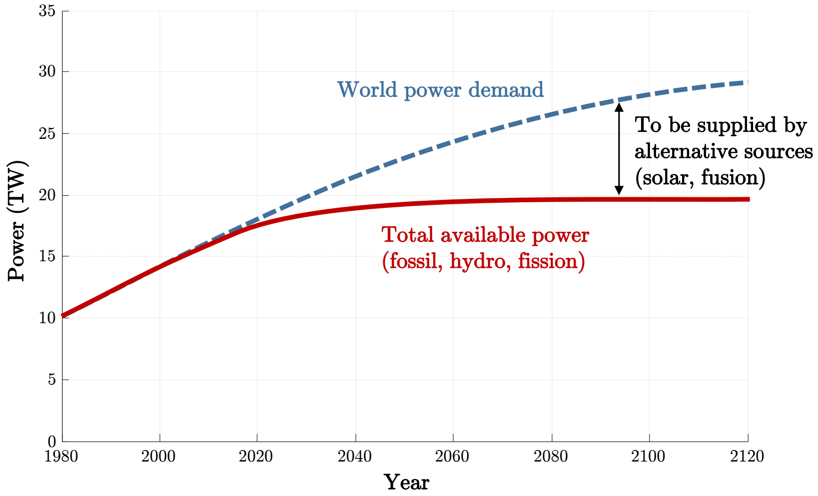

Figure 1.1: World energy supply and demand (source: World Energy Council)

The demand for electricity is increasing twice as fast as the overall demand for energy. In order to meet future demands, global electricity generation is expected to increase between 123% (Symphony) and 150% (Jazz) by 2050. Regrettably, a majority of renewable sources rely strongly on intermittent environmental conditions, which therefore cannot guarantee their constant contributions to electricity production. To provide baseload electricity, predictable and continuous sources of energy are needed. For this reason, nuclear fission will keep contributing extensively to electricity generation, but its growth could be limited by a lack of political and public acceptance.

Last but not least, fusion will offer a secure, long-term source of electric power with important advantages (no production of greenhouse gases, only short-life radioactive waste recyclable within 100 years, inherent safety and an almost unlimited fuel supply). Economic models indicate that plant reliability and output power are key parameters driving electricity production costs. Based on current estimates, the cost of fusion-generated electricity is predicted to be in the vicinity of the other options. For these reasons, long-term models show that fusion could be introduced during the second half of this century and could play a key role in the energy market of the future, reaching a significant share of electricity generation by 2100 (estimated around 20%).

1.1.2 Fundamentals of nuclear fusion

Current nuclear power plants use heat generated by nuclear fission. This reaction occurs when a heavy atomic nucleus (usually uranium or plutonium) splits to form two new smaller atoms, thus releasing a large amount of energy.

Conversely, nuclear fusion occurs when multiple light atomic nuclei collide with enough energy to bind together and form a heavier nucleus. This process is accompanied by the release or absorption of massive amounts of energy; in the case of very light nuclei (such as hydrogen with just one proton) the amount of energy released is three to four times more than that released in fission. Generally, fusing two nuclei with masses lower than iron will release energy, while the fusion of nuclei heavier than iron will absorb energy.

While fission does not normally occur in nature, nuclear fusion occurs naturally in the cores of stars and is a source of tremendous heat. In the Sun, hydrogen isotopes (deuterium or tritium) fuse together to form a helium atom (see Fig. 1.2). During that conversion, a small amount of mass is converted into energy. This combination of two nuclei with the same charge requires high kinetic energies that exceed the electrostatic repulsion between the nuclei. The extremely high temperature causes electrons to be stripped off the atoms, leaving only the nuclei. This state of matter is called plasma.

In comparison with the rest of the universe, the Sun is a relatively young star that is mostly

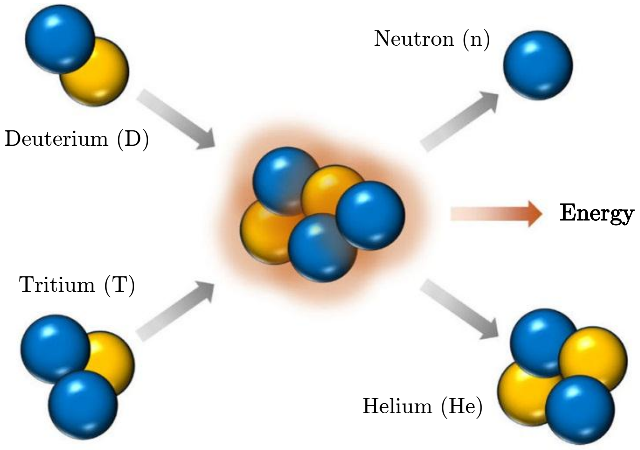

Figure 1.2: Deuterium-tritium fusion reaction

made of hydrogen. High temperatures in the centre of young stars trigger a nuclear fusion process in which hydrogen is converted into helium. However, once their core temperature reaches 130×10^6 K, stars also begin to fuse helium into carbon and oxygen. Larger stars continue to fuse carbon and oxygen into neon, neon is then fused into silicon and silicon is fused into iron.

1.1.3 Advantages of fusion power

While antagonistic concerns grow about global warming and declining fossil fuel resources, new, cleaner, safer and sustainable ways to supply the increasing energy demand are needed. Power stations based on fusion would offer a number of advantages:

- abundance of primary fuel - Deuterium can be extracted from sea water while tritium can be produced from lithium, which is readily available in the Earth's crust; fuel supplies would theoretically last for millions of years;
- energy efficiency - 1 kg of fusion fuel would provide the same amount of energy as 10^7 kg of fossil fuel;
- no carbon emissions - Limited amounts of helium are the only by-products of fusion reactions;
- no long-lived radioactive waste - Activated or tritium-contaminated components will be safe to recycle or dispose of conventionally within 100 years;
- safety - Moderate amounts of fuel needed, together with the inherent impossibility of chain reactions, prevent the occurrence of a nuclear accident;
- no nuclear proliferation - Low-level nuclear waste will not be weapons-grade nuclear material;
- affordable cost - Fusion power plants would provide baseload electricity supply at costs roughly similar to other energy sources.

1.1.4 Basic principles of controlled fusion and fusion reactors

In the light of the above, nuclear fusion is one of the most promising options for producing large amounts of carbon-free electrical power in the future.

For many years, fusion scientists and engineers have been developing the various technologies required to build nuclear power stations allowing a sustained fusion reaction. To achieve high fusion reaction rates, several factors must be controlled. First, since very high kinetic energies are needed for nuclei to fuse, the plasma in which fusion occurs must be extremely hot. Temperatures over 100 million degrees Celsius—six times hotter than the Sun—are required for the easiest fusion reaction to take place, which occurs between deuterium and tritium. However, plasmas are fluids and, as such, they do not have any permanent shape and quickly disperse if not confined. Moreover, a 100-million-degree plasma would vaporise any container it was placed in. For this reason, an intense confinement is also required to contain this incredibly hot, thin and fragile plasma.

Today, two approaches can be taken to contain fusion reactions:

- Magnetic confinement: this approach has the most attention to date. Since charged particles move in circles perpendicular to a magnetic field, it is possible to confine them inside a magnet shaped like a torus whose field lines go around in endless circles. This concept gave birth to the so-called tokamak ("toroidal magnetic chamber" in Russian), in which hot plasma is confined by powerful magnets (see Fig. 1.3 and section 1.1.5). The ITER project is based on the tokamak concept. Other concepts of magnetic confinement devices exist, such as the Stellarator, which is distinct from the tokamak in the sense that it is not azimuthally symmetric but helically twisted in order to improve plasma confinement and stability properties (see Fig. 1.4).

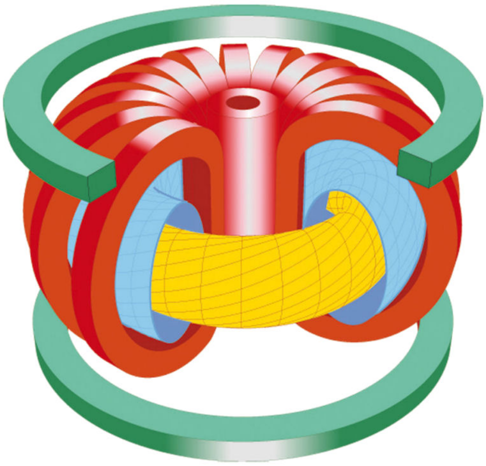

Figure 1.3: Tokamak concept (image courtesy of Max-Planck-Institut für Plasmaphysik IPP)

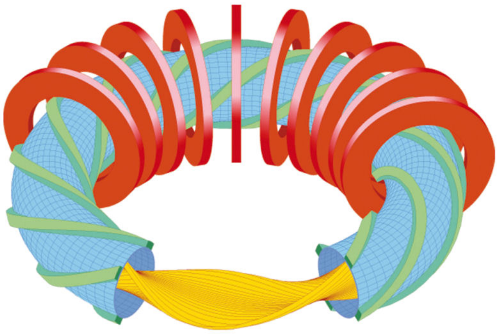

Figure 1.4: Stellarator concept (image courtesy of Max-Planck-Institut für Plasmaphysik IPP)

- Inertial confinement: the idea behind this alternative approach is to make the fusion reaction occur so quickly that the fuel does not have time to disperse before its energy is released. This concept makes use of large, intense lasers (1.8 million joules) to bombard and heat up a frozen pellet of fusion fuel and cause fusion to occur in less than one-millionth of a second (see Fig. 1.5). Whereas magnetic confinement devices maintain steady-state hot plasmas, devices based on inertial confinement operate in pulses. Typical examples of inertial confinement devices are the National Ignition Facility (NIF) in the United States (Fig. 1.6) and the Laser Megajoule (LMJ) in France (Fig. 1.7). This concept is presented for the sake of completeness and will not be addressed further in this thesis.

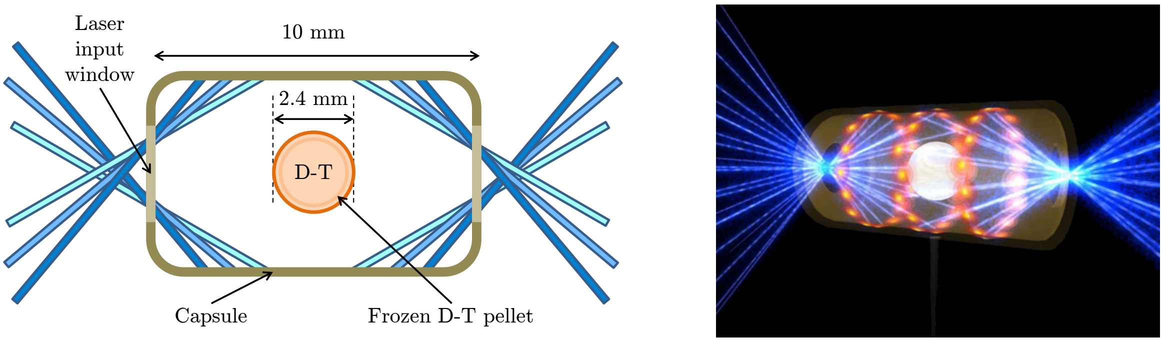

(a) (b)

Figure 1.5: Schematic (a) and artist rendering (b) showing a target pellet inside a capsule fired by laser beams (image (b) courtesy of the Lawrence Livermore National Laboratory)

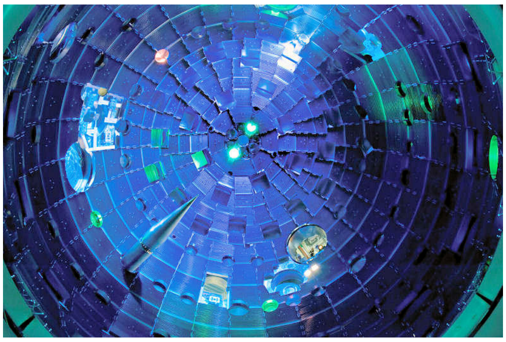

Figure 1.6: NIF target chamber (image courtesy of the Lawrence Livermore National Laboratory)

Figure 1.7: LMJ experimental chamber after installation (image courtesy of CEA DAM)

In both confinement methods, once energy has been released by the fusion reaction, its conversion to electric power could be similar to what takes place in contemporary nuclear or conventional power plants: the thermal flux generated during operation passes through heat exchangers in order to produce steam delivered to turbines via a secondary loop. The efficiency of a fusion reactor is defined by the energy gain factor Q, which represents the amount of thermal energy generated by the fusion reaction divided by the amount of external energy required to sustain it. A Q of 1 is called the break-even point, where the amount of power needed to heat the plasma equals the amount of fusion energy produced.

1.1.5 The tokamak and its main in-vessel components

As mentioned in the previous section, the tokamak, which is based on magnetic confinement, is the most developed fusion machine concept. It was invented by Russian scientists Andreï Sakharov and Igor Tamm in the 1950s [2] and was soon adopted by researchers around the world (see section 1.1.6 for more details).

Temperatures of 100 million degrees Celsius are necessary to induce nuclear fusion. However, no solid container can confine such hot plasma. In a tokamak, this problem is solved by confining the electrically charged plasma particles within a magnetic field so they cannot touch the vessel walls. This magnetic cage is achieved by combining the effects of a toroidal magnetic field and a poloidal magnetic field (see Fig. 1.8). The toroidal magnetic field is generated by electric currents circulating in a series of toroidal field coils evenly positioned around the torus. In basic tokamaks, the poloidal magnetic field is produced by a central solenoid that acts as the primary winding of a transformer. A transient electric current circulating inside this central solenoid induces a current in the plasma ring, which creates a poloidal field and heats the plasma. In more advanced tokamaks, such as JET or ITER, the plasma current is seconded by a set of poloidal field coils located around the vessel in order to induce the poloidal field. This combination of magnetic fields results in a helically wound torus-shaped magnetic cage transporting the charged plasma particles along closed and therefore infinite magnetic field lines.

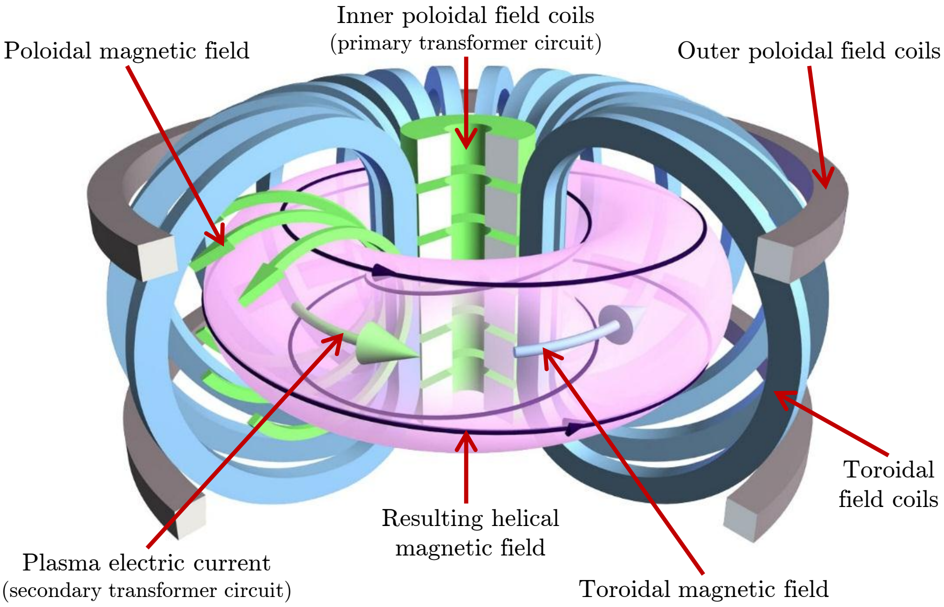

Figure 1.8: Principle of a tokamak (image courtesy of EFDA)

To provide further insight into the principle of a tokamak fusion reactor, and to introduce some technical terminology that will be used throughout this thesis, the following paragraphs describe the main internal components of the ITER tokamak (see also Fig. 1.9).

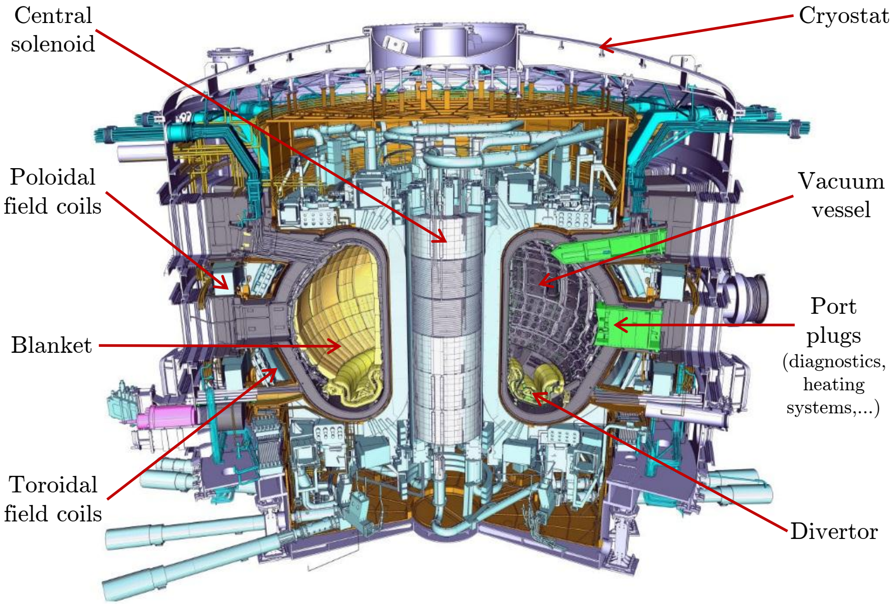

Figure 1.9: Main inner components of the ITER tokamak

Vacuum vessel

The vacuum vessel (VV) is a hermetically sealed, torus-shaped container made of steel. It houses the fusion reaction and acts as the first safety containment barrier. The size of the VV dictates the volume of the fusion plasma: the larger the vessel, the greater the power that can be produced. In ITER, the volume of the plasma (850 m^3) will allow an energy gain Q around 10, meaning that the produced fusion power will be 10 times greater than the input heating power. In future commercial fusion power plants, this factor should reach 30–40. To allow access to the heating systems, diagnostics and remote maintenance equipment, 44 ports are distributed around the VV surface at three levels.

Magnets

The burning plasma is contained within a magnetic field that keeps it away from the VV walls. The ITER tokamak comprises toroidal field coils, poloidal field coils (a.k.a. outer poloidal field coils), a central solenoid (a.k.a. inner poloidal field coils) and a set of correction coils that magnetically confine, shape and control the plasma. Additional coils may be implemented to mitigate edge localised modes (ELMs) that cause the plasma to lose part of its energy if left uncontrolled. To limit energy consumption, ITER uses superconducting magnets that lose their resistance when cooled below their critical temperature (in the order of 4 K).

Cryostat

The cryostat is a large (29.3 m tall and 28.6 m wide) stainless steel, thermally insulated container surrounding the VV and the magnets. It provides a 4 K secondary vacuum necessary to the low-temperature operation of the superconducting magnets.

Heating systems

In order for the fusion reaction to take place, the gas injected inside the VV must attain temperatures close to 150 million degrees Celsius. To reach and sustain these extreme temperatures, ITER relies on internal heating (ohm effect from the high-intensity current induced by the central solenoid) and external heating from three sources working in concert: neutral beam injection (neutral hydrogen atoms are injected at high speed into the plasma and transfer their energy as they slow down) and two sources of high-frequency electromagnetic waves (high-frequency oscillating currents are induced in the plasma by external coils or waveguides). Ultimately, researchers hope to achieve a burning plasma in which the energy produced by the fusion reaction is sufficient to maintain a high enough temperature to allow the drastic reduction or switching off of all external heating.

Blanket

The inner surface of the VV is covered with the blanket, which provides shielding to the external components from the high-energy neutrons generated by the fusion reaction. To ease its maintenance, the ITER blanket consists of 440 modules, each measuring 1 m × 1.5 m and weighing up to 4.6 tons. Each segment is made of a detachable first wall, directly facing the plasma and removing the plasma heat load, and a semi-permanent blanket shield dedicated to neutron shielding. There, neutrons are slowed down and their kinetic energy is transformed into heat collected by coolants. In future commercial fusion power plants, this energy will be used for electrical power production.

Divertor

Located at the very bottom of the VV, the ITER divertor is situated at the intersection of magnetic field lines where the high-energy plasma particles strike the VV. As in the blanket modules, their kinetic energy is transformed into heat (up to 10 $\mathrm{MW/m^2}$) that is expelled by active water cooling. To ease its maintenance, the divertor is made of 54 remotely-removable cassettes, each holding three plasma-facing targets, known as the inner and outer vertical targets and the dome.

Diagnostics

To provide the measurements necessary to control the plasma performance and to better understand plasma physics, ITER requires an extensive diagnostic system.

In order to operate, these internal components must be supplemented by external systems such as the vacuum pumping system, the remote maintenance system or the fuel cycle and cooling water system. More details on these various components can be found in [3].

1.1.6 Past, present and future of tokamak fusion reactors

As explained in the beginning of this chapter (see section 1.1.1), fusion power is expected to become a major part of the energy mix during the second half of this century. The first commercial fusion power plants could be operating by 2050. This would be the conclusion of a century of scientific and technological research carried out all over the world.

Research on nuclear fusion began soon after World War II. As previously discussed, most research efforts were directed towards magnetic confinement technologies at that time.

By the mid-1950s, fusion machines were being studied in the Soviet Union, the United Kingdom, the United States, France, Germany and Japan.

During this period, Sakharov and Tamm developed the tokamak concept, although their invention was not declassified until 1957. In 1958, the now-historic 2$^{\text{nd}}$ International Conference on the Peaceful Uses of Atomic Energy was held in Geneva, which kickstarted international scientific collaboration on nuclear fusion development. In Europe, this research effort was coordinated by the Euratom treaty.

In 1968, Russian scientists from the Kurchatov Institute of Moscow announced that they had achieved performance in a tokamak device largely superior to anything achieved thus far. From that point, the tokamak became the dominant concept in fusion research and supplanted the other magnetic confinement configurations.

From 1970 to 1990, many tokamaks of various dimensions were built worldwide (Russia, Japan, USA, France, Germany, Italy, UK). During this period, considerable progress was achieved in understanding plasma physics and developing technologies for fusion reactors. All the key issues posed by fusion energy were tackled, and most of them were solved.

Many works carried out during that period demonstrated that plasma confinement efficiency improves in conjunction with the size of the experimental device. Consequently, the conception of larger tokamaks began in the late 1970s with the Joint European Torus (JET) in Europe, JT-60 in Japan and the Tokamak Fusion Test Reactor (TFTR) in the United States. These three large projects aimed at reaching the so-called break-even point ($Q = 1$), from which a device releases as much energy as it requires to produce fusion. However, all three fell short of this goal (see Table 1.1).

Experiments using a mix of deuterium and tritium (D-T) as fusion fuel began in the early 1990s at TFTR and JET (see Fig. 1.11). The world's first controlled release of fusion power was achieved at JET in 1991. While JET and TFTR produced a significant amount of fusion power with a Q close to 1, exceptionally long-duration plasma pulses were achieved in Tore Supra (Cadarache, France). As far as it is concerned, JT-60 lacked

Table 1.1: Major tokamak reactors

Reactor	**Country**	**Operation**	**Minor radius (m)**	**Major radius (m)**	**Magnetic field (T)**	**Fuel**	**Fusion power (MW)**	**Energy gain Q**
TFTR	USA	1982–1997	0.85	2.5	5.6	D-T	10.7	0.3
JET	Europe	1983–ongoing	1	2.96	3.5	D-T	16	0.6
JT-60	Japan	1985–ongoing	0.85	3.2	4.4	D-D	?	<1
Tore Supra	France	1988–ongoing	0.7	2.25	4.2	H-H D-D	N/A	≈ 0
ITER	International	2025–2045	2	6.2	5.3	D-T	500	10
DEMO	?	2033–2050	?	?	?	D-T	2000	25

H: hydrogen, D: deuterium, T: tritium. Figures for DEMO are projected.

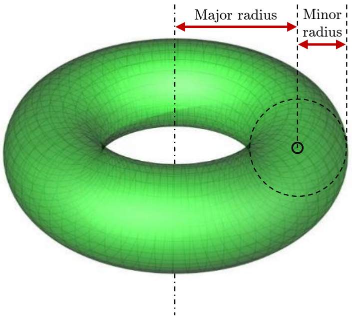

Figure 1.10: Minor and major radii of a tokamak

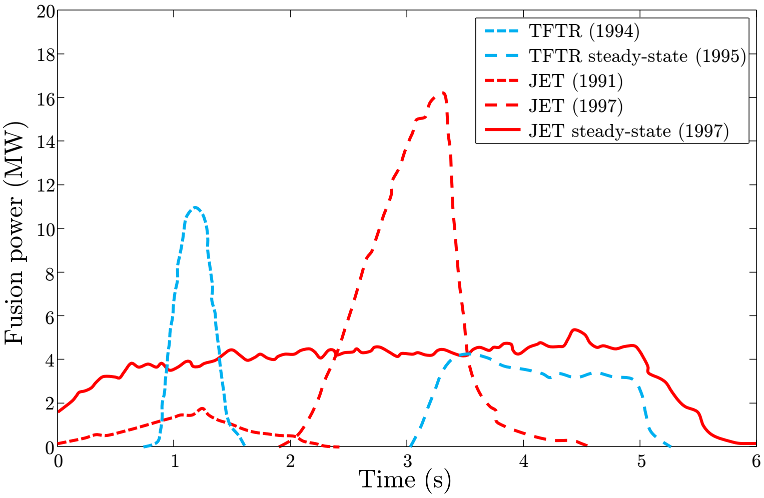

Figure 1.11: Best plasmas achieved in TFTR and JET

tritium-handling facilities and was consequently limited to deuterium-only operations. However, the Japanese reactor achieved the highest values of the three key parameters on which fusion depends: density, temperature and confinement time, which would have yielded break-even fusion if a deuterium-tritium mix had been used.

Today, around 200 tokamaks have been built worldwide. With JET, TFTR and JT-60, scientists have gradually approached the so-called break-even point. ITER's main objective is to go much further and release 10 times as much energy as it will use to initiate the fusion reaction (50 MW of input power, 500 MW of output power). ITER will pave the way for a demonstration power plant (DEMO) in the 2030s with an objective of reaching an energy gain factor in the order of $Q = 25$.

The following paragraphs focus on four major tokamak projects (see Fig. 1.12) paving the way for commercial fusion power plants:

- JET, which currently holds the record of producing 16 MW for an input power of 24 MW ($Q = 0.65$);
- Tore Supra, which holds the record for the longest plasma achieved in a tokamak (6 minutes 30 seconds and over 1000 MJ of energy injected and extracted in 2003);

- ITER, to be commissioned in France around 2025, will be the first fusion experiment producing more power from D-T fusion than energy necessary to heat the plasma; and
- DEMO, which is intended as a prototype commercial fusion reactor building upon the expected success of ITER.

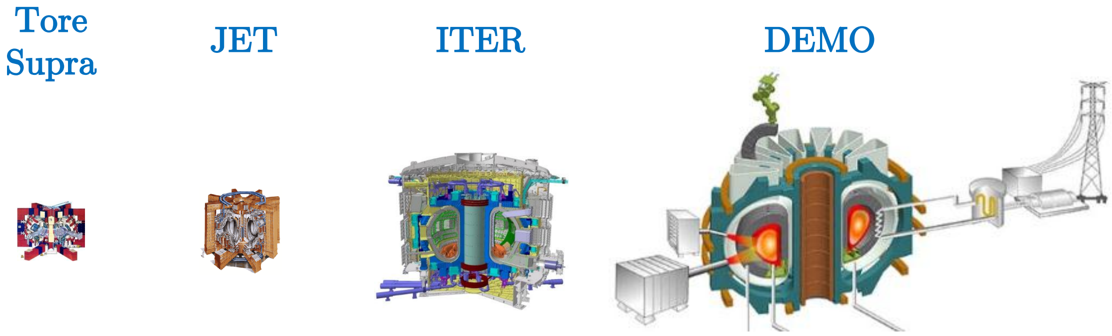

D = 4.8 m
V = 25 m^3
Q ≈ 0
P ≈ 0 MW_{th}

D = 5.92 m
V = 80 m^3
Q ≈ 0.6
P ≈ 16 MW_{th}

D = 12.4 m
V = 800 m^3
Q ≈ 10
P ≈ 500 MW_{th}

D ≈ 13–19 m
V ≈ 1000–3500 m^3
Q ≈ 25
P ≈ 2000–4000 MW_{th}

Figure 1.12: Comparison of Tore Supra, JET, ITER and DEMO

Joint European Torus (JET)

JET was conceived during the 1970s as the flagship of the European Fusion Programme. It marked a key step in international collaboration within Europe and, in 1991, achieved the world's first controlled release of fusion power.

Its main goal was to obtain and study plasmas in conditions and dimensions approaching those needed in a thermonuclear reactor, therefore in a machine the parameters of which would be at least an order of magnitude larger than in any other machine. JET represented major progress since the largest machine in Europe at that time was the Tokamak de Fontenay-aux-Roses (TFR) in France, which had an average plasma volume of 1 m^3, i.e. 100 times less than JET. JET is still the largest Tokamak in the world.

The device was constructed in Culham (UK) between 1979 and 1983 (see Fig. 1.13). Its very first plasma was achieved on 25 June 1983, but its first controlled fusion power was not produced until November 1991. The record-setting power of 16 MW was achieved for one second in 1997 using mixed deuterium-tritium fuel with a Q factor of 0.65, quite close to the break-even point ($Q = 1$). Its main features are summarised in Table 1.1.

Many of the technological and scientific difficulties of achieving controlled fusion were overcome through years of JET exploitation. Besides demonstrating the technical feasibility of fusion using deuterium and tritium, JET made it possible to study and validate new technologies required by D-T operations: management of the tritium cycle and development of a remote handling (RH) system. In particular, the latter made it possible to replace the whole divertor by remote means in 1998.

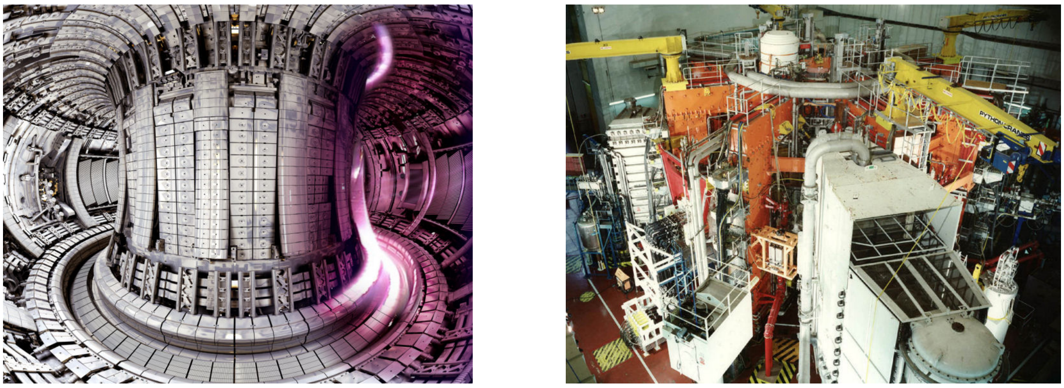

(a) (b)

Figure 1.13: Views from inside and outside the Joint European Torus (image courtesy of EFDA-JET)

Tore Supra

Tore Supra is a French tokamak situated within the Cadarache nuclear research centre. It began operating in 1988 after the discontinuation of TFR (see Fig. 1.14). With a major radius of 2.25 m and a minor radius of 0.70 m, Tore Supra is still the third largest operating tokamak in the world after JET and JT-60. It has been, for a very long time, the only large tokamak featuring superconducting toroidal magnets, which allows the generation of a permanent toroidal magnetic field. Tore Supra is also the only tokamak with actively cooled plasma-facing components. For these reasons, Tore Supra was unique in its time for its capacity to explore long-duration plasmas.

Since 2003, Tore Supra has held the world record for the longest plasma achieved in a tokamak device, with a plasma lasting 6 minutes and 30 seconds and producing more than 1 GJ of energy. The practically uninterrupted operation of its superconducting magnet, since 1988, represents in itself a considerable breakthrough that will benefit ITER and its successors.

In the late 2000s, the Tore Supra tokamak was fitted with more powerful heating antennas that allowed the implementation of experiments that were as ITER-relevant as possible. However, the machine was not designed to realise D-T fusion reactions (hydrogen, helium or deuterium-only plasmas); therefore, no fusion power production can ever be expected from it.

Recently, it was transformed into the Tungsten (W) Environment in Steady-state Tokamak (WEST) facility [4] dedicated to studying ITER divertor issues.

(a) (b)

Figure 1.14: Inside and outside views of Tore Supra (image courtesy of CEA IRFM)

ITER

The ITER project gives context to this thesis. Consequently, it is described more in-depth.

The ITER project brings together the world's tokamak research community in a single international collaboration. The current participants in the project are the European Union, Japan, the People's Republic of China, the Republic of India, the Republic of Korea, the Russian Federation and the United States (see Fig. 1.15). Currently under construction in France, ITER will be several times larger than any previous tokamak.

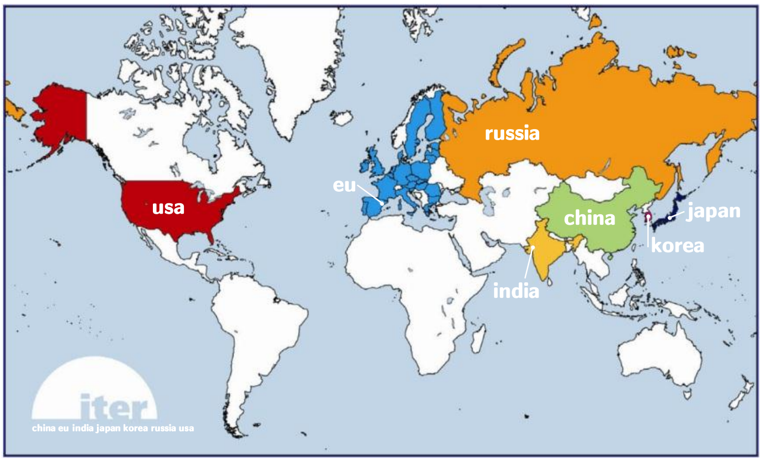

Figure 1.15: Countries participating in the ITER project (image courtesy of the IO)

Although fusion research has made significant scientific progress thanks to the large fusion experiments constructed in the 1980s (short energetic pulses in JET, long pulses in Tore Supra), it was clear from an early stage that larger, more powerful devices would be needed to create the conditions expected in a fusion reactor and to demonstrate the scientific and technical feasibility of fusion energy. This reactor should be the synthesis of all the technologies developed individually in other smaller-scale fusion experiments.

The idea for ITER originated at a Cold War-era summit organised in Geneva in November 1985 between Soviet General Secretary Mikhail Gorbachev and U.S. President Ronald Reagan. First proposed by French President François Mitterrand as a possible collaboration between the United States and the Soviet Union, an international project gathering the former Soviet Union, the United States, the future European Union (via Euratom) and Japan was set up to develop fusion energy for peaceful purposes. The ITER project was later enlarged to include additional parties such as the People's Republic of China (since 2003), the Republic of Korea (since 2003) and the Republic of India (since 2005).

Conceptual design work began in 1988 ans was followed in 1992 by engineering design activities. The final ITER design was approved by all parties in 2001. Negotiations on the joint implementation of ITER began in 2003. These negotiations drew up the international agreement for the construction, exploitation and decommissioning of ITER, deciding how costs would be shared and how the project would be organised in general. Signed in 2006, the ITER Agreement led to the establishment of the ITER International Fusion Energy Organization (ITER Organization), which would be responsible from that moment for the construction, operation and decommissioning of ITER.

The process of selecting a location for ITER took a long time and was finally successfully concluded on 28 June 2005, when it was officially announced that ITER would be built in the European Union at the Cadarache site, near Aix-en-Provence in the South of France. Other candidates were Clarington (Canada), Vandellòs (Spain) and Rokkasho-Mura (Japan). In addition to fulfilling all the technical requirements, the Cadarache site had the advantage of already hosting Tore Supra (which was the world's largest superconducting fusion experiment at that time) and of providing existing technical expertise and support facilities. The ITER site at Cadarache covers a total surface area of 42 ha.

Site clearing and leveling took place in 2007 and 2008, respectively. The building construction process began in 2010 (see Fig. 1.16), which should lead to the first plasma between 2021 and 2025. This will be followed by an exploitation phase of about 20 years aimed at testing essential physics and technologies for future fusion power plants.

ITER's construction costs have been estimated to be around 12 billion euro, to be spread over more than 10 years. Since ITER will be built in Europe, the EU will contribute up to half of the construction costs while the other parties will share the remaining costs equally. Most of the components are designed, manufactured and delivered by the ITER parties as in-kind contributions rather than funding the ITER Organization to procure the whole machine. In order to manage their respective contributions to the project, each ITER member established its own domestic agency, which is responsible for the research and development (R&D), design coordination and fabrication of its share of components. Europe's contribution to ITER is managed by Fusion for Energy (F4E), which was established in Barcelona (Spain) in 2007.

(a) (b)

Figure 1.16: Architectural view (a) and construction (b) of the ITER site (images courtesy of the IO)

The main objective of ITER is "to demonstrate the scientific and technological feasibility of fusion power for peaceful purposes". This general objective is developed through three specific technical objectives:

- first, ITER should generate more power than it consumes by producing fusion energy with an energy gain factor Q around 10 (corresponding to 500MW) during pulses of several hundred seconds and Q larger than 5 up to an hour;
- second, ITER must validate basic design choices with a view to future commercial power plants, in particular by demonstrating key technologies such as superconducting magnets and remote maintenance; and
- third, ITER must test concepts for tritium breeding.

If ITER will not be an electricity producer, scientists will study plasmas in conditions similar to those expected in an electricity-generating fusion power plant. It will burn a fuel mix of deuterium-tritium to produce 500 MW of fusion power for extended periods of time, from an energy input of 50 MW. It will therefore be the first fusion experiment to produce net power. To achieve this, ITER will be twice the size of JET and 16 times as heavy as any previous tokamak (more than 5000 t). It will also be equipped with superconducting magnets in order to sustain long plasma pulses (see Fig. 1.17).

As previously mentioned, the central solenoid is the key component that will induce a powerful current in the ITER plasma and maintain it during long plasma pulses. In JET, the solenoid generates plasma currents of about 5 MA in plasma pulses lasting up to 60 s (see Fig. 1.11 on p. 10). Because the plasma volume in ITER will be 8 times higher than in JET, the magnetic energy required from the central solenoid will be much higher as well. It will initiate and sustain a plasma current of 15 MA for durations in the range of 300–500 s.

Another example of the scale effect in ITER is found in the levels of neutron flux and fluence, which will be about 10 and 10000 times higher, respectively, than the harshest

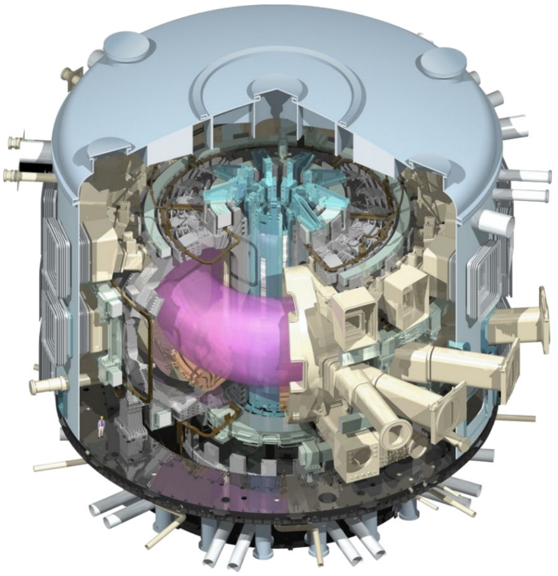

Figure 1.17: ITER tokamak (image courtesy of the IO)

levels experienced in existing machines. This severe environment will strongly impact the design of a large range of components, including diagnostic and RH systems, which will have to cope with phenomena not previously encountered while performing accurately and precisely (see section 1.1.9).

IFMIF and DEMO

Constructing and operating ITER is undoubtedly an essential step towards large-scale fusion energy generation, but ITER is not an end in itself. The long-term objective of fusion research remains the construction of power station prototypes demonstrating operational safety, environmental compatibility and economic viability. Before reaching that point, technological progress is still required in several areas, particularly in the development of plasma-facing materials able to withstand the extreme conditions resulting from high-energy fusion neutrons. To minimise the quantity of radioactive waste produced by future reactors, these materials will also have to demonstrate low activation properties.

In parallel with ITER and as part of the so-called Broader Approach Agreement [5], a joint European/Japanese facility known as the International Fusion Materials Irradiation Facility (IFMIF) will be constructed to test materials against neutron damage and irradiation. IFMIF is an accelerator-based neutron source that will use deuterium-lithium stripping reactions to simulate 14 MeV neutrons from deuterium-tritium fusion reactions. It will produce high-energy neutrons and fire them at samples of materials identified as suitable for the walls of future commercial fusion power plants. A site for the facility has already been identified in Japan, and operations are planned to begin in mid-2017.

The next step after ITER is known as DEMO. This demonstration power plant should exhibit large-scale electrical power production and tritium fuel self-sufficiency, thus paving the way for commercially viable fusion power plants. It is currently being designed and should be constructed during ITER and IFMIF operations (2025–2045) and begin operations 30–35 years after ITER construction commences (2040–2045).

On an indicative basis, DEMO should be able to produce at least four times as much fusion power as ITER (2 GW) on a continual basis, with an energy gain around 25.

Unfortunately, there is presently no international consensus on DEMO's exact parameters or scope. Unlike ITER, most of the work on DEMO has been done without much international collaboration. Many divergent conceptual ideas for DEMO designs have been produced over the years. On one hand, Europe and Japan are cooperating on DEMO design work as part of the Broader Approach. On the other hand, Korea has already proposed a concept for DEMO known as K-DEMO [6]. The target completion date for K-DEMO is currently set at the end of 2037. Since it will lack important feedback from ITER and IFMIF at that time, K-DEMO will be used during its first operational phase as a component test facility. This phase should extend from 2037 to approximately 2050, after which it should begin a second phase involving full steady-state operation and electricity generation.

If it is successful, DEMO will lead fusion into its industrial era and will open the way towards the first generation of commercial fusion power plants.

1.1.7 Maintenance of fusion reactors

Fusion reactors require maintenance in three situations:

- first, in cases of system failure preventing the normal operations of the facility (e.g. major leak resulting in the loss of the primary vacuum);
- then, due to the normal ageing of systems, thus necessitating periodic preventive replacements (e.g. divertor cassettes, blankets); and
- finally, in case of system upgrades for experimental purposes in reactors such as ITER or to boost the power-generating capacity of future commercial fusion power plants.

As a general rule, ITER components with a probability of failure greater than 1 in 20 years of reactor operations require scheduled preventive maintenance or replacement. Components with a probability of failure between 1 in 200 years and 1 in 20 years do not require scheduled maintenance but are likely to require unscheduled maintenance.

In addition to these anticipated maintenance operations, maintenance systems in fusion reactors are required to allow for the conduct of unscheduled interventions resulting from unexpected events, such as plant failures, unexpected deformations in the tokamak, project demands for tasks that were not previously identified, or even failure of the maintenance equipment itself. In all cases, any unplanned event occurring during a scheduled or unscheduled shutdown will invariably imply the need for remote inspection prior to a systematic analysis of the event.

To the maximum possible extent, such maintenance operations shall be performed manually by qualified workers in full accordance with the “as low as reasonably achievable” (ALARA) principle. As an example, a target maximal exposure dose rate for hands-on maintenance in ITER has been set to 100 μSv/h. However, the option of hands-on maintenance becomes impractical, difficult or simply impossible in many circumstances, such as high biological dose rates. In this case, maintenance tasks will be performed with RH techniques.

Remote handling is the synergistic combination of technology and engineering management systems to enable operators to safely, reliably and repeatedly perform manipulation of items without being in personal contact with those items.

The current approach to RH maintenance on fusion reactors has benefited greatly from the experience gained in existing experimental fusion reactors such as JET. RH was first conducted inside the JET tokamak in 1998 after 15 years of machine operation. The RH experience gained from JET shows that successful remote maintenance mainly relies on two aspects:

- the detailed preparation of the RH tasks; and
- the design of reactor components for RH compatibility.

As a general rule, the preparation of remote maintenance operations requires three times as much time as that needed to perform the maintenance task [7]. This preparation can involve the extensive use of mock-ups in order to validate each RH task prior to its execution. For obvious cost and time considerations, virtual mock-ups are always favoured, although full-scale physical mock-ups may also be necessary to develop and validate tasks with higher physical uncertainties, such as structural compliance.

Experience gained from JET also demonstrates that the feasibility of remotely maintaining a reactor that has not previously been designed to be RH-compatible varies from being impossible to being possible but with significant investments required in time, money and risk. When remote maintenance of non RH-compatible systems was deemed feasible, a costly work programme including the design and development of new RH equipment and operations was implemented. Moreover, the duration needed to perform the maintenance tasks was found to be 3–5 times longer than similar tasks involving components that had been designed with RH compatibility [8].

In cases where such a remote intervention was judged impossible, e.g. due to access and mass limitations, the tasks were performed manually within the limits of permissible personnel radiation exposure, which the radiation and contamination levels in ITER will not permit. For this reason, ITER represents an unequalled challenge in terms of RH system design because it will be much more demanding and complex than any other remote maintenance system previously designed. After the machine enters its active phase, it will be impossible to carry out in-vessel interventions or inspections other than by RH means.

The speed, efficiency and flexibility of RH operations will directly and significantly impact the overall ITER tokamak availability. These aspects will become even more important in future fusion power plants because high plant availability is the only prerequisite to lowered energy production costs.

1.1.8 Robotic devices for the inspection and maintenance of fusion reactors

As stated in the previous section, the maintenance of the ITER tokamak will rely, to a significant extent, on the ITER RH capability [9]. Wherever possible, manual maintenance methods will be used. However, all the in-vessel components must be inspected, handled and maintained using RH methods. With the exception of the Neutral Beam (NB) cell, all the remotely maintainable ITER systems will be transported from the Tokamak Building to the Hot Cell (HC) facility for maintenance and repair. Additionally, a mixed approach involving both RH and manual operations may be necessary in some areas of the port cells and Tokamak Building galleries.

As discussed in the previous section, the efficiency and safety of RH operations in ITER is significantly related to the RH compatibility of the items being handled and to the design and operation of the RH equipment itself.

The baseline RH equipment for ITER currently comprises the following systems:

- Blanket Remote Handling System (BRHS)
- Divertor Remote Handling System (DRHS)
- Cask and Plug Remote Handling System (CPRHS)
- In-Vessel Viewing System (IVVS)
- Neutral Beam Remote Handling System (NBRHS)
- Hot Cell Remote Handling System (HCRHS)
- RH supervisory Control System (RHCS)
- Multi-Purpose Deployer (MPD)

In order to provide the reader with the necessary insight to grasp the complexity of the ITER remote maintenance equipment, the following sections will briefly describe each of these systems.

Blanket Remote Handling System (BRHS)

By absorbing radiant heat flux and charged particle flux from the plasma, the ITER blanket structure contributes to providing shielding to reduce heat and neutron loads in the VV and ex-vessel components. It is composed of 440 modules, each of which comprises a first-wall panel and a shield block, that are designed for individual replacement. This replacement involves the remote handling of 4.5 t-blanket modules with 2 mm position accuracy in a space-constrained, in-vessel environment under gamma radiation up to 10 kGy/h. To meet these requirements, the Blanket Remote Handling System (BRHS) has been designed as a rail-mounted vehicle and manipulator system that will be deployed through four RH ports located at the equatorial level of the machine.

The BRHS will provide the following main functions:

- removal and installation of 440 blanket modules of 30 different types;
- replacement of all first-wall panels within a period of 24 months;
- transportation of blanket modules and first-wall panels into and out of the VV;
- blanket module and RH tool exchange at the equatorial port;
- bolting for fixing modules by flexible supports;
- insertion of NB duct liner maintenance tools;
- cooling pipe connection/disconnection, cutting, welding and weld inspection; and
- leak testing of cooling pipe joints.

The current reference design of the BRHS consists of the following materials:

- an in-vessel transporter (IVT) that transports and handles blanket modules and tools inside the VV. The IVT comprises the following elements:
  - two articulated semi-circular rails, deployable from two RH ports and forming a continuous 360° toroidal rail when installed (see Figs. 1.18 and 1.20);
  - two vehicle/manipulator systems operated simultaneously and travelling along the rail, each of which incorporates a telescopic manipulator capable of accessing all in-vessel areas except the divertor area (see Fig. 1.19);
  - a blanket handling gripper mounted on the telescopic manipulator that grips a blanket module and temporarily bolts it to the VV wall (see Fig. 1.21);
  - dedicated rail supports that assist in the deployment of the final rail elements;
  - the rail deployment equipment that, by means of a dedicated vehicle manipulator, assembles and deploys the rails; and
  - the umbilical handling equipment that handles the long and complex umbilical during 180° vehicle and manipulator travel.

- a blanket transport that delivers blanket modules and tools to the IVT with access through an equatorial RH port.
- a blanket pipe tool system that provides a set of tools to cut, weld and inspect the module water cooling pipes.
- bolting tools to fix and secure the blanket modules.
- an in-cask storage rack that provides storage for three modules inside the transfer cask (see also section on the CPRHS, p. 23).

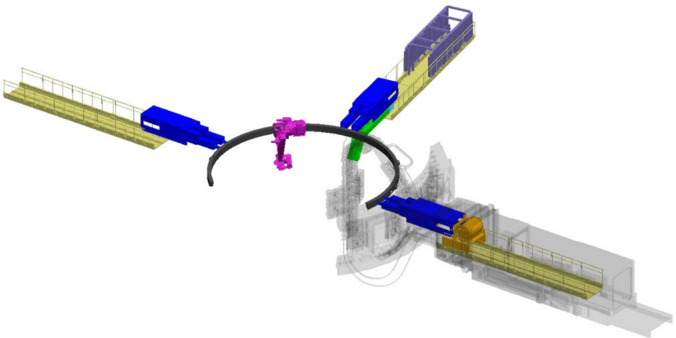

Figure 1.18: Configuration with partial rail deployment (240°-deployed rail covering 180°) (image courtesy of JADA)

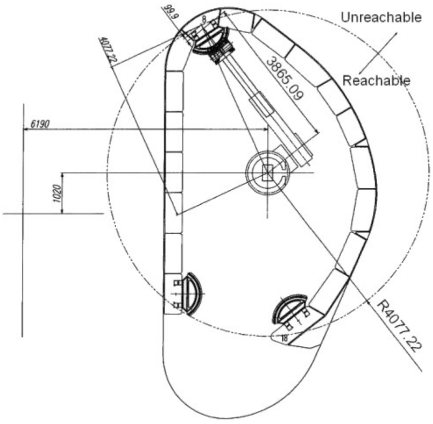

Figure 1.19: Telescopic manipulator (image courtesy of JAERI)

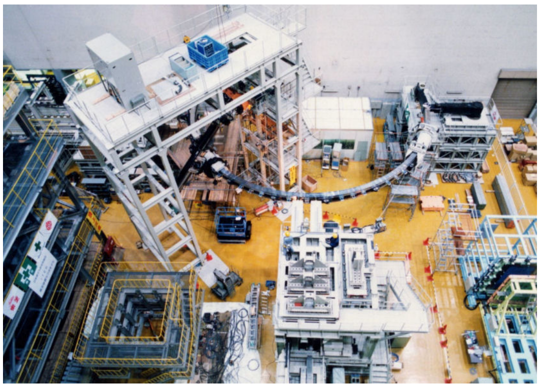

Figure 1.20: Full-scale demonstration of rail deployment (image courtesy of JAERI)

Figure 1.21: Full-scale demonstration of blanket handling (image courtesy of JAERI)

Divertor Remote Handling System (DRHS)

Similar to the blanket system, the ITER divertor provides shielding to reduce radiation and particle loads affecting the lower part of the plasma chamber while allowing neutral particles to be exhausted in the vacuum system. Due to the erosion of the plasma-facing components, the replacement of the divertor is foreseen several times during ITER's lifetime. Due to a combination of radiological hazards (dust, tritium and activation), this replacement involves the remote removal and installation of 54 removable cassettes (9–11 t, typical dimensions of 3.3 × 2.3 × 0.8 m^3). Severe space constraints require all cassettes to be handled in a cantilevered fashion within very tight tolerances. To carry out this task, specific RH equipment has been designed to remotely replace the divertor system through three lower-level ports.

The DRHS will provide the following main functions:

- extraction and insertion of 54 divertor cassettes;
- transportation of cassettes to/from dedicated transfer casks docked at the RH ports;
- extraction and insertion of diagnostic assemblies located at the divertor level;
- transportation of diagnostic assemblies to/from a dedicated transfer cask;
- removal and replacement of the RH port primary closure plate (PCP);
- dust removal in the divertor region during cassette extraction; and
- cutting, welding and inspection of cassette and diagnostic rack cooling pipes.

The current reference design of the DRHS includes the following materials:

- two cassette multi-functional movers (CMM), including a tractor and a set of changeable end-effectors, which implement the radial transport of components along the RH ports (see Figs. 1.22 and 1.23);
- two cassette toroidal movers (CTM) that implement the toroidal transport of cassettes from the RH port to their final assembly location inside the VV (see Fig. 1.24);
- several dexterous manipulator arms, equipping both CMM and CTM, for tool handling and general purpose manipulation (see Fig. 1.25);
- a set of CMM end-effectors providing the interface for transporting in-vessel components (e.g. divertor cassettes) and RH equipment (e.g. tooling);
- remote-handled vacuum cleaners, installed in both CMM and CTM, for the removal of radioactive dust from the divertor region; and
- various tooling sets to cut, align, weld and inspect the divertor cooling pipes; operate the divertor cassette locking system; and remove and replace the diagnostic rack.

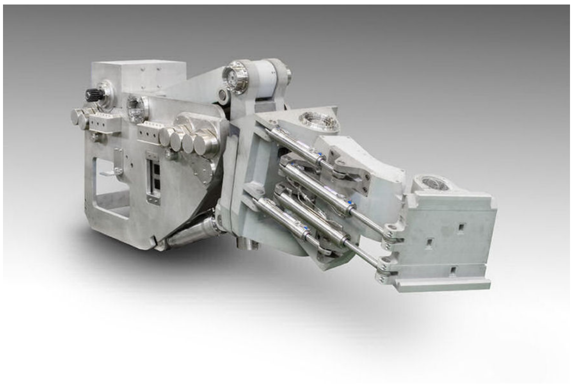

Figure 1.22: Realistic rendering of the CMM (image courtesy of VTT-TUT)

Figure 1.23: The full-scale divertor test platform DTP2, which is used for the design validation and demonstration of cassette operation capabilities (image courtesy of VTT-TUT)

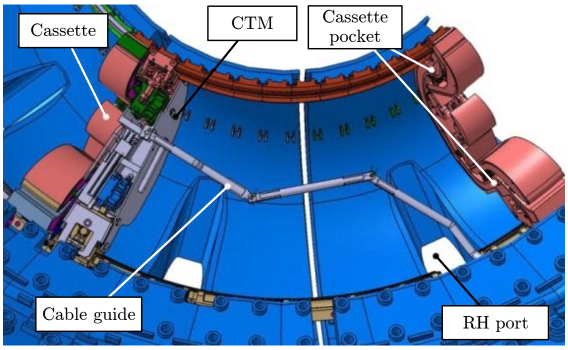

Figure 1.24: CTM carrying a divertor cassette (image courtesy of VTT-TUT)

Figure 1.25: Demonstration of the manipulator arm mounted on the CMM at DTP2 (image courtesy of VTT-TUT)

Cask and Plug Remote Handling System (CPRHS)

The Cask and Plug Remote Handling System (CPRHS) is devoted to the confinement and transportation of ITER's in-vessel components, such as port plugs, between the Tokamak Building and the HC facility where they are repaired, refurbished, tested or disposed of. In addition, the CPRHS also hosts other RH equipment, such as the BRHS or DRHS equipment, which are deployed for removal/replacement of in-vessel components (blanket modules or divertor cassettes). This transfer involves 21 autonomous and remotely operated transfer casks (max 100 t, 8.5 m long, 3.7 m high and 2.6 m wide) that can access VV ports at all three levels of the Tokamak Building.

The CPRHS will provide the following main functions:

- remote transfer of clean/activated/contaminated in-vessel components between the VV and the HC facility (see Fig. 1.28);
- remote transfer of RH equipment between the VV and the HC facility;
- primary confinement during all transfer phases;
- docking and un-docking onto the VV or HC docking flange, including alignment features (see Fig. 1.29);
- preserving confinement during opening and closing of VV and HC access; and
- installation and removal of components into/from the VV and the HC.

The current reference design of the CPRHS (see Figs. 1.26 and 1.27) includes the following materials:

- a cask envelope providing confinement of the transported in-vessel components or RH equipment during transfer that is equipped with a front double-door system interfacing with the VV port flange and a back double-door system facilitating rescue operations;
- a pallet supporting the weight of the docked cask envelope, enabling alignment with the docking flange and supporting the large multi-connector that supplies the necessary services to the whole CPRHS unit when docked; and

- an autonomous cask transfer system (CTS) supporting the weight of the cask envelope and the pallet during transfer and holding the necessary driving, steering, navigation and guidance systems.

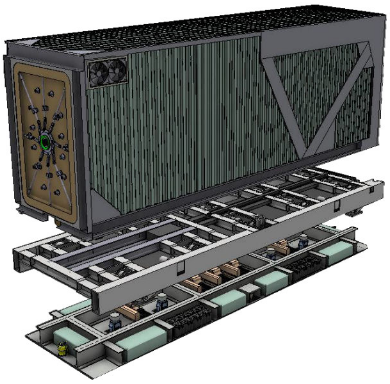

Figure 1.26: Exploded view of the CPRHS (image courtesy of Fusion for Energy)

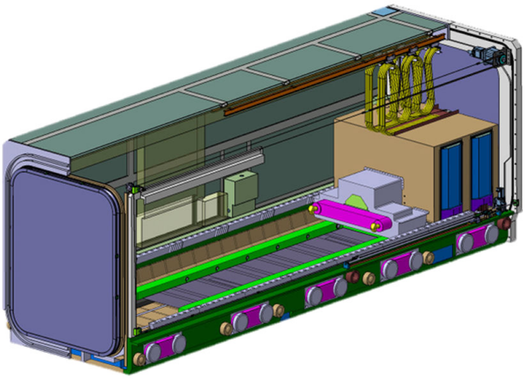

Figure 1.27: CPRHS including a port plug in-cask mover (image courtesy of Fusion for Energy)

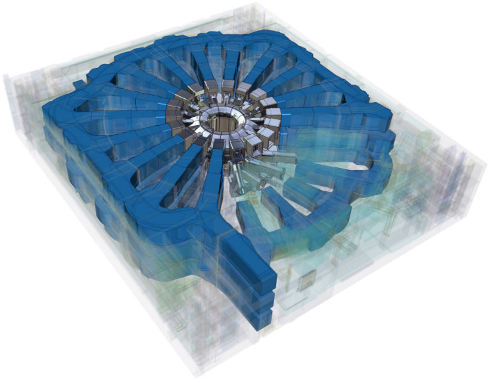

Figure 1.28: Complete set of CPRHS trajectories (swept volumes) within the Tokamak Building (image courtesy of Fusion for Energy)

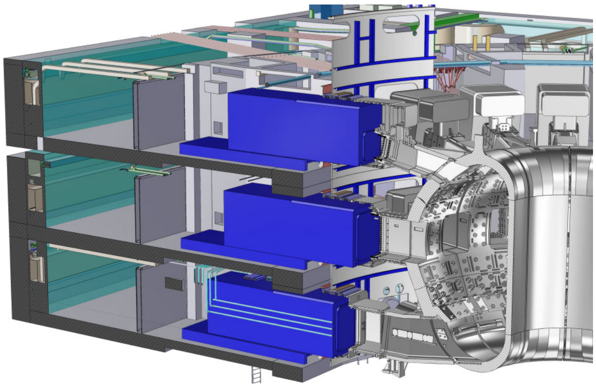

Figure 1.29: CPRHS docked at ports from the various tokamak levels (image courtesy of Fusion for Energy)

In-Vessel Viewing System (IVVS)

The In-Vessel Viewing System (IVVS) is a fundamental tool for ITER's operations that aims at performing visual inspections and providing information related to the erosion of the in-vessel components (blanket modules, divertor cassettes, heating/diagnostic plugs, test blanket modules). Six IVVS units will be installed in six lower-level port extensions. Each unit comprises a viewing/metrology probe mounted on a deployment arm. Periodically (e.g. during planned shutdowns) or on request (e.g. after a plasma disruption with suspected damages) the IVVS probes will be deployed from their storage positions into the plasma chamber, between the divertor outer target and the lower blanket module, in order to perform viewing and metrology tasks on the plasma facing-components (see Fig. 1.30).

The IVVS will provide the following main functions:

- inspection of the first wall and other in-vessel plasma-facing components with a spatial resolution better than 1 mm at short range and better than 3 mm further;
- production of range measurements of the first wall and other in-vessel plasma facing components, with a precision allowing the evaluation of the in-vessel erosion and the amount of mobilised dust with an indicative maximal error of ±100 kg;
- providing maximum coverage of the divertor region, avoiding blind spots;
- operation under a high magnetic field;
- self-illumination without relying on any external light source; and
- shielding the viewing/metrology probe when not in operation.

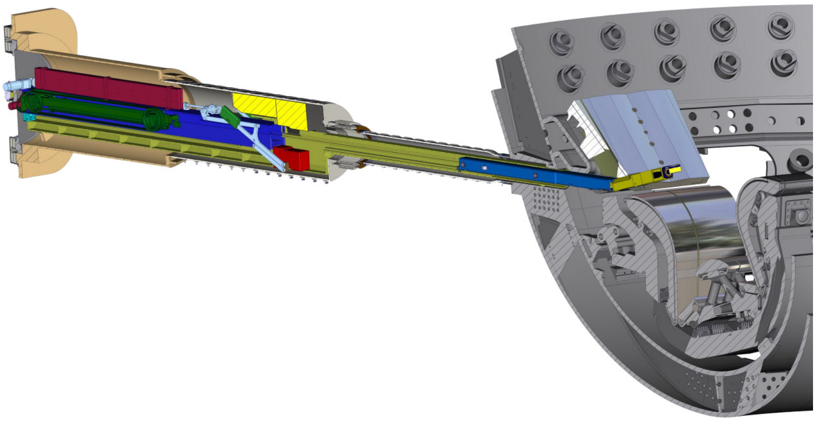

Figure 1.30: IVVS in deployed position (image courtesy of Fusion for Energy)

The current reference design of one IVVS unit includes the following materials:

- a guide tube permanently located in the IVVS port extension;
- fixed shield blocks located around the resident guide tube at the level of the stowed scanning probe in order to protect the IVVS from scattered neutrons;
- an electrical and optical vacuum feed-through; and
- a 4.2 m-long removable cartridge (see Fig. 1.31) that can be extracted from the port extension into a dedicated transfer cask allowing the maintenance, replacement and/or upgrade of the system. The IVVS cartridge is composed of the following materials:
  - a 3.8 m-long mobile assembly consisting of a scanning probe relying on the amplitude modulation of a coherent single-mode laser to perform viewing and ranging tasks (see Fig. 1.32), a longitudinal trolley travelling linearly on the guide tube from the cartridge towards the VV and a hinged section allowing the rotation of the scanning probe once deployed inside the VV;
  - an actuation system relying on a rigid chain that pushes or pulls the mobile assembly from the rear. The chain is stored in a three-layer magazine situated on the top of the cartridge. Its actuation is achieved through a single stepper motor placed near the outer end of the port extension, where the low magnitude of the magnetic field permits its operation;

- a cable reeling system that manages the 7.5 m-long cable required for the deployment of the mobile assembly. It consists of two fixed pulleys and two traveling pulleys whose translation is synchronised with the rigid chain drive so they move at the exact speed required by the cable deployment;
- a moveable shield block made of B_4C that protects the scanning probe from direct neutron streaming. The block is lowered to allow the passage of the mobile assembly when an inspection is requested; and
- an electrical and optical service connector.

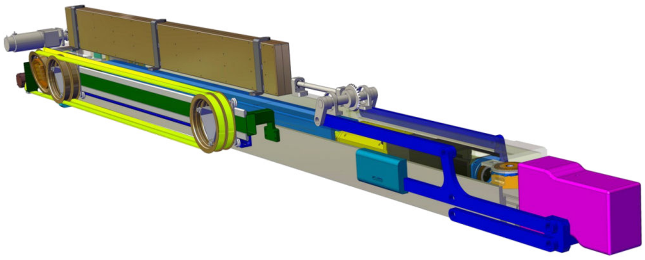

Figure 1.31: IVVS cartridge (image courtesy of Fusion for Energy)

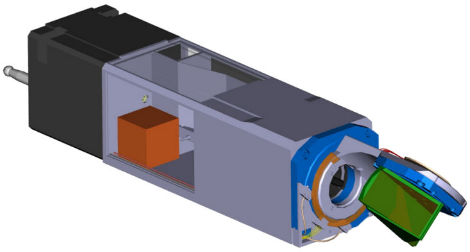

Figure 1.32: IVVS scanning probe (image courtesy of Fusion for Energy)

Neutral Beam Remote Handling System (NBRHS)

The neutral beam cell hosts one diagnostic neutral beam injector, two heating and current drive neutral beam injectors and three diagnostic plugs. Due to neutron activation and tritium contamination, these systems will require remote maintenance. The Neutral Beam Remote Handling System (NBRHS) includes a variety of devices, such as a crane, manipulators, support cradles, tooling, etc., that must coordinate in order to accomplish various maintenance tasks.

The NBRHS will provide the following main functions:

- removal and replacement of the caesium ovens;
- removal and replacement of the 26 t beam source;
- removal and replacement of the beam-line components;
- removal and replacement of the neutral beam-gate valve and duct bellows; and
- assistance in the hands-on repair of the active correction and compensation coils.

The current reference design of the NBRHS includes the following materials:

- a 90 m-long 50 t monorail crane system that includes a hoist and a single rail, which comprises up to 7 switching points allowing the selection of which region the crane should travel to (see Figs. 1.33 and 1.34);
- a beam source manipulator mounted on a trolley that includes a mast and a boom (see Fig. 1.35);
- a beam-line transporter and manipulator system (see Fig. 1.36); and

- a large number of tools necessary to assist and execute bolting, unbolting, cutting and welding tasks on pipes and lip seals.

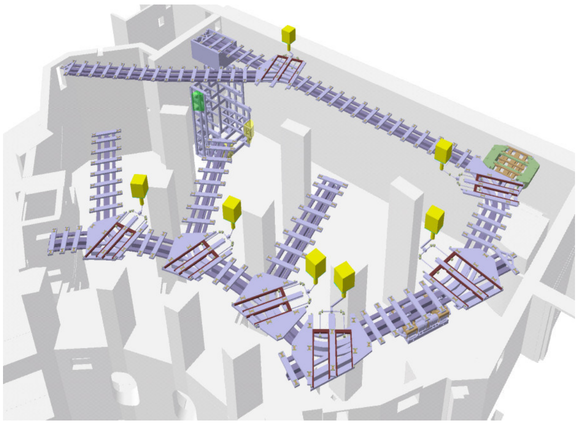

Figure 1.33: Monorail crane layout (image courtesy of CCFE)

Figure 1.34: Main hoist attached to the monorail (image courtesy of CCFE)

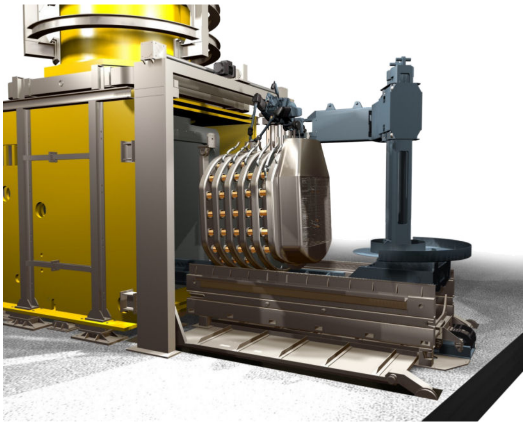

Figure 1.35: Neutral beam source maintenance (image courtesy of CCFE)

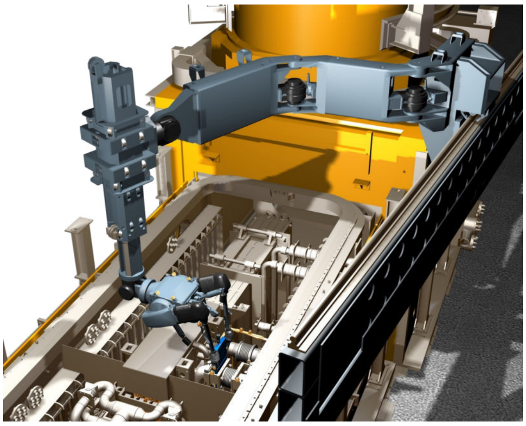

Figure 1.36: Beam-line transporter and manipulator system (image courtesy of CCFE)

Hot Cell Remote Handling System (HCRHS)

Maintenance of in-vessel or neutral beam injection components will generally be accomplished by the replacement of spent components with new or refurbished units. The activated and contaminated components (divertor cassettes, blanket modules, etc.) will be transported to the HC facility for eventual repair, refurbishment or disposal (see Fig. 1.37). The Hot Cell Remote Handling System (HCRHS) provides space and handling facilities for the reception, dispatching, decontamination, storage, repair, refurbishment and testing of these radioactive and/or contaminated tokamak components and for the maintenance and storage of the in-vessel and HC RH tools.

The HCRHS will provide the following main functions:

- remote maintenance of blanket modules, divertor cassettes, port plugs, diagnostic systems, IVVS cartridge, torus cryopumps and primary closure plates;

- cask storage and maintenance of in-cask equipment;
- testing and maintenance of RH equipment;
- cleaning, dust removal and inspection of components; and
- operation procedure checking and full-scale training in the cold RH test facility.

The current reference design of the HCRHS includes the following materials:

- refurbishment work stations (including booms, local gantry cranes, mast);
- dexterous telemanipulators end-effectors;
- direct viewing manipulators;
- inspection equipment (including weld NDT, visual inspection, metrology);
- cleaning workstations (see Fig. 1.38);
- cell maintenance equipment (including telescopic mast-mounted manipulator);
- a hot RH test facility (hot RHTF) including the following appropriate interface mock-ups:
  - a 60° divertor-level VV sector and the necessary port extensions; and
  - docking flanges for all levels (including IVT/MPD interfaces).
- a cold RH test facility (cold RHTF), transferred to the Assembly Hall, including the following full-scale mock-ups (see Fig. 1.39):
  - a 120° VV sector with blanket modules attachments, divertor rails and the necessary port extensions and docking flanges;
  - a set of dummy reconfigurable blanket modules;
  - a set of dummy divertor cassettes (central, second, standard cassettes); and
  - dummy ELM and vertical stability coils.
- blanket, divertor, plug and neutral beam component storage facilities.

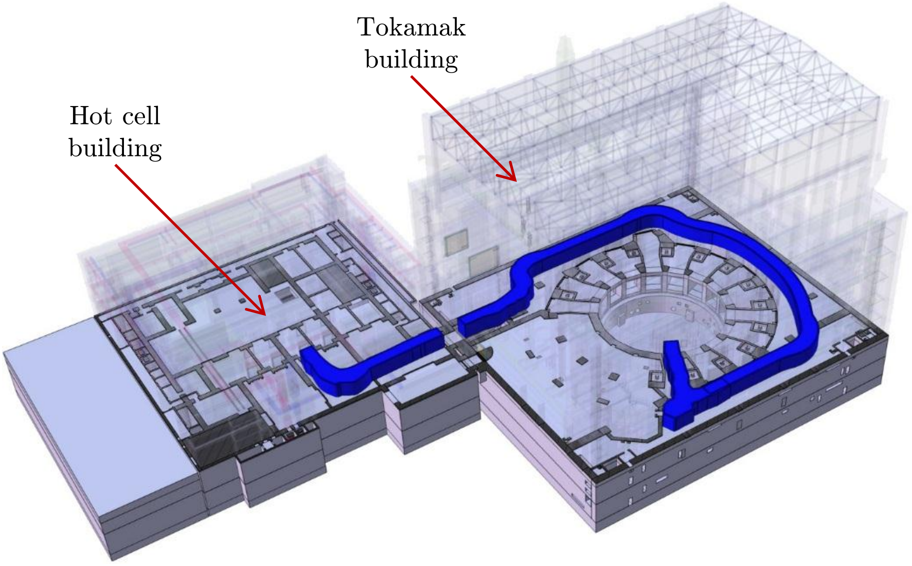

Figure 1.37: Building configurations (image courtesy of the IO)

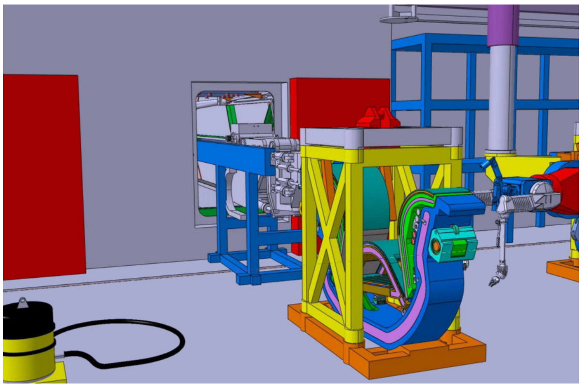

Figure 1.38: Main cell reception and cleaning area (image courtesy of the IO)

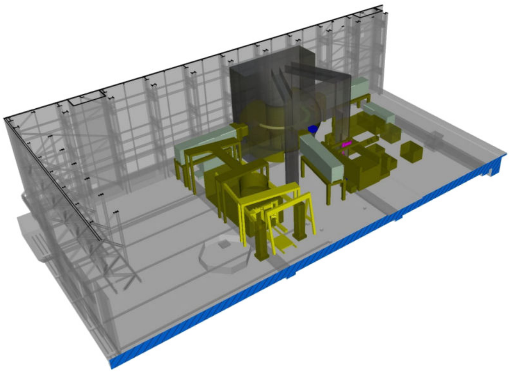

Figure 1.39: Layout of the cold RHTF (image courtesy of the IO)

Remote Handling Supervisory Control System (RHCS)

The ITER RH equipment described in the previous pages comprises a number of local controllers providing real-time control of individual equipment. The overall control system is estimated to contain approximately 250 control cubicles. The RH Supervisory Control System (RHCS) integrates these individual control systems together to form a uniform control system operating from the RH control room (see Fig. 1.40), with the exception of IVVS, which is operated from the main control room.

The RHCS will provide the following main functions:

- control, command and status monitoring of the RH equipment;
- selection and control of remote viewing;
- simulation of remote operations for procedure planning; and
- integration with the Control, Data Access and Communication (CODAC) system.

The command and control sub-system provides human-machine interfaces (HMI) between the operators and equipment controllers. The viewing subsystem provides video signal processing and signal interconnection to any monitor in the control room.

(a) (b)

Figure 1.40: Two examples of RH control room prototypes implemented (a) at Oxford Technologies Ltd (Abingdon, UK) and (b) at the FOM Institute DIFFER (Nieuwegein, The Netherlands).

Multi-Purpose Deployer (MPD)

The in-vessel RH equipment (including BRHS and DRHS) will be deployed during a long-term ITER shutdown to perform scheduled and routine maintenance operations on the main plasma-facing components. As explained in section 1.1.7, in addition to this baseline maintenance scheme, the ITER remote maintenance system is expected to allow the performance of "non-baseline" interventions. An upgrade of the BRHS's IVT was considered, but its inability to reach the divertor region and the top surface of the vessel rendered this option impossible. This implied the need for a Multi-Purpose Deployer (MPD) which would be deployed in-vessel in order to perform these additional tasks during a remote maintenance period. The MPD concept is based on an anthropomorphic robotic arm providing a series of roll, pitch and yaw rotations for in-vessel tool or component deployment (see Fig. 1.41). This concept provides full in-vessel coverage from four equatorial-level ports and provides a high payload capacity.

The MPD will provide the following main functions:

- transportation of in-vessel tools and components in and out of the VV from/to a transfer cask through the equatorial ports during the maintenance period;
- positioning of tools or components inside the VV with an accuracy of ±10 mm;
- removal and replacement of in-vessel components;
- deployment and positioning of in-vessel tools;
- exchange and storage of in-vessel tools (end-effectors, manipulators, task modules);
- in-vessel water leak localisation;
- in-vessel close-up viewing during long-term maintenance;
- dust measurement and partial cleaning;
- tritium monitoring;
- in-vessel diagnostics maintenance;
- ELM coil maintenance; and
- rescue of RH equipment.

The current reference design of the MPD includes the following materials:

- a high-payload-articulated transporter mounted on an equatorial port and composed of two-degree-of-freedom (DOF) linear translational joints and eight-DOF rotary joints mounted on the translational joint, which handles in-vessel components and tools such as a manipulator, end-effectors and task modules;
- in-cask equipment transferring in-vessel tools and components between the transporter and the cask where they are stored;
- a seven-DOF dual-arm manipulator providing force feedback capabilities;
- task modules deployed at the transporter's end to provide task specific tooling; and
- end-effectors deployed at the end of the transporter to provide specific handling capabilities.

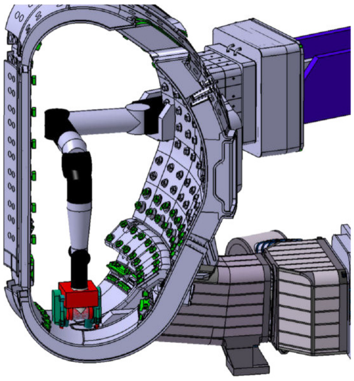

Figure 1.41: MPD transporter deployed with in-vessel tools to perform in-vessel remote maintenance tasks (image courtesy of the IO)

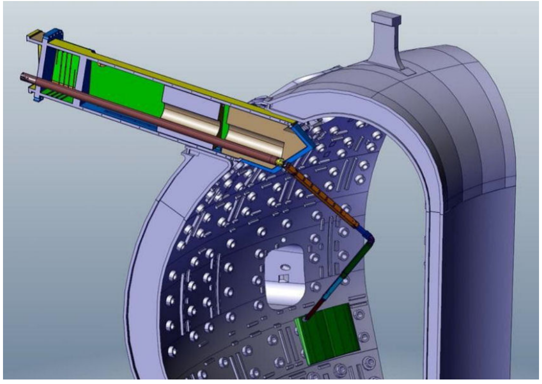

Figure 1.42: FDD deployed inside the VV to perform leak localisation (image courtesy of the IO)

The next two sections describe robotic device systems that are not ITER remote maintenance equipment but that are fully relevant to the maintenance of fusion reactors.

Fast Deployment Device (FDD)

During ITER operation, it is expected that cooling water will leak into the VV and that helium will leak into the cryostat. In order to limit the impact of these leaks on the availability of the ITER machine, a fast solution for leak localisation and repair is required. The Fast Deployment Device (FDD) is expected to deploy a still-to-be-defined leak-detection device from five upper ports (see Fig. 1.42). When stowed, each unit is retracted into a contamination containment enclosure attached to the VV port but is isolated from the vessel by vacuum isolation valves. The system will operate in air or nitrogen at atmospheric pressure and in the absence of a magnetic field. To date, the FDD is not considered part of the RH system (it is developed under the responsibility of the ITER Vacuum Group), although it shares many commonalities with the ITER RH equipment, both in terms of requirements and operational conditions.

The FDD will provide the following main functions:

- deployment into the VV and/or the cryostat within one week of the cessation of plasma operations;
- transportation of a 0.1 kg leak localisation tool within 100 mm of any point of the plasma-facing surface; and
- 100% coverage of the plasma-facing surface (corresponding to a maximum distance of 9 m to be reached from the entry point into the vessel).

The current reference design of one FDD unit includes the following materials:

- an arm that enters the VV and positions the leak sensor using five servo axes arranged in a conventional “roll-pitch-pitch-roll-pitch” kinematics;
- a torque tube that provides support and guidance within the port plug; and
- a deployer that transfers the arm between its stowed and deployed positions.

Articulated Inspection Arm (AIA)

The Articulated Inspection Arm (AIA) is another remote inspection tool for fusion reactors; it has recently been used in Tore Supra.

In the early 2000s, the Euratom-CEA Association launched an R&D program to demonstrate the feasibility of close inspection tasks in fusion reactors using a long-reach robotic arm equipped with a viewing system. A feasibility analysis drove the design of the AIA demonstrator [10], which is an 8 m-long, multi-link arm with five identical titanium modules 160 mm in diameter. Each module includes pitch (±45° in the vertical plane) and yaw (±90° in the horizontal plane) joints linked with a parallelogram structure (four-bar mechanism) that maintains a vertical yaw joint axis. This combination of elevation and rotation motions gives the robot eight DOF (see Fig. 1.43). With a payload up to 10 kg and a total weight of 150 kg, this polyarticulated arm can be introduced through a narrow port 250 mm in diameter. To cope with the high temperature requirements, all AIA articulations are actuated by embedded electromechanical components qualified up to 120°C in use and 200°C when switched off. All the camera's inner electronic components (CCD sensor, zoom, LEDs, etc.) are actively cooled by nitrogen gas to keep the operating temperature below 60°C (see Fig. 1.45). Other diagnostic tools are currently developed for tokamak in-vessel inspection, such as a leak-detection system based on helium sniffing or a compact laser system for carbon codeposited layer characterisation or treatment [11].

In 2008, the AIA equipped with a vision process was qualified after it carried out an inspection (see Fig. 1.46) inside the Tore Supra tokamak (see section 1.1.6), which operates under the same vacuum and temperature conditions as ITER.

The AIA was initially designed to be a prototype for the ITER IVVS deployer. However, recent changes in the project requirements forced the IO to sideline it in favour of alternative concepts able to operate in strong magnetic fields and highly activated environments. The AIA is now an inspection tool dedicated to Tore Supra [12]. Even though this arm will never be used in ITER, it is a rare, fully operational remote inspection tool for fusion reactors.

The AIA provides the following main functions:

- viewing and inspection of first wall and other in-vessel plasma-facing components;
- insertion through exiguous access ports (250 mm);
- high mobility allowing access to any point inside the VV;
- operation in high vacuum (10^{-6} Pa) and at high temperature (120°C);
- self-illumination without relying on any external light source; and
- possibility of plugging various processes (payload up to 10 kg).

The AIA consists of the following materials:

- a robotic arm composed of five identical modules and a prismatic joint at the base (see Fig. 1.44). Each module is a two-DOF mechanism comprised of two electrical rotary joints and a parallelogram structure that keeps the elevation axis vertical to minimise the cantilever. Each module includes on-board temperature-hardened control electronics qualified up to 120°C when in use and 200°C when switched off.
- a video process designed and assembled by ECA/HYTEC comprising a CCD colour sensor, zooming and rotating capabilities and high-intensity LED ring lights. All its components are actively cooled by nitrogen gas (see Fig. 1.45).
- an 11 m-long cask ensuring vacuum and temperature conditioning and precise guiding through the port. It is equipped with a double valve separating the stowed robot arm from the primary vacuum without impacting the tokamak operating conditions.

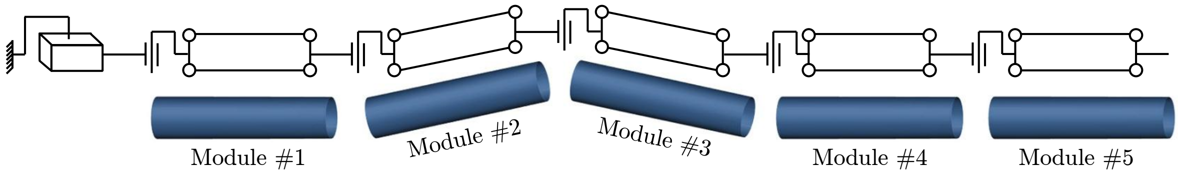

Figure 1.43: Kinematics model of the parallelogram structure of AIA

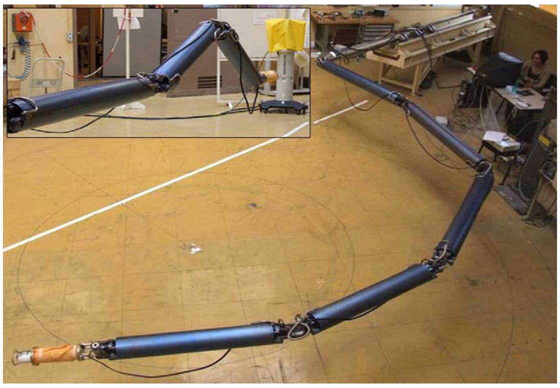

Figure 1.44: Overview of the fully deployed AIA (image courtesy of CEA LIST)

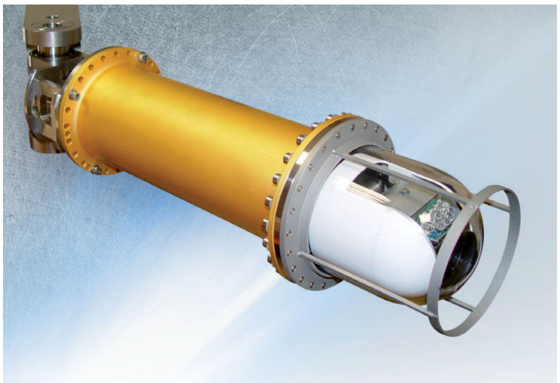

Figure 1.45: Viewing system equipping the AIA (image courtesy of ECA/HYTEC)

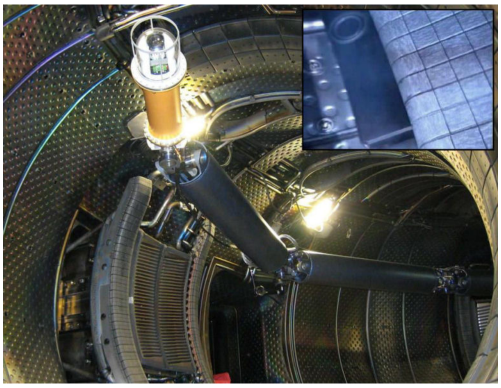

Figure 1.46: Deployment of the AIA inside Tore Supra (image courtesy of CEA IRFM)

1.1.9 Environmental operating conditions of the ITER RH equipment

The interior of a nuclear fusion reactor is a hostile environment for humans. This is the main rationale behind the built-in RH system, which enables the operator to perform maintenance without being physically present on-site. Unfortunately, harsh conditions for humans are harsh for the maintenance equipment as well. By its very nature, the RH equipment will be subjected to exceptionally challenging environmental conditions that are likely to affect its performance. Depending on its mode of operation, the tokamak environment can include various subsets of the following features: elevated temperatures, strong magnetic fields, high levels of radiation, radiological contamination and atmospheric (air, gas, vacuum) and electromagnetic interference.

The following table summarises the main environmental conditions the ITER remote maintenance equipment will be subject to during operation. The NBRHS, the DRHS and the IVVS have been chosen to illustrate several levels of harshness. Environmental conditions during blanket handling (BRHS), MPD operation and cask transfer operation (CPRHS) are globally equivalent to those applied to the DRHS. Table 1.2 does not report requirements on humidity (≈ 0 %) or contamination by tritium and activated dust (Be, W), which are common to all the systems.

Table 1.2: Environmental conditions related to various RH systems

Level	**System**	**Pressure**	**Temperature**	**Typical radiation levels**	**Magnetic field**
Conventional	NBRHS (see p. 26)	≈ 1 bar (dry air)	Ambient	Gamma radiation only; Outside beam line: $< 10^{-2}$ Gy/h; Outside magnetic shield: $< 10^{-4}$ Gy/h; Around fast shutter: $< 10^{-1}$ Gy/h	≈ 0.1 T
Severe	DRHS (see p. 21)	≈ 1 bar (dry air)	< 50°C	Gamma radiation only; 10^6 s after plasma operations; CTM: 2.2–120 Gy/h; up to 3.3–180 kGy during full divertor exchange campaign	< 1 mT
Very severe	IVVS (see p. 24)	During operation: 5×10^{-4} Pa; During shutdown: ≈ 1 bar (dry air)	Operating temperature: 120°C; Bake-out temperature: < 200°C	Gamma radiation and neutrons; Probe during in-vessel deployment: <6 kGy/h, up to 10 MGy; Through storage plug during plasma pulses: $<4 \times 10^{17}$ n/cm^2, spectrum from 10^{-7} MeV to 14 MeV	In deployed position: up to 8 T; In storage: 0.3 T

Integrated radiation doses and neutron fluences are given after 20 years of ITER operation. In particular, the integrated radiation dose during operation mode 0 (active plasma phase, D-D and D-T) have been evaluated considering a total operation time of 4600 h. Similarly, the integrated radiation dose during operation mode 1 (shutdown phase) have been evaluated considering a total shutdown time of 170,000 h (about 19.7 years).

1.1.10 Viewing capabilities in ITER

Several of ITER's RH systems rely on the principle of "man-in-the-loop" remote operations (BRHS, DRHS, NBRHS). It is widely admitted that the ability to perform efficient and safe man-in-the-loop operations is directly linked to viewing capabilities. The ITER RH viewing system (not to be confused with the In-Vessel Viewing System) aims to provide operators with visual feedback of the remote environment.

The RH viewing system will provide the following main functions:

- select images from specific cameras and display them on monitors located in the RH control room;
- control images/video streams by setting their main parameters (orientation, zoom, focus, contrast, brightness, colour balance, image size, framerate);
- enhance image/video content (noise reduction, edge sharpening, contrast stretching); and
- manage the data flow (data encoding, compression).

No reference design is currently in place for ITER's RH viewing system. Nevertheless, it is possible to extrapolate its main characteristics from the experience gained at JET. Whereas approximately 10 cameras were used by a four-person team at JET, it is expected that 100 cameras could be simultaneously operated in the ITER RH control room during a typical RH task. In all, ITER's RH viewing system is likely to include between 500 and 700 cameras with a mix of rad-hardened and conventional, analogue and digital cameras. The quality of the camera views will be critical to the speed and accuracy of remote operations inside the torus. In comparison to more conventional plants, two additional factors will influence the quality of the acquired images: illumination and radiation.

First, adequate illumination of the scene is vital. Indeed, one must bear in mind that the ITER in-vessel environment will be pitch black once the tokamak assembly is completed. Illumination must be carefully placed to perform effective RH operations and must allow active directional control; on-board cameras should be able to track the end-effector position in order to ensure that the task remains in the field of view. Figure 1.47 illustrates that suitably setting up the camera's position and direction is important for obtaining a view that provides that operator with as much of an understanding of the remote environment as possible.

Second, high radiation dose rates inside the VV lead to the required use of radiation-tolerant cameras. For instance, at the in-vessel dose rate of 500 Gy/h found in the BRHS or IVVS (see Table 1.2), a radiation-hardened camera able to withstand a total dose rate of 1 MGy would allow approximately 2000 hours of operations, which is considered quite acceptable for a system that may be readily replaceable.

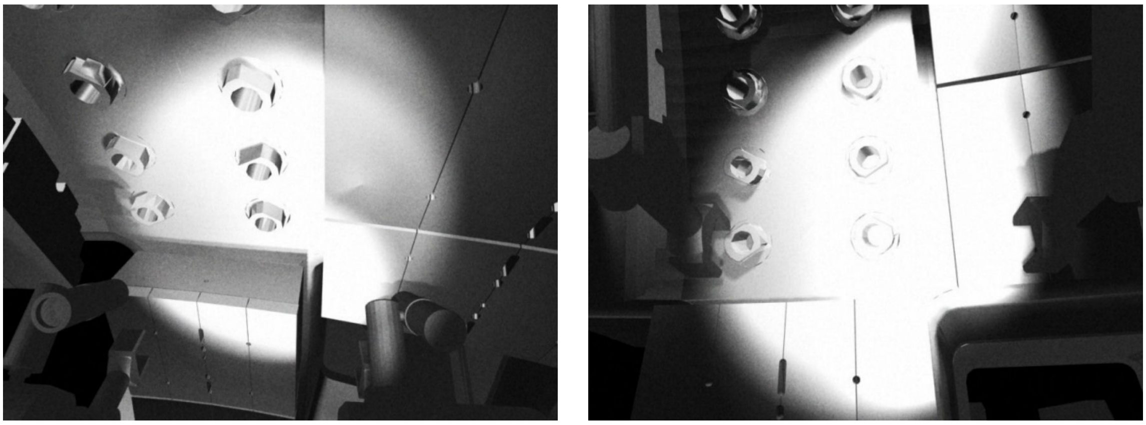
(a) (b)

Figure 1.47: Simulated in-vessel views from cameras equipping the MPD arms with representative light intensity (image courtesy of Oxford Technologies Ltd)

An extensive market survey on radiation-hardened cameras has not been carried out within the framework of the present thesis. If such a survey is performed, it should explore the trade-off between optical performance, tolerance to high radiation exposure, market availability, protection from obsolescence and cost. It should also consider the possibility of using disposable but cheap conventional cameras instead of costly rad-hardened devices.

Nevertheless, a brief market analysis performed for this thesis (see Table 1.3) shows that most of the available rad-hardened viewing systems are based on analogue Chalnicon or Vidicon tube cameras, charge-integration devices (CID), charge-coupled devices (CCD), and complementary metal-oxide semiconductor (CMOS) sensors. In general, the quality of rad-hard cameras is improving, but their cost remains high (between one and several dozens of kEuro). In terms of radiation limits, the CMOS sensors developed for space applications do not meet the requirements for fusion reactors.

Table 1.3: Examples of available rad-tolerant cameras

Manufacturer	**Model**	**Type**	**Resolution (TV lines)**	**Weight (kg)**	**Maximum dose rate (kGy/h)**	**Maximum cumulated dose (MGy)**	**Price range**	**Ref.**
Ahlberg	N35HR	Tube	700	1,2	30	2	C	[13]
Centronic Raditec	CR2224 (Fig. 1.48)	Tube	650	0.9	10	3	-	[14]
Diakont	D40	Tube	600	1.5	30	2	C	[15]
Diakont	Star camera (Fig. 1.49)	Digital	500	5	1	0.1	B	[16]
Eca Robotics	VS 370 N	Tube	600	2.5	30	3	-	[17]
Eca Robotics	VS 390 N (Fig. 1.50)	Digital	500	-	1	0.1	-	[18]
Mirion	IST-REES R93 MK3	Tube	500	1.25	30	2	C	[19]
Mirion	IST-REES R985	Digital	550	1	1	0.1	A	[20]
Visatec	VT5065RR	Tube	460	1,75	25	2.5	-	[21]

Price range: A) inexpensive (<10keur) / B) medium (10keur<...<25keur) / C) expensive (>25keur)

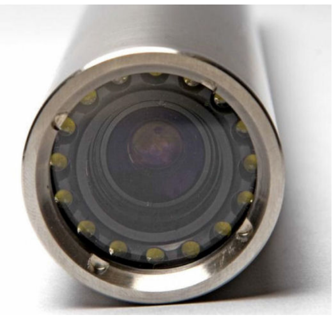

Figure 1.48: Centronic Raditec CR2224 (image courtesy of Centronic)

Figure 1.49: Diakont Star (image courtesy of Diakont)

Figure 1.50: ECA VS 390 N (image courtesy of ECA Robotics)

As a result of long-term exposure to radiation, the quality of direct viewing from these cameras (analogue or digital) is expected to degrade over time. Therefore, some front-end processing may be required. The availability of FPGA- and GPU-based image processing solutions has increased, and COTS front-end processors are now available from several suppliers. The accessibility to open-source computer-vision libraries including GPU computational capabilities (e.g. Open-CV) make these solutions even more attractive.

Image enhancement and data compression can both be implemented using low-level control system equipment. Indeed, the data flow generated by a large number of cameras running at usual framerates is likely to be large. This data flow will depend strongly on the sensor resolution, framerate and colour dynamic range. As an example, a single 25 fps 8-bit monochrome video stream with a reasonable resolution (1400×1000) would generate 35 MB/s of data, leading to approximately 3.5 GB/s in the case of 100 simultaneously running cameras. Standard compression techniques are available on the market.

Another way of enhancing the camera images may be to supplement them with additional information derived from a virtual reality (VR) system. The basic principle of this technique, which is referred to as “synthetic viewing” [22], consists of combining the limited or degraded information received from a camera with prior knowledge of the environment (e.g. from 3D models). The operator views a synthetic reconstruction of the remote environment that is updated online by the data received from the field sensor.

1.2 Motivation

1.2.1 Industrial flexible robot arms operating under hazardous conditions

The main objective of this brief review is to report on how the vibration control problem is addressed in various ITER-relevant, industrial-grade robotic devices performing under hostile environmental conditions. Systems designed for remote maintenance tasks in a nuclear fuel reprocessing plant, in JET and in ITER are considered first. This brief review subsequently broadens to include space manipulators, which share many commonalities with tokamak remote maintenance devices: high structural flexibility, remote operation and imperative tolerance to radiation, vacuum and extreme temperatures.

Hot cells in the Cogema/Areva La Hague nuclear fuel reprocessing plant

Nuclear fuel reprocessing plants are complex facilities comprising several work areas where numerous chemical and mechanical operations are performed. These operations generate a wide variety of radiological hazards that sometimes preclude direct human intervention.

In 1966, France opened the La Hague plant on the Cotentin Peninsula, thus launching a reprocessing program for recycling spent nuclear fuel for civilian purposes. This effort was broadly supported by other European countries who, together with Japan, signed up for French reprocessing services in the 1970s. A major argument for reprocessing is that it dramatically reduces the volume of radioactive waste (see Fig. 1.51). Between 1976 and 2006, approximately 23,000 t of light water reactor (LWR) fuel were reprocessed in the two reprocessing lines of La Hague. Since 2000, the plant has processed approximately 1100 t annually. Until 2004, almost half the LWR spent-fuel processed at La Hague was owned by foreign countries.

In industrial reprocessing plants, components exposed to mechanical and/or chemical actions often result in technical problems; hands-on maintenance is usually adopted for these problems, provided that radiological conditions (activation, contamination) allow it. However, remote maintenance systems have always been extensively applied to a variety of tasks, with benefits such as dose reductions for workers or increase in operational

Figure 1.51: Nuclear fuel cycle, according to Areva (image courtesy of Areva)

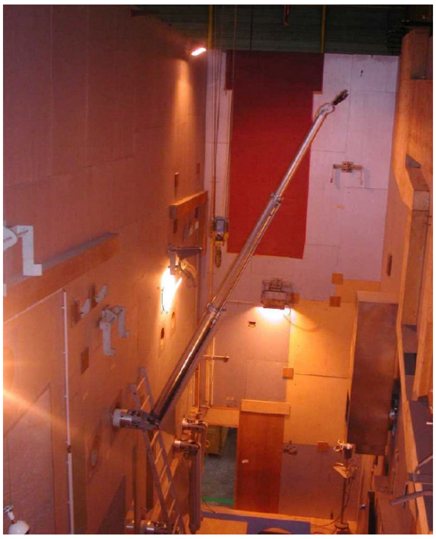

Figure 1.52: MT200 in the La Hague reprocessing plant (image courtesy of Areva)

performance, with important implications for the plant's economics. For this reason, RH systems have been an integral part of La Hague's HC facilities. The result of this is that these systems have not necessarily been upgraded since the 1970s.

Since 2005, the MT200-TAO telerobotic system has been evaluated in the HC refurbishment facility in the La Hague reprocessing plant [23]. This is the result of several attempts to replace the conventional, through-the-wall MT200 telescopic telemanipulator commercialised by La Calhène. The main objective of these developments was threefold: to automate some repetitive tasks; to improve security for difficult tasks; and to enhance workstation ergonomics.

The slave-arm is a six-DOF (five rotary joints and a telescopic mechanism) 4 m-long manipulator (see Fig. 1.52). Its payload capacity is up to 20 kg for 40 kg of its own weight (maximum torques of 1540 Nm and 385 Nm, respectively, for the two main joints). Its transmission is based on gears and screws for the upper part and cables and chains for the lower joints, which makes the whole system very flexible and subject to vibrations.

A force-controlled master-slave mode is achieved using the TAO2000 software developed by CEA LIST. It allows the operators to perform new functions, such as active weight balancing, accurate force surveillance, tool weight compensation, adjustable velocity and effort scaling ratios, play-back robotic modes, virtual mechanism modes and automatic pursuit of the gripper by remote cameras. These features help the operators optimise their working conditions inside a working volume that is three times as large as the original. It is also interesting to note that automated play-back modes are made available even though their precision is inherently limited by the high flexibility and the hysteresis of this class of slave arms.

Similar to what will occur in ITER (DRHS, HCRHS), remote maintenance operations in La Hague require handling objects and the dexterous use of tools, such as saws, hydraulic shears or impact wrenches. The ITER RH systems would undoubtedly benefit from the experience gained in developing and testing this computer-aided force-feedback teleoperation system. Unfortunately, in spite of the quality features made available thanks to TAO2000, no particular scheme was implemented to limit or avoid vibrations.

Installation of the ICRH antenna in JET

ITER and future fusion power plants will need more powerful plasma heating systems than those present in current experimental fusion reactors. As previously mentioned (c.f. sections 1.1.4 and 1.1.5), in order to produce fusion energy in ITER, it will be necessary to raise the plasma temperature to over 100 million degrees Celsius. To reach this extreme temperature, several heating systems will be available. The Ion Cyclotron Resonance Heating (ICRH) antenna [24] is one of these systems. Since JET is the closest machine to

ITER in terms of plasma conditions, it was decided in the 2000s that an ITER-like ICRH antenna would be installed and tested in JET (see Fig. 1.53).

The ITER-like ICRH antenna was fully installed through RH during the 2007 shutdown, which was mainly devoted to refurbishing and installing a number of new systems significantly improving JET's capabilities. JET is currently the only fusion device whose maintenance is performed fully remotely [25]. Over the past 20 years, the JET RH system has demonstrated many ITER-relevant features, including manipulating heavy loads.

The 300 kg antenna was transported into the vessel on a sub-frame connected to the RH-articulated boom via a specific end-effector (see Fig. 1.54). The 10 m-long JET RH boom (see Fig. 1.55) has 19 degrees of freedom and can be controlled either from a joystick, a keyboard or using pre-taught sequences of motion. For the rough approach, the tip was moved along smooth trajectories using pre-defined moves, or teach files, and a virtual rail, which avoids stimulating the natural modes of the assembly (except in an emergency stop at full speed). The final approach was performed using man-in-the-loop guidance on the basis of the contact forces exerted on the antenna by its wall-mounted support and was measured using a six-axis force and torque sensor equipping the end effector. Once the antenna was fully engaged, fixing bolts were fastened from outside the vessel.

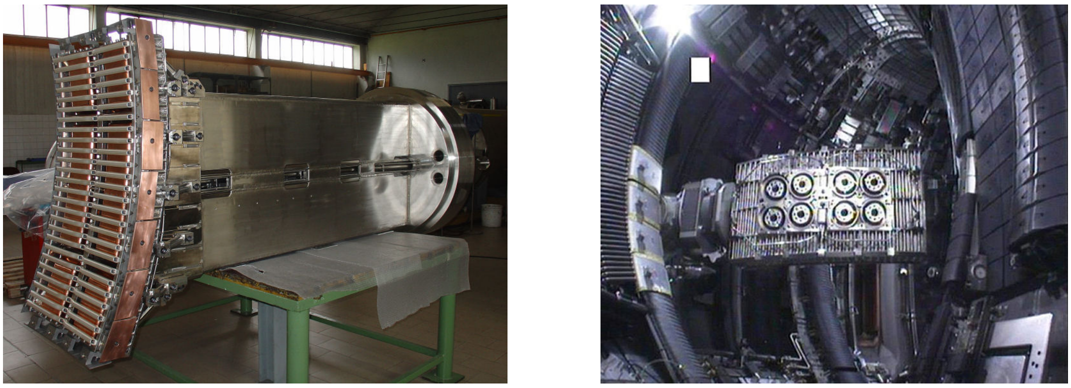

(a) (b)

Figure 1.53: The ITER-like antenna after manufacturing (left) and during installation in JET (right) (image courtesy of EFDA-JET)

As expected, disengaging the boom from the bolted antenna was a critical task because fastening the fixing bolts had induced constraints on the sub-frame and the boom. Load transfer issues were addressed using the compliance of the boom to minimise the load distribution before disconnecting. The overall installation methodology based upon a six-axis force and torque sensor proved to be an efficient method for avoiding undesirable vibrations in the robotic arm during disengagement. Despite the differences between the ITER and JET in-vessel environments, the unique knowledge gained by JET engineers during this operation may serve as a basis for future developments on devices such as ITER.

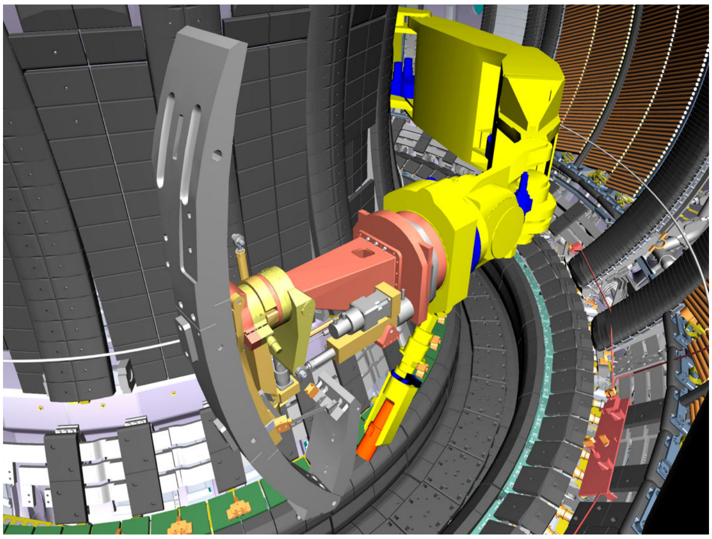

Figure 1.54: Virtual reality view showing the articulated boom carrying a heavy component (poloidal limiter) inside the JET VV (image courtesy of EFDA-JET)

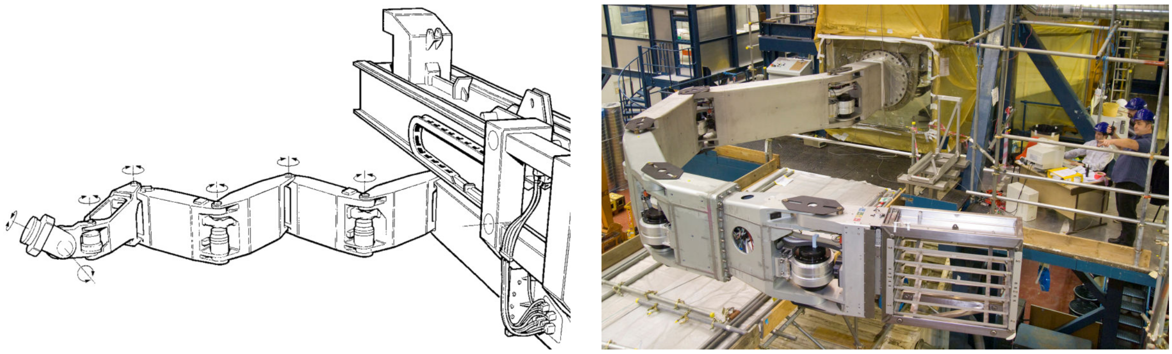

(a)

(b)

Figure 1.55: The JET articulated boom (image courtesy of EFDA-JET)

The In-Vessel Viewing System (IVVS) for ITER

The In-Vessel Viewing System (IVVS) is an ITER machine operations tool aimed at performing visual inspections and range measurements of the plasma-facing components, such as the blanket, the divertor, the heating/diagnostic plugs or the test blanket modules. These inspections and measurements are performed periodically (e.g. during planned shutdowns) or on request (e.g. after unforeseen events such as plasma disruptions with suspected damages).

While the R&D supporting the scanning probe concept has been extensively documented over the past 15 years [26–28], the IVVS deployment system remained relatively underdeveloped until a recent design activity laid the foundations of an integrated IVVS concept in late 2011 [29, 30]. The IVVS successfully passed its conceptual design review in spring 2014. For more information on this system, please refer to section 1.1.8.

The reference design for the IVVS scanning probe is a hybrid viewing and ranging system relying on the amplitude modulation of a coherent single mode laser transmitted to the target via a rotating prism. The intensity and phase of the light backscattered from the target are detected concurrently and compared to the emitted signal. Greyscale 2D images are obtained from the intensity, while range data is generated from the phase shifting (see Fig. 1.56). In terms of viewing capabilities, the IVVS should provide greyscale 2D images with a normal resolution better than 1 mm for targets in the range 0.5–4 m and better than 3 mm for targets situated up to 10 m. With respect to metrology, the IVVS should be capable of providing range data with a standard deviation of approximately 500 µm.

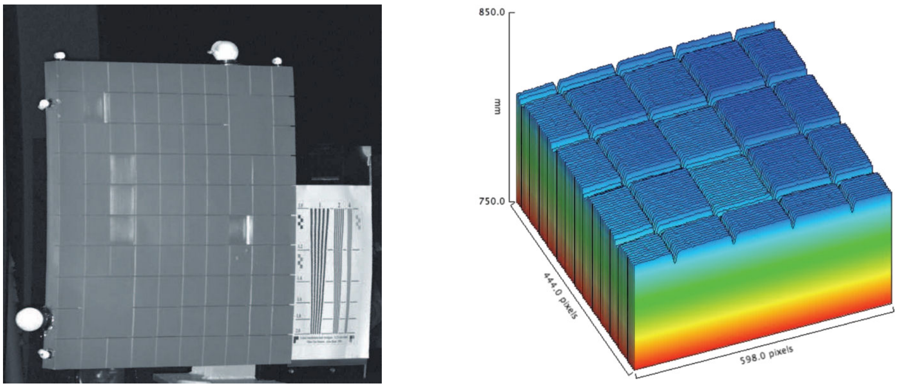

(a) (b)

Figure 1.56: Examples of 2D picture (a) and 3D model (b) of a target acquired by the IVVS (image courtesy of ENEA)

When they are not in operation, each IVVS unit is housed in a storage plug mounted on a long, narrow VV port extension. Therefore, they stay within the ITER primary vacuum, close to the plasma (c.f. environmental conditions, section 1.1.9) in order to allow quick deployment after the last plasma pulse. The deployment system has been designed to allow the radial transport of the scanning probe from its storage position at the rear of the plug to its maximal deployed position, 7.5 m away towards the vessel centre. There, the probe can perform one or a series of scans in a fully cantilevered condition.

Unfortunately, in such a working position, the quality of the measurements will very likely be affected by both internal vibrations, which are induced by the prism rotation, and external vibrations, due to vibrating neighbouring systems such as the cryopumps.

In order to cope with these perturbations, the UTFUS unit of ENEA carried out a series of parametric tests in 2009–2010 to assess how the IVVS viewing performance was affected by a probe vibrating at low frequencies (frequency < 1 Hz, 1 mm amplitude). To do so, they used the IVVS probe proof-of-principle prototype developed in the early 2000s (see Fig. 1.57) and placed it on an adjustable vibrating table (see Fig. 1.58).

ENEA also investigated possible methodologies to avoid or limit the effects of vibrations on the acquired images. Instead of attempting to damp these vibrations, they developed

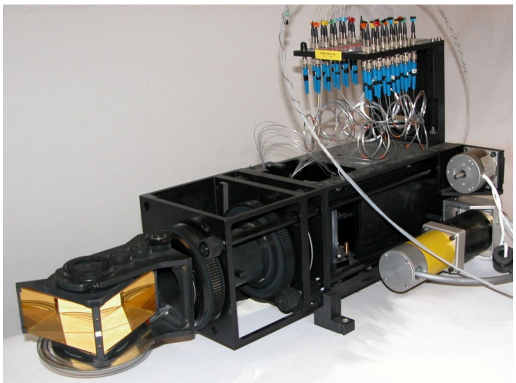

Figure 1.57: IVVS probe prototype developed at ENEA UTFUS (image courtesy of ENEA)

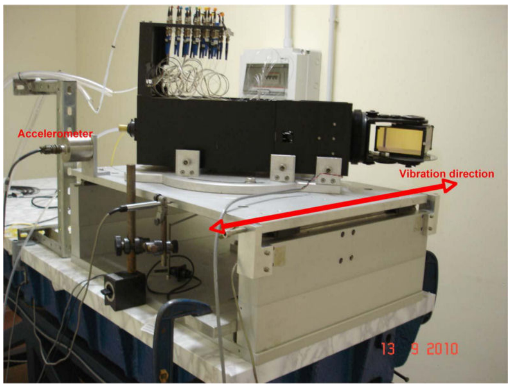

Figure 1.58: Experimental setup (image courtesy of ENEA)

a post-processing vibration correction algorithm compensating for the effect of vibrations from the acquired data.

The image is acquired and stored as a continuous stream of data comprising, among other information, the backscattered light intensity and the encoder positions. Pixels are subsequently formed by assigning a single intensity value to a pair of pan and tilt angular values. These angles are first converted into spherical coordinates and then into Cartesian coordinates.

When the probe vibrates, the target point associated to a set of pan and tilt angles changes over time. ENEA's method for filtering out the effect of vibrations in IVVS pictures is to reassign the correct coordinates to the light intensity signal. For each acquired point, the displacement of the probe is calculated by double integrating the signal measured by an embedded accelerometer. This displacement is decomposed along perpendicular axes and is added to the Cartesian coordinates deduced from the encoder measurements.

The proposed algorithm was implemented and tested on the aforementioned probe prototype. To that end, a Wilcoxon Research Model 731A/P31 high-performance accelerometer was used.

Figures 1.59 through 1.61 show resolution test patterns images acquired using the experimental setup. These test patterns consist of three series of converging black-white lines that create a continuum of spatial frequencies. They allow a rough estimation of the spatial resolution of imaging systems by determining the point at which black lines merge and can no longer be distinguished from one another. It is notable that the resolution chart chosen by ENEA is calibrated in horizontal line pairs per arbitrary unit; thus it can only be used for relative resolution measurements and not absolute ones.

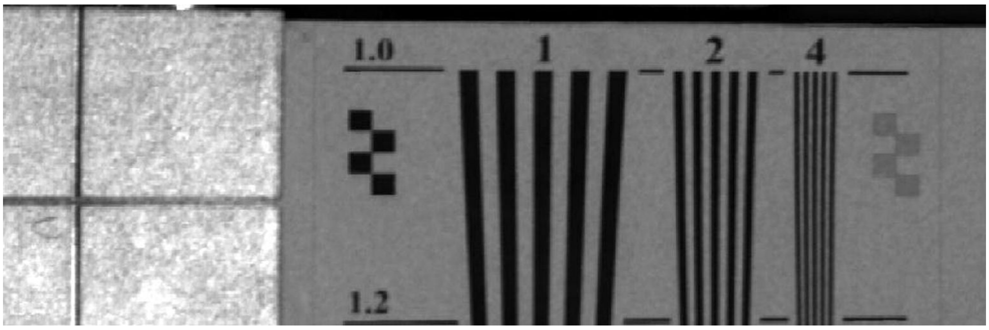

Figure 1.59: Original image acquired by the IVVS probe prototype – distance about 3.5 m, no vibration) (image courtesy of ENEA)

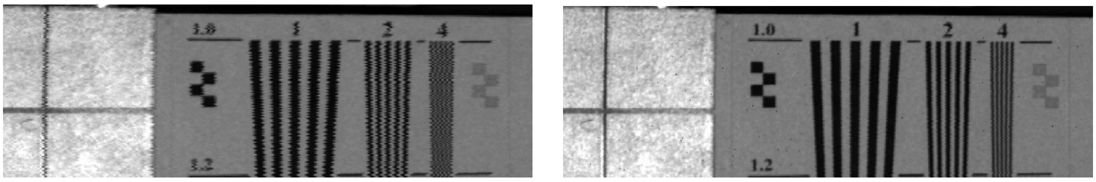

(a)

(b)

Figure 1.60: Original (a) and post-processed (b) images acquired by the IVVS probe prototype – distance about 3.5 m, vibration at 1 Hz, 1.2 mm amplitude (image courtesy of ENEA)

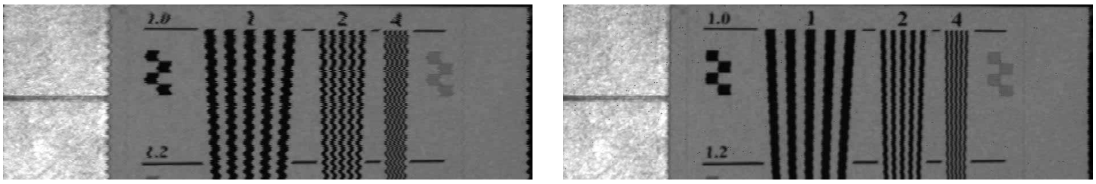

(a)

(b)

Figure 1.61: Original (a) and post-processed (b) images acquired by the IVVS probe prototype – distance about 3.5 m, vibration at 0.5 Hz, 1.5 mm amplitude (image courtesy of ENEA)

The Blanket Remote Handling System (BRHS) for ITER

The schedule maintenance for ITER's blanket system has been previously discussed in sections 1.1.7 and 1.1.8. For ease of replacement, it has been segmented into 440 modules of 4.5 t each. A rail-mounted vehicle manipulator system was adopted as the most suitable RH equipment to handle these heavy modules with high positioning accuracy (±2 mm at about 5.5 m). The IVT consists of a vehicle travelling along a rail deployed inside the vessel. It entails a telescopic manipulator capable of accessing all in-vessel areas except the divertor area (see Fig. 1.62).

In order to meet the aforementioned positioning requirement, it is essential to suppress the dynamic deflection and vibrations of the RH equipment due to the sudden weight transfer from/to the back-plate supports to/from the manipulator during the installation and removal of the modules. The first natural frequency of the system made of the rail plus manipulator was found to be approximately 3 Hz.

In 2000, the team developing the IVT within the Japan Atomic Energy Research Institute (JAERI) proposed avoiding load transfer by using pre-defined positions [31]. The load conditions during installation are based on the opposite load conditions encountered during module removal, i.e. the configuration of the vehicle/manipulator system is pre-defined based on the configuration of the unloaded manipulator during module removal. Conversely, the load conditions during removal are based on the opposite load conditions encountered during module installation. Figure 1.64 illustrates the difference between the unloaded and loaded end-effector positions (A and B, respectively). The measured deflection was, in Cartesian space, $\Delta x = 5.3$ mm, $\Delta y = 82.5$ mm and $\Delta z = 69.8$ mm. The proposed methodology allowed a decrease in the amplitude of the dynamic deflection during module installation from 4.66 mm to nearly zero (see Fig. 1.65).

The main drawback of this approach is its high sensitivity to the measurement uncertainty and its poor adaptability. According to the proposed method, the end-effector position must be accurately measured using an external device (e.g. a laser tracker) during the ITER machine assembly. As a consequence, the pre-defined positions will not be able to consider any changes due to local erosion or defects after machine operation.

In 2003, JAERI proposed a new sensor-based control [32], which combines distance sensors for rough positioning and contact sensors for fine positioning (see Fig. 1.63). Indeed, contact sensors have a high potential for fine positioning as well as simplicity and high reliability, whereas the positioning accuracy of distance sensors is generally affected by surface conditions and reflections. Consequently, a combination of laser-type distance sensors and three-axes strain-gauge contact sensors was judged appropriate.

This newly developed control scheme was validated on the full-scale mock-up while installing a 4T module with high positioning accuracy. The installation was successfully achieved due to the passive compliance of the manipulator, similar to what JET engineers achieved later during the installation of the ICRH antenna (see p. 39).

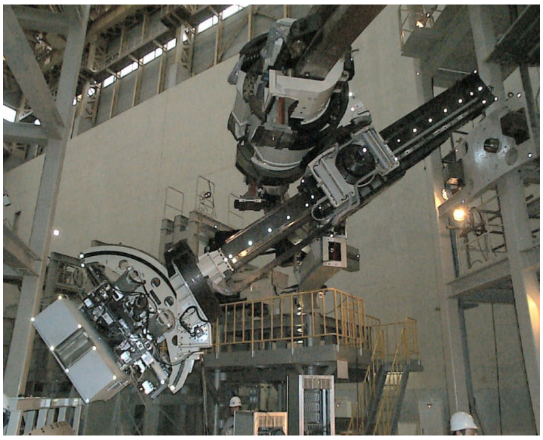

Figure 1.62: IVT prototype (image courtesy of JAERI)

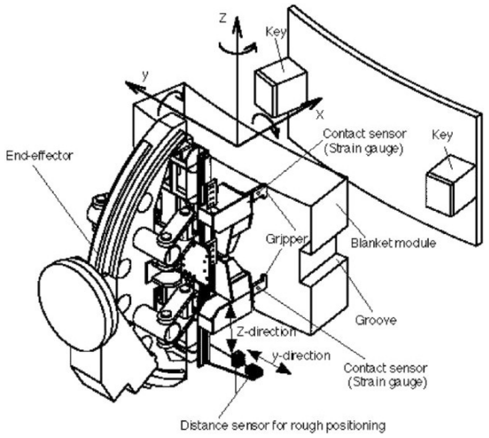

Figure 1.63: Location of sensors (image courtesy of JAERI)

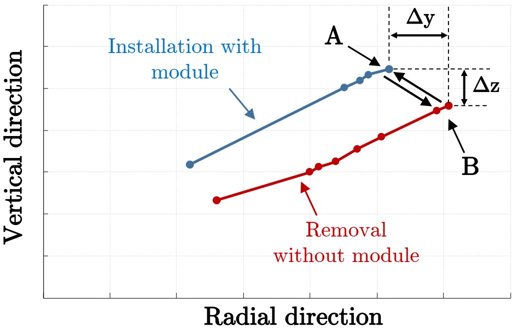

Figure 1.64: Unloaded and loaded manipulator positions (source: JAERI)

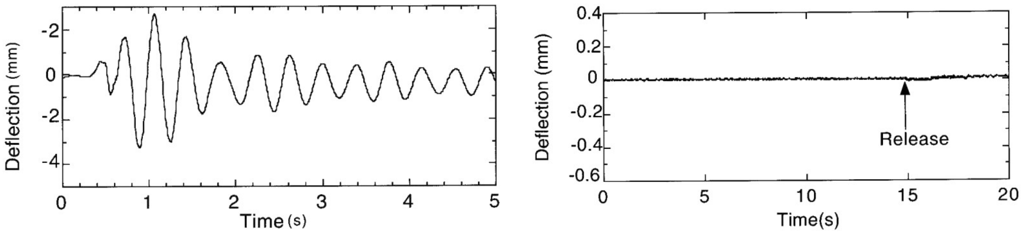

(a) (b)

Figure 1.65: Dynamic deflection of the rail during module installation without (a) and with (b) vibration control (image courtesy of JAERI)

Although teaching-playback techniques suitably addressed the issue of load transfer between the blanket module and its wall-mounted support, the whole system still suffered from a lack of repeatability in the mechanical positioning of the manipulator before grasping the module (error in the order of ±25 mm). To ensure the required 5 mm position accuracy and 1° angular accuracy between the gripping hole and the gripper, JAERI engineers adopted a machine vision system as a non-contact sensing solution and visual servoing as control scheme. Visual servoing (VS), a.k.a. vision-based robot control, is a technique using information from a vision sensor to control the motion of a robot. In basic VS applications, a camera is mounted at the tip of a manipulator and the manipulator moves so the current picture matches a reference picture (c.f. section 2.3).

First, a low-resolution radiation-resistant camera was chosen (2 MGy rad-tolerant Chalnicon tube camera from Toshiba Teli). Unfortunately, the low resolution of the sensor, in addition to the simplicity of the shapes to be tracked (two circular gripping holes) made the VS highly inaccurate. To cope with these issues, a stereovision system was adopted. It had the additional advantage of providing depth information. JAERI also identified illumination as a major problem and subsequently mounted a ring light concentrically with the camera (see Fig. 1.67).

The IVT machine vision system was tested using the full-scale manipulator prototype and a dummy blanket module [33] (see Fig. 1.66). For this specific test, two inexpensive commercial off-the-shelf CCD cameras (Flea2 by Point Grey Research Inc. [34]) with resolutions similar to rad-tolerant tube cameras (640×480) were used. OpenCV was used as the real-time computer vision function library to analyse the pictures. The experiment demonstrated positive results since positioning and angular accuracies of 1 mm and 0.05°, respectively, were achieved (see Fig. 1.68).

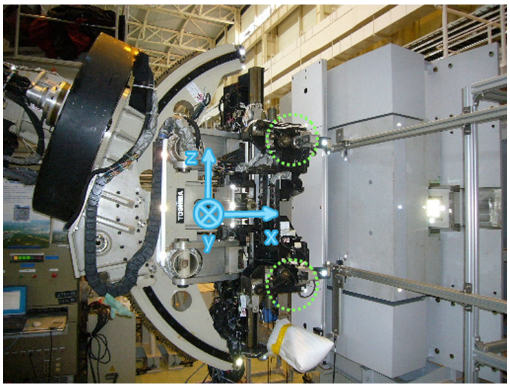

Figure 1.66: Test setup incl. manipulator, blanket mock-up, calibration board and cameras (green circles) (image courtesy of JAERI)

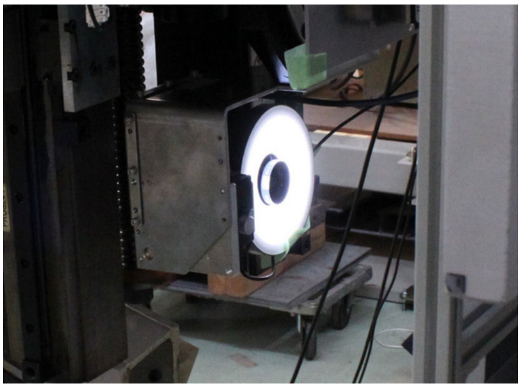

Figure 1.67: Diffuse ring light and camera on the end-effector of the IVT (image courtesy of JAERI)

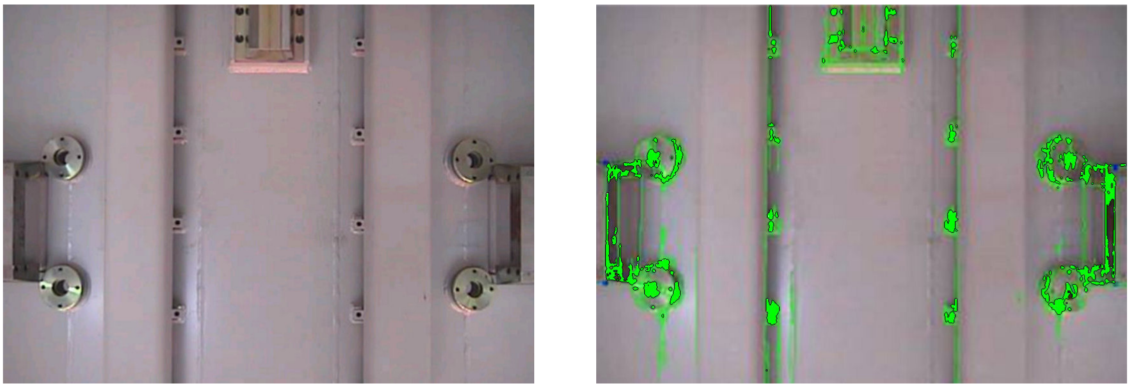

(a) (b)

Figure 1.68: Images acquired by the IVT machine vision system: (a) original, (b) image including the output of a typical features detection algorithm (original image courtesy of JAERI)

Space manipulators

As conventional nuclear power activities started to decline in the 1980s and 1990s, remote operation technologies migrated towards other fields, including space. Experience gained from teleoperation within nuclear environments clearly influenced the space shuttle remote manipulator system and the short-lived Flight Telerobotic Servicer program.

The first robotic arm used in orbit was the Space Shuttle Remote Manipulator System (SRMS), which was known as Canadarm because it was developed by the Canadian Space Agency (CSA) (see Fig. 1.69). The SRMS is a 15 m-long six-DOF mechanical arm that is deployed from the payload bay of the space shuttle in order to manoeuvre and release a payload [35]. Since its first use in 1981 (space shuttle mission STS-2), it has been used more than 100 times during space shuttle flights for various tasks such as payload deployment, assisting human extravehicular activities, maintaining the Hubble Space Telescope and building the International Space Station (ISS). After the Columbia space shuttle accident in 2003, the National Aeronautics and Space Administration (NASA) outfitted the SRMS with a boom containing instruments to inspect the shuttle's exterior for possible damage to the thermal protection system [36].

The Space Station Remote Manipulator System (SSRMS), also known as Canadarm 2, was the next generation of space remote manipulator systems designed for specific use on the ISS (see Fig. 1.71) [37]. Launched in 2001, the SSRMS played a key role in the construction and maintenance of the ISS, both by assisting astronauts during extravehicular activities and by receiving payloads from the space shuttle's SRMS. The 17.6 m-long seven-DOF SSRMS can be equipped with the Special-Purpose Dexterous Manipulator (SPDM) to facilitate delicate assembly tasks.

The European Space Agency (ESA) will also provide a robotic manipulator system, the European robotic arm (ERA), for the ISS (Fig. 1.70). Currently scheduled for launch in 2015, it should be attached to the Russian segment of the station [38]. The arm is 11.3 m long and has seven DOF. Its basic configuration and functionality are similar to SSRMS.

In Japan, the Japanese Experiment Module Remote Manipulator System (JEMRMS), shown in Fig. 1.71, has been developed by the Japan Aerospace Exploration Agency (JAXA) [39]. The JEMRMS consists of two components: a 9.9 m-long six-DOF main arm and a shorter 1.9 m-long six-DOF arm for fine tasks; together, the two arms form a serial 12-DOF macro-micro manipulator system. After installation, the arm will be used to handle experiment payloads attached to the exposed facility of the Japanese Experiment Module [40].

Figure 1.69: SRMS used as a platform for an extravehicular activity (image courtesy of NASA)

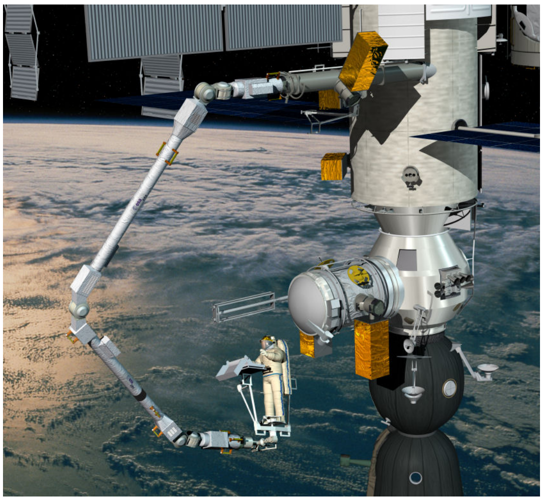

Figure 1.70: European Robotic Arm (image courtesy of ESA)

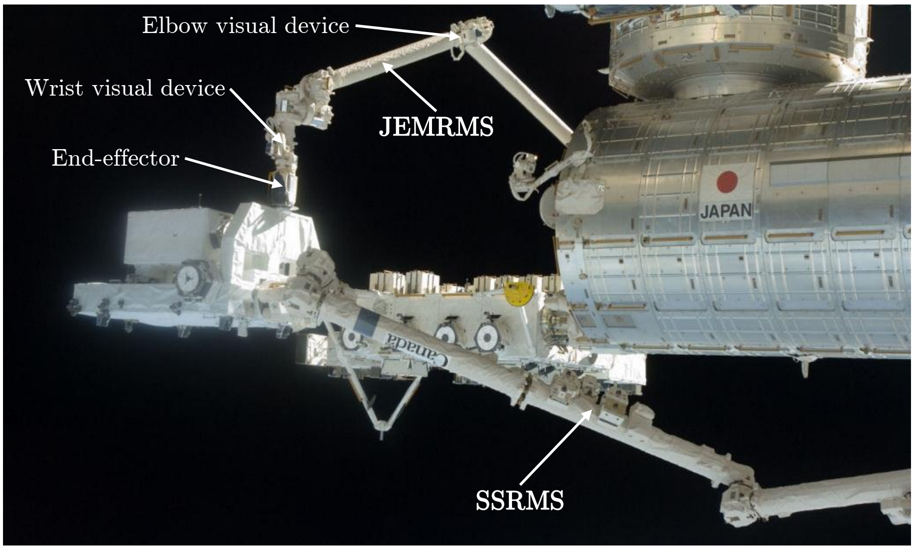

Figure 1.71: The SSRMS and JEMRMS arms operating on the ISS (image courtesy of NASA)

As explained in section 2.2.7, a robot system comprising a relatively short arm for fine manipulation mounted on a larger arm for coarse positioning is called a macro–micro manipulator system. The SSRMS equipped with the SPDM and the JEMRMS are relevant examples. In these systems, the base body is the interface between the macro arm's end-point and the micro arm's root (Fig. 1.72(a)). When the macro arm is locked after operating, the system is considered to be a flexible-based manipulator (Fig. 1.72(b)).

The booms of the long-reach arms are usually relatively stiff, but flexibility is gained from the low stiffness of the joints and gear trains. In addition, lightweight properties and microgravity make the structure extremely sensitive to vibrations, and the surrounding vacuum only provides a reduced damping effect to the structure. For these reasons, the macro subsystems of the SSRMS or JEMRMS are subject to vibrations that may not decrease for a long time after coarse positioning operations. During fine manipulation, the macro arms behave as passive flexible structures. Nevertheless, they may still vibrate as a result of the micro arm's motion. These vibrations degrade the overall performance of these systems. Given the astronomical costs of space flights, reducing this time would

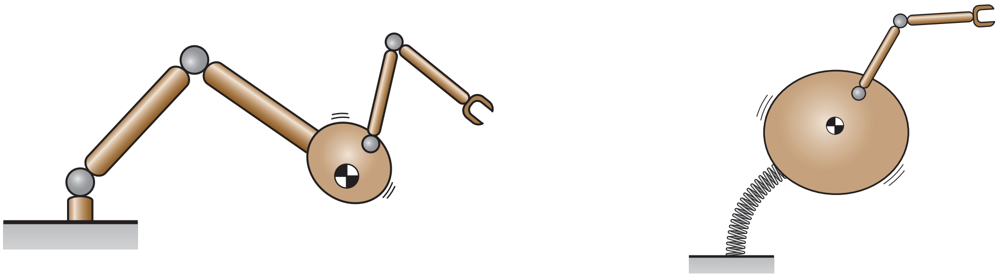

(a) (b)

Figure 1.72: Two basic types of moving base robots: (a) Macro-micro manipulator system, (b) flexible-structure-based manipulator system

result in significant cost savings.

Conventionally, the issue of vibrations on the SRMS and the SSRMS has been managed by increasing well-trained astronauts' operational skills and by limiting the maximum operational velocity according to the inertia of the handled object. However, if an advanced controller was introduced, astronauts' training time could be reduced and the operational speed could be increased.

To suppress the vibrations affecting the macro arm, a control method called "coupled vibration suppression control" [41] has been used with some success. In this method, the micro arm's motion is adjusted so it damps the vibrations of the macro arm. This specific trajectory of the micro arm is calculated using feedback from the linear and angular velocities measured at the end-point. It should be noted that the proposed control method requires precise information on dynamic characteristics, such as the arms' inertia and the exact weight of the payload. Therefore, this limitation could certainly be overcome by implementing parameter identification or adaptive control features, which would guarantee the convergence of the control scheme even with imprecise a priori knowledge of the dynamic parameters.

In the 1990s, a research program aimed at developing new control algorithms for flexible manipulators in space in order to mitigate and compensate for vibrations [42]. In particular, a planning technique known as "coupling mapping" method (see section 2.2.5) generates graceful system motions that do not cause excessive excitation of the structural modes. A second control algorithm known as "inferred end-point control" compensates for potential residual vibrations in the end-effector using strain measurements, regardless of uncontrolled vibrations in the supporting structure. More recently, another new approach for determining the response of the SRMS in handling large, rigid, overhanging payloads was presented [43].

Conclusion of the industrial review

This brief review collected information on how the problem of vibration control is addressed in some of the most ITER-relevant robotic devices performing in hostile environmental conditions. Although interesting vibration compensation methods have been found, in particular for RH systems specially designed for fusion applications, the question of how extreme operating conditions affect the performance of these advanced correction schemes has, unfortunately, not been addressed.

Telerobotic systems such as those equipping the La Hague reprocessing plant perfectly illustrate the advantages of introducing a man-in-the-loop during operations in constrained environments such as hot cells or the ITER in-vessel. Nevertheless, no satisfying industrial experience on master-slave systems implicating a flexible arm except the one gained through space activities has been identified. In nuclear fusion activities, problems with stimulating dynamics have, up to now, been sidestepped by using robotic modes and predefined teach files including very smooth trajectories. In terms of load transfer, one can undoubtedly take advantage of the experience gained at JET and the current developments on the IVT. The two approaches are quite similar, even though the former is based on a force/torque measurement and the latter is based on position and contact measurement. The main drawback of these methods is that they both rely on the extensive use of additional electronics that will presumably either increase the probability of failure of the system or show poor radiation resistance.

ENEA's approach to vibrations affecting the IVVS is interesting, although it requires extensive post-processing, which makes the method unsuitable for real-time applications. In particular, real-time double integration and noise reduction in the accelerometer signal are likely to pose difficulties. As a result, the proposed solution deals more with image enhancement than with vibration control.

Finally, recent developments carried out by JAERI on the IVT machine vision system are very encouraging. Although they do not deal directly with vibration sensing, they open up new prospects in the use of radiation-tolerant cameras.

1.2.2 Limitation of commercial off-the-shelf accelerometers

Typical vibration measurement systems include an accelerometer to sense vibrations. This was illustrated in the previous section with the vibration correction algorithm developed for IVVS (see p. 41). Recent advances in microelectronic mechanical systems (MEMS) have produced high-performance, high-accuracy, low-cost commercial off-the-shelf (COTS) accelerometers. However, if one is interested in measuring vibration amplitude, accelerometers require two integrations and are consequently subject to drift in position measurement. Moreover, in the case of electronics intended for use in radiation environments, the type of radiation, the dose rates and the integrated dose are factors that may limit the lifetime and the reliability of the equipment.

In general, mechanical sensors made of metallic parts are very resistant to radiation as long as their insulators and connectors are not damaged. However, many mechanical sensors, particularly accelerometers and pressure gauges, also use semiconductor elements, which are very sensitive to radiation [44–47]. A large majority of the COTS accelerometers are piezoelectric, piezoresistive or capacitive. Piezoelectric accelerometers are the most commonly used sensors for vibration monitoring applications. Usually, piezoelectric sensors are radiation-tolerant and operate without failure up to 100 kGy. This is confirmed by a quick market survey on COTS rad-tolerant accelerometers (see Table 1.4).

Table 1.4: Examples of available rad-tolerant accelerometers

Manufacturer	**Model**	**Type**	**Range (g)**	**Sensitivity**	**Total integrated dose (TID) (Gy)**	**Ref.**
Measurement Specialties	34201A	?	±2	1000 mV/g	10	[48]
Silicon Designs	2430	Capacitive	±2	2500 mV/g	10	[49]
Monitran	MTN 1100-R	?	±80	100 mV/g	10^5	[50]
Wilcoxon Research	793R	Piezo	±50	100 mV/g	10^5	[51]
Meggitt Sensing Systems	Endevco 2273A	Piezo	±1000	3 pC/g	$6.2 \cdot 10^8$	[52]
PCB	357B53	Piezo	±150	100 pC/g	10^6	[53]

The first conclusion of this survey is that the market for radiation-tolerant accelerometers is very narrow. Most commercially available products are not able to withstand doses at the level of the kGy. The frequency response of ultrasonic sensors degrade very quickly, with decreased amplitudes of 20–50% and shifts in their resonance frequencies of 1–2%. Very few manufacturers claim to offer products able to withstand an integrated gamma dose in the order of the MGy as required by most of the ITER RH systems. Such is the case for Meggitt Sensing Systems and PCB, who offer charge output sensors tolerating high radiation levels. However, the low sensibility of these two products makes them inappropriate for our applications. They only generate output signals of a few picocoulombs (less than 100 pC/g) with very high impedance that can then be converted into voltage using methods such as a de Sauty bridge. However, vibration control in systems such as the IVVS or the BRHS requires the detection of accelerations whose maximal values are 0.0395 m/s^2, i.e. $0.004 \times g$ (1 Hz, 1 mm amplitude) and 1.4220 m/s^2, i.e. $0.145 \times g$ (3 Hz, 4 mm amplitude) respectively, which would require high sensitivity accelerometers (in the range of 1000 mV/g or 5000 pC/g at a minimum).

Finally, it should be noted that the radiation resistance claimed by Meggitt Sensing Systems for their Endevco 2273A model is questionable. Indeed, the qualification of this component under gamma radiation up to 620 MGy would require between 7 and 10 years in high-activity ^{60}Co irradiation facilities, such as SCK-CEN's BRIGITTE [54] or the Institute of Isotopes' SSL-01 type irradiator, for an overall cost of some millions of euros.

In conclusion, no COTS accelerometer meets the very specific requirements for vibration sensing in the ITER in-vessel RH equipment. The customisation and qualification of existing products or the investigation of cutting-edge concepts (e.g. fibre Bragg grating—FBG—vibration sensing) might be considered. However, these options would inevitably involve high development costs.

1.2.3 The problem of vibration control in the ITER RH equipment

The introduction of man-in-the-loop capabilities in the robotic arms designed for ITER maintenance would provide useful assistance during unplanned events, such as inspections, and provide the operator the ability and flexibility to locate and examine unplanned targets (c.f. IVVS operations). It would also ease peg-in-hole tasks, such as the installation of heavy modules (c.f. BRHS operations).

However, vibrations due to the high flexibility of the robotic structure are most likely the main problem identified in such a master-slave mode. Mechanical flexibilities are present for two reasons: the use of compliant transmission elements for safety reasons and the design of lightweight and slender structures due to the size and arduous accessibility to the reactor. These two types of flexibility induce static and dynamic deflections between the configuration of the joints and the end-effector position, thereby greatly complicating the motion control. The completion of positioning tasks with the accuracy required would certainly benefit from the integration of high-level compensation schemes.

From a general standpoint, the stimulation of the structural modes can result from the following factors:

- a critical trajectory imposed by the operator;
- a collision or interaction with the environment (load transfer, e.g. during installation of blanket modules); or
- internal non-modelled dynamics (from carried processes, e.g. IVVS rotating prism).

Input-shaping techniques [55, 56] are efficient ways to avoid critical trajectories by adjusting the input command to the actuators in such a way that the vibrational modes are not excited. Considering the two other origins, the vibrational behaviour of the arm cannot be foreseen, and it needs to be damped as soon as it occurs.

In the majority of standard industrial applications, additional sensors can be added to a system to control its flexible states. Unfortunately, conditions that are harsh for humans are hard on equipment as well. Most of the ITER RH equipment will be subjected to cumulative radiation doses of several MGy. Many types of mechanical sensors, particularly accelerometers, are very sensitive to radiation (c.f. section 1.2.2). Moreover, in-vessel inspections will be carried out within strong, non-uniform magnetic fields. Therefore, sensors subject to capacitive coupling, such as strain gauges, would suffer from the inherent high noise due to electromagnetic interferences in addition to the problems raised by radiation. Using redundant sensors may help limit these issues in some very specific cases, but utilising many sensors necessitates large wiring bundles and makes the manipulator design more complex, which also increases the probability of system failure.

Such constraints limit the use of dedicated off-the-shelf electronics to control vibrations in the ITER in-vessel environment.

1.3 Scope, objectives and limitations of the thesis

1.3.1 Scope of the thesis

The main aim of this thesis is to control the oscillatory behaviour of a flexible remote manipulator arm without considering any extra sensors apart from the embedded rad-hardened vision devices that will inevitably be used to provide real-time visual feedback to the operators. The tip displacement induced by vibrations is estimated by exploiting a simple physical model of the manipulator. Using a camera mounted in an eye-in-hand configuration [57], this model is then readjusted using direct measurement of the oscillations in the tip with respect to the static environment.

An extensive amount of work has been published on the study of flexible manipulators, mainly in the 1980s and 1990s. However, the use of vision devices to stabilise an oscillating arm is quite recent, and it seems this promising solution has not been discussed at length. Parts of this work continue along the lines of several other works on the vibration control of flexible links using visual data [58–62]. In particular, [62] proved the feasibility of using a two-timescale Kalman filter to observe the arm's vibrational behaviour. However, the tracking in this previous work is based on the detection of a set of particular markers (red dots on a plain background). Even if no information is assumed regarding their geometry, the problem is greatly simplified since the need for robust tracking is toned down.

This thesis addresses the following nine topics:

- **Robust tracking of features from an unknown environment:** the first issue addressed in this thesis deals with vibration suppression by using visual data without any markers or a priori knowledge of the environment. Particular attention must be paid to obtaining an algorithm whose robustness is ensured at every step.

- **Vibration reconstruction using a fusion of visual data and joint movements:** in this thesis, the vibration to be rejected must be reconstructed based on visual data. To ensure that the proposed method is robust against visual troubles, these data must be fused with the joint movements through a model of the arm.

- **Incorporation of time-delayed measurements in a Kalman filter:** vision devices have the drawback of a long processing time that yields delayed measurements and low update rates. Such issues require modifications in the Kalman filter.

- **Online estimation of image capture delay based on timestamp exchange:** most VS control algorithms are implemented astride a real-time high sampling rate controller and a non-real-time supervisor whose sampling rate is aligned with the camera's framerate. Exchanging timestamps between these two systems makes it possible to estimate the image capture time with an accuracy of several ms.

- **Online estimation of image capture delay based on a synchronisation sensor:** for visual servoing applications requiring more accurate estimates of the image capture delay, one can benefit from using a secondary embarked sensor to synchronise the delayed visual data with the physical phenomenon. The estimation of the capture delay is based on the concept of the cross-correlation function.

- **Derivation of an advanced computationally light model of a flexible arm:** today, industrial cameras provide framerates enabling the observation of three or four modes. Classical methods often yield a set of non-linear equations that are accurate but hardly implementable in real-time (RT) applications. Consequently, the importance of obtaining a precise but computationally light model of a flexible arm to be used in the Kalman filter has been emphasised.

- **Vibration reconstruction using sinusoidal regression:** this thesis also considers sinusoidal regression as an alternative to Kalman filtering. The vibration is reconstructed under the single assumption that it is mainly sinusoidal.

- **Change detection:** the previous topic implies performing a least-square regression over a sliding window. Clearly, the choice of the window length is a critical parameter because it is responsible for stability during steady-state and reactivity during transients. Therefore, this thesis also examines the notion of change detection to properly adjust the length of the time window.

- **Simultaneous joint positioning and vibration rejection:** the control problem is to use the joint torque to track the desired joint position and reject the unwanted oscillation in the structure.

1.3.2 Objectives

The thesis presented in this document is the following:

> *In hostile environments limiting the use of usual or dedicated sensors, vibration control of RH equipment could benefit from the use of all information supplied by embedded rad-hardened cameras, i.e. by considering vision devices as full sensors providing quantitative data and not merely as plain visual feedback providing only qualitative information to the operator.*

Consequently, the following are the objectives of the present thesis:

- to make available a study addressing the problems that occur when performing maintenance operations in a fusion reactor with flexible robotic devices;

- to highlight some promising solutions that could be used as a basis for further developments during the preliminary design of the ITER remote maintenance system and for other applications characterised by particularly hazardous environments limiting the use of common sensors (e.g. decommissioning activities); and

- to contribute to the already widely explored field of vibration control in flexible robot arms by promoting vision-based techniques made possible by recent improvements in vision sensor performance.

1.3.3 Restrictions

Only flexible n-DOF manipulators in free space motions will be considered in this thesis. Consequently, contact dynamics and force control will not be addressed. The problem of modelling impact dynamics is also out of the scope of this thesis. Cooperating robots are left for future studies as well.

1.4 Material presented within the thesis

Most of the results described in this thesis are based on six peer-reviewed publications. With the exception of the first, all these articles were published with the author of this thesis as the main author.

The first paper [63] aimed to highlight the problems encountered during the manipulation of heavy loads with a light structure: vibrations, critical trajectory, etc. This study mainly provided an opportunity to build a representative, flexible, experimental device that would be used to validate the upcoming results. With the help of a numerical finite-element model of the mock-up, preliminary investigations were made to identify the main contributors to the positioning error.

The second paper [64] presented industrial and academic state-of-the-art studies on flexible arm modelling and control. Although a significant number of theoretical and experimental works had been achieved on the topic, no real control strategy of the arm's internal dynamics had ever been implemented in industrial RH systems.

In the third [65] and fourth [66] papers, a robust vibration control was presented for a flexible inspection arm moving in an unknown environment, with an emphasis on academic development in the former and the benefit to the fusion community in the latter. The proposed method entailed a vibration estimator that reconstructed the vibrations from visual data without any a priori knowledge of the surroundings. The whole control scheme was validated on the single-joint flexible experimental device introduced in [63].

The fifth paper [67] describes an online sinusoidal regression algorithm which makes the proposed vision-based vibration control suitable, regardless of the origin of the vibrational behaviour. To obtain appropriate tracking capability and estimation accuracy, this new method included the use of a variable-sized window coupled with a signal change detector. As before, the proposed algorithm was validated on the single-joint mock-up [63] until the availability of RH system prototypes for ITER makes it possible to test it at full-scale.

The sixth and last paper [68] highlighted the limitations of the capture delay estimation implemented in the previous works. Consequently, a new method using a synchronisation sensor was proposed. Based on a cross-correlation technique, a novel algorithm for effective time-delay estimation was derived. Experimental validation demonstrated that this method yielded an improved estimation, which could be beneficial to vibration damping.

1.5 Structure and contribution of the thesis

This thesis is organised as follows. Chapter 2 establishes an exhaustive state-of-the-art on the modelling and control of robotic arm flexibilities and introduces the main concepts of visual servoing and visual tracking. Chapter 3 proposes a vision-based method to solve the problem of vibrations affecting remote maintenance operations in fusion reactors. The proposed technique uses visual features from the tokamak in-vessel environment without using any a priori knowledge or markers. In particular, section 3.1 considers the problem of designing an online vibration estimator fusing visual data and joint movements using a Kalman filter based on a simple model of the arm's flexibilities. In section 3.2, an advanced model considering previously neglected inertia terms is derived for use in this Kalman filter. Section 3.3 considers sinusoidal regression instead of Kalman filtering to reconstruct the vibration from visual data. Chapter 4 describes the experimental validation of these theoretical results on a single-axis, flexible test setup. Chapter 5 concludes the thesis.

The primary contributions of the thesis are as follows:

- implementation of a markerless tracker to determine the velocity of a tip-mounted camera in an untrimmed environment in order to stabilise an oscillating robotic arm;
- modification of an online interaction matrix estimator to make it self-adjustable (i.e. stable when the arm hardly moves and very sensitive when it moves fast);
- derivation of a multimodal dynamic model to be used for vision-based vibration control of a flexible rotating beam;
- development of a new vision-based method using sinusoidal regression to reconstruct the oscillation to be rejected; and
- contribution to the online estimation of the image capture delay for visual servoing applications with high dynamics.

2. REVIEW OF THE STATE-OF-THE-ART

The main objective of this chapter is to review the state-of-the-art that has been identified as relevant to meeting the objectives of this thesis. The modelling of flexible robotic arms is addressed in section 2.1. Control methodologies specific to flexible robotic arms are presented in section 2.2. Finally, the main concepts of visual tracking are introduced in section 2.3.

2.1 Modelling flexible robotic arms

Over the last decade, the control problems of flexible manipulators have been intensively studied due to the demand of fast, precise robots in various industrial applications. The strategy presented in most of the literature is not only to control the motion of the rigid mode with reasonable accuracy but also to control the vibrations of the highest modes in order to achieve high speeds and precise tip positioning. A considerable amount of theoretical and experimental research has been carried out in this field from very different perspectives.

Most control algorithms rely on models of the robots' dynamic behaviour. In these model-based approaches, the key to successful control is the model's accuracy. An arbitrarily selected model may exclude some significant parameters or, conversely, complicate the possible identification procedure by including useless parameters.

Flexibility can be considered to be concentrated at the robot's joints or distributed along the robot's links. If this first assumption does not have sound consequences on the modelling step, the resulting models will have quite different properties from a control point of view. Consequently, cases involving robots with flexible joints and robots with flexible links will be presented separately.

The topic of flexible robot modelling has been widely covered from very different perspectives, which requires being selective. Therefore, flexibility-oriented design, which is aimed at stiffening a flexible manipulator by adding structural mass or improving the material distribution or properties (composite materials with inherent damping, smart materials), will not be addressed. Non-linear dynamic behaviours arising from large rotations of flexible structures, which may be attributed to stretching in the axial direction as they deflect, will not be considered either. A simple linear beam theory is no longer applicable in such a situation. Discussions of the non-linear dynamics of multibody mechanical systems composed of Euler-Bernoulli beams can be found in [69, 70]. Finally, other efficient methods for modelling flexible arms, such as fuzzy logic [71], offer elevated modelling capabilities and simplicity in the identification phase. These advanced or exotic modelling methods will not be covered in this review.

This part, dealing with the modelling of flexible robotic arms, is organised as follows Section 2.1.1 describes a classical, energy-based method for deriving a model of an arm with flexibilities concentrated in the joints. Section 2.1.2 focuses on the assumed modes method which is widely used to model flexible links. Of course, joint and link flexibilities may be present at the same time. Many of the presented results can be extended to this case as well. Therefore, section 2.1.3 provides a few references for modelling flexible structures made of both flexible joints and links. Next, the question of modelling moving flexible arms, which sometimes implies the use of time-dependent boundary conditions, will be addressed in section 2.1.4 with a special emphasis on rotating beams. The following relevant topics are discussed and additional information is provided: the impact of elastic deformation on rigid body displacement (section 2.1.5); model order reduction (section 2.1.6); and the identification of model parameters (section 2.1.7). Finally, section 2.1.8 briefly discusses how the various modelling methodologies presented in this state-of-the-art review will be used in the developments detailed in Chapter 3.

2.1.1 Modelling flexibilities of the joints

The presence of flexibility in the joints is common in robotics when particular motion transmission/reduction elements (belts, long shafts, cables, harmonic drives, cycloidal gears) are used. They can have different purposes, such as improving the dynamic efficiency of the arm by relocating the actuators next to the base or guaranteeing high reduction ratios with power-efficient compact devices. Unfortunately, one major drawback of such technical solutions lies in their intrinsic flexibility when high forces/torques are transmitted. This flexibility introduces a complex displacement between the position of an actuator and the link that it drives. Without a specific control action, an oscillatory behaviour can be observed at the robot end-effector during free motion as well as some form of instability during contact tasks.

From a modelling point of view, the advantage of this kind of flexibility is that the defection can be modelled as being concentrated at the joints. Consequently, the dynamic model of a flexible-joint/rigid-link robot requires only twice the number of generalised coordinates compared to the rigid case in order to completely characterise the configuration of all bodies.

Most previous investigations of the dynamics of flexible joint manipulators have considered rotary joints. Although flexible arms involving a prismatic joint [72–74] represent another interesting problem that may be worth investigating, they will not be addressed in the present review.

In this section, the dynamic model of a robot with flexible joints is derived using the Lagrangian approach, which is a variational method based on energy principles. Lagrange's equations originate from Hamilton's principle, which is likely the most applied method for obtaining continuous models. However, unlike Hamilton's principle, they do not require integration by parts, which represents the main advantage of this method. Moreover, the Lagrangian approach permits choosing both discrete and distributed variables as generalised coordinates. For these reasons, this method can easily be implemented on a computer. Nevertheless, since they have the same origin, Hamilton's principle and Lagrange's equations usually give the same model for the same set of assumptions.

Complete model

Let us consider a robot with flexible joints as an open kinematic chain composed of $n + 1$ rigid bodies (the base and the n links) interconnected by n (rotary or prismatic) flexible joints and actuated by n drives. From a mechanical point of view, each drive (electrical, hydraulic, etc.) is an additional rigid body with inertial properties. The masses of the links are noted m_{Li} and those of the drives are noted m_{Ri}. The notations are those from [75], where more details on the model derivation can also be found. Conventionally, if reduction gearings are involved, they are modelled as being placed before the joint deflection occurs.

The following standard assumptions are made.

- Joint deflections are small; therefore, the flexibility effects are limited to the domain of linear elasticity. Consequently, the elasticity at joint i is modelled by a spring of stiffness $K_i > 0$, which is torsional for rotational joints and linear for translational ones. Most of the time, linear stiffness is considered for flexible joints but non-linear stiffness characteristics can also be assumed, provided that the map from deflection to force is invertible.
- The rotors of the actuators are statically and dynamically balanced. This implies that the inertia and gravity terms of the arm model will be independent of the drive's angular position.
- Each motor is located in a position preceding the driven link. The simplest situation is when the i^{th} motor moves link i and is mounted on link $i - 1$ with its rotation axis aligned with the i^{th} joint.

As previously noted, kinematic and dynamic analyses only require $2n$ frames attached to the $2n$ moving rigid bodies: the link frames $\mathcal{L}_i$ and the motor frames $\mathcal{R}_i$ (with $1 \leq i \leq n$). The standard Denavit-Hartenberg convention can be used for the definition of the link frames $\mathcal{L}_i$. The frames $\mathcal{R}_i$ are attached to the motor stators and are aligned with the axes of symmetry of the motors and the z-axis along the spinning direction of the rotor (see Fig. 2.1). Accordingly, $2n$ generalised coordinates will be needed. A possible set of coordinates is given by:

$$\boldsymbol{\delta} = \left[\boldsymbol{\theta} \; , \boldsymbol{q}\right]^{\top} \in \mathbb{R} \tag{2.1}$$

where $\boldsymbol{\theta}$ is the vector of the n link positions and $\boldsymbol{q}$ is the vector of the n rotor positions as reflected through the transmission/reduction gears (see Fig. 2.2).

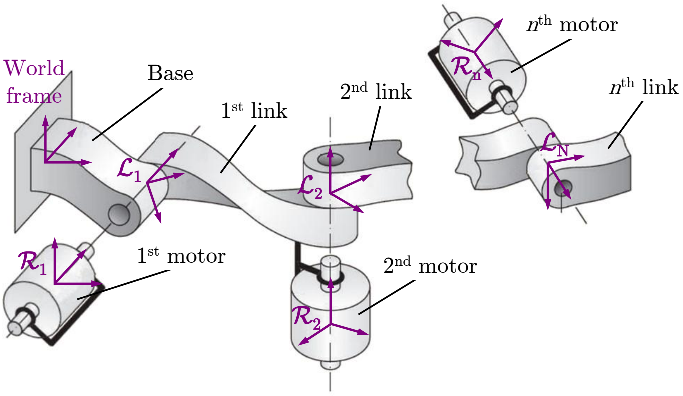

Figure 2.1: Arrangement of motors and links in an open kinematic chain

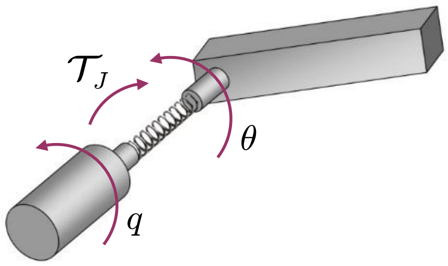

Figure 2.2: Schematic representation of an elastic joint

This choice of variables is particularly convenient for the following reasons:

- the obtained model is formally independent from the reduction ratios;
- these position variables have a similar dynamic range; and
- the arm kinematics only depends on $\boldsymbol{\theta}$ (which are already beyond the joint flexibilities); therefore, direct/inverse kinematics problems are identical to cases involving rigid robots.

It might also be useful to define secondary variables; these can include the following:

- $\boldsymbol{q_m}$, which is the vector of the n drive positions before reduction. These are the quantities directly measured by encoders mounted on the drives. For a motor directly placed on the i^{th} joint axis, one has the relation $\dot{q}_{mi} = gr_i \dot{q}_i$, where $gr_i \geq 1$ is the gear ratio at the i^{th} joint;
- $\delta\theta_i = \theta_i - q_i$, which is the deflection at the i^{th} joint; and
- $\tau_i = K_i(q_i - \theta_i)$, which is the quantity measured by a joint torque sensor, whenever present.

Note that the set $(\boldsymbol{q}, \boldsymbol{\delta\theta})$ is also commonly used in the literature.

Following the Lagrangian approach, one must express the two types of energy contributing to the Lagrangian $\mathcal{L} = \mathcal{T}(\boldsymbol{\delta}, \dot{\boldsymbol{\delta}}) - \mathcal{U}(\boldsymbol{\delta})$.

The potential energy $\mathcal{U}$ is due to two factors.

- Gravity, which is related to the position of the link/motor barycentre:

$$\mathcal{U}_{grav}(\boldsymbol{\theta}) = \mathcal{U}_{grav,link}(\boldsymbol{\theta}) + \mathcal{U}_{grav,motor}(\boldsymbol{\theta}) \tag{2.2}$$

- Joint elasticity:

$$\mathcal{U}_{elast}(\boldsymbol{\theta}, \boldsymbol{q}) = \frac{1}{2}(\boldsymbol{\theta} - \boldsymbol{q})^\top \boldsymbol{K}(\boldsymbol{\theta} - \boldsymbol{q}) \tag{2.3}$$

  where $\boldsymbol{K}$ is a diagonal matrix of the form $\boldsymbol{K} = diag(K_1, ..., K_n)$.

As a result, the following is obtained for potential energy:

$$\mathcal{U}(\boldsymbol{\theta}, \boldsymbol{q}) = \mathcal{U}_{grav}(\boldsymbol{\theta}) + \mathcal{U}_{elast}(\boldsymbol{\theta}, \boldsymbol{q}) \tag{2.4}$$

The kinetic energy $\mathcal{T}$ is due to two factors.

- The links, which introduce no difference with respect to the standard rigid robot case:

$$\mathcal{T}_{link} = \frac{1}{2}\dot{\boldsymbol{\theta}}^\top \boldsymbol{M_L}(\boldsymbol{\theta})\dot{\boldsymbol{\theta}} \tag{2.5}$$

  where $\boldsymbol{M_L}(\boldsymbol{\theta})$ represents the positive-definite symmetric link inertia matrix.

- The rotors:

$$\begin{aligned} \mathcal{T}_{rotor} &= \sum_{i=1}^{n} \mathcal{T}_{rotor,i} & (2.6) \\ &= \sum_{i=1}^{n} \left(\frac{1}{2} v_{Ri}^\top m_{Ri} v_{Ri} + \frac{1}{2} {}^{\mathcal{R}i}\boldsymbol{\omega_{Ri}}^\top \, {}^{\mathcal{R}i}\boldsymbol{I_{Ri}} \, {}^{\mathcal{R}i}\boldsymbol{\omega_{Ri}} \right) & (2.7) \end{aligned}$$

  where v_{Ri} is the linear velocity of the centre of mass of the i^{th} rotor and ${}^{\mathcal{R}i}\boldsymbol{\omega_{Ri}}$ is the angular velocity of the i^{th} rotor body. v_{Ri} can be expressed as a function of $\boldsymbol{\theta}$ and $\dot{\boldsymbol{\theta}}$ only. According to the assumption made on the drive's balancing, the rotor inertia matrix is diagonal:

$${}^{\mathcal{R}i}\boldsymbol{I_{Ri}} = diag(I_{Rixx}, I_{Riyy}, I_{Rizz}) \tag{2.8}$$

  with $I_{Rixx} = I_{Riyy}$. Moreover, the angular velocity of the i^{th} rotor has the general expression:

$${}^{\mathcal{R}i}\boldsymbol{\omega_{Ri}} = \sum_{j=1}^{i-1} \boldsymbol{J_{Rij}}(\boldsymbol{\theta})\dot{\boldsymbol{\theta}}_{\boldsymbol{j}} + \begin{bmatrix} 0 \\ 0 \\ \dot{q}_{mi} \end{bmatrix} \tag{2.9}$$

  where $\boldsymbol{J_{Rij}}(\boldsymbol{\theta})$ is the j^{th} column of the Jacobian relating the link velocities $\dot{\boldsymbol{\theta}}$ to the angular velocity of the i^{th} rotor in the robot chain.

By substituting (2.9) and (2.8) into (2.7), and by expressing $\dot{\boldsymbol{q}}_{\boldsymbol{m}}$ in terms of $\dot{\boldsymbol{q}}$, it can be shown that:

$$\mathcal{T}_{rotor} = \frac{1}{2}\dot{\boldsymbol{\theta}}^\top \left(\boldsymbol{M_R}(\boldsymbol{\theta}) + \boldsymbol{S}(\boldsymbol{\theta})\boldsymbol{B}^{-1}\boldsymbol{S}^\top(\boldsymbol{\theta}) \right) \dot{\boldsymbol{\theta}} + \dot{\boldsymbol{\theta}}^\top \boldsymbol{S}(\boldsymbol{\theta})\dot{\boldsymbol{q}} + \frac{1}{2}\dot{\boldsymbol{q}}^\top \boldsymbol{B}\dot{\boldsymbol{q}} \tag{2.10}$$

where:

- $\boldsymbol{B}$ is the constant diagonal inertia matrix collecting the rotors' inertial components I_{Rizz} around their spinning axes;
- $\boldsymbol{M_R}(\boldsymbol{\theta})$ contains the rotor masses and, possibly, the rotors' inertial components along the other principal axes; and
- $\boldsymbol{S}(\boldsymbol{\theta})$ is a square matrix expressing the inertial couplings between the rotors and the previous links in the robot chain.

Summing up, the total kinetic energy of the robot is:

$$\mathcal{T} = \frac{1}{2}\dot{\boldsymbol{\delta}}^{\top}\boldsymbol{M}(\boldsymbol{\delta})\dot{\boldsymbol{\delta}} \tag{2.11}$$

$$= \frac{1}{2}\begin{bmatrix}\dot{\boldsymbol{\theta}}^{\top} & \dot{\boldsymbol{q}}^{\top}\end{bmatrix}\begin{bmatrix}\boldsymbol{M_{TOT}}(\boldsymbol{\theta}) & \boldsymbol{S}(\boldsymbol{\theta}) \\ \boldsymbol{S}^{\top}(\boldsymbol{\theta}) & \boldsymbol{B}\end{bmatrix}\begin{bmatrix}\dot{\boldsymbol{\theta}} \\ \dot{\boldsymbol{q}}\end{bmatrix} \tag{2.12}$$

with

$$\boldsymbol{M_{TOT}}(\boldsymbol{\theta}) = \boldsymbol{M_L}(\boldsymbol{\theta}) + \boldsymbol{M_R}(\boldsymbol{\theta}) + \boldsymbol{S}(\boldsymbol{\theta})\boldsymbol{B}^{-1}\boldsymbol{S}^{\top}(\boldsymbol{\theta}) \tag{2.13}$$

As anticipated, the total inertia matrix $\boldsymbol{M}$ of the robot only depends on $\boldsymbol{\theta}$.

Using the Lagrange equations finally yields the complete dynamic model:

$$\begin{bmatrix}\boldsymbol{M}(\boldsymbol{\theta}) & \boldsymbol{S}(\boldsymbol{\theta}) \\ \boldsymbol{S}^{\top}(\boldsymbol{\theta}) & \boldsymbol{B}\end{bmatrix}\begin{bmatrix}\ddot{\boldsymbol{\theta}} \\ \ddot{\boldsymbol{q}}\end{bmatrix} + \begin{bmatrix}\boldsymbol{c}(\boldsymbol{\theta}, \dot{\boldsymbol{\theta}}) + \boldsymbol{c_1}(\boldsymbol{\theta}, \dot{\boldsymbol{\theta}}, \dot{\boldsymbol{q}}) \\ \boldsymbol{c_2}(\boldsymbol{\theta}, \dot{\boldsymbol{\theta}})\end{bmatrix} + \begin{bmatrix}\boldsymbol{g}(\boldsymbol{\theta}) + \boldsymbol{K}(\boldsymbol{\theta} - \boldsymbol{q}) \\ \boldsymbol{K}(\boldsymbol{\theta} - \boldsymbol{q})\end{bmatrix} = \begin{bmatrix}0 \\ \boldsymbol{\tau}\end{bmatrix} \tag{2.14}$$

where the inertial terms, the Coriolis and centrifugal terms and the potential terms have been written separately. In particular, $\boldsymbol{g}(\boldsymbol{\theta}) = (\partial \mathcal{U}_{grav}(\boldsymbol{\theta})/\partial \boldsymbol{\theta})^{\top}$ while $\boldsymbol{\tau_J} = \boldsymbol{K}(\boldsymbol{q} - \boldsymbol{\theta})$ is the elastic torque transmitted through the joints.

The first n equations of the dynamic model (2.14) are referred to as the link equations, whereas the last n equations are referred to as the motor equations.

All non-conservative generalised forces should appear on the right-hand side of (2.14). When dissipative effects are not considered, only the motor torques $\boldsymbol{\tau}$ producing work on the $\boldsymbol{q}$ variable are present in the motor equations. If the robot end-effector is in contact with the environment, the 0 in the right-hand side of the link equations should be replaced by $\boldsymbol{\tau_{ext}} = \boldsymbol{J_{\theta}}^{\top}(\boldsymbol{\theta})\boldsymbol{F}$, where $\boldsymbol{J_{\theta}}(\boldsymbol{\theta})$ is the robot Jacobian with respect to the articular positions and $\boldsymbol{F}$ is the vector of the forces/torques acting from the environment on the robot.

In the presence of energy-dissipating effects, additional terms appear in the right-hand side of (2.14). For example, viscous friction at both sides of the transmissions and spring damping yield the term:

$$\begin{bmatrix}-\boldsymbol{F_q}\dot{\boldsymbol{\theta}} - \zeta(\dot{\boldsymbol{\theta}} - \dot{\boldsymbol{q}}) \\ -\boldsymbol{F_{\theta}}\dot{\boldsymbol{q}} - \zeta(\dot{\boldsymbol{q}} - \dot{\boldsymbol{\theta}})\end{bmatrix} \tag{2.15}$$

where the diagonal, positive-definite matrices $\boldsymbol{F_q}$, $\boldsymbol{F_\theta}$ and $\boldsymbol{\zeta}$ contain, respectively, the viscous coefficients on the link side and on the motor side as well as the damping of the elastic springs at the joints.

Broader forms of non-linear friction can be considered. Note that, in principle, friction acting on the motor side can be fully compensated by a suitable choice of the control torque $\boldsymbol{\tau}$, while this is not true for friction acting on the link side due to the non-collocation.

This dynamic model (2.14) also shares some properties with the rigid case:

- the model equations admit a linear parameterisation in terms of a suitable set of dynamic coefficients, including joint stiffness and motor inertia, which is useful for model identification and adaptive control;
- the Coriolis and centrifugal terms can always be factorised as $\boldsymbol{\mathcal{C}_{cc}}(\boldsymbol{\delta}, \dot{\boldsymbol{\delta}})\dot{\boldsymbol{\delta}}$, in such a way that matrix $\dot{\boldsymbol{M}} - 2\boldsymbol{\mathcal{C}_{cc}}$ is skew-symmetric, which is a property used in control analysis; and
- for robots having only rotational joints, the gradient of the gravity vector $\boldsymbol{g}(\boldsymbol{\theta})$ is globally bounded in norm by a constant.

Finally, when the joint stiffness is extremely large ($\boldsymbol{K} \to \infty$), then $\boldsymbol{q} \to \boldsymbol{\theta}$ while $\boldsymbol{\tau_J} \to \boldsymbol{\tau}$. It is easy to check that the dynamic model (2.14) tends towards the standard model of fully rigid robots.

Reduced model

In general, the link and motor equations in (2.14) are not only dynamically coupled through the elastic torque $\boldsymbol{\tau_J}$ at the joints but also through the inertial components of matrix $\boldsymbol{S}(\boldsymbol{\theta})$ (i.e. at the acceleration level). The relevance of these inertial couplings depends on the kinematic arrangement of the manipulator arm and, in particular, on the specific location of the motors and transmission devices. In some cases, the matrix $\boldsymbol{S}$ is constant (e.g. the planar case) or zero (e.g. for a single link with an elastic joint or for a robot with $n = 2$ links having the two motors mounted at the joints and orthogonal). When this occurs, the dynamic equations can be simplified considerably.

For a generic robot with elastic joints, one can take advantage of the presence of large reduction ratios (with gr_i in the order of 100–150) and simply neglect energy contributions due to the inertial couplings between the motors and the links. This is equivalent to considering the following simplifying assumption instead of (2.9):

$$^{\boldsymbol{\mathcal{R}i}}\boldsymbol{\omega_{Ri}} = \begin{bmatrix} 0 \\ 0 \\ \dot{q}_{mi} \end{bmatrix} \tag{2.16}$$

which implies that the angular velocity of the rotors is only due to their own spinning.

As a result, the total angular kinetic energy of the rotors comes down to $\frac{1}{2}\dot{\boldsymbol{q}}^{\top}\boldsymbol{B}\dot{\boldsymbol{q}}$ (since $\boldsymbol{S} \equiv 0$), and the dynamic model (2.14) reduces to:

$$\boldsymbol{M}(\boldsymbol{\theta})\ddot{\boldsymbol{\theta}} + \boldsymbol{c}(\boldsymbol{\theta}, \dot{\boldsymbol{\theta}}) + \boldsymbol{g}(\boldsymbol{\theta}) + \boldsymbol{K}(\boldsymbol{\theta} - \boldsymbol{q}) = 0 \tag{2.17}$$

$$\boldsymbol{B}\ddot{\boldsymbol{\theta}} + \boldsymbol{K}(\boldsymbol{q} - \boldsymbol{\theta}) = \boldsymbol{\tau} \tag{2.18}$$

with $\boldsymbol{M}(\boldsymbol{\theta}) = \boldsymbol{M_L}(\boldsymbol{\theta}) + \boldsymbol{M_R}(\boldsymbol{\theta})$. Centrifugal and Coriolis torques are reduced to $\boldsymbol{c}(\boldsymbol{\theta}, \dot{\boldsymbol{\theta}})$. The main advantage of this model is that the link and motor equations are dynamically coupled only through the elastic torque $\boldsymbol{\tau_J} = \boldsymbol{K}(\boldsymbol{q} - \boldsymbol{\theta})$. Moreover, the motor equations are now fully linear.

2.1.2 Modelling flexibilities of the links

As illustrated in the previous section, flexibility is a dynamic behaviour in which kinetic energy, stored in moving inertia, interacts with elastic potential energy, stored in compliant members. In flexible links, inertia and compliance are both distributed along the structure. For this reason, the dynamics of mechanical systems with distributed flexibility are described using infinite-dimensional mathematical models.

However, it is extremely difficult to practically design controllers based on such infinite models. A popular approach is to obtain a finite dimensional dynamic system by truncation and employ this reduced order model to design the controller (c.f. section 2.1.6). The higher order modes are then treated as disturbances that must be rejected.

Widely used techniques for deriving such finite dimensional descriptions are based on the experimental modal analysis method [76–78], the analytical resolution of governing partial differential equations (PDE) [79], the lumped elements method, the transfer matrices method, the assumed modes method, the finite elements method and the Ritz expansion. Each approach has its own characteristics in terms of complexity and accuracy [80]. Consequently, mathematical models of link flexibility result from a trade-off between accuracy and ease of implementation.

The lumped-element method (LEM) is a way of simplifying the behaviour of spatially distributed systems into a topology consisting of discrete entities that approximate the behaviour of the distributed system under certain assumptions. It is based on the same mathematical considerations that establish rigid transformation matrices. The 4 × 4 homogenous transformation matrix that describes position can be used to describe deflection as well. By connecting massless elements and rigid, lumped masses, a linear spatial model is obtained [81]. The Laplace transformation of these linear equations into the frequency domain, followed by the conversion of the boundary conditions into a matrix-vector product, results in a technique known as the transfer matrix method (TMM) [82].

Similar to the LEM, the finite element method (FEM), also known as the finite element analysis (FEA), is a computational technique aimed at expressing a continuously varying field variable in terms of a finite number of values evaluated at the nodes of a mesh. The elementary beam theory, which will be presented in the following paragraphs, can be applied to develop a beam element capable of properly exhibiting a transverse bending effect. The assembly of these elementary elements is similar in static and dynamic cases; the global mass/stiffness matrix is directly assembled using the individual mass/stiffness matrices in conjunction with the element-to-global displacement relations. Then, knowing the structure's elastic and inertia characteristics, modal analysis can be performed [83].

As far as these methods (LEM, TMM and FEM) are concerned, if the entire system assembly is procedurally straightforward, the process is quite tedious when carried out by hand. Moreover, for systems with no energy removal mechanism, the resulting equations of motion are the same as those given by the Lagrangian approach and the variational principle. For this reason, these three methods will not be discussed in depth here because they will not be used in the framework of this thesis. In any case, the modelling of flexible link manipulators using FEM has been widely covered in the literature; for further information on this topic, one can refer to [84–87], among other very valuable contributions.

This section first provides a short introduction on the beam theory. Next the assumed modes method is presented in detail. This technique assumes linear elasticity and light damping. Small deflections are assumed, and rotational motions are considered slow enough that centrifugal stiffening can be ignored.

Introduction to the beam theory

All researchers recognise that the bending effect is the predominant effect in a transversely vibrating beam. Consequently, the simplest beam model, the Euler-Bernoulli model, includes strain energy due to bending and kinetic energy due to lateral displacement. The Euler-Bernoulli model dates back to the 18th century. Jacob Bernoulli (1654–1705) first discovered that the curvature of an elastic beam at any point is proportional to the bending moment at that point. His nephew, Daniel Bernoulli (1700–1782), first formulated the differential equation of motion of a vibrating beam. Later, Leonhard Euler (1707–1783) used Jacob Bernoulli's theory in his investigation of the shape of elastic beams under various loading conditions [88]. The Euler-Bernoulli beam theory is the most commonly used because it is simple and provides reasonable engineering approximations for many problems. However, the Euler-Bernoulli model tends to slightly overestimate the natural frequencies, particularly those of the higher modes. Moreover, the prediction is better for slender beams than non-slender beams.

The Rayleigh beam theory [89] provides a marginal improvement on the Euler-Bernoulli theory by including the effect of rotation of the cross-section. Consequently, it partially corrects the overestimation of natural frequencies in the Euler-Bernoulli model. Nevertheless, the natural frequencies are still overestimated. In 1937, Davies studied the effect of rotary inertia on a fixed-free beam [90]. The shear model adds shear distortion to the Euler-Bernoulli model, which considerably improves the estimate of the natural frequencies. It should be noted that this is different from the "pure shear" model, which only includes the shear distortion and rotary inertia, and from the "simple shear" model, which only includes the shear distortion and lateral displacement. Neither the pure shear nor the simple shear model fits our purpose of obtaining an improved model to the Euler-Bernoulli model because both exclude the most important factor: the bending effect.

Timoshenko [91] proposed a beam theory that adds the shear effect and the rotation effect to the Euler-Bernoulli beam. The Timoshenko model is a major improvement for non-slender beams and high-frequency responses where shear or rotary effects are not negligible.

Following Timoshenko, several authors have obtained frequency equations and mode shapes for various boundary conditions. Kruszewski [92] obtained the first three antisymmetric modes of a cantilever beam and three antisymmetric and symmetric modes of a free-free beam. Traill-Nash and Collar [93] obtained and experimentally validated the expressions for the frequency equation and mode shapes for six common boundary conditions: fixed-free, free-free, hinged-free, hinged-hinged, fixed-fixed and fixed-hinged. Huang [94] independently obtained the frequency equations and expressions for the mode shapes for all six end conditions. The frequency equations are difficult to solve, except in cases involving simply supported beams. Even when the roots of the frequency equations are obtained, it is a challenge to present them in a meaningful way.

Despite current efforts [95, 96] to develop a new and better beam theory, the Euler-Bernoulli and Timoshenko beam theories are still widely used. Detailed derivations of the Euler-Bernoulli model can be found in [97], but the basics can be described as follows.

A long structural member with forces and moments perpendicular to its long axis is subject to bending. Static bending relates the moment M at the axial location x to the displacement v through the following relation:

$$M(x) = EI(x)\frac{\partial^2 v}{\partial x^2} \tag{2.19}$$

where E is the elastic modulus of the material and $I(x)$ is the area moment of inertia around the neutral axis of the cross-section. The deflection at any point is obtained by integrating this equation from a reference point to a desired point, e.g. from one extremity of the link to the other.

This description of compliance can be used when mass is isolated from elasticity. If mass is distributed throughout the beam with a material mass density per unit volume ρ, the time t must be incorporated so

$$\mu(x)\frac{\partial^2 v(x,t)}{\partial t^2}+\frac{\partial^2}{\partial x}\left(EI(x)\frac{\partial^2 v(x,t)}{\partial x^2}\right)=0 \tag{2.20}$$

Here, $\mu(x)$ is the mass density per unit length, which incorporates the material properties and the cross-sectional area at x. (2.20) is the Euler-Bernoulli equation. As previously explained, it implicitly assumes a minimal impact of shear distortion and rotational inertia of the cross-section of the beam, which is valid for long beams.

Torsional deflection of an angle ϕ results if a twisting moment T around the long axis of the beam occurs, such that, in the static case, the following takes place:

$$\phi=\frac{TL}{J_x\varphi} \tag{2.21}$$

where φ is the the shear modulus of the material and J_x is the polar area moment of inertia arond the neutral axis of the beam. Again, the addition of a distributed mass and the consideration of the dynamics produces a partial differential equation with independent variables in space and time:

$$\kappa(x)\frac{\partial^2\phi}{\partial t^2}=\varphi J_x\frac{\partial^2\phi}{\partial x^2} \tag{2.22}$$

where $\kappa(x)$ is the rotary mass moment of inertia per unit length of the shaft.

Tension and compression effects should also be acknowledged, although they tend to be the least significant. The deflection u in the x-direction, which is the long axis of the member, obeys the partial differential equation of flexibility:

$$\rho(x)\frac{\partial^2 u}{\partial t^2}=E\frac{\partial^2 u}{\partial x^2} \tag{2.23}$$

Note that these effects are special cases of the more general elastic behaviour of a member subject to acceleration and external loading, which is specialised to the member with one long axis.

Assumed modes

Deriving a state-space model in the time domain is attractive because it enables the use of powerful state-space control design techniques. Moreover, this approach is compatible with the non-linear behaviour of arms undergoing excessive motion and experiencing centrifugal and Coriolis forces. The assumed modes method [98] allows the construction of such a model.

[76] used the assumed modes method to solve problems related to the control of single-link flexible manipulators in which the sensors are not collocated with the actuators. [98] used the recursive Lagrangian formulation to model flexible link manipulators where the link deflection is assumed to be moderate; thus, the link transformation is represented in terms of additional modal shapes. [99] presented closed-form equations of motion for planar robot arms using assumed modes to obtain a finite-dimensional linear model. [100] studied the accuracy of the modal approximation for a single-link flexible robot arm in the design of suitable feedback controllers.

The flexible kinematics of the links must be expressed as a sum of basis functions, which are also known as assumed modes (shapes) $W_i(x)$ with time-variable amplitudes $\eta_i(t)$:

$$v(x,t) = \sum_{i=1}^{\infty} W_i(x)\eta_i(t) \tag{2.24}$$

The amplitudes and their derivatives become the states of the model. Joint angles and their derivatives are also included as the rigid-state variables.

The flexible and rigid kinematics combined describe the position and velocity of every point on the arm and can be used to express the kinetic energy $\mathcal{T}$ and the potential energy $\mathcal{V}$, as shown in section 2.1.1. These expressions are used in the conservative form of Lagrange's equation:

$$\frac{d}{dt}\frac{\partial \mathcal{T}}{\partial \dot{\theta}_i} - \frac{\partial \mathcal{T}}{\partial \theta_i} + \frac{\partial \mathcal{V}}{\partial \theta_i} = \mathcal{F}_i \tag{2.25}$$

where $\mathcal{F}_i$ is the force performing work as a result of the variations of θ_i.

Equation (2.25) separates into two equations involving rigid variables and flexible variables respectively. Then, by grouping the second derivatives of the rigid and flexible coordinates, one obtains:

$$\begin{aligned} &\begin{bmatrix} \boldsymbol{M_{rr}}(\boldsymbol{\theta},\boldsymbol{e}) & \boldsymbol{M_{rf}}(\boldsymbol{\theta},\boldsymbol{e}) \\ \boldsymbol{M_{fr}}(\boldsymbol{\theta},\boldsymbol{e}) & \boldsymbol{M_{ff}}(\boldsymbol{\theta},\boldsymbol{e}) \end{bmatrix} \begin{bmatrix} \ddot{\boldsymbol{\theta}} \\ \ddot{\boldsymbol{e}} \end{bmatrix} + \begin{bmatrix} 0 & 0 \\ 0 & \boldsymbol{K_s} \end{bmatrix} \begin{bmatrix} \boldsymbol{\theta} \\ \boldsymbol{e} \end{bmatrix} = \\ &\qquad \boldsymbol{\mathcal{C}_{cc}}(\boldsymbol{\theta},\boldsymbol{e},\dot{\boldsymbol{\theta}},\dot{\boldsymbol{e}}) \begin{bmatrix} \dot{\boldsymbol{\theta}} \\ \dot{\boldsymbol{e}} \end{bmatrix} + \boldsymbol{g}(\boldsymbol{\theta},\boldsymbol{e}) + \boldsymbol{\mathcal{R}}(\boldsymbol{\theta},\boldsymbol{e},\dot{\boldsymbol{\theta}},\dot{\boldsymbol{e}},\boldsymbol{\tau_{ext}}) \end{aligned} \tag{2.26}$$

where $\boldsymbol{\theta}$ is a vector of rigid coordinates, usually the joint variables; $\boldsymbol{e}$ are the flexible coordinates; $\boldsymbol{M_{ij}}$ is the mass matrix for rigid and flexible coordinates corresponding to the rigid $(i,j = r)$ or flexible $(i,j = f)$ coordinates and equations; $\boldsymbol{\mathcal{C}_{cc}}$ contains the non-linear Coriolis and centrifugal terms; $\boldsymbol{g}$ captures gravity effects; $\boldsymbol{\tau_{ext}}$ represents the externally applied forces; and $\boldsymbol{\mathcal{R}}$ captures the effect of external forces and all other non-conservative forces, including friction.

2.1.3 Modelling flexibilities of joints and links simultaneously

As mentioned in the previous two sections, most studies carried out on flexible manipulators can be categorised into two groups: those considering flexible structures with rigid joints and those considering rigid structures with flexible joints. However, joint and link flexibilities may be present at the same time.

[101] describes two approaches for obtaining the dynamic model of a single-DOF robot manipulator including structural and joint flexibility. A simplified model leads to a set of decoupled dynamic equations. A more detailed model leads to a set of cross-coupled dynamic equations. It has been shown that these two models are very close in terms of small deflection and rotation.

In [102] the authors derived a dynamic model for flexible robot arms with joint and link elasticity under very general assumptions. Hamilton's principle is used to derive a dynamic model for a large class of flexible robot arms. The resultant dynamic model consists of a distributed-parameter system described by a set of partial differential-integral equations and a set of dynamic boundary conditions. These dynamic boundary conditions could degenerate to lower-order differential equations or even to algebraic constraints. In [103], the dynamic model previously obtained was compared in detail to several other dynamic models. The one-link arm model includes forces that have been partially or fully neglected until now: inertia force, centrifugal force and Coriolis force due to deformation. It is also shown that the dynamic model found for a multi-link flexible robot can be reduced to the model provided by [98], provided that some assumptions are made. On the other hand, the model under study does not include axial forces, as shown in other works [72]. However, these forces can easily be included in addition to damping forces.

[104] derives a finite-dimensional dynamic model using only the deformations at the tip of the link by neglecting the link deformation's effect on the system's kinetic energy and expressing the elastic potential energy in terms of the generalised spring constant matrix. Although these finite-dimensional approximations are simpler, they may not provide enough information about the original system, which limits control possibilities. To avoid this pitfall, [105] chooses to model the flexible links as a chain of rigid sublinks interconnected by elastic joints. To obtain satisfactory results, one must use a large number of sublinks with elastic joints to represent a multi-link system. Unfortunately, this method leads to a high-order system model, which further complicates the controller design.

In [106], the singular perturbation approach, which has been shown to be promising in dealing with flexible-joint manipulators, is used to analyse flexible-link manipulators via the asymptotic perturbation methods applied in [107]. The non-linear partial integro-differential equation that arises from the dynamics of a one-link flexible robot is derived from the extended Hamilton principle. The resulting model considers the effects of the centripetal forces, centrifugal stiffening and Coriolis. Thereafter, parameters representing the stiffness of the link and joint compliance are embedded into the dynamics of the manipulator, and an asymptotic perturbation approach is used to analyse the dynamics.

2.1.4 Modelling of moving flexible arms

One common but simplistic idea in literature is that vibrations are always due to the robotic arm's moving parts. However, the arm base itself may be a source of significant flexibility. For example, if the arm is supported by a rail-mounted structure, the most appropriate solution to evaluate this source of flexibility might be empirical (c.f. section on the ITER BRHS, p. 44). In terms of modelling, there is no elastic connection to an inertial reference frame, and a fundamentally different approach is needed. Such a situation has been explored by others. [108] presented a model using Timoshenko's beam theory in conjunction with an oscillating base oscillatory. The following year, [109] investigated the flexible beam slewing modelling problem, in which the base of the beam is able to rotate and translate in a plane.

From a general standpoint, moving flexible structures can be modelled by considering time-dependent boundary conditions. In such cases, several options are available to model the vibration of a uniform Euler-Bernoulli beam with classical time-dependent boundary conditions. If the functions involved are simple, an efficient approach consists of using the closed-form Laplace transformation [110, 111]. However, it is not always easy to invert the solution of the obtained closed-form system. A more general transformation known as Mindlin-Goodman is proposed in [112] and [113] to convert systems with time-dependent boundary conditions into a forced system with homogeneous boundary conditions. It introduces four shifting polynomials of the fifth degree. By properly selecting these shifting polynomial functions, the non-homogeneous boundary conditions are transformed into homogeneous ones. Thus, the classical approach involving the separation of variables can be applied to obtain a series solution involving the superposition of eigenfunctions. The Mindlin-Goodman method has been extended to various types of applications: rods [114, 115], beams [112, 116], membranes [117] and plates [118, 119]. In particular, the vibration of uniform Timoshenko beams with classical time-dependent boundary conditions was solved in [120]. Another approach, known as the Williams method, is studied in [121], which introduces an auxiliary quasi-static problem. The proposed method transforms the initial system into an alternative one similar to that obtained using the Mindlin-Goodman method. Applications of the Williams method can be found for rods [115, 122], beams [123], membranes [124] and plates [125]. Improvements in the Mindlin-Goodman and Williams methods are discussed in [115, 126, 127].

A special case involving the modelling of moving flexible arms is the modelling of rotating beams. Because of the coupling of flexible deformations and rigid motions, the problem with transverse vibration control in rotating beams is more complex than for non-rotating beams. The importance of this coupling was observed by [128] for Euler-Bernoulli beams and by [129] for Timoshenko beams. Dynamic modelling of a rotating-beam system neglecting the influence of the centrifugal force on transverse deformations was studied by [130–132] for Euler-Bernoulli beams and by [133, 134] for Timoshenko beams. Considering the centrifugal stiffening effect, [128] and [135] derived the coupling equations for the motion of the flexible beam and the rigid body. Rotating beams with tip masses were studied by [136] for Euler-Bernoulli beams and by [137] for Timoshenko beams along with the centrifugal stiffening effect. Although [132] does not include the stiffening effect, all the models above neglect the axial motion of the beam. [138] was the first to propose a model describing the axial, transverse and rotational motions of a rotating uniform Euler-Bernoulli beam by including the centrifugal stiffening effect in the derivation. This model comprises fully coupled, non-linear integro-differential equations derived by using the extended Hamilton's principle.

The dynamic response of a loaded rotating beam has been examined by a number of researchers using various theories with different boundary conditions and considering assorted loads moving at constant [139] or non-constant [140] speed with a time-dependent [141], displacement-dependent [142] or random magnitude [143, 144].

Finally, structural damping may significantly affect system dynamics and should not be neglected during the modelling phase. In [145], an explicit expression for the natural frequencies of an Euler-Bernoulli beam is derived, including damping, modelled by the partial integro-differential equation proposed by [146]. It is shown that the distribution of the natural modes is similar to that of a beam with a uniform damping constant acting opposite to the rate of change of the bending moment. The main results of this paper are essentially the same as those in [147]. In other words, the attenuation rate is proportional to the natural frequency when the frequency is high.

2.1.5 Impact of elastic deformation on the rigid body displacement

In most investigations on flexible multi-body dynamics, it is assumed that the elastic deformation of the mechanical components does not have any significant effect on the rigid body displacements. Under this assumption, the mechanical system is treated as a rigid multi-body system. Consequently, rigid body methodologies can be used to determine the inertia and joint forces that subsequently lead to deformation coordinates after solving a linear elasticity problem. Finally, the total displacement of the component is obtained by superimposing the elastic deflection and the rigid motion.

However, assuming that the elastic deformation does not affect the rigid body cannot be justified in many applications. As noted in section 2.1.4, the vibrations of a rotating structure are governed by a set of non-linear differential equations that exhibit a strong coupling between the rigid displacement and the elastic deformations. This dynamic coupling is mainly due to the geometric non-linearities that arise from the large rotations of the structures [148]. Another source of non-linearities is the geometric, elastic, non-linear, strain displacement relationship. The non-linear geometric stiffness matrix [149, 150] accounts for the geometric stiffening effect, which becomes an important factor in maintaining the stability of beams as their velocity increases [133, 151]. As a result, the moments and the products of inertia are no longer constant, which makes control of lightweight structures harder at relatively high speeds.

[152] demonstrated that instability in the elastic modes could have a significant effect on the rigid body motion. It was proved that the instability limits depend on the difference between the axial and bending stiffness coefficients. [153] identified the instability regions in various combinations of the excitation frequencies, based on the results from [154], which studied the dynamic stability of ordinary differential equations with periodic coefficients and derived a criterion for instability.

2.1.6 Model order reduction

Since the theoretical order of a flexible arm is infinite, one should be prepared to deal with certain issues when controlling it using a finite order model. Various approaches can be adopted to reduce the order of a model. For example, one may decide to keep the first finite number of modes and truncate the rest. In this case, the criterion for selecting the appropriate number of modes is unclear, and truncation usually results in a model with a higher or lower order than is necessary.

The balanced truncation method [155] is based on a procedure transforming the state space description of a stable system to a balanced set of coordinates so the input-to-state and state-to-output couplings are weighted equally. The next step is to find the singular values that characterise the contribution of each state to the input-output map of the system. Finally, the states that weakly contribute to the input-output map can be deleted. However, one limitation of this method is that model reduction using balancing techniques is only applicable to stable systems [155–158].Very few research articles discuss the model reduction of unstable systems [159]. Some researches have applied the balancing method to flexible structures by assuming lightly damped and widely separated modes [160–162].

2.1.7 Model parameter identification

Most of the previously described approaches yield models that depend on some physical parameters for which it is necessary to determine numerical values. Several techniques can be considered for this purpose.

- One can use data provided by manufacturers and values obtained by geometric considerations. The main disadvantage of such a method is linked to the necessity of dismantling the robot to obtain measurements.
- Otherwise, one can use some identification techniques to determine the numerical values of the model's parameters. These techniques allow the parameters' determination on-site, and the numerical values that are found allow the best correlation between the mathematical model and the process.

System identification is a common engineering tool [163] that is often used on rigid robots [164–166]. The identification of robots containing flexibilities has been studied in [167–170]. In [170], the identification was based on closed-loop data. Some other online identification schemes are based on input-output autoregressive moving-average (ARMA) representations [171–173]. Most of the time, it is necessary to find a compromise between the model's complexity and its computational cost [174, 175]. [176] studied the problem of the minimality of the standard set of parameters. A sufficient condition related to the choice of the shape functions is given. In [168], the same authors presented a heuristic method to determine the exciting trajectories for a single-flexible-link planar robot. They proposed a new method to determine the minimal parameters that are not identifiable based on the total energy variation principles.

2.1.8 Conclusion of the state-of-the-art in modelling flexible robotic arms

The robotic equipment involved in the maintenance of ITER is characterised by large longitudinal and short transverse dimensions, mainly due to the size of the plasma chamber and the narrowness of its access ports. For this reason, flexibilities in links are deemed to prevail over joint flexibilities. Consequently, as far as the works carried out within the present thesis (discussed in Chapter 3 and validated in Chapter 4) are concerned, it has been decided to model the link flexibilities only. A model derived from the assumed modes method and similar to the one given in (2.26) has been chosen to build a model-based vibration control (see section 3.1.1). The question of time-dependent boundary conditions, which was broached in section 2.1.4, will be addressed again in section 3.2, where an advanced model of a rotating bending beam is derived. Finally, section 2.1.5 touched on the identification of model parameters. It will benefit to the experimental works described in Chapter 4.

2.2 Control of flexible robotic arms

The case of flexible robotic arms is one example of systems in which the number of control inputs is strictly inferior to the number of mechanical degrees of freedom. This explains why the design of control schemes to realise standard motion tasks is often more difficult than for rigid robots. Methods to attenuate the vibratory behaviour of flexible robotic systems have been widely studied. They can be separated into two main categories: passive damping control and active damping control.

On one hand, passive approaches consist of either planning the manipulator motion in advance to prevent the vibratory motion or placing mechanical dampers at the manipulator's grippers to guarantee the performance [177]. The advantage of such methods is that the robot position and/or force control strategy does not interfere with the damping process. However, the main drawbacks are reduced speeds, limited trajectories due to the design criteria and non-guaranteed stability of the operations.

On the other hand, active control to damp vibrations in flexible manipulators has been an active theoretical research area for a long time [171, 178, 179]. One option is to attach sensors, such as strain gauges, directly onto the arm/payload since strain measurements provide a valuable indication of the state of a flexible link. For uniform, one-link, flexible robotic arms, [180] and [181] showed that, if the strain signal at the root of the flexible arm is measured and directly fed back, the closed-loop system becomes asymptotically stable and the vibration can be suppressed. However, it has previously been mentioned (see section 1.2.3) that the use of strain gauges in the very specific case of a tokamak environment is made almost impossible due to the radiation and electromagnetic interferences. For these reasons, this control strategy, known as direct strain feedback, will not be addressed in the following sections.

Several works have addressed the problem of payload estimation and load adaptive control [182–185]. A majority of these methods are based either on model reference adaptive control (MRAC) [186, 187] or on a two-stage process, in which a system identification stage is followed by the adaptation of the controller as a function of the identified system parameters [183, 188]. Following a general growing interest in genetic algorithms, the application of neural networks to the adaptive control of flexible manipulators has been intensively studied over the past two decades [189–192]. Another alternative to the conventional model-based control techniques consists of using fuzzy logic [193, 194], which does not require a mathematical model of the plant and can be applied equally to linear and non-linear systems. Given the stringent regulatory requirements for handling activated or contaminated materials inside nuclear plants, one can assume that the dimensions and weight of the payloads to be handled are accurately known. Even though erosion may affect the plasma-facing components in fusion reactors, their weight will not vary by a range larger that a thousandth of a percent. For this reason, previous works dealing with online payload estimation—and more generally with adaptive control—will not be covered by this review.

The following sections are organised as follows. Section 2.2.1 describes different classical controllers used for the specific control of flexible joints. Section 2.2.2 focuses on classical, open-loop command generation used to control flexible links. To complete the review of classical controllers, section 2.2.3 deals with the feedback control of flexible links. Robust control is addressed in section 2.2.4. Section 2.2.5 presents approaches that are more specific: sliding mode control, repetitive control, the coupling map method and the singular perturbation method. Sections 2.2.6, 2.2.7 and 2.2.8 are dedicated to the control of rotating beams and to more specific considerations about the control of flexible arms in the framework of RH applications.

2.2.1 Control of flexible joints

This section focuses on the control of manipulators made of flexible joints. The motor torques in flexible joints, which are used to command the robot, and the disturbance torques, which are due to joint flexibility, are physically collocated. This is an important difference with respect to controlling flexibility distributed along the links, which will be addressed in sections 2.2.2 and 2.2.3. This characteristic is very helpful in rejecting vibrations and controlling the overall robot motion. For example, it enables the use of input commands acting before the source of flexibility in order to ensure that output variables defined beyond the flexibility behave in the desired way.

Proportional-derivative controller

In this section, the problem of controlling the motion of a robot with joint elasticity will be considered. No trajectory planning is involved in this problem, and a feedback law must be found in order to achieve asymptotic stabilisation around a desired closed-loop equilibrium.

To that end, one must define only a constant reference $\boldsymbol{\theta_d}$ (with $\dot{\boldsymbol{\theta}}_{\boldsymbol{d}}(t) = 0$) for the link coordinates. When the system is at rest, the complete and reduced models obtained in section 2.1.1 can be used to deduce that a unique set of motor variables $\boldsymbol{q_d}$ are associated with the desired $\boldsymbol{\theta_d}$:

$$\boldsymbol{q_d} = \boldsymbol{\theta_d} + \boldsymbol{K}^{-1}\boldsymbol{g}(\boldsymbol{\theta_d}) \tag{2.27}$$

where $\boldsymbol{K}$ is the joint stiffness matrix and $\boldsymbol{g}(\boldsymbol{\theta_d})$ is the gravity vector at a steady state. In such a case, the static torque to be applied at a steady state by any feasible controller is $\boldsymbol{\tau_0} = \boldsymbol{g}(\boldsymbol{\theta_d})$.

A major aspect of the presence of joint elasticity is that a feedback control law can generally depend on four variables for each joint: the motor and link positions and the motor and link velocities. However, a maximum of two sensors are generally available in most robots for measurement at the joints: a position sensor (encoder) and, in some cases, a velocity sensor (tachometer). When no velocity sensors are present, the velocity is typically reconstructed using a suitable numerical differentiation of the position measurements.

In the absence of gravity (e.g. for space applications), a proportional-derivative (PD) controller based only on motor measurements is sufficient to achieve the desired regulation task [75]. The closed-loop system will be asymptotically stable provided that the gain matrices $\boldsymbol{K_P}$ and $\boldsymbol{K_D}$ of the PD controller are chosen properly:

$$\boldsymbol{\tau} = \boldsymbol{K_P}(\boldsymbol{q_d} - \boldsymbol{q}) - \boldsymbol{K_D}\dot{\boldsymbol{q}} \tag{2.28}$$

To design this controller, diverse partial state feedback combinations would be possible, depending on the available sensing devices. Moreover, mounting a strain gauge on the transmission shaft would provide a direct measure of the elastic torque $\boldsymbol{\tau_J} = \boldsymbol{K}(\boldsymbol{q} - \boldsymbol{\theta})$. Consequently a full-state feedback could be designed to guarantee asymptotic stability and considerably improve the transient behaviour. However, this would be obtained at the cost of additional sensors.

The presence of gravity requires the addition of some form of gravity compensation to the PD controller's action [195]. In common practice, robot joints are stiff enough to have, under the load of the robot's own weight, a unique equilibrium link position associated with any given motor position. The simplest way to deal with the presence of gravity is to consider the addition of a constant term that compensates for the gravity load at the desired steady-state position:

$$\boldsymbol{\tau} = \boldsymbol{K_P}(\boldsymbol{q_d} - \boldsymbol{q}) - \boldsymbol{K_D}\dot{\boldsymbol{q}} + \boldsymbol{g}(\boldsymbol{\theta_d}) \tag{2.29}$$

where the gravitational term $\boldsymbol{g}(\boldsymbol{\theta_d})$ is the same as that for an equivalent rigid robot. Then, only the error on $\boldsymbol{g}(\boldsymbol{\theta_d})$ and the uncertainty on the joint stiffness $\boldsymbol{K}$ affect the performance of the controller.

Although it is more complicated, another method of compensating for gravity consists of determining the gravity vector in all configurations during motion, which should normally offer a better transient behaviour. Nevertheless, the gravity vector depends on the link variables $\boldsymbol{\theta}$, which are assumed not to be measurable at this stage. It is easy to see that using $\boldsymbol{g}(\boldsymbol{q})$, with the measured motor positions in place of the link positions, generally leads to an incorrect closed-loop equilibrium. Moreover, even if $\boldsymbol{\theta}$ were available, adding $\boldsymbol{g}(\boldsymbol{\theta})$ to a motor PD error feedback has no guarantee of success because this compensation, which appears in the motor equation, does not instantaneously cancel the gravity load acting on the links. Therefore, a PD control with online gravity compensation can be introduced [196]:

$$\boldsymbol{\tau} = \boldsymbol{K_P}(\boldsymbol{q_d} - \boldsymbol{q}) - \boldsymbol{K_D}\dot{\boldsymbol{q}} + \boldsymbol{g}(\tilde{\boldsymbol{q}}) \tag{2.30}$$

with

$$\tilde{\boldsymbol{q}} = \boldsymbol{q} - \boldsymbol{K}^{-1}\boldsymbol{g}(\boldsymbol{\theta_d}) \tag{2.31}$$

The use of this online gravity compensation scheme typically provides a smoother time course and a noticeable reduction in positional transient errors.

A possibility for refining the online gravity compensation scheme, again based only on motor position measurement, is offered by the use of a fast iterative algorithm that elaborates the measure $\boldsymbol{q}$ in order to generate a quasi-static estimate $\bar{\boldsymbol{\theta}}(\boldsymbol{q})$ of $\boldsymbol{\theta}$ [197].

Trajectory tracking

Like for rigid robot arms, the problem of tracking desired time-varying trajectories is harder for robots with elastic joints than achieving constant regulation. In general, solving this problem requires the use of full-state feedback and knowledge of all the terms in the dynamic model.

In this section, two approaches are addressed: the feedback linearisation method and a simpler linear model-based controller.

Feedback linearisation – The feedback linearisation approach [179], also known as the inverse dynamics method, is a non-linear state feedback law that leads to a closed-loop system with decoupled and exactly linear behaviour for each of the n DOF. The tracking errors along the reference trajectory are forced to be globally exponentially stable, with a decaying rate that can be directly specified through the choice of the controller feedback gains. This is the direct extension of the well-known computed torque method for rigid robots.

However, in the presence of joint elasticity, the design of a feedback linearisation law is not straightforward. Furthermore, the dynamic model (2.14) will not satisfy the necessary conditions for exact linearisation when only a static feedback law from the full state is allowed. Therefore, we will restrict our attention to the more tractable case of the reduced dynamic model (2.18) and only briefly sketch the more general picture [198].

Let us consider the reduced model defined by (2.17) and (2.18), and let the reference trajectory be specified by a desired smooth link motion $\boldsymbol{\theta_d}(t)$. The control design will proceed by system inversion using the current measures of the state variables ($\boldsymbol{\theta}$, $\boldsymbol{q}$, $\dot{\boldsymbol{\theta}}$, $\dot{\boldsymbol{q}}$). The outcome of the inversion procedure is the definition of a torque vector $\boldsymbol{\tau}$ in the form of a static-state feedback control law, which cancels the original robot dynamics and replaces it with a desired linear and decoupled dynamics of a suitable differential order. In this sense, the control law stiffens the dynamics of the robot with elastic joints. The feasibility of inverting the system from the chosen output $\boldsymbol{\theta}$ without causing instability problems (related to the presence of unobservable dynamics in the closed-loop system after cancellation) is a relevant property of robots with elastic joints. In fact, this is the direct generalisation of the non-linear, multiple-input multiple-output (MIMO) case of the possibility of inverting a scalar transfer function in the absence of zeros.

Let us rewrite the link equation in a compact form equivalent to (2.17):

$$\boldsymbol{M}(\boldsymbol{\theta})\ddot{\boldsymbol{\theta}} + \boldsymbol{n}(\boldsymbol{\theta}, \dot{\boldsymbol{\theta}}) + \boldsymbol{K}(\boldsymbol{\theta} - \boldsymbol{q}) = 0 \tag{2.32}$$

where $\boldsymbol{n}(\boldsymbol{\theta}, \dot{\boldsymbol{\theta}}) = \boldsymbol{c}(\boldsymbol{\theta}, \dot{\boldsymbol{\theta}}) + \boldsymbol{g}(\boldsymbol{\theta})$. None of the above quantities depends instantaneously on the input torques $\boldsymbol{\tau}$. Therefore, by differentiating twice one obtains:

$$\boldsymbol{M}(\boldsymbol{\theta})\boldsymbol{\theta}^{[4]} + 2\dot{\boldsymbol{M}}(\boldsymbol{\theta})\boldsymbol{\theta}^{[3]} + \ddot{\boldsymbol{M}}(\boldsymbol{\theta})\ddot{\boldsymbol{\theta}} + \ddot{\boldsymbol{n}}(\boldsymbol{\theta}, \dot{\boldsymbol{\theta}}) + \boldsymbol{K}(\ddot{\boldsymbol{\theta}} - \ddot{\boldsymbol{q}}) = 0 \tag{2.33}$$

where $\ddot{\boldsymbol{q}}$ now appears. The motor acceleration is at the same differential level of $\boldsymbol{\tau}$ in the motor equation:

$$\boldsymbol{B}\ddot{\boldsymbol{q}} + \boldsymbol{K}(\boldsymbol{q} - \boldsymbol{\theta}) = \boldsymbol{\tau} \tag{2.34}$$

thus, by replacing $\ddot{\boldsymbol{q}}$ from (2.34), we get:

$$\boldsymbol{M}(\boldsymbol{\theta})\boldsymbol{\theta}^{[4]} + 2\dot{\boldsymbol{M}}(\boldsymbol{\theta})\boldsymbol{\theta}^{[3]} + \ddot{\boldsymbol{M}}(\boldsymbol{\theta})\ddot{\boldsymbol{\theta}} + \ddot{\boldsymbol{n}}(\boldsymbol{\theta}, \dot{\boldsymbol{\theta}}) + \boldsymbol{K}\ddot{\boldsymbol{\theta}} = \boldsymbol{K}\boldsymbol{B}^{-1}[\boldsymbol{\tau} - \boldsymbol{K}(\boldsymbol{q} - \boldsymbol{\theta})] \tag{2.35}$$

We note that, using (2.32), the last term $\boldsymbol{K}(\boldsymbol{q} - \boldsymbol{\theta})$ in (2.35) may also be replaced by $\boldsymbol{M}(\boldsymbol{\theta})\ddot{\boldsymbol{\theta}} + \boldsymbol{n}(\boldsymbol{\theta}, \dot{\boldsymbol{\theta}})$.

Since the matrix $\boldsymbol{H}(\boldsymbol{\theta}) = \boldsymbol{M}^{-1}(\boldsymbol{\theta})\boldsymbol{K}\boldsymbol{B}^{-1}$ is always non-singular, an arbitrary value $\boldsymbol{u}$ can be assigned to the fourth derivative of $\boldsymbol{\theta}$ by a suitable choice of the input torques $\boldsymbol{\tau}$. The matrix $\boldsymbol{H}(\boldsymbol{\theta})$ is known as the decoupling matrix of the system, and its non-singularity is a necessary and sufficient condition for imposing a decoupled input-output behaviour using non-linear, static-state feedback.

Moreover, (2.35) indicates that each component θ_i of $\boldsymbol{\theta}$ needs to be differentiated four times in order to be algebraically related to the input torques $\boldsymbol{\tau}$. Since there are n link variables, the total sum of the relative degrees is $4n$, which is equal to the dimension of the state of a robot with elastic joints. All these facts taken together lead to the conclusion that when inverting (2.35) to determine the input $\boldsymbol{\tau}$ that imposes $\boldsymbol{\theta}^{[4]} = \boldsymbol{u}$ there will be no other dynamics left other than the one appearing in the closed-loop input-output map.

Consequently, the control law:

$$\begin{aligned}\boldsymbol{\tau} = \boldsymbol{B}\boldsymbol{K}^{-1}\Big[&\boldsymbol{M}(\boldsymbol{\theta})\boldsymbol{u} + \ddot{\boldsymbol{M}}(\boldsymbol{\theta})\ddot{\boldsymbol{\theta}} + 2\dot{\boldsymbol{M}}(\boldsymbol{\theta})\boldsymbol{\theta}^{[3]} + \ddot{\boldsymbol{n}}(\boldsymbol{\theta},\dot{\boldsymbol{\theta}})\Big] \\ &+ \Big[\boldsymbol{M}(\boldsymbol{\theta}) + \boldsymbol{B}\Big]\ddot{\boldsymbol{\theta}} + \boldsymbol{n}(\boldsymbol{\theta},\dot{\boldsymbol{\theta}})\end{aligned} \tag{2.36}$$

leads to a closed-loop system described by:

$$\boldsymbol{\theta}^{[4]} = \boldsymbol{u} \tag{2.37}$$

The complete control law (2.36) is expressed only as a function of the linearising coordinates ($\boldsymbol{\theta}$, $\dot{\boldsymbol{\theta}}$, $\ddot{\boldsymbol{\theta}}$, $\boldsymbol{\theta}^{[3]}$). Considering today's technology in the field, it is feasible to have a set of sensors for elastic joints measuring the motor position $\boldsymbol{q}$ (and, possibly, its velocity $\dot{\boldsymbol{q}}$), the joint torque $\boldsymbol{\tau_J} = \boldsymbol{K}(\boldsymbol{q} - \boldsymbol{\theta})$ and the link position $\boldsymbol{\theta}$ in a reliable and accurate way. Therefore, only one numerical differentiation may be needed to obtain an accurate estimate of $\dot{\boldsymbol{\theta}}$ and/or $\dot{\boldsymbol{\tau}}_{\boldsymbol{J}}$. Note that, depending on the specific sensor resolution, it may also be convenient to evaluate $\boldsymbol{\theta}$ using the measures of $\boldsymbol{q}$ and $\boldsymbol{\tau_J}$ as $\boldsymbol{q} - \boldsymbol{K}^{-1}\boldsymbol{\tau_J}$.

Moreover, it is easy to see that the following three sets of $4n$ variables ($\boldsymbol{\theta}$, $\dot{\boldsymbol{\theta}}$, $\ddot{\boldsymbol{\theta}}$, $\boldsymbol{\theta}^{[3]}$) , ($\boldsymbol{\theta}$, $\boldsymbol{q}$, $\dot{\boldsymbol{\theta}}$, $\dot{\boldsymbol{q}}$) and ($\boldsymbol{\theta}$, $\boldsymbol{\tau_J}$, $\dot{\boldsymbol{\theta}}$, $\dot{\boldsymbol{\tau}}_{\boldsymbol{J}}$) are all equivalent state variables for a robot with elastic joints and are related by globally invertible transformations. Therefore, under the assumption that the dynamic model is available, the feedback linearising control law (2.36) can be completely rewritten in terms of the more conventional state ($\boldsymbol{\theta}$, $\boldsymbol{q}$, $\dot{\boldsymbol{\theta}}$, $\dot{\boldsymbol{q}}$) or, taking advantage of a joint torque sensor, in terms of ($\boldsymbol{\theta}$, $\boldsymbol{\tau_J}$, $\dot{\boldsymbol{\theta}}$, $\dot{\boldsymbol{\tau}}_{\boldsymbol{J}}$).

Based on (2.37), the trajectory tracking problem is solved by setting

$$\boldsymbol{u} = \boldsymbol{\theta_d}^{[4]} + \boldsymbol{k_3}(\boldsymbol{\theta_d}^{[3]} - \boldsymbol{\theta}^{[3]}) + \boldsymbol{k_2}(\ddot{\boldsymbol{\theta}}_{\boldsymbol{d}} - \ddot{\boldsymbol{\theta}}) + \boldsymbol{k_1}(\dot{\boldsymbol{\theta}}_{\boldsymbol{d}} - \dot{\boldsymbol{\theta}}) + \boldsymbol{k_0}(\boldsymbol{\theta_d} - \boldsymbol{\theta}) \tag{2.38}$$

where it is assumed that the reference trajectory $\boldsymbol{\theta_d}(t)$ is at least three times continuously differentiable and the diagonal matrices $\boldsymbol{k_0}$,..,$\boldsymbol{k_3}$ have elements such that

$$s^4 + k_{3,i}s^3 + k_{2,i}s^2 + k_{1,i}s + k_{0,i}, \qquad i = 1, ..., n \tag{2.39}$$

are Hurwitz polynomials. The choice of the gains $k_{0,i}$,...,$k_{3,i}$ can be made by a pole placement procedure.

When the link and motor inertia values are very different from each other, or when the joint stiffness is very large, the above fixed choice of gains has the drawback of generating control efforts that are too large. In those cases, a more tailored set of eigenvalues can be assigned by adjusting their placement as a function of the physical data of robot inertia and joint stiffness.

When compared to the computed torque method for rigid robots, this feedback linearisation control for trajectory tracking requires the inversion of the inertia matrix $\boldsymbol{M}(\boldsymbol{\theta})$ and the additional evaluation of the inertia matrix derivatives and of other terms in the dynamic model.

This feedback linearisation approach can also be applied without any changes in the presence of viscous or smooth friction at the motor and link side. The inclusion of spring damping leads instead to a third-order decoupled differential relation between the auxiliary input $\boldsymbol{u}$ and $\boldsymbol{\theta}$, thus leaving an n-dimensional unobservable, but asymptotically stable, dynamics in the closed-loop system. In this case, only input-output (and not full-state) linearisation and decoupling is achieved.

Linear control design – The feedback linearisation approach yields a rather complex non-linear control law. The main advantage of globally enforcing linear and decoupled behaviour on the trajectory error dynamics can be traded off with a control design that achieves only local stability around the reference trajectory but is much simpler to implement and may run at higher sampling rates.

A simpler tracking controller combines a model-based feed-forward term with a linear feedback term using the trajectory error. The linear feedback locally stabilises the system around the reference state trajectory, whereas the feed-forward torque is responsible for maintaining the robot along the desired motion when the error has vanished.

Using full-state feedback, two possible controllers of this kind are:

$$\boldsymbol{\tau} = \boldsymbol{\tau_0} + \boldsymbol{K_{P,q}}(\boldsymbol{q_d} - \boldsymbol{q}) + \boldsymbol{K_{D,q}}(\dot{\boldsymbol{q}}_{\boldsymbol{d}} - \dot{\boldsymbol{q}}) + \boldsymbol{K_{P,\theta}}(\boldsymbol{\theta_d} - \boldsymbol{\theta}) + \boldsymbol{K_{D,\theta}}(\dot{\boldsymbol{\theta}}_{\boldsymbol{d}} - \dot{\boldsymbol{\theta}}) \tag{2.40}$$

and

$$\boldsymbol{\tau} = \boldsymbol{\tau_0} + \boldsymbol{K_{P,q}}(\boldsymbol{q_d} - \boldsymbol{Q}) + \boldsymbol{K_{D,q}}(\dot{\boldsymbol{q}}_{\boldsymbol{d}} - \dot{\boldsymbol{q}}) + \boldsymbol{K_{P,J}}(\boldsymbol{\tau_{J,d}} - \boldsymbol{\tau_J}) + \boldsymbol{K_{D,J}}(\dot{\boldsymbol{\tau}}_{\boldsymbol{J,d}} - \dot{\boldsymbol{\tau}}_{\boldsymbol{J}}) \tag{2.41}$$

These trajectory tracking schemes are the most common in the control practice for robots with elastic joints. In the absence of full-state measurements, they can be combined with an observer of non-measurable quantities. An even simpler realisation is:

$$\boldsymbol{\tau} = \boldsymbol{\tau_0} + \boldsymbol{K_P}(\boldsymbol{q_d} - \boldsymbol{q}) + \boldsymbol{K_D}(\dot{\boldsymbol{q}}_{\boldsymbol{d}} - \dot{\boldsymbol{q}}) \tag{2.42}$$

which uses only motor measurements and relies on the results obtained for the regulation case.

The different gain matrices used in (2.40), (2.41) and (2.42) must be tuned using a linear approximation of the robot system. This approximation may be obtained at a fixed equilibrium point or around the actual reference trajectory, which leads to a linear time-invariant or a linear time-varying system, respectively.

Finally, it should be noted that such a control approach to trajectory tracking problems can also be used for robots with flexible links.

2.2.2 Command generation for flexible links

The trajectory undertaken by a flexible arm can dramatically affect the consequences of its flexibility. Purely open-loop anticipation of the flexible dynamics has been used to create motion profiles in which the motion itself cancels the oscillation created by earlier motions. This strategy—referred to as command shaping—adjusts the input command to the joint actuators so vibrations are eliminated [199, 200]. This can be accomplished either by colouring the input so no energy is injected around the flexible modes [201], filtering out the frequencies around the flexible modes using a notch filter [55], constructing input commands from versine or ramped sinusoid functions [202], extending the inverse dynamics approach to flexible robots [203] or implementing a near-minimum-time open-loop optimal control [204].

The validity of these methods depends on the exact knowledge of the flexible structure dynamics. Some of these algorithms can be modified to provide robustness with respect to the unknown dynamics, but the trade-off is in the speed of the transient response. Due to space constraints, only the input-shaping and inverse dynamics techniques will be discussed in the following sections.

Input shaping

Input shaping is a feed-forward vibration-reduction technique implemented by convolving a sequence of impulses with a desired system command to produce a shaped input that is then used to drive the system (see Fig. 2.3).

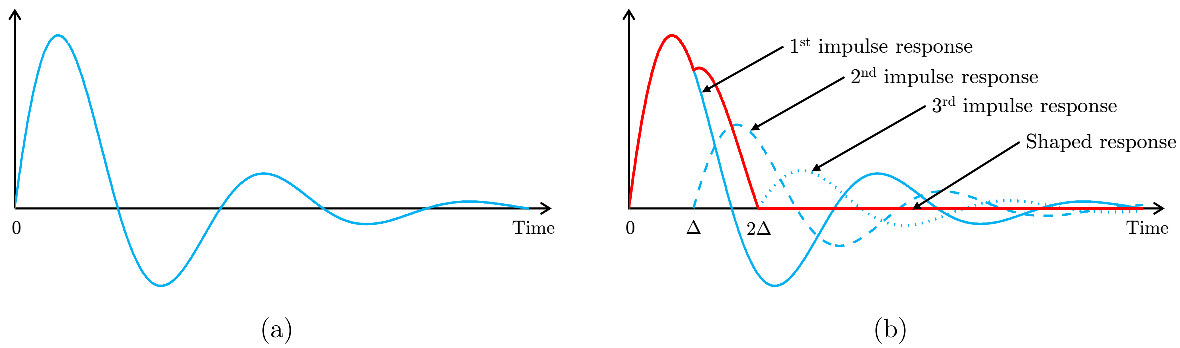

(a) (b)

Figure 2.3: Effect of a shaper on a vibratory system: (a) single impulse, (b) single impulse shaped by a three-term shaper

An input shaper is designed by solving a set of equations that limit the dynamic response of the system. Many types of constraint equations will yield acceptable input shapers, and several types of shapers have been determined in closed form. Their use only requires evaluating simple equations using estimates of the natural frequencies and damping ratios to obtain the amplitudes and time locations of the impulses that compose the input shaper.

The simplicity of implementation is illustrated in Fig. 2.4, where the relationships between the filter parameters and the mode parameters are:

$$\text{Coefficient } 1 = \frac{1}{1 - 2\cos\omega_d\Delta\exp(-\zeta\omega_d\Delta) + \exp(-2\zeta\omega_d\Delta)} \tag{2.43}$$

$$\text{Coefficient } 2 = \frac{-2\cos\omega_d\Delta\exp(-\zeta\omega_d\Delta)}{1 - 2\cos\omega_d\Delta\exp(-\zeta\omega_d\Delta) + \exp(-2\zeta\omega_d\Delta)} \tag{2.44}$$

$$\text{Coefficient } 3 = \frac{\exp(-2\zeta\omega_d\Delta)}{1 - 2\cos\omega_d\Delta\exp(-\zeta\omega_d\Delta) + \exp(-2\zeta\omega_d\Delta)} \tag{2.45}$$

where

- $\omega_d = \omega\sqrt{1-\zeta^2}$: damped natural frequency
- ζ: damping ratio
- Δ: selected time delay, an integer number of samples

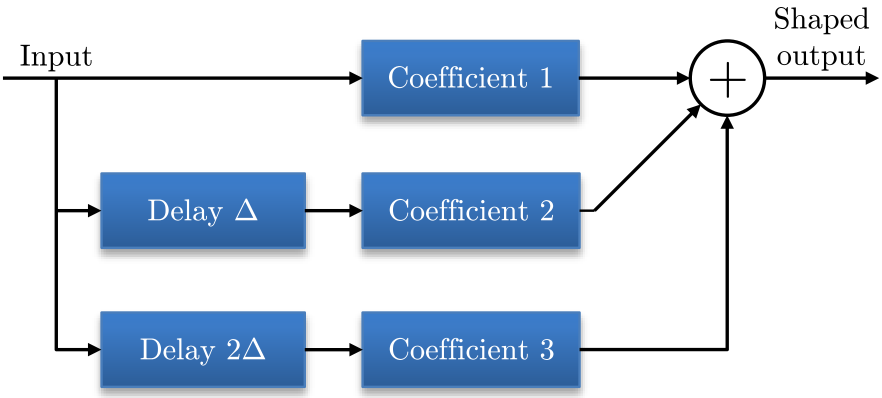

Figure 2.4: Block diagram representation of the command-shaping algorithm

Many papers have been published on input shaping since its original presentation [56]. Although it was mainly developed for linear systems, it has also shown effectiveness in various ways for non-linear systems. First, non-linear shaping schemes can be developed to directly target non-linear dynamics [205, 206]. However, this approach tends to be computationally expensive, and its results are generally limited to single-mode vibratory systems. Second, input shaping developed for linear systems can be made very robust against modelling errors [56, 178]. In particular, robustness has been enhanced by using more output impulses and the appropriate selection of impulse spacing, which translates into satisfactory performance in slightly non-linear systems. Third, input shaping can be performed adaptively so changing dynamics can be compensated for. [207] investigated command shaping for systems with varying parameters and presented an adaptive technique for kinematic structures that vary their configurations. In [208], command shaping is accomplished with adaptive filters based on the crane dynamic model. [209] implemented an adaptive input-shaping scheme that keeps the length of the impulse sequence to a minimum, thereby minimising any time-delay effects. The identification of critical parameters (modal frequencies) is performed in the frequency domain because frequency domain methods converge faster, are relatively insensitive to noise and do not suffer from over- or under- parameterisation [173].

Due to its ease of implementation and robustness to modelling errors, input shaping has been implemented in applications ranging from precision machinery [178, 210] to large gantry cranes [211]. In particular, a large gantry crane operating in a nuclear environment was equipped with input shaping to enable swing-free operation and precise payload positioning [212]. Input-shaping techniques were also proposed as a method for reducing residual vibrations in long-reach manipulators. [213] presented experimental verification of a command-shaping boom crane control when the source of payload oscillation was attributed to the operator's commands without addressing the question of external disturbances.

The constraint equations used to design an input shaper usually require positive values for the impulse amplitudes. However, motion times can be significantly reduced by allowing the shaper to contain negative impulses [214]. The equivalence of time-optimal control and special negative input shaping has been demonstrated [215] and explored [216]. Similarly, [217] proved that minimum-time zero-vibration (ZV) and zero-vibration and derivative (ZVD) shapers are equivalent to traditional time-optimal control. An important consequence of this equivalence is that many properties and numerical procedures relating to well-studied time-optimal control techniques can be applied to the relatively newer field of input shaping. A comparison of positive and negative input shapers [218] demonstrated that the former provide a higher level of vibration reduction and robustness compared to negative shapers. On the other hand, when using negative input shapers such as specified negative amplitude zero-vibration (SNA-ZV) or zero-vibration derivative derivative (ZVDD) shapers, the response time is slightly improved at the expense of a decrease in the level of vibration reduction.

Input shaping is a form of finite impulse response (FIR) filtering. However, input shapers and traditional filters such as Butterworth or Chebyshev have key differences. Input shapers are not designed as pass bands. Furthermore, they are usually designed in the time domain, not the frequency domain. This allows shapers to account for damping in mechanical systems, whereas most traditional FIR filters assume undamped frequencies. Since input shapers have been identified as a special class of FIR filters, conventional FIR filters can also be successfully used for robust vibration suppression provided that certain design requirements are properly addressed [219]. Similar properties have also been demonstrated for infinite impulse response (IIR) filters [220]. Although input shapers, FIR filters and IIR filters show attractive vibration suppression properties, they present different characteristics in terms of time delay, robustness to system changes, residual vibration and computational costs. A thorough comparison of these filters has been performed in [221] to fully evaluate the advantages and drawbacks of each filter type. Input shaping is incontestably more effective on mechanical systems than traditional digital filtering [222]. Moreover, IIR filters introduce larger delays as a general rule than FIR filters. However, their overall performance in certain cases can be better than that obtained using FIR filters [223].

Inverse dynamics

In contrast to the limited amount of knowledge required about a system for input shaping, the inverse dynamics of a flexible link manipulator require advanced knowledge of the system. This can cause problems in cases involving non-modelled, high-frequency dynamics or variations in a plant's parameters. An appropriate model, such as the one discussed in section 2.1.2, is required. Consequently, the method is conceptually simple but often requires a large amount of computation. This method was previously presented in relation to flexible joint control in section 2.2.1.

A compensator obtained using this method may be used as an open-loop or a closed-loop control [224]. In cases using closed-loop control, the method may be used in two ways: as a part of the closed-loop controller or as a feed-forward compensator. [225] showed that the performances of these two closed-loop schemes are similar, particularly when no perturbations occur. However, the feed-forward control scheme may be more stable.

When inverting the dynamics of a flexible link arm, the following issues should be considered:

- multi-link flexible arm dynamics are non-linear and coupled; therefore, calculating the inverse arm dynamics requires a large amount of computation;
- flexible arms are typically non-minimum phase systems; therefore, inverting their dynamics produces unstable controllers and unbounded control signals;
- when moving a flexible arm, nearly undamped vibrations appear in the mechanical structure; the frequencies of these vibration typically vary with the relative position of the links; and
- controllers are usually implemented on a computer; therefore, the discretisation of these controllers affects the inverse dynamics model.

[226] described the application of a discrete model inversion technique to the feed-forward control of single-link flexible arms. The behaviour of the discrete controller differs from

the continuous controller when the sampling rate is low compared to the dynamics of the system.

[227] analysed a design method of a robust tracking control system of a one-link flexible arm using inverse dynamics. This design method constructs a two-degrees-of-freedom control system with feedback and feed-forward parts. The feedback controller is devoted to robust stability against internal disturbances (non-modelled dynamics) and performance robustness against external disturbances (friction forces), while the feed-forward part is devoted to enhancing performance towards an a priori reference trajectory eliminating undershoot and overshoot of the response and shortening the settling time.

2.2.3 Feedback control of flexible links

Extensive research has been conducted on the feedback control of flexible links. Quite often, flexibility in links is controlled in the same way as concentrated flexibility in joints. [76], among others, showed that most feedback techniques presented for joint control also work for flexible link arms, even if the non-collocated nature of the system worsens the sensitivity to modelling errors.

Position control of a single-link flexible beam has been investigated using an output feedback controller with a shaft encoder and a slope sensor used as feedback signals [145]. In a case using a flexible robot arm controlled by a feedback law based on a reduced-order model requiring only one sensor and one actuator, [228] suggested that the position of the sensor had to be as close to the support of the arm as possible to obtain a stable response.

When direct sensing of the flexibility is not possible, state observers have been widely used to design feedback controllers. For large spatial structures [229] or civil engineering [230], modal observers [231] or estimators [232] allow the reconstruction of the modal state. To prevent possible instabilities due to structure interference phenomena, Meirovitch and his team developed independent modal control strategies that are entirely designed in the modal space and focused on maintaining independence in the feedback equations in the controlled system [233]. They suppressed the boundary problems related to modal observation by using modal filters based on the orthogonal properties of the modes.

Observer designs for flexible-link robots described by ordinary differential equations (ODE) has also been studied [147, 234]. [235] considered an observer design for linear flexible structures described by FEM. [236] presented a method to construct observers for linear second-order distributed-parameter systems using parameter-dependent Lyapunov functions. [237] applied the contraction theory [238] to an observer design for a class of linear distributed-parameter systems. The damping forces were included in the last two cases. Thus, exponentially stable observers can easily be designed. [239] designed an exponentially stable observer for a motorised Euler-Bernoulli beam described using a combination of ODE, PDE and a set of static boundary conditions. As opposed to the works in [147, 234, 235, 240], the proposed observer design method was based on an infinite-dimensional model. The stability of this observer was proven using semigroup theory; however, the inertial forces of the tip load were initially omitted. These results were extended by considering the tip load's dynamics during the observer design.

2.2.4 Robust control

H_2-optimisation

Since a flexible robot arm is an infinite dimensional plant, various approaches have been proposed to approximate an original model with finite dimensional models [76, 241, 242]. For the finite dimensional models, the difficulty with control, as pointed out in [76], is the non-collocatedness of actuators and sensors. [77] showed that the arm studied in [76] could be controlled with better performance by compensators designed by employing the stable factorisation method in conjunction with H_2-optimisation.

Sensitivity analysis and H_∞ control

Using the sensitivity analysis, one can find the stable domain of parameter uncertainties in cases where linear quadratic (LQ) optimal control law is employed. [243] showed how to analyse the sensitivity of a mathematical model against parameter uncertainties. [244] described the relationship between the sensitivity analysis and the control law. For sensitivity analysis, the control law is designed first, and the domain in which the closed-loop system is stable is examined second. For robust control law, the admissible domain of parameter uncertainties is determined first and then the control law is designed. The robust control method procedure is inverse to the sensitivity analysis. The robust control law is contained by the H_∞ control method [245].

[246] used the H_∞ control method to show that the stability condition for a scalar system depends on the arbitrary parameters of the control law. It was shown that the stability domain could be enlarged by increasing the arbitrary parameters.

In [247], the control system uses an inner loop for the control of the hub position on which the base of the arm is clamped. The inner loop has a high bandwidth compared to the arm dynamics. The outer loop uses only the measurements of the tip position (obtained from two measurements), and the plant input is the reference to the inner position loop. Discrete-time models of the arm (including the internal hub position loop) are directly estimated from data and used to design a robust digital controller by combining the pole placement with the shaping of the sensitivity functions. While the robust control design used in [247] belongs to the "H_∞-culture", it differs with respect to the standard

H_∞-approach by the means used to shape the sensitivity functions. In the standard H_∞-approach, one iteratively selects an appropriate weighting filter and carries out for each selected filter a H_∞-optimisation on the weighted sensitivity function to meet the desired specifications. In the approach proposed in [247], the iterations are carried out by scanning the sensitivity functions in the frequency domain and correcting it in each frequency region where the specifications are violated. A comparative evaluation of the two approaches for the control of a very flexible mechanical transmission [248] has shown that the standard H_∞-approach gives neither better performance nor a simpler controller. The results obtained in H_∞-optimisation are highly dependent upon the weighting filter used. A systematic design of these filters for very flexible mechanical structures does not seem to be available yet.

Linear quadratic Gaussian (LQG) control

In [87], the control objective is to regulate the load angular position to the desired reference input, which is subject to bounded variations of the load mass and the load position. A linear quadratic Gaussian (LQG) control is chosen to represent a simple optimal control scheme, which by nature does not provide a robustness guarantee. The authors use LQG to compare with a well-known robust control technique: loop shaping. Although the linear quadratic regulator (LQR) control inherits robustness properties [249], this is not the case for the LQG technique. [250] introduced the loop transfer recovery (LTR) method to recover robustness of the LQG system. The assumptions of the LQG theory seriously mismatch several industrial control problems. Accurate models may not be available, and the external disturbances' statistical properties are not known in advance. For industrial flexible arms, some parameters, such as payload mass and position, are known to be within some operating range. Therefore, it is necessary to incorporate these parametric uncertainties in the design procedure. The loop-shaping method, which is based on Nyquist stability criterion, is selected since it is a simple robust control technique that requires only a basic background in control theory.

Although the LQG algorithm does the necessary work in cases involving a one-link flexible arm, it has its limitations and drawbacks [251]. For example, the robust behaviour of the system cannot be guaranteed, the controller must be re-designed for different loads and it cannot be applied to the multi-link flexible manipulator.

[252] proposed two different "robust" or "deterministic" controllers applied to a single-input multiple-output system with a 6×6-large system matrix. A similar design procedure can also be applied to a MIMO system. The designed controllers have performance characteristics (such as overshoot, response time and insensitivity to parameter variation) equivalent to LQG controllers. However, their main feature is that their performance is guaranteed if the real-time change of the uncertain system parameters remains within some prescribed boundaries. A reduced order observer provides feedback information

needed for the controllers (i.e. the state vector of the system) in this design. The reduced order observer is an optimised version of a full-state observer, the main function of which is to provide real-time information about the state of the system if it is not available from the system's measurable output and input.

μ-synthesis

[253] showed that the μ-synthesis technique applied to a suitable model can lead to the design of robust controllers for single-link and two-link flexible robot manipulators. The designed controllers are robust against high-frequency dynamics, noise corruption and uncertainty in the frequency variations. Different combinations of feedback signals are used to derive the control laws. All designed controllers use hub angle information and one of the following pieces of sensor measurement information: relative tip deflections, relative tip accelerations or hub angular rates. It is worth mentioning that when hub angle and hub angular rate feedback were used, the authors were not able to design a robust controller for the two-link flexible robot manipulator.

2.2.5 Sliding-mode control

The theory of sliding-mode control (SMC) has now been developed to the point that its robustness and performance are demonstrated on a wide variety of MIMO systems [254, 255]. In principle, a sliding-mode control consists of a control law that switches with infinite speed to drive the system on a specified state trajectory, which is known as the sliding surface, and is capable of keeping the state on this surface. The control variable becomes the duration of a constant input rather than its amplitude. [254] proposed an original discontinuous control that introduces a trade-off between robustness and tracking accuracy. Clearly, this type of control is intrinsically non-linear and falls into the broader class of pulse modulated control systems. One remarkable characteristic of sliding-mode control is that its design can be performed using analytical tools typical of linear systems.

It is well known that sliding-mode control systems are an established, robust method of controlling uncertain systems [256]. Sliding-mode control systems for flexible arms have been studied by many authors since the 1990s [257–259]. In most of these works, a discontinuous approach is employed to design the controller and analyse its stability. However, the discontinuous approach is approximated by a differentiable one when the control laws are implemented. Thus, a difference exists between the theoretical analysis and the practical implementation. Further, the upper bounds of the uncertainties are usually assumed as a priori knowledge, which may not be easily obtained in practice.

[260] aimed to improve the performance of the end-point of a flexible arm in terms of robustness to non-modelled dynamics and parameter variations and to reduce vibrations in

the transient and steady state. For this purpose, a chattering free-sliding-mode technique [261] is designed forcing the angular position of the hub unit to track a desired trajectory while minimising the strain.

In [262], the higher-order vibration modes are treated as disturbances and are compensated for by introducing a disturbance observer. Thus, a reduced-order model is obtained for the flexible arm. Further, because the payload mass can generally not be determined, the system parameters are usually unknown. Therefore, the tip position control of the flexible arm can be attributed to the control problem for the systems with uncertainties, in which the upper and lower bounds of the uncertainties are unknown. By expressing the obtained system in state space, the sliding-mode control input is designed so the state converges to the sliding surface. The sliding-mode surface is designed so that the dynamics of the closed-loop system on this surface are stable. The traditional discontinuous control input, which may result in chattering, is modified by a differentiable one. The stability of the closed-loop system is analysed based on this approach, which uses the fact that a part of the control input is the approximate estimate of the uncertainties. The upper and lower bounds of the uncertainties are adaptively updated online.

In [263], the sliding-mode-based partial feedback linearisation control method has been applied to the setpoint control of a single-flexible-link arm for the tip position. The results have been compared with the PD-based controller's performance. The proposed method has been proven to improve the performance.

In [264], various issues raised by the design of sliding-mode controllers have been analysed in detail. Among these issues, the most important are the design of the sliding surface and the reduction of the chattering phenomenon.

In [265], a time-varying sliding surface is proposed to minimise the reaching phase without increasing the chattering for a second-order variable structure system. The sliding surface initially passes initial conditions that are given arbitrarily and subsequently moves towards a predetermined sliding surface by rotating and/or shifting. This method is applied to a single-link flexible manipulator to develop a sliding-mode controller for effective vibration suppression. After establishing the dynamic model characterised by a non-collocated control system, a sliding surface that guarantees a stable sliding-mode motion on the sliding surface itself is constructed via the LQR approach. The surface is then modified to adapt to arbitrarily given initial conditions for the reduction of the reaching phase. Next, a discontinuous control law satisfying the sliding condition is designed for the uncertain system that considers the frequency and damping ratio variations. A decoupled reduced-order observer is formulated to estimate velocity state variables, while the position state variables are obtained directly from output sensor measurements (joint angle sensor, tip position sensor and strain gauges).

In [266], the trade-off between the SMC's robustness and tracking accuracy is reduced using an online perturbation estimation process. The resulting controller is appropriately known as a sliding-mode control with perturbation estimation (SMCPE). In [267], an additional robustness mechanism is suggested by selecting the time-varying sliding surfaces utilising the frequency-shaping techniques. Frequency shaping used in conjunction with SMCPE (FS-SMCPE) penalises the tracking errors at certain frequency ranges. This combination provides two advantages:

- it filters out certain frequency components of the perturbations, therefore eliminating the possible excitation of the non-modelled dynamics; and
- it drives the state to the desired trajectory despite the perturbations.

[268] proposed applying the FS-SMCPE technique to the inertia wheel problem and compared the results to other control techniques presented in [269] and [270]. The performance index in [267] is modified to introduce a prescribed degree of stability for fast, accurate motion control.

The disturbance estimator proposed in [271] has a form similar to the SMCPE. However, it does not include state derivative terms (included in the SMCPE) that may cause undesirable noise and chattering in the estimation process. Instead, the integrated average value of the imposed disturbance is used over a certain sampling period to avoid noise and chattering phenomena. It has been demonstrated through experimental implementation that the proposed control methodology can offer accurate estimations of the imposed disturbance, thus providing superior control performance of the system subjected to external disturbance.

Repetitive control

Repetitive control is a technique whose main property is tracking with zero steady-state error periodic references and rejecting periodic disturbances in the transient and steady state [272, 273]. Applications for trajectory tracking after repetitive learning can be found in [274] for single-link arms and in [275] to control a two-link flexible manipulator, which combines repetitive control with fuzzy logic. These controllers work if the arm has to follow a repetitive closed trajectory and need to repeat the trajectory several times until the flexibility effects are cancelled.

The approach in [276] is completely different from the previously mentioned works because it does not need to iterate in repetitive trajectories. The proposed control system is composed of two terms. The first term is designed to attain a fast tip response for the arm, and the second term, which is the repetitive subsystem, cancels the higher-order steady-state vibrations. Such a design makes this controller very simple and easy to tune, and it cancels the vibrations very quickly. Moreover, it only needs feedback from two signals: motor angle and torque measured by a strain gauge placed on the base of the arm.

One main drawback is that this repetitive control can only be applied if the vibration modes of the arm are a multiple of a basic frequency. In order to achieve this, some changes must be introduced in the mechanics of the arm by adding some point masses at specified link locations.

Coupling map based planning algorithms

While the input-shaping method works successfully with linear systems such as simple one-link manipulators, relatively few studies have examined problems with flexibly supported manipulators. These studies have largely examined problems in terrestrial or industrial systems by focusing on the controls using and end-point control or an equivalent [277].

A method known as the coupling map (CM) has been proposed for studying “graceful path” motions. The CM shows how the non-linear dynamic characteristics of a manipulator can be exploited to develop planning algorithms that find manipulator motions in joint space resulting in a minimum transfer of energy between the manipulator and its supporting structure. This minimises the amount of support vibration excited by the manipulator’s motion. [278] explores the non-linear dynamic characteristics of a rigid manipulator, such as the SPDM, mounted on a highly flexible supporting structure, such as the SSRMS (see section 1.2.1). The non-linear nature of the system makes it possible to plan paths taken by the rigid manipulator between given end-points that reduce its dynamic disturbance to the elastic supporting structure and, hence, its vibrations. These paths may also be used in conjunction with filtering techniques to find the velocity profiles along the paths that further reduce vibration levels. These reduced vibration paths are planned using the CM, which is an analytical tool describing non-linear dynamic interaction between the manipulator and its elastic base. The CM evolved from a technique called the enhanced disturbance map (EDM), which has proven effective in understanding the problem of dynamic disturbances to free-flying spacecraft caused by manipulator motions and in finding paths that reduce such disturbances [279].

Singular perturbation method

An efficient control strategy based on a singular perturbation approach was proposed in [280]. A two-timescale analysis of the system is performed: a slow subsystem that is similar to a rigid arm and a fast linear subsystem in which the slow state variables play the role of parameters. A composite control [281] is then adopted; a slow model following control can be first designed to track a desired joint trajectory, and a linear fast state feedback control stabilises the deflections along the trajectory. The flexible state variables that model the deflections of the arm along the trajectory can be sensed through strain gauge measurements [242]. For full state feedback design, however, the derivatives of the deflections must be estimated.

2.2.6 Control of rotating beams

Applications that require control of a rotating beam generally face many problems regarding sensors' placement on the beam, such as high speeds and high centrifugal forces.

Usually, classic Euler-Bernoulli beam theory is applied in the controller design dedicated to rotating beams. The assumed-modes method is then used to obtain the discretised finite-dimensional dynamic model of vibration control [136, 282]. Some techniques, such as the optimal control [136, 282], shear force feedback control [283] and sliding-modes control [265], have been used to suppress vibrations. However, when coupling transverse flexible deformations and rigid motions, a concept to control the attitude of the rigid hub can be introduced to suppress the transverse vibration of the beam. One such technique is the momentum exchange feedback (MEF) control [284]. By combining this technique with other control methods, such as the positive position feedback approach [285], the vibration suppression can increase effectively.

[286] proposed the control of a rotating beam mounted on a rigid hub using a linear quadratic regulator, which required placing the sensor and actuator on the rotating beam. [287–289] all suggested placing sensors at various locations along the span of the beam for monitoring and control purposes. However, their research focused on either non-rotating beams or large space structures.

Another challenge faced by many research studies dealing with the vibration control in flexible rotating beams is that they are limited to deterministic models of the system. In reality, however, structural and mechanical system components often exhibit considerable stochastic variations in their properties. Thus, the characteristics of a structure corresponding to these properties show some stochastic variations. This makes it necessary to consider the uncertainties of system parameters if highly reliable models and/or control schemes are to be utilised.

To eliminate the need for sensor placement on rotating flexible beams, [290] proposed a linear quadratic estimator (LQE) technique for estimating the vibration of any point of a rotating flexible beam undergoing large planar deformation and subject to measurement noise. Starting from a non-linear model of the beam-hub system, a reduced-order linear model is obtained using FEA [291]. The LQE, whose optimal Kalman gains are determined from the steady-state solution of a Riccati differential equation, reconstructs the system state, including the transverse deflection of the beam.

2.2.7 Macro-micro manipulator

The concept of a macro-micro manipulator system was introduced by Sharon and Hardt [292]. A compact, high-bandwidth manipulator was mounted on the end of a larger one, and the former was controlled to compensate for inaccuracy due to the latter. In other words, a long-reach macro-manipulator is characterised by a “slow” response due to its size, while a short-reach micro-manipulator is characterised by a modest work volume with fast, precise manipulation capability. Such manipulator systems are also referred to as flexible structure-mounted manipulator systems (FSMS). This concept has evolved over the years to meet two primary types of application demands: nuclear waste clean-up [293, 294] and space robotics [295].

The simplest method of designing the controller is to assume that no coupling exists between the subsystems and to partition the control design into a macro-controller, i.e. controlling the macro-manipulator in the global frame, and a micro-controller, i.e. controlling the micro-manipulator in response to a reference input. Because the micro rides on the macro, a dynamic coupling will take place between the two that degrades performance but does not cause instability when the micro reference input is static. [296] developed independent controllers for a macro/micro system, in which the macro was a two-link flexible manipulator. [297] used the micro as a proof mass actuator to control the macro’s vibrations. This work only examines the applicability of using the micro control torques to damp the macro’s vibration and ignores system performance issues. [298] addressed the use of the micro to damp the macro’s vibrations when the task occurred outside the mini’s workspace. Simulations illuminate the shortcomings of partitioning the control. Once the task enters the mini’s workspace, the mini not only stops damping the vibration modes but also allows the energy previously removed from the macro to return to the macro subsystem. The performance of the system can be quite poor.

The literature shows that three main control subtasks can be identified for a single-arm FSMS:

- base vibration suppression control [297, 298];
- design control inputs that induce minimum vibrations (the “reactionless path tracking”) [299]; and
- end-point control in the presence of vibrations [76, 300].

Most of the time, these control subtasks have been tackled separately. Only a few attempts have been made to combine control subtasks into one controller with improved performance [299, 301]. [302] proposed a composite control law capable of solving all three control subtasks described above. This composite control combines two methods developed earlier for free-flying space robot control and for flexible-link manipulator control. It uses a vibration suppression control law similar to the one in [303].

2.2.8 Master-slave systems

Some conventional bilateral control methods have been developed for a master-slave manipulator (MSM) [304–306]. However, all arms were controlled as rigid arms in these conventional MSM systems. Two main problems arise in controlling a flexible master-slave manipulator (FMSM) system consisting of a conventional compact rigid master arm and a flexible slave arm. The first is the vibration of the slave arm. In an FMSM, an operator controls the slave position using a master arm. In this case, when vibrations occur in a slave arm, it becomes difficult to detect the position of said slave. The second problem is the deformation of a flexible link. When an operator adds a large force to an object through a flexible slave arm, the link deforms or breaks easily. For these reasons, vibration control and precise control of the reflection force are necessary. As illustrated in the previous sections, many researchers have studied the vibration control of a flexible arm. However, they only dealt with a flexible slave arm. In an FMSM, the operator directly controls a flexible slave arm using a master arm. A few studies have been conducted on the control method and the control design method for this system.

[307] presented an alternative control architecture of an FMSM based on the concept of dual compliance models following control with the vibration control. The key idea of this concept is to design each compliance model considering the elasticity of a master and slave arm. In [308], an assist control method was proposed for positioning tasks with a master-slave system with elasticity in the slave arm [307].

In general, it is difficult to discuss the stability of a master-slave system because an operator and an environment are both included in a system. For this reason, it is important to discuss the passivity of the input-output relations of a master-slave system. [309] represented these relations as a two-terminal network model and proposed a controller based on the passivity. Moreover, from the viewpoint of passivity, [310] proposed an alternative control algorithm for a scaled tele-manipulation system based on a task-oriented virtual tool. The stability of the resultant system was analysed based on the system's passivity, and the total stability was guaranteed for a human operator and a passive environment.

The passivity-based control of flexible manipulators has been discussed in [311]. [312] discussed the robust passivity of multi-link, flexible manipulators. It was shown that when the joint angular velocity and the joint torque are regarded as the input and output variables, respectively, the controlled input–output system becomes robust and stable by using control laws based on passivity. In [313], the passivity of a one-DOF FMSM system under a symmetric bilateral control configuration was studied. The distributed-parameter model of a rigid master–flexible slave (RMFS) system was derived using Hamilton's principle, which consists of two ODEs of the master and slave angles and a PDE with boundary conditions for the bending vibration of a slave arm. The passivity of the FMSM system was proven for positioning and pushing operations using the Lyapunov method.

2.2.9 Conclusion of the state-of-the-art on the control of flexible robotic arms

As demonstrated above, the topic of controlling flexible robot manipulators has been widely covered from very different perspectives. The objective of this thesis is not to invent yet another control scheme. As reflected in its title, it focuses instead on the problem of vibration sensing.

The idea of estimating the vibration of a rotating flexible beam using the LQE technique, which was introduced in section 2.2.6, will be at the centre of the model-based vibration control scheme described in section 3.1.

Although a variety of control methods have been presented, the LQR approach will be used as a controller in the works detailed in Chapter 3 and validated in Chapter 4. A crucial property of LQR controllers is that their state-feedback closed-loop is asymptotically stable and robust against process uncertainty (in observable and controllable systems). These inherent robustness properties make LQR controllers particularly suitable to vision-based vibration control, the performance of which is likely to be affected by outliers resulting from the extraction of visual features. For further information on the properties of LQRs, one can refer to chapter 39 of [314]. The question of LQ visual servoing will also be touched upon briefly in section 2.3.1.

Although they will not be considered in the following chapters, the input-shaping techniques presented in detail in section 2.2.2 would be very efficient to avoid that critical trajectories imposed by the remote operator stimulate the flexible modes of the system. In such a case, the output of the input shaper could be convolved with the feed-forward command resulting from the LQR.

Finally, for the works carried out within the present thesis, other kinds of controllers that would have allowed a performance comparison will not be implemented. Nevertheless, previous works on CMs and the control of macro-micro and master-slave systems (respectively touched upon in sections 2.2.5, 2.2.7 and 2.2.8) remain very relevant to RH operations, particularly in applications such as the ITER BRHS or the ITER MPD.

2.3 Visual servoing

The idea of suppressing vibrations on a flexible robotic arm using a camera resembles the concept of visual servoing. Visual servo control refers to the use of computer vision data to control the motion of a robotic arm. This visual information may be acquired by a stationary camera or a camera directly mounted on the arm. The latter configuration is known as the eye-in-hand configuration. Other configurations may be envisaged (camera mounted on a pan-tilt head, for instance), but the theory behind these cases is usually similar to the above-mentioned eye-in-hand problem.

The two basic approaches in visual servoing are image-based visual servo (IBVS) control and position-based visual servo (PBVS) control; both were developed in the late 1980s [315]. While the first approach only uses information that is immediately available from the camera image (2D coordinates), PBVS considers a set of 3D parameters, which involves the geometric interpretation of the information extracted from the camera image. Hybrid approaches also exist that are based on a combination of 2D and 3D servoing.

PBVS control schemes [316, 317] use the pose of the camera with respect to a reference coordinate frame. Computing this pose from an image requires the 3D model of the observed object or environment to be known. However, for obvious reasons (evolution of the tokamak topology in time, difficulties distinguishing between similar in-vessel components), such an approach may pose a challenge in solving the problem addressed by the present thesis. Therefore, position-based visual servo will not be considered in the present review.

In this section, we will only consider the image coordinates of interest points as visual features. However, since the scene observed by a camera cannot always be conveniently described by a collection of points, other geometrical primitives can be used [318]: segments, straight lines, spheres, circles and cylinders. Recent works also considered using the image moments corresponding to planar objects of any shape [319, 320]. Stereovision problems posed by the use of multicamera systems will not be addressed either. Switching schemes and the potential field approach will not be touched upon. Finally, we will limit ourselves to considering a stationary target, meaning that changes in the image will only depend on the camera's motions.

This third and last part of the state-of-the-art review is organised as follows. The basic principles of image-based visual servo control are described in section 2.3.1, where the concept of interaction matrix is introduced using the formalism established by several major references in the field of visual servo [57, 321, 322]. An example of a widely used velocity controller is presented, and the question of vision-based optimal control is addressed. In practice, approximating the interaction matrix is often required; this topic is therefore addressed in section 2.3.2. The question of controlling eye-in-hand systems offering less than six degrees of freedom is discussed in section 2.3.3. Section 2.3.4 deals with the problem of feature selection and tracking. Finally, section 2.3.5 briefly discusses how the various visual servo concepts presented in this state-of-the-art review will be used in the developments detailed in Chapter 3.

2.3.1 Basics of image-based visual servo control

The general aim of vision-based control is to minimise an error $\epsilon(t)$ defined by:

$$\boldsymbol{\epsilon}(t) = \boldsymbol{\xi}(\boldsymbol{m}(t), \boldsymbol{a}) - \boldsymbol{\xi}^* \tag{2.46}$$

where $\boldsymbol{\xi}$ represents a set of r visual features.

Visual servo control schemes mainly differ in the manner in which the visual features are defined. Traditional image-based visual servo control (IBVS) schemes [315] generally use the image-plane coordinates $\boldsymbol{m}(t)$ of a set of interest points to define $\boldsymbol{\xi}$, but it is also possible to use the parameters of a set of image segments. $\boldsymbol{a}$ corresponds to a set of additional parameters characterising the vision system, such as the camera's intrinsic parameters or the 3D models of the observed objects. The vector $\boldsymbol{\xi}^*$ contains the desired values of the visual features. In this review, this vector will be assumed to be constant (i.e. motionless target).

The selection of relevant image features will be discussed later in this review (see section 2.3.4). Once the vector $\boldsymbol{\xi}$ is built, the most straightforward control scheme may consist of a velocity controller. This approach requires defining the relationship between the time variation of $\boldsymbol{\xi}$ and the spatial velocity of the camera $\boldsymbol{v_c} = (\boldsymbol{v_c}, \boldsymbol{\omega_c})$, where $\boldsymbol{v_c}$ and $\boldsymbol{\omega_c}$ respectively denote the instantaneous linear and angular velocities of the origin of the camera frame. We consider here the motion control of a camera attached to the end effector of a six-DOF arm in an eye-in-hand configuration.

The relationship between $\dot{\boldsymbol{\xi}}$ and $\boldsymbol{v_c}$ is given by:

$$\dot{\boldsymbol{\xi}} = \boldsymbol{L_\xi} \boldsymbol{v_c} \tag{2.47}$$

where $\boldsymbol{L_\xi} \in \mathbb{R}^{r \times 6}$ is the interaction matrix related to $\boldsymbol{\xi}$.

Using (2.46) and (2.47), the relationship between the camera velocity and the tracking error $\boldsymbol{\epsilon}$ is obtained:

$$\dot{\boldsymbol{\epsilon}} = \boldsymbol{L_\xi} \boldsymbol{v_c} \tag{2.48}$$

Considering $\boldsymbol{v_c}$ as the controller input, an exponentially converging speed control scheme ensuring $\dot{\boldsymbol{\epsilon}} = -\frac{1}{\tau}\boldsymbol{\epsilon}$ can be achieved with:

$$\boldsymbol{v_c} = -\frac{1}{\tau} \boldsymbol{L_\xi^+} \boldsymbol{\epsilon} \tag{2.49}$$

where $\boldsymbol{L_\xi^+} \in \mathbb{R}^{6 \times r}$ stands for the Moore-Penrose pseudoinverse of $\boldsymbol{L_\xi}$. If $r = 6$ and $\det(\boldsymbol{L_\xi}) \neq 0$, $\boldsymbol{L_\xi}$ is fully invertible; this leads to the system input $\boldsymbol{v_c} = -\frac{1}{\tau}\boldsymbol{L_\xi^{-1}}\boldsymbol{\epsilon}$.

In practice, it is almost impossible to accurately set the terms of $\boldsymbol{L_\xi}$. Consequently, an approximation of the interaction matrix must be considered (see section 2.3.2). This leads to the slightly altered control law:

$$\boldsymbol{v_c} = -\frac{1}{\tau}\widehat{\boldsymbol{L_\xi^+}}\boldsymbol{\epsilon} = -\frac{1}{\tau}\widehat{\boldsymbol{L_\xi^+}}(\boldsymbol{\xi} - \boldsymbol{\xi}^*) \tag{2.50}$$

in which $\widehat{\boldsymbol{L_\xi^+}}$ denotes the approximation of the interaction matrix pseudoinverse. Inserting (2.50) into (2.48) leads to the closed-loop equation:

$$\dot{\boldsymbol{\epsilon}} = -\frac{1}{\tau}\boldsymbol{L_\xi}\widehat{\boldsymbol{L_\xi^+}}\boldsymbol{\epsilon} \tag{2.51}$$

Equation (2.51) characterises the real behaviour of the closed-loop system, which is to some degree different from $\dot{\boldsymbol{\epsilon}} = -\frac{1}{\tau}\boldsymbol{\epsilon}$ as long as $\boldsymbol{L_\xi}\widehat{\boldsymbol{L_\xi^+}} \neq \boldsymbol{I}$, where $\boldsymbol{I}$ is the identity matrix.

The speed control presented in the previous paragraphs is the basic scheme implemented by most visual servoing applications. However, it is also possible to design controllers optimising the system performance in various ways. An example of LQG control design is given in [323] and [324], in which gains are chosen in order to minimise a linear combination of state and control inputs. This approach explicitly balances the trade-off between tracking errors (by driving $\boldsymbol{\epsilon}$ to zero) and robot motion. A similar concept is proposed in [325], in which the positioning task and joint limit avoidance constraints are considered simultaneously. One difficulty in multicriteria optimal control is found in properly defining constraints that might often be contradictory. In some cases, this would lead to the visual servo task failing due to local minima in the cost function to be minimised. To avoid this problem, which is classical in robotics, [326] and [327] proposed applying the gradient projection method to visual servoing.

2.3.2 Estimation of the interaction matrix

Let us take $\boldsymbol{\xi} = (x, y)$, which are the coordinates of an interest point in the acquired image. For a point whose 3D coordinates are $\boldsymbol{X} = (X, Y, Z)$ in the camera frame and whose 2D coordinates in the image plane are (x, y), we obtain by projection [328]:

$$x = X/Z = \alpha_c(x_u - c_u)/f_c \tag{2.52}$$

$$y = Y/Z = (x_v - c_v)/f_c \tag{2.53}$$

where $\boldsymbol{m} = (x_u, x_v)$ are the 2D coordinates of the point expressed in pixel units; and the set of camera intrinsic parameters $\boldsymbol{a}$ is composed of c_u and c_v, which are the coordinates of the image centre (point of intersection of the image plane with the optical axis); f_c, which is the focal length; and α_c, which is the aspect ratio induced by non-square sensors.

Taking the time derivative of equations (2.52) and (2.53), we reach:

$$\begin{aligned} \dot{x} &= \dot{X}/Z - X\dot{Z}/Z^2 = (\dot{X} - x\dot{Z})/Z \qquad (2.54) \\ \dot{y} &= \dot{Y}/Z - Y\dot{Z}/Z^2 = (\dot{Y} - y\dot{Z})/Z \qquad (2.55) \end{aligned}$$

Moreover, the velocity of the 3D point can be related to the camera spatial velocity by:

$$\dot{\boldsymbol{X}} = -v_c - \omega_c \times \boldsymbol{X} \qquad (2.56)$$

Inserting (2.56) into (2.54) and (2.55), and using (2.52) and (2.53), we obtain a system that can be written as such:

$$\dot{\boldsymbol{\xi}} = \boldsymbol{L_{\xi} v_c} \qquad (2.57)$$

where the interaction matrix $\boldsymbol{L_{\xi}}$ is given by

$$\boldsymbol{L_{\xi}} = \begin{bmatrix} -\frac{1}{Z} & 0 & \frac{x}{Z} & xy & -(1+x^2) & y \\ 0 & -\frac{1}{Z} & \frac{y}{Z} & 1+y^2 & -xy & x \end{bmatrix} \qquad (2.58)$$

Only three points $\boldsymbol{\xi} = (\boldsymbol{\xi_1}, \boldsymbol{\xi_2}, \boldsymbol{\xi_3})$ are necessary to control a six-DOF manipulator. Concatenating the interaction matrices obtained for these three points results in $\boldsymbol{L_{\xi}} = [\boldsymbol{L_{\xi 1}}, \boldsymbol{L_{\xi 2}}, \boldsymbol{L_{\xi 3}}]^{\top}$. However, with such an interaction matrix, in some configurations $\boldsymbol{L_{\xi}}$ is singular and four global minima cannot be distinguished [329].
Consequently, more than three points are usually considered.

As discussed in section 2.3.1, using a matrix $\boldsymbol{L_{\xi}^{+}}$ directly deduced from (2.58) in the control scheme ensures an exponential decrease in the error $\boldsymbol{\epsilon}$. The parameter Z in (2.58) is the depth of the 3D point expressed in the camera frame. Therefore, this approach implies estimating the current depth Z of each point at each iteration of the control scheme [57]. As a result of the local asymptotic stability of such a control scheme, the trajectories of the points in the image are almost straight lines when the error is small. Nevertheless, the induced 3D motion can be very unsatisfactory when the error is large.

Several strategies can be used to obtain the estimate $\widehat{\boldsymbol{L_{\xi}^{+}}}$ of the interaction matrix pseudoinverse to be used in a control law. One possibility is to choose $\widehat{\boldsymbol{L_{\xi}^{+}}} = \boldsymbol{L_{\xi^*}^{+}}$. In this case, $\boldsymbol{L_{\xi^*}}$ is the value of $\boldsymbol{L_{\xi}}$ for the desired final position and is consequently constant. Only the desired depth of each point must be set, which greatly simplifies the visual servo. Although its output converges, such a controller is generally characterised by unsatisfactory 2D and 3D trajectories when the error is large. As an alternative, [330] recently proposed using $\widehat{\boldsymbol{L_{\xi}^{+}}} = (\boldsymbol{L_{\xi}}/2 + \boldsymbol{L_{\xi}^{*}}/2)^{+}$. However, since $\boldsymbol{L_{\xi}}$ is involved, the current depth of each point still must be available. This method provides satisfactory performance in practice and smooth trajectories in the image and the 3D space.

In all the above-mentioned methods, the camera's intrinsic parameters are involved in the calculation of x and y. In practice, evaluating these parameters accurately is often difficult. For this reason, using an analytical estimation of $\widehat{\boldsymbol{L}_{\boldsymbol{\xi}}^{+}}$ in (2.49) is sometimes impossible, and one may decide to numerically estimate the interaction matrix using either an offline learning step or an online estimation scheme. In both cases, the proposed methods rely on the observation of a variation of the visual features due to a known or measured camera motion.

When opting for an offline learning step, it is possible to estimate $\boldsymbol{L}_{\boldsymbol{\xi}}$ from (2.47) and a set of N_c independent camera motions ($N_c \geq 6$) by solving:

$$\boldsymbol{L}_{\boldsymbol{\xi}} \boldsymbol{M}_{\boldsymbol{c}} = \boldsymbol{M}_{\boldsymbol{\xi}} \tag{2.59}$$

where the columns of $\boldsymbol{M}_{\boldsymbol{c}} \in \mathbb{R}^{6 \times N_c}$ and $\boldsymbol{M}_{\boldsymbol{\xi}} \in \mathbb{R}^{r \times N_c}$ are respectively formed with the set of camera motions and the corresponding motions of the features. The least square solution is given by $\widehat{\boldsymbol{L}_{\boldsymbol{s}}} = \boldsymbol{M}_{\boldsymbol{\xi}} \boldsymbol{M}_{\boldsymbol{c}}^{+}$. It is also possible to directly estimate the numerical value of $\boldsymbol{L}_{\boldsymbol{\xi}}^{+}$, which provides a better behaviour in practice [331]. Methods based on neural networks have also been developed to estimate $\boldsymbol{L}_{\boldsymbol{\xi}}$ [332, 333].

As far as methods estimating the interaction matrix online are concerned, they usually discretise (2.47) and use an iterative updating scheme to refine $\widehat{\boldsymbol{L}_{\boldsymbol{\xi}}}$ at each stage [334–336]. The main benefit of using such numerical estimations in the control scheme is to avoid the modelling and calibration steps. It is particularly useful when using features whose interaction matrix cannot be obtained in an analytical form. On the other hand, one drawback of these methods is that they do not allow analyses of theoretical stability and robustness.

2.3.3 Joint-space control of eye-in-hand systems

In the previous sections, we considered the motion control of a six-DOF eye-in-hand camera using the six components of the camera velocity for controller input. For robotic devices with fewer degrees of freedom that are therefore unable to achieve the six-DOF motion of the camera, the control law must be expressed in the joint space. The general equation of such a system can be written:

$$\dot{\boldsymbol{\xi}} = \boldsymbol{J}_{\boldsymbol{\xi}} \dot{\boldsymbol{\theta}} + \frac{\partial \boldsymbol{\xi}}{\partial t} \tag{2.60}$$

Here, $\frac{\partial \boldsymbol{\xi}}{\partial t}$ is the time variation of $\boldsymbol{\xi}$ due to the potential object motion (assumed to be null here). n is the number of robot joints. $\boldsymbol{J}_{\boldsymbol{\xi}} \in \mathbb{R}^{r \times n}$ is the feature Jacobian matrix, which is linked to the interaction matrix by the following relationship:

$$\boldsymbol{J_\xi} = \boldsymbol{L_\xi}\, {}^{\boldsymbol{c}}\boldsymbol{T_n} \boldsymbol{J_\theta}(\boldsymbol{\theta}) \tag{2.61}$$

where $\boldsymbol{J_\theta}(\boldsymbol{\theta})$ is the robot Jacobian expressed at the end-effector and ${}^{\boldsymbol{c}}\boldsymbol{T_n}$ is the transformation matrix between the camera frame and the end-effector frame, which is usually assumed to be constant if the camera is rigidly attached to the end-effector.

From here, it is possible to apply the same procedure as the one described in section 2.3.1 to design a joint-space control ensuring the exponential decrease of ϵ:

$$\dot{\boldsymbol{\theta}} = -\frac{1}{\tau}\widehat{\boldsymbol{J_\xi^+}}\boldsymbol{\epsilon} - \widehat{\boldsymbol{J_\xi^+}}\widehat{\frac{\partial \boldsymbol{\epsilon}}{\partial t}} \tag{2.62}$$

2.3.4 Visual tracking

Visual tracking is a broad term used in very diverse problems. Two kinds of vision-based tracking can be distinguished.

- "Outside-in" tracking, in which cameras observe moving objects within a scene from fixed positions. A fixed transformation matrix is present between the repective coordinate systems of the scene and of each camera.
- "Inside-out" tracking, in which the camera is attached to a moving object and observes a static scene. In this case, the relation between scene coordinates and camera coordinates changes over time.

Despite some commonalities, these two concepts differ in various aspects, such as the size of the tracked objects, acceptable size of the scene, accuracy of the results and, therefore, algorithmic possibilities. Due to the nature of the problem addressed by the present thesis, only the second approach will be touched upon in the following sections.

Determining the self-motion of a camera represents a key step in a large number of computer vision applications. A large majority of the existing visual motion-tracking algorithms employ visual features (shape, edges, colour, corners, etc.) to estimate the instantaneous position of a tracked object in the camera image or the instantaneous pose of the camera in the 3D environment. By estimating this position/pose from video frame to video frame, an object tracker generates the trajectory of the object/camera over time. To achieve this, some algorithms require that reference objects remain in the field of the camera, while others implement continuous detection of features to compensate for lost information.

In recent decades, a number of visual tracking systems/algorithms have been developed, each with their own advantages and restrictions. They usually differ in motivation, aim or implementation. Nevertheless, one tracking cycle can generally be described as follows. Each time a frame is acquired, a detector identifies candidate features for tracking, and a feature descriptor is computed for each of these candidates. This descriptor is then compared to the descriptors of the features selected in the previous frame. Usually, this matching step is limited to features belonging to the same area of the image. As a feature is tracked, it becomes a series of two-dimensional coordinates (a “track”) representing the position of the feature across a series of frames. From there, most tracking algorithms compute the feature displacement using optical flow or other differential techniques. The generally high number of matched features allows for the removal of outliers before being used for 2D motion tracking or to calculate 3D information.

According to [337], the most desirable properties of a visual feature are its locality (the feature should be local in order to be less sensitive to deformations and occlusions), its distinctiveness (the feature should be easily distinguished and permit a low false-positive rate), its accuracy (the feature should be accurately localised), its quantity (the number of detected features should be sufficiently large and controllable), its efficiency (the feature should be detected fast enough to allow for time-critical applications) and its repeatability (the same feature should be detected in spite of changing viewing conditions). Clearly, the importance of these different properties depends on the application, and compromises have to be made quite often. For instance, distinctiveness and locality are competing properties and cannot be fulfilled simultaneously.

The most common visual features include the following.

- Colour: Colour features are perhaps the most basic features of an image. They are defined within a particular colour space. In image processing, no specific colour space prevails over the others. The red, green, blue (RGB) colour space is frequently used, although its dimensions are highly correlated. Another colour space particularly used in the area of object tracking is the hue, saturation, value (HSV) space, which has the specificity of separating the image intensity from the colour information.

- Edges: Edge features are a set of adjacent points of a high gradient magnitude that form a boundary between two image regions (see Fig. 2.5(b)). Theoretically, this boundary can have any shape; however, edge detection algorithms usually apply additional constraints to limit their outputs to specific patterns (straight lines, smooth curves, etc.). Compared to colour features, they are less sensitive to illumination changes.

- Corners: Also known as interest points, corner features were originally strongly linked to the concept of edges and represented the intersection of two edges or rapid changes in their direction (see Fig. 2.5(c)). For this reason, corners can be defined as sets of adjacent points characterised by high levels of curvature in the image gradient. They have a local two-dimensional structure, whereas edges are locally one-dimensional. It should be noted that corner features do not only correspond to corners in the traditional sense but also to isolated local intensity maxima or minima (bright spots on a dark background or vice versa).

- Blobs: Blob features represent areas of an image that are too smooth to be identified by a corner detector (see Fig. 2.5(d)). Contrary to edges and corners, which deal with points, blobs provide complementary information on the image in terms of regions. For this reason, they are sometimes also referred to as regions of interest. However, since the difference between a region and a point depends greatly on the distance between the camera and the scene, many blob detectors may also be regarded as interest-point detectors.

- Ridges: In contrast to edges, which draw the boundary of an object, ridge features are curves capturing the major axis of symmetry of elongated objects. They are usually harder to extract than edge, corner or blob features.

- Optical flow: Optical flow is a field of vectors describing the apparent motion of the brightness pattern, i.e. the displacement within a region of pixels of constant brightness from one frame to another. It renders the motion of visual objects caused by the relative movement between the camera and the scene.

- Texture: Texture features represent the spatial distribution of colours or intensities in a specific region of an image. They can be seen as repeating patterns of local intensity variations that are too fine to be distinguished as separate objects. Whereas colour characterises a single pixel, texture is a common property to a group of pixels and is often used to quantify properties such as smoothness and regularity. Like edge features, texture features are less sensitive to illumination changes than colour features.

As mentioned above, every tracking method requires a feature detection mechanism. Many algorithms have been proposed to accomplish this task. The most common of these can be categorised as interest point detectors, segmentation techniques, background subtractors and supervised classifiers. Only corner detectors will be addressed in the following paragraphs, but the reader can refer to [332, 338–340] for further information on the other types of detectors.

Corners are among the most low-level features used for tracking. Although there is no specific definition for what makes a point interesting, Shi and Tomasi provided a pragmatic explanation in [341]: “the right features are exactly those that make the tracker work best”.

In order to identify interest points, Moravec’s corner detector [342] computes the gradient of image intensity in 4×4 patches in the horizontal, vertical, diagonal and anti-diagonal

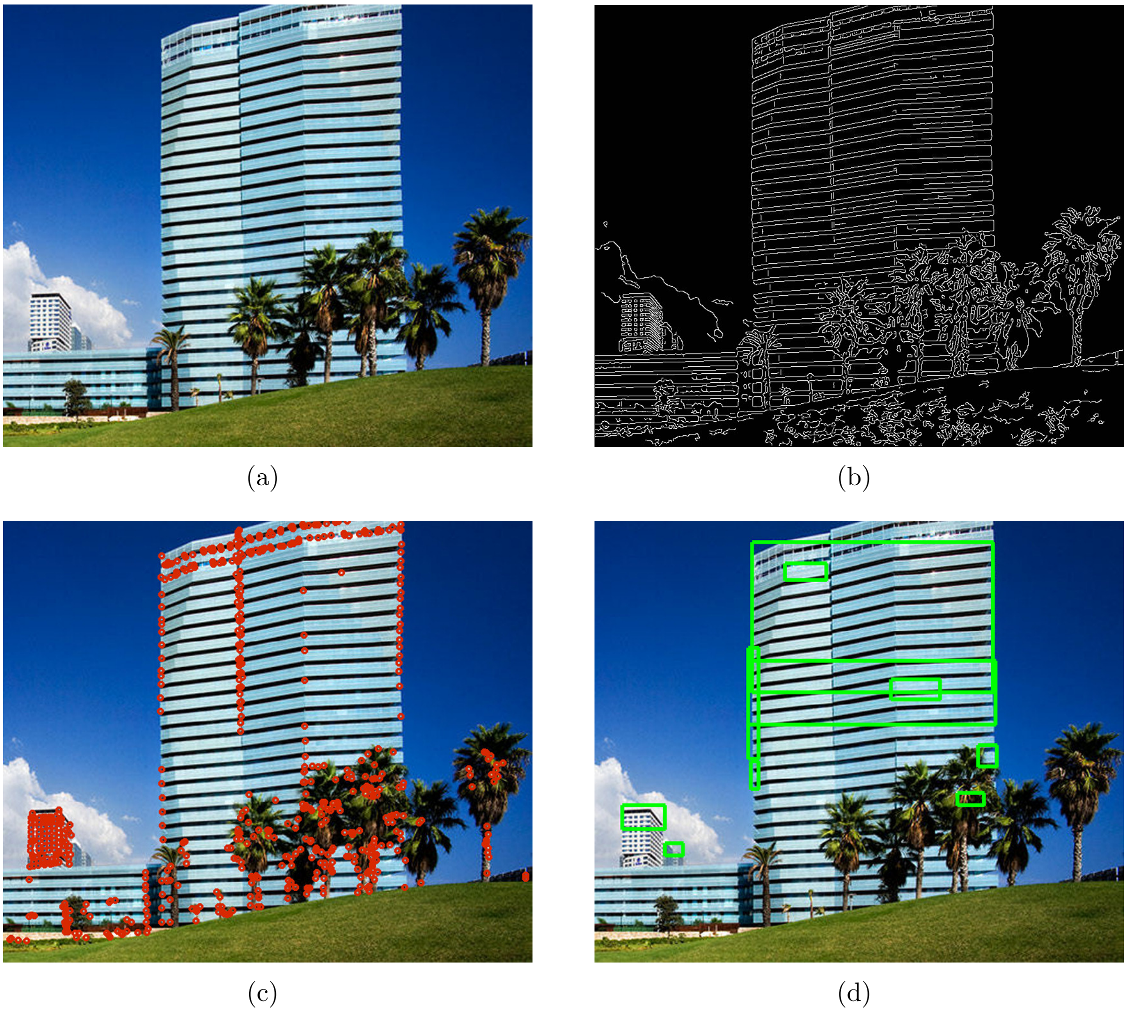

Figure 2.5: Examples of image features: (a) original image, (b) edges, (c) corners, (d) blobs

directions. The minimum of these four values defines the score of each patch. A point is declared interesting if its score is a local maximum in a 12 × 12 window.

Inspired by the previous approach, the Harris corner detector [343] computes the gradient of image intensity for every pixel in the horizontal and vertical directions. The second moment matrix M is calculated in the near neighbourhood; [343] proposed using a Gaussian window, but a simpler rectangular window can also be chosen. Since the eigenvalues and eigenvectors of M characterise the curvature and shape of the window intensities, the eigenvalues λ_1 and λ_2 can be used to determine whether the pixel is a corner (λ_1 andλ_2 are both large) or whether it belongs to an edge ($\lambda_1 \ll \lambda_2$ or $\lambda_1 \gg \lambda_2$) or to a uniform region (λ_1 and λ_2 are both small). To avoid the explicit computation of λ_1 and λ_2, [343] assigns the following score to each pixel:

$$Score_{Harris} = \lambda_1\lambda_2 - k \cdot (\lambda_1 + \lambda_2)^2 = \det(M) - k \cdot [trace(M)]^2 \tag{2.63}$$

where k is a constant tuning parameter. A point is declared interesting after undergoing thresholding and non-maximum suppression.

The second moment matrix of the windowed image also forms the basis of the Förstner detector [344] and the Kanade-Lucas-Tomasi (KLT) tracking method by Shi and Tomasi [341]. In the latter, a confidence score is computed for each candidate point using the smallest eigenvalue of M. A point is declared interesting after thresholding of this score and rejection of the candidates close to each other. Since they are both based on the measure of the image intensity variations, the Harris and KLT detectors usually identify the same set of corners in practice. One main difference is the additional constraint within the KLT algorithm that imposes a certain distance between the detected interest points.

Although the matrix M defined above is invariant to both rotation and translation, it is not invariant to affine transformations or projections. [345] proposed an approach to make the Harris detector robust under different image transformations. The scale-invariant feature transform (SIFT) method [346] generates a set of difference-of-Gaussians (DoG) images by convolving the image with Gaussian filters at different scales. Candidate interest points are then selected from the minima and maxima of the DoG images. After eliminating candidates that are low contrast or are located along the edges, the remaining corners are assigned orientations from the gradient maximum across the neighbourhood. Generally the SIFT detector generates a high number of interest points compared to other algorithms because it accumulates points from different scales and resolutions. Other affine-invariant detectors are proposed in [347, 348].

A comparative evaluation of these commonly-used corner detectors can be found in [349]. To provide a complete picture, other, more specific intensity-based corner detectors are described in [350–352].

After points of interest have been identified, a feature descriptor must be computed for each of them so they can be identified and matched across frames. Most of the time a given visual feature can be represented in various manners. For instance, an edge can be represented in each image point as a Boolean variable describing whether an edge is present or not at that point. Alternatively, this Boolean variable can be replaced by a certainty measure and combined with information on the edge orientation. Similarly, the colour of a specific region can either be represented by its average value or by more complex descriptions, such as a colour histogram [353], colour moments [354], colour coherence vector [355] or colour correlogram [356]. Each of these representations of a feature is referred to as a feature descriptor. In some cases, a very detailed feature descriptor may be necessary to solve a specific problem, but this occurs at the cost of higher computational complexity. Therefore, selecting a suitable feature type and descriptor is a key requirement in visual tracking applications. Ideally, the descriptor should capture the surrounding texture and be invariant to changes in illumination, scale and rotation.

The most basic description of a corner is the image patch around the corner itself, which only requires subsampling the image at given locations. This descriptor is not affected by uniform illumination changes; however, it is far too simplistic to offer any of the desired invariance properties mentioned above.

A more advanced feature descriptor is used in the SIFT method, in which the scale and orientation assigned to each corner define a new local coordinate system. There, an orientation histogram of B bins is computed in $N \times N$ Gaussian-weighted patches around the various corners. The descriptor consists of the $N \times N \times B$ histogram values.

A comparison of commonly used feature descriptors and usual detector-descriptor combinations can be found in [357].

After a set of visual features has been detected and described, the last stage of each tracking method consists of the object tracker itself. [358] separates the most frequent tracking methods into three categories.

- Point tracking: Point-tracking algorithms [359–361] associate points in consecutive frames on the basis of their previous state, which usually includes position and motion. This approach requires an external feature detector in order to identify the tracked objects in every frame.
- Kernel tracking: Kernel-tracking algorithms [362–364] are based on the utilisation of a coarse representation of the tracked object's shape and appearance (the "kernel"). It can be, for instance, a rectangular template or an ellipsoid region associated with an histogram. Features are tracked by examining consecutive frames to determine the motion of the kernel in terms of rotation, translation and affine transformation.
- Silhouette tracking: Silhouette-tracking algorithms [365–367] require a more detailed representation of the tracked object, such as its appearance density, its initial contour and/or its motion parameters. Given the object model, silhouettes are tracked by either shape matching or contour evolution.

Since they represent a good compromise between oversimplified and overdetailed representations of the object, only kernel-tracking methods will be addressed in the following paragraphs. As mentioned earlier, kernel-tracking techniques estimate the parametric motion of features that are represented by a simple shape regions (rectangle, ellipse). These algorithms usually differ in terms of the number of tracked objects, appearance representation and motion calculation. Tracking multiple objects is useful for cases involving interactions between several objects (partial or complete occlusion for instance) or between an object and the background. This specific case, in which the background and all moving objects are explicitly tracked, will not be addressed in the following paragraphs, which will rather focus on single-object tracking.

In methods using a multiview appearance model, different views of the object are examined offline in order to overcome the problem of major changes in the object appearance during tracking. These methods require prior knowledge of the object to be tracked. Template matching is more widely used in practice because of its relative simplicity and the possibility of generating models online. The main limitation of template-matching algorithms is their high computation cost due to the brute force search for the object template (usually intensity or colour patterns) throughout each frame. To decrease this computational burden, one option is to limit the object search to the vicinity of its previous positions. More sophisticated algorithms have also been proposed to overcome the high computational cost of brute force searching [364, 368].

Another kernel-based approach consists of computing the translation of the rectangular or ellipsoid region using an optical flow method. This computation, which is only carried out in the neighbourhood of the feature, can either be algebraic [369] or geometric [370]. Shi and Tomasi proposed the KLT tracker, which iteratively computes the translation $\boldsymbol{d}$ of a $N \times N$ patch centred on a corner. Once the corner location is updated, the KLT tracker evaluates the quality of the tracked patch by computing the following affine transformation between corresponding patches in consecutive frames:

$$\boldsymbol{\delta\xi} = \boldsymbol{D\xi} + \boldsymbol{d} \tag{2.64}$$

where $\boldsymbol{D}$ is a deformation matrix and $\boldsymbol{d}$ is the translation of the patch. The tracker then computes a measure of dissimilarity based on the sum of square difference between coinciding patches. If this dissimilarity is high the feature is discarded; otherwise, it is kept for the next tracking cycle.

To conclude, commonly used feature trackers are now able to track several hundreds of points up to 60Hz or higher. Nevertheless, most of these fast visual feature trackers are limited by the speed of detection of new features and often require all the CPU's available processing power. For this reason, it is important to select a suitable type and associated descriptor of the features to be tracked, which is a key requirement in visual tracking applications.

2.3.5 Conclusion of the state-of-the-art on visual tracking

Since the 1990s, visual servoing and visual feature tracking have been major areas of research in the field of computer vision. Because one thesis would not be enough to review all the works carried out in these respective domains, the present state-of-the-art review has briefly introduced their main trends; only the theoretical elements that will be used in Chapter 3 have been presented in detail.

The concept of the interaction matrix will be employed in section 3.1.1 in order to build a model of a flexible arm equipped with a camera mounted in an eye-in-hand configuration. An online interaction matrix estimator will be implemented in section 3.1.6.

In order to evaluate the motion of the camera in its static environment, an inside-out visual feature tracking system will be used. Due to the nature of the main problem addressed by the present thesis (vibration sensing in a nuclear environment) such a system requires visual tracking to be robust, accurate and fast enough to be computed in real-time. For these reasons, the KLT feature-tracking algorithm discussed in section 2.3.4 will be implemented in section 3.1.4.

3. DEVELOPMENTS: VIBRATION CONTROL USING VISUAL FEATURES FROM THE ENVIRONMENT

The main objective of this thesis is to investigate the feasibility of controlling a remotely operated flexible arm's oscillatory behaviour without considering any extra sensor besides the embedded vision devices that will inevitably be used to provide operators real-time visual feedback. In this chapter, vision processes are viewed as full sensors providing quantitative data that can be processed by the control scheme and not only as plain visual feedback providing qualitative information.

In section 3.1, the vibration to be rejected is reconstructed from visual data. To ensure that the proposed method is robust against visual perturbations, this data is fused with the joint movements derived from a simple model of the manipulator. To that end, a Kalman filter is used. Its equations have been modified to deal with delayed measurements and low update rates resulting from the long processing time inherent to vision devices.

However, one unforeseen effect of such a model-based control is the impact on the beam behaviour of hitherto neglected inertia terms as sudden transient articular accelerations are applied to the system to damp the oscillations. Consequently, section 3.2 suggests replacing the model used in the prediction step of the proposed Kalman filter with a more sophisticated, multimode dynamic model. Particular attention is paid to obtaining a computationally light model without making any detrimental compromises to its accuracy. This change should make the overall scheme more efficient by decreasing the prediction error during control.

Although the proposed vibration sensing method provides successful results, it still has one main drawback. The Kalman filter used as a vibration estimator is based on a model whose input can be either joint acceleration or applied torque. Consequently, the problem addressed remains unsolved when the vibration is not due to joint dynamics but rather to an embedded process or a shock with the environment. The camera may perceive a vibration, whereas the internal input-output model still believes the arm is stationary, which is detrimental to the accuracy of the estimation. Section 3.3 remedies this problem by considering sinusoidal regression instead of a Kalman filter to reconstruct the vibration from the visual data. Since the only assumption made here is that the vibration has a sinusoidal shape—which is verified strictly if one aspires to damp only the fundamental—the proposed method adapts well for any vibration of any origin.

Finally, in methods such as online sinusoidal regression or vibration estimation from a Kalman filter, synchronisation between the measured signal and the physical vibrational phenomenon is critical to properly damp vibrations. Therefore, section 3.4 revisits the capture delay estimation performed in previous sections, highlights its limitations and proposes a novel algorithm for effective time delay estimation based on a cross-correlation technique with a synchronisation sensor.

3.1 Robust model-based vibration control

Following the developments in [65] and [66], this section addresses the problem of designing an online vibration estimator using a camera without any a priori knowledge of the environment (see Fig. 3.1). It is also assumed that no markers have been placed in this environment. The first step involves evaluating the velocity of the environment in the camera basis. To that end, the KLT feature-tracking algorithm, which extracts and tracks features from the camera images, has been implemented. An M-estimator rejects the outliers from this set of features that possibly result from the extraction noise and provides a robust estimation of the environment's overall displacement as seen by the camera. Afterwards, this signal is filtered and its low-dynamic part is used to reconstruct the interaction matrix, which relates the motion of the environment in the 2D image and the motion of camera in the 3D world. In the last step of the proposed algorithm, the online estimated interaction matrix and the high-dynamic part of the image features displacement both feed a discrete time Kalman filter. Due to visual data's long processing time, the Kalman filter is modified to deal with delayed measurements.

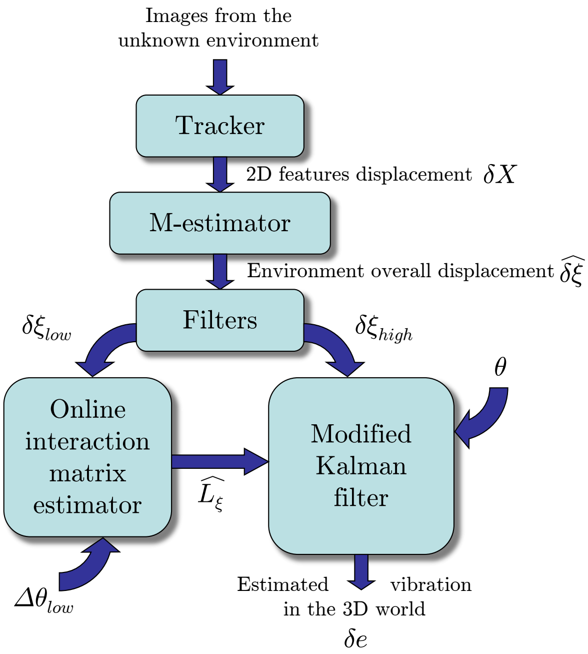

Figure 3.1: Principle of the vibration estimator

The following sections are organised as follows. After deriving a dynamic model of an n-DOF flexible link robot arm in sections 3.1.1 and 3.1.2, section 3.1.3 describes a two-time scale state observer that reconstructs the arm's vibrations from delayed visual measurements obtained by an eye-in-hand-mounted camera. Sections 3.1.4, 3.1.5 and 3.1.6 present in detail how the velocity of the camera is evaluated from the online tracking of visual features. Section 3.1.7 describes the LQR chosen to address the control problem.

3.1.1 System equations

As the ITER remote maintenance equipment is characterised by large and slender structures, flexibilities in links are deemed to prevail over joint flexibilities. Let us consider a robotic arm consisting of n flexible links, which are rigidly attached to n rotating frames subjected to a vector of external torques $\boldsymbol{\tau}(t)$ (see Fig. 3.2).

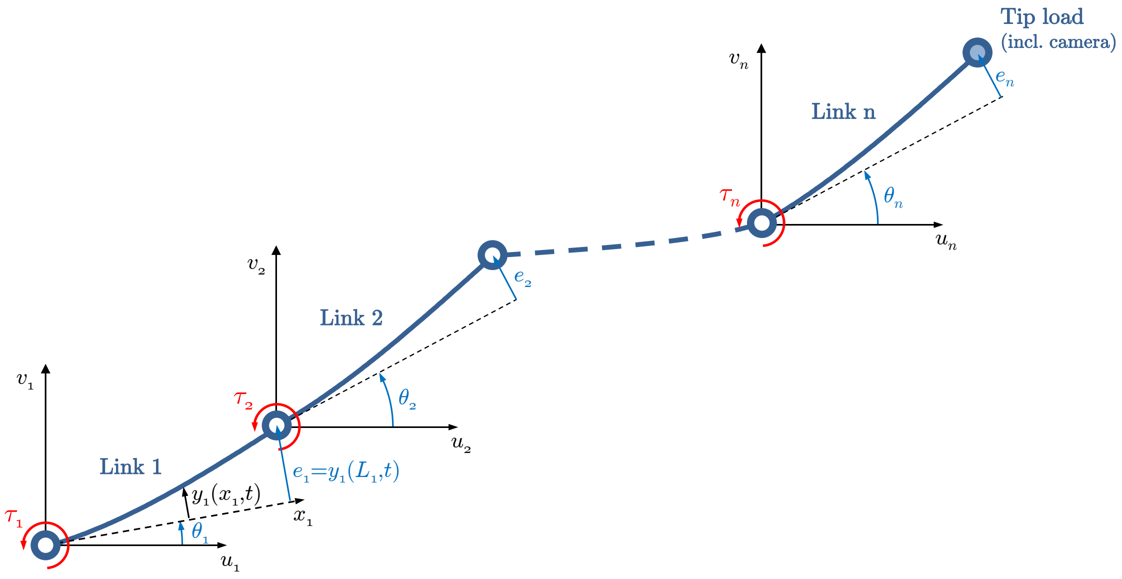

Figure 3.2: Schematic of the considered n-DOF flexible link robot arm

Its state-space model is constructed using the assumed modes method (see section 2.1.2). High order vibrational modes are neglected. By applying the standard procedure based on Lagrange equations, two dynamic equations similar to (2.26) can be written as follows:

$$\boldsymbol{M_{rr}}(\boldsymbol{\theta},\boldsymbol{e})\ddot{\boldsymbol{\theta}} + \boldsymbol{M_{rf}}(\boldsymbol{\theta},\boldsymbol{e})\ddot{\boldsymbol{e}} + \boldsymbol{\mathcal{C}_r}(\boldsymbol{\theta},\boldsymbol{e},\dot{\boldsymbol{\theta}},\dot{\boldsymbol{e}}) + \boldsymbol{g_r}(\boldsymbol{\theta},\boldsymbol{e}) = \boldsymbol{\tau} \tag{3.1}$$

$$\boldsymbol{M_{fr}}(\boldsymbol{\theta},\boldsymbol{e})\ddot{\boldsymbol{\theta}} + \boldsymbol{M_{ff}}(\boldsymbol{\theta},\boldsymbol{e})\ddot{\boldsymbol{e}} + \boldsymbol{K_s}\boldsymbol{e} + \boldsymbol{\mathcal{C}_f}(\boldsymbol{\theta},\boldsymbol{e},\dot{\boldsymbol{\theta}},\dot{\boldsymbol{e}}) + \boldsymbol{g_f}(\boldsymbol{\theta},\boldsymbol{e}) = 0 \tag{3.2}$$

where $\boldsymbol{\theta} = [\theta_1 ... \theta_n]^\top$ is the vector of the n joint angles and $\boldsymbol{e} = [e_1 ... e_m]^\top$ is the vector of the m deflections variables. $\boldsymbol{M_{rr}}$, $\boldsymbol{M_{rf}}$, $\boldsymbol{M_{fr}}$ and $\boldsymbol{M_{ff}}$ are inertia matrices. $\boldsymbol{M_{rf}}$ and $\boldsymbol{M_{fr}}$ are such that $\boldsymbol{M_{fr}} = \boldsymbol{M_{rf}}^\top$. $\boldsymbol{K_s}$ is a stiffness matrix, $\boldsymbol{\mathcal{C}_r}$ and $\boldsymbol{\mathcal{C}_f}$ are the centrifugal and Coriolis torques and forces vectors, $\boldsymbol{g_r}$ and $\boldsymbol{g_f}$ are gravitational terms vectors and $\boldsymbol{\tau}$ represents the joints' input torques.

Since remote maintenance operations deal with relatively slow motions, the following will assume that the action of $\boldsymbol{\mathcal{C}_r}$ and $\boldsymbol{\mathcal{C}_f}$ can be neglected. Similarly, the action of viscous friction on the links is neglected. Joint friction is only considered as a term impacting the rigid motion. In addition, the influence of the deflections on the gravity terms is ignored. Thus, the non-linear dynamic model given by (3.1) and (3.2) can be approximated by a linear model around a given steady-state position. Such an equilibrium is characterised by the following conditions:

$$\boldsymbol{g_r}(\boldsymbol{\theta_s}) = \boldsymbol{\tau_0} \tag{3.3}$$

$$\boldsymbol{K_s}\boldsymbol{e_0} + \boldsymbol{g_f}(\boldsymbol{\theta_s}) = 0 \tag{3.4}$$

where $\boldsymbol{e_0}$ is the static deflection for a given steady-state joint position $\boldsymbol{\theta_s}$ and $\boldsymbol{\tau_0}$ is the constant torque that balances gravity.

Let us consider $\boldsymbol{\delta e} = \boldsymbol{e} - \boldsymbol{e_0}$ and $\boldsymbol{\delta\tau} = \boldsymbol{\tau} - \boldsymbol{\tau_0}$ as the deviations of $\boldsymbol{e}$ and $\boldsymbol{\tau}$ from their respective static values. After subtracting (3.3) from (3.1) and (3.4) from (3.2), the following linearised model is obtained:

$$\underbrace{\begin{bmatrix} \boldsymbol{M_{rr}} & \boldsymbol{M_{rf}} \\ \boldsymbol{M_{rf}}^\top & \boldsymbol{M_{ff}} \end{bmatrix}}_{\boldsymbol{M}} \begin{bmatrix} \ddot{\boldsymbol{\theta}} \\ \ddot{\boldsymbol{\delta e}} \end{bmatrix} + \underbrace{\begin{bmatrix} 0 & 0 \\ 0 & \boldsymbol{K_s} \end{bmatrix}}_{\boldsymbol{K}} \begin{bmatrix} \boldsymbol{\theta} \\ \boldsymbol{\delta e} \end{bmatrix} = \underbrace{\begin{bmatrix} I \\ 0 \end{bmatrix}}_{\boldsymbol{U}} \boldsymbol{\delta\tau} \tag{3.5}$$

As shown in section 2.1.2, the lower part of (3.5) can be seen as the dominant equation for the vibrational behaviour. It can be extracted from system (3.5) and expressed as the following state-space model:

$$\begin{bmatrix} \dot{\boldsymbol{\delta e}} \\ \ddot{\boldsymbol{\delta e}} \end{bmatrix} = \begin{bmatrix} 0 & \boldsymbol{I} \\ -\boldsymbol{M_{ff}}^{-1}\boldsymbol{K_s} & 0 \end{bmatrix} \begin{bmatrix} \boldsymbol{\delta e} \\ \dot{\boldsymbol{\delta e}} \end{bmatrix} + \begin{bmatrix} 0 \\ -\boldsymbol{M_{ff}}^{-1}\boldsymbol{M_{rf}}^\top \end{bmatrix} \ddot{\boldsymbol{\theta}} \tag{3.6}$$

Equation (3.6) fully describes the vibrational dynamics of the considered arm. One could also decide to include $\boldsymbol{\delta\tau}$ in this model by replacing $\ddot{\boldsymbol{\theta}}$ in the lower part of (3.5) with its expression in the upper part. As further explained below, this choice is mainly motivated by the ease of measuring $\ddot{\boldsymbol{\theta}}$ as the model input rather than $\boldsymbol{\delta\tau}$. With this model, an observer of the deflection deviation $\boldsymbol{\delta e}$ can be built provided that a measurement equation is added to (3.6). In the present case, the measurement is made using visual data taken from feature points of the static environment projected in the image plane.

The velocity $\dot{\boldsymbol{\xi}}$ of these 2D features can be related to the velocity $\boldsymbol{v_c}$ of the eye-in-hand-mounted camera using the interaction matrix (see section 2.3.1):

$$\dot{\boldsymbol{\xi}} = \frac{\partial\boldsymbol{\xi}}{\partial\boldsymbol{p_c}}\boldsymbol{v_c} = \boldsymbol{L_\xi}\boldsymbol{v_c} \tag{3.7}$$

An online estimator of $\boldsymbol{L_\xi}$ will be described in section 3.1.6. The velocity of the tip camera

$\boldsymbol{v_c}$ depends on the rigid motion $\dot{\boldsymbol{\theta}}$ and the elastic motion $\dot{\boldsymbol{e}}$ of the arm:

$$\boldsymbol{v_c} = \frac{\partial \boldsymbol{p_c}}{\partial \boldsymbol{\theta}}\dot{\boldsymbol{\theta}} + \frac{\partial \boldsymbol{p_c}}{\partial \boldsymbol{e}}\dot{\boldsymbol{e}} = \boldsymbol{J_\theta}\dot{\boldsymbol{\theta}} + \boldsymbol{J_e}\dot{\boldsymbol{e}} \tag{3.8}$$

From (3.7) and (3.8), one can deduce the following:

$$\dot{\boldsymbol{\xi}} = \boldsymbol{L_\xi}\boldsymbol{J_\theta}\dot{\boldsymbol{\theta}} + \boldsymbol{L_\xi}\boldsymbol{J_e}\dot{\boldsymbol{e}} \tag{3.9}$$

where $\boldsymbol{J_\theta}$ and $\boldsymbol{J_e}$ refer to the Jacobian matrices of the end-point with respect to the articular positions and the deflection variables, respectively.

Following the developments in [62], let us consider that the velocity $\dot{\boldsymbol{\xi}}$ of the features can be split in a low dynamics component $\dot{\boldsymbol{\xi}}_{\boldsymbol{low}}$ and a high dynamics component $\dot{\boldsymbol{\xi}}_{\boldsymbol{high}}$. It is plausible to assume that $\dot{\boldsymbol{\xi}}_{\boldsymbol{low}}$ mainly results from the articular movement, whereas $\dot{\boldsymbol{\xi}}_{\boldsymbol{high}}$ mainly results from the vibration. Therefore, by considering the linear approximation of $\boldsymbol{\xi_{high}}$ for a deflection $\boldsymbol{e}$ around $\boldsymbol{e_0}$:

$$\boldsymbol{\xi_{high}} \approx \boldsymbol{\xi_{high,0}} + \boldsymbol{L_\xi}\boldsymbol{J_e}\left(\boldsymbol{e} - \boldsymbol{e_0}\right) \tag{3.10}$$

which can be written according to the state vector of (3.6):

$$\boldsymbol{\delta\xi_{high}} \approx \begin{bmatrix} \boldsymbol{L_\xi}\boldsymbol{J_e} & 0 \end{bmatrix} \begin{bmatrix} \boldsymbol{\delta e} \\ \dot{\boldsymbol{\delta e}} \end{bmatrix} \tag{3.11}$$

Consequently, the process to be estimated can be expressed as the following continuous state-space model:

$$\begin{aligned} \dot{\boldsymbol{x}}_{\boldsymbol{1}}(t) &= \boldsymbol{A_1}\boldsymbol{x_1}(t) + \boldsymbol{B_1}\ddot{\theta} + \boldsymbol{w_1}(t) && (3.12) \\ \boldsymbol{z_1}(t) &= \boldsymbol{C_1}\boldsymbol{x_1}(t) + \boldsymbol{v_1}(t) && (3.13) \end{aligned}$$

where $\boldsymbol{x_1} = \begin{bmatrix} \boldsymbol{\delta e} & \dot{\boldsymbol{\delta e}} \end{bmatrix}^\top$ and $\boldsymbol{z_1} = \boldsymbol{\delta\xi_{high}}$. $\boldsymbol{w_1}$ and $\boldsymbol{v_1}$ are the usual white Gaussian noises, with the respective covariances $\boldsymbol{Q_1}$ and $\boldsymbol{R_1}$. The matrices $\boldsymbol{A_1}$, $\boldsymbol{B_1}$ and $\boldsymbol{C_1}$ are defined by:

$$\boldsymbol{A_1} = \begin{bmatrix} 0 & \boldsymbol{I} \\ -\boldsymbol{M_{ff}}^{-1}\boldsymbol{K_s} & 0 \end{bmatrix} \quad \boldsymbol{B_1} = \begin{bmatrix} 0 \\ -\boldsymbol{M_{ff}}^{-1}\boldsymbol{M_{rf}}^\top \end{bmatrix}$$

$$\boldsymbol{C_1} = \begin{bmatrix} \boldsymbol{L_\xi}\boldsymbol{J_e} & 0 \end{bmatrix}$$

3.1.2 Incorporation of the acceleration estimation

The robust vibration estimation algorithm described throughout this section is based on the dynamic model (3.12); therefore, it assumes that the joints' accelerations $\ddot{\boldsymbol{\theta}}$ are known exactly. As is commonly the case in robotics, only the joint positions $\boldsymbol{\theta}$ are available from optical encoders and the joint velocities $\dot{\boldsymbol{\theta}}$ and accelerations $\ddot{\boldsymbol{\theta}}$ must be estimated from these discrete-time quantised signals. The classic Euler approximation combined with low-pass filtering can be considered, but it yields poor results at high sampling rates. Moreover, such filtering often excessively smoothes the measurement of transient dynamics that stimulate the flexible arm but cannot be considered in the vibration estimator. Consequently, stochastic methods are preferred to deterministic ones in order to reduce the variances while reconstructing the accelerations. A more sophisticated method to estimate the velocities is to use an optimised Kalman filter for the following continuous model [371]:

$$\dot{\boldsymbol{x}}_{\boldsymbol{2}}(t) = \boldsymbol{A}_{\boldsymbol{2}}\boldsymbol{x}_{\boldsymbol{2}}(t) + \boldsymbol{\Gamma}_{\boldsymbol{2}}\boldsymbol{w}_{\boldsymbol{2}}(t) \tag{3.14}$$

$$\boldsymbol{z}_{\boldsymbol{2}}(t) = \boldsymbol{C}_{\boldsymbol{2}}\boldsymbol{x}_{\boldsymbol{2}}(t) + \boldsymbol{v}_{\boldsymbol{2}}(t) \tag{3.15}$$

where $\boldsymbol{x}_{\boldsymbol{2}} = \begin{bmatrix} \boldsymbol{\theta} & \dot{\boldsymbol{\theta}} & \ddot{\boldsymbol{\theta}} \end{bmatrix}^\top$. The white, zero-mean Gaussian noise $\boldsymbol{w}_{\boldsymbol{2}}(t)$ is a surrogate for the jerk $\boldsymbol{\theta}^{[\boldsymbol{3}]}$, which must be considered as a wide-band signal for better reconstruction. Its covariance $\boldsymbol{Q}_{\boldsymbol{2}}$ may be regarded as a filtre parameter to be adjusted. $\boldsymbol{v}_{\boldsymbol{2}}(t)$ represents the quantisation error, which is assumed to be white, zero-mean, and of constant variance $\boldsymbol{R}_{\boldsymbol{2}}$. The matrices $\boldsymbol{A}_{\boldsymbol{2}}$, $\boldsymbol{C}_{\boldsymbol{2}}$ and $\boldsymbol{\Gamma}_{\boldsymbol{2}}$ are defined by the following equations:

$$\boldsymbol{A}_{\boldsymbol{2}} = \begin{bmatrix} 0 & \boldsymbol{I} & 0 \\ 0 & 0 & \boldsymbol{I} \\ 0 & 0 & 0 \end{bmatrix} \quad \boldsymbol{C}_{\boldsymbol{2}} = \begin{bmatrix} \boldsymbol{I} & 0 & 0 \end{bmatrix} \quad \boldsymbol{\Gamma}_{\boldsymbol{2}} = \begin{bmatrix} 0 \\ 0 \\ \boldsymbol{I} \end{bmatrix}$$

Therefore, systems (3.12–3.13) and (3.14–3.15) can be merged by incorporating the joint position, velocity and acceleration as part of the state and reconstructing the latter from the encoder measurement:

$$\dot{\boldsymbol{x}}(t) = \boldsymbol{A}\boldsymbol{x}(t) + \boldsymbol{w}(t) \tag{3.16}$$

$$\boldsymbol{z}(t) = \boldsymbol{C}\boldsymbol{x}(t) + \boldsymbol{v}(t) \tag{3.17}$$

where $\boldsymbol{x} = \begin{bmatrix} \boldsymbol{\theta} & \dot{\boldsymbol{\theta}} & \ddot{\boldsymbol{\theta}} & \boldsymbol{\delta e} & \dot{\boldsymbol{\delta e}} \end{bmatrix}^\top$, $\boldsymbol{z} = \begin{bmatrix} \boldsymbol{\theta}_{\boldsymbol{meas}} & \boldsymbol{\delta\xi}_{\boldsymbol{high}} \end{bmatrix}^\top$, $\boldsymbol{w}(t)$ and $\boldsymbol{v}(t)$ are zero-mean white Gaussian noises whose covariances are $\boldsymbol{Q}$ and $\boldsymbol{R}$, respectively:

$$\boldsymbol{Q} = \begin{bmatrix} \boldsymbol{\Gamma}_{\boldsymbol{2}}\,\boldsymbol{Q}_{\boldsymbol{2}}\,\boldsymbol{\Gamma}_{\boldsymbol{2}}^\top & 0 \\ 0 & \boldsymbol{Q}_{\boldsymbol{1}} \end{bmatrix} \qquad \boldsymbol{R} = \begin{bmatrix} \boldsymbol{R}_{\boldsymbol{2}} & 0 \\ 0 & \boldsymbol{R}_{\boldsymbol{1}} \end{bmatrix}$$

The matrices $\boldsymbol{A}$ and $\boldsymbol{C}$ are defined by the following equations:

$$\boldsymbol{A} = \left[\begin{array}{cc|c} \multicolumn{2}{c|}{\boldsymbol{A}_{\boldsymbol{2}}} & 0_{(3n\times 2m)} \\ \hline 0_{(2m\times 2n)} & \multicolumn{1}{|c|}{\boldsymbol{B}_{\boldsymbol{1}}} & \boldsymbol{A}_{\boldsymbol{1}} \end{array}\right] \qquad \boldsymbol{C} = \left[\begin{array}{c|c} \boldsymbol{C}_{\boldsymbol{2}} & 0_{(n\times 2m)} \\ \hline 0_{(1\times 3n)} & \boldsymbol{C}_{\boldsymbol{1}} \end{array}\right]$$

In order to verify the state observability of the system (3.16–3.17), let us calculate the observability matrix $\boldsymbol{\mathcal{O}} \in \mathbb{R}^{(n+r)(3n+2m)\times(3n+2m)}$ defined by:

$$\boldsymbol{\mathcal{O}} = \begin{bmatrix} \boldsymbol{C} \\ \boldsymbol{CA} \\ \boldsymbol{CA}^2 \\ \vdots \\ \boldsymbol{CA}^{3n+2m-1} \end{bmatrix} = \left[\begin{array}{ccccc} \boldsymbol{I} & 0 & 0 & 0 & 0 \\ 0 & 0 & 0 & \boldsymbol{L_\xi J_e} & 0 \\ \hline 0 & \boldsymbol{I} & 0 & 0 & 0 \\ 0 & 0 & 0 & 0 & \boldsymbol{L_\xi J_e} \\ \hline 0 & 0 & \boldsymbol{I} & 0 & 0 \\ \vdots & \vdots & \vdots & \vdots & \vdots \end{array}\right] \tag{3.18}$$

The rank of $\boldsymbol{\mathcal{O}}$ is the size of the largest collection of linearly independent columns or rows. From its first $3n + 2r$ rows, it is clear that $\boldsymbol{\mathcal{O}}$ is of rank $3n + 2m$ if and only if $\boldsymbol{L_\xi J_e}$ has full rank m. As stated in section 2.3.2, only three points are necessary to control a six-DOF manipulator. However, in this case, there will exist configurations for which $\boldsymbol{L_\xi}$ is singular. For this reason, more than three points are usually considered. Consequently, if the r visual features are chosen so $\boldsymbol{L_\xi J_e}$ has full rank ($m \leq 6$), then $\boldsymbol{\mathcal{O}}$ has full rank ($3n + 2m$) and the given system is completely state-observable. From here, a linear state observer can be designed using a discrete steady-state Kalman filter whose gains are optimised for the above assumed noises.

3.1.3 Incorporation of delayed measurements in the Kalman filter

Let us consider that the linear discrete system derived from the continuous system (3.16–3.17) is observed by non-delayed measurements where the process and measurements are both influenced by additive Gaussian noises:

$$\boldsymbol{x_{k+1}} = \boldsymbol{A_k x_k} + \boldsymbol{w_k} \tag{3.19}$$

$$\boldsymbol{z_k} = \boldsymbol{C_k x_k} + \boldsymbol{v_k} \tag{3.20}$$

where the noise $\boldsymbol{v_k}$ and $\boldsymbol{w_k}$ are independent (respective constant variances $\boldsymbol{R}$ and $\boldsymbol{Q}$). $\boldsymbol{A_k}$ is assumed to be invariant ($\boldsymbol{A_k} = \boldsymbol{A}$).

The optimal state estimator minimising the variance of the estimation error will then be a Kalman filter:

$$\boldsymbol{\hat{x}_k^-} = \boldsymbol{A\hat{x}_{k-1}^+} \tag{3.21}$$

$$\boldsymbol{P_k^-} = \boldsymbol{AP_{k-1}^+A}^\top + \boldsymbol{Q} \tag{3.22}$$

$$\boldsymbol{K_k} = \boldsymbol{P_k^- C_k}^\top[\boldsymbol{C_k P_k^- C_k}^\top + \boldsymbol{R}]^{-1} \tag{3.23}$$

$$\boldsymbol{\hat{x}_k^+} = \boldsymbol{\hat{x}_k^-} + \boldsymbol{K_k}[\boldsymbol{z_k} - \boldsymbol{C_k\hat{x}_k^-}] \tag{3.24}$$

$$\boldsymbol{P_k^+} = [\boldsymbol{I} - \boldsymbol{K_k C_k}]\boldsymbol{P_k^-} \tag{3.25}$$

Compared to other kinds of sensors used in robotics, vision devices have the disadvantage of a long processing time. This leads not only to delayed measurements but also to potentially low update rates. In this work, the visual data measurement $\boldsymbol{\delta\xi_{high}}$ is delayed by about one sample and is updated approximately every 60–70 ms (sometimes 100 ms) depending on the load of the supervisor computer that runs a non-real-time operating system (OS). On the other hand, the estimation of $\boldsymbol{\delta e}$ is expected to be performed at the servo rate, i.e. every 10 ms.

To overcome these two issues, the method described in [372] should be followed and the results should be extended using the following proposals. A two-timescale Kalman filter composed of four blocks is considered (see Fig. 3.3).

- Block #1: the time update equations (3.21) and (3.22) are executed at the servo rate; these estimate the state variables as quickly as needed to achieve a stable and accurate control.
- Block #2: the measurement update equations (3.23), (3.24) and (3.25) corresponding to the optical encoder measurement are also executed at the servo rate; these correct the state estimation regarding the measured articular position.
- Block #3: an adaptable delay compensator [forthcoming equation (3.27)] extrapolates the measured visual data to the present time using past and present estimates.
- Block #4: the camera measurement update equations [forthcoming equations (3.28), (3.29) and (3.30)] are executed at the visual data refresh rate; these refine the state estimation regarding the measured image features displacement.

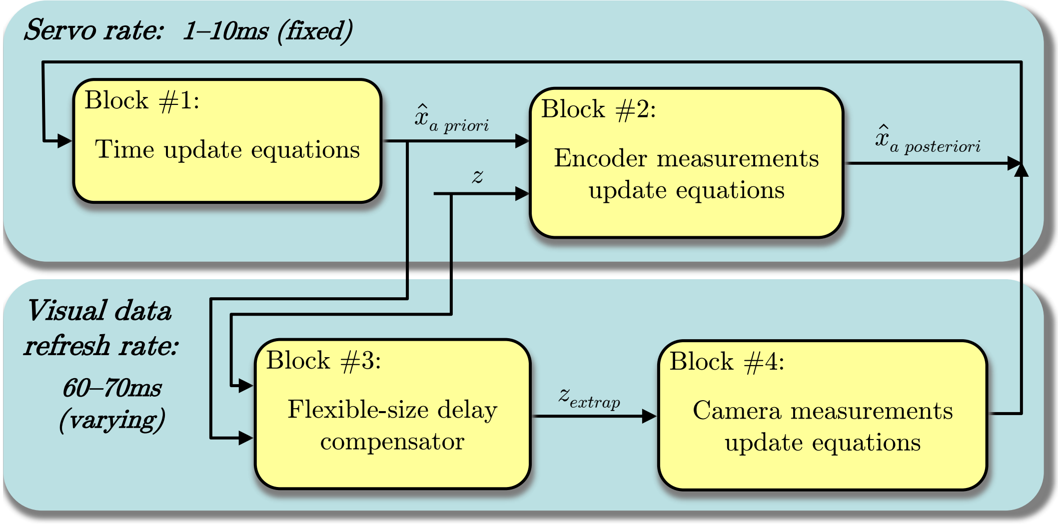

Figure 3.3: Modified Kalman filter

An important point to be noted is that the time update equations, which are intrinsically stable, never stop predicting the state vector. As a result, this method is robust against practical limitations, such as a limited field of view, partial occlusions or camera failure.

In order to avoid phase-lag between the real state and the estimated state, it is necessary to consider the delay due to the visual features' processing time. To that end, one can use a delay compensator that extrapolates the measured output to the present time using past and present estimates. The delay is assumed constant in [62], which is quite limiting. When the visual data processing application runs on a non-real-time OS, the delay can vary significantly and it is almost impossible to predict if previous measurements are fused in this delay period. Therefore, the method proposed by [62] has been adapted in order to obtain a variable delay compensator.

Let us consider that the output corresponding to the visual data in system (3.19–3.20) is delayed by an indeterminate number of samples ΔN. The new output equation is:

$$\boldsymbol{z_k^*} = \boldsymbol{C_s^*}\boldsymbol{x_s} + \boldsymbol{v_k}^* \tag{3.26}$$

where the covariance of $\boldsymbol{v_k^*}$ is $\boldsymbol{R}^*$ and $s = k - \Delta N$. This delayed measurement cannot be fused using the regular Kalman filter equations (3.21–3.25), but it requires some modifications in the structure of the filter. If the measurement $\boldsymbol{z_k^*}$ is delayed by ΔN samples and fused at time k, the data update should reflect the fact that the ΔN data updates from time s to k. Therefore, the state and covariance estimates have all been affected by the delay. A new optimal Kalman gain is computed in order to minimise the variance of the estimation error that is also affected by the delay. The measurement update equations of this modified discrete-time Kalman filter can then be written:

$$\begin{aligned}
\boldsymbol{z_k^{ext}} &= \boldsymbol{z_k^*} + \boldsymbol{C_k^*}\boldsymbol{\hat{x}_k} - \boldsymbol{C_s^*}\boldsymbol{\hat{x}_s} && (3.27)\\
\boldsymbol{K_k} &= \boldsymbol{M_*}\boldsymbol{P_s}\boldsymbol{C_s^*}^\top[\boldsymbol{C_s^*}\boldsymbol{P_s}\boldsymbol{C_s^*}^\top + \boldsymbol{R}^*]^{-1} && (3.28)\\
\boldsymbol{\hat{x}_k^+} &= \boldsymbol{\hat{x}_k^-} + \boldsymbol{K_k}[\boldsymbol{z_k^{ext}} - \boldsymbol{C_k}\boldsymbol{\hat{x}_k^-}] && (3.29)\\
\boldsymbol{P_k^+} &= \boldsymbol{P_k^-} - \boldsymbol{K_k}\boldsymbol{C_s^*}\boldsymbol{P_s}\boldsymbol{M_*}^\top && (3.30)
\end{aligned}$$

where:

$$\boldsymbol{M_*} = \begin{cases} \boldsymbol{I} & \text{if } \Delta N = 0 \\ \displaystyle\prod_{i=0}^{\Delta N-1} \left(\boldsymbol{I} - \boldsymbol{K'_{k-i}}\boldsymbol{C_{k-i}}\right)\boldsymbol{A} & \text{if } \Delta N > 0 \end{cases} \tag{3.31}$$

The prime on K' means that these Kalman gain matrices have been calculated using a covariance matrix updated at time s with the covariance of the delayed measurement.

This method guarantees all time-optimality and limits the computational burden, in contrast to other approaches [373]. From a practical point of view, it should be noted that the measurement equations of blocks #2 and #4 can be merged and executed together when the visual data is updated.

In this section, a dynamical model of the arm's vibrational behaviour has been established.

Its output is the reconstructed measurement of the tip deflection to be controlled. The model inputs are the measurements of the joint angle and the environmental fast movement seen by the camera. The following subsection will explain how this measurement is derived from the camera images.

3.1.4 Tracking features from the environment

In order to evaluate the velocity of the environment in camera-base coordinates and therefore deduce the velocity of the camera in the static environment coordinate system, the KLT feature-tracking algorithm has been implemented. It is assumed that no a priori knowledge on the environment is available and that no markers have been placed in this environment.

As the manipulator and its tip-mounted camera move, the patterns of image intensities change in a complex way. This image motion can be represented by an affine motion field $\boldsymbol{\delta\xi} = \boldsymbol{D\xi} + \boldsymbol{d}$ where $\boldsymbol{D}$ is a deformation matrix and $\boldsymbol{d}$ is the translation of the window's centre. The tracking goal is to select a pool of features and determine the parameters that appear in the deformation matrix $\boldsymbol{D}$ and the displacement vector $\boldsymbol{d}$.

Feature selection in image processing usually deals with extracting attributes resulting in some quantitative information of interest. An appropriate feature is a textured patch with high-intensity variations in both x and y directions, e.g. a corner or an edge. The particularity of the KLT algorithm (see section 2.3.4) lies in the fact that it is designed to select features that are more than traditional "interest" measures, which are often based on a preconceived and arbitrary idea of what a suitable feature is; therefore, the features are not guaranteed to be the most reliable for the tracking algorithm. On the contrary, the selection criterion of the KLT tracker is defined suitably with the tracking method; consequently, it selects the features that make the tracker work best. As a result, the selection criterion is optimal by construction and makes KLT trackers extremely robust.

When tracking the selected features through a sequence of images, the algorithm defines a measure of dissimilarity that quantifies each feature's change in appearance between the first and the current image. If it has changed too much, it is discarded (see Fig. 3.4). When features are lost, the proposed algorithm replaces them by finding new features in the next image in order to keep a constant pool of features. To ensure that the newly detected features do not correspond to already detected features, a mask image containing the current pool of tracked features is built; new features that match this mask are filtered out. To avoid optical distortion, features in the image borders are also discarded. Last, a minimum distance between the extracted features is set to secure a representative estimation of the environment displacement (to be discussed in section 3.1.5).

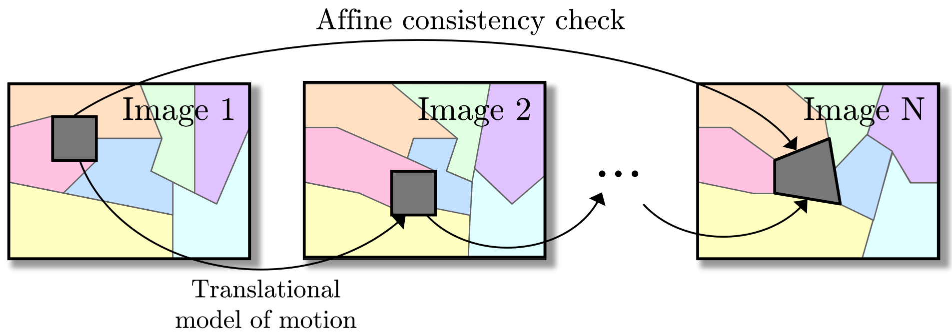

Figure 3.4: Tracking method

As shown in Fig. 3.5, the spatial distribution of the tracked features tends to be relatively regular due to the above-mentioned minimum distance between them. In addition, the selected features are concentrated in the centre of the image.

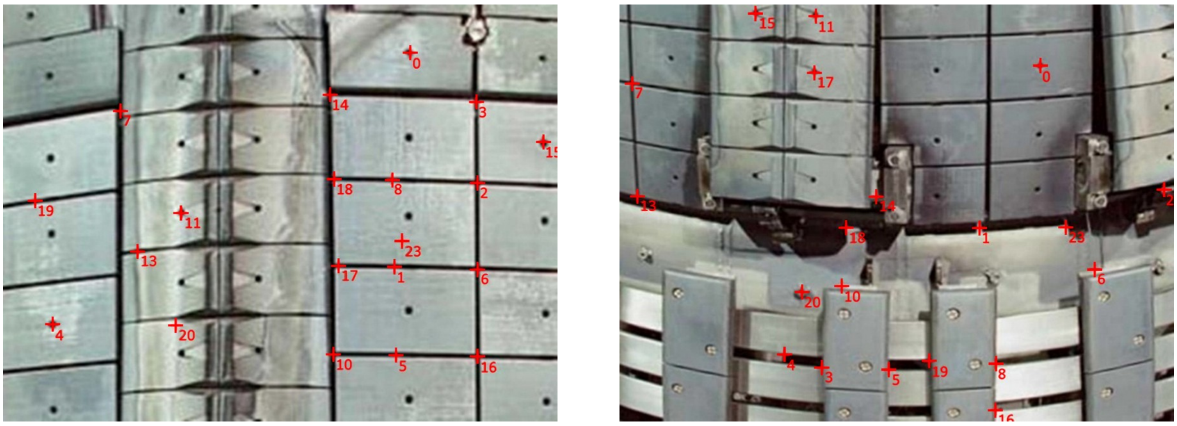

(a)

(b)

Figure 3.5: Examples of tracked features in an unknown and "untrimmed" environment (close-ups of the JET ITER-like wall)

Thanks to this KLT algorithm, visual features are tracked from one image to the other. A set of $2 \times r$ coordinates corresponding to the r tracked features is obtained for each image.

3.1.5 Robust estimation of feature displacement

As stated in section 3.1.1, the quality of the vibration reconstruction is based on the accuracy of the environment displacement measurement. Indeed, because of the feature extraction noise, outliers can corrupt the state observer and the $\boldsymbol{L}_{\boldsymbol{\xi}}$ estimator. Robust statistics is employed to minimise the influence of these outliers. This makes it possible to recover the structure that best fits the majority of the data while identifying and rejecting deviating substructures.

M-estimators can be considered a more general form of maximum likelihood estimators (MLE) because they permit the use of different minimisation functions that do not necessarily correspond to normally distributed data. This class of estimators can be written as:

$$\hat{\boldsymbol{\delta\xi}} = \underset{\boldsymbol{\delta\xi}}{\operatorname{argmin}} \left[\sum_{i=1}^{r} \Lambda(\boldsymbol{\delta X_i}, \boldsymbol{\delta\xi}) \right] \tag{3.32}$$

where Λ is an influence function (Huber's, Cauchy's, etc.). Tukey's influence function has been chosen to obtain a proper estimation of the environment displacement in the image:

$$\Lambda(\chi) = \begin{cases} \frac{1}{6}[1-(1-\chi^2)^3] & \text{if } |\chi| \leq 1 \\ \frac{1}{6} & \text{if } |\chi| > 1 \end{cases} \tag{3.33}$$

where $\chi = \frac{\delta X - \delta\xi}{h \times MAD}$. MAD represents the median absolute deviation estimator and h is a tuning parameter that adjusts the asymptotic efficiency of the obtained M-estimator. This influence function completely rejects outliers by giving them a zero weight. This prevents detected outliers from having any effect on $\hat{\boldsymbol{\delta\xi}}_{\boldsymbol{high}}$, which is particularly suitable for this work. The output of the above-described M-estimator is $\hat{\boldsymbol{\delta\xi}}$, which can be filtered and used as one of the two inputs of the Kalman filter described in sections 3.1.1, 3.1.2 and 3.1.3.

3.1.6 Online interaction matrix estimator

The vibration estimator built in section 3.1.1 assumes that the velocity of the tip camera can be related to the velocity of the image features through the interaction matrix.

As mentioned in section 2.3.1, analytically determining this matrix is not simple. The camera's intrinsic parameters (focal distance, image centre coordinates, aspect ratio, distortion coefficients) and the depth estimation (translations and rotations between the camera and the features) must be considered.

Several online interaction matrix estimators have been proposed to deal with changing or unknown environments (see section 2.3.2). In these methods, the matrix is estimated recursively by simply observing the process without using any a priori model or introducing any extra calibration movements.

The estimation of the interaction matrix using the Broyden method [374] is an underdetermined problem. A family of solutions can be chosen as Broyden updating formulas. Among this infinite number of solutions, [334] proposes an estimator that can be formulated as:

$$\hat{\boldsymbol{L}}_{\boldsymbol{\xi,t}} - \hat{\boldsymbol{L}}_{\boldsymbol{\xi,t-dt}} = \frac{(\boldsymbol{\delta\xi_{low,t}} - \hat{\boldsymbol{L}}_{\boldsymbol{\xi,t-dt}}\boldsymbol{\Delta\theta_t})\ \boldsymbol{\Delta\theta_t}^{\top}\ \boldsymbol{W_t J_\theta^+}}{\varrho + \boldsymbol{\Delta\theta_t}^{\top}\ \boldsymbol{W_t}\ \boldsymbol{\Delta\theta_t}} \tag{3.34}$$

where $\boldsymbol{\Delta\theta_t} = \boldsymbol{\theta_t} - \boldsymbol{\theta_{t-dt}}$. $\boldsymbol{W}(t)$ and $\varrho(0 \leq \varrho \leq 1)$ denote a full-rank weighting matrix and a forgetting factor, respectively. Its goal is not to estimate the true parameters of $\boldsymbol{L_\xi}$ but to provide an estimation $\boldsymbol{\hat{L}_\xi}$ that satisfies the following relation at any time:

$$\boldsymbol{\dot{\xi}_{low}} = \boldsymbol{\hat{L}_\xi J_\theta \dot{\theta}} \tag{3.35}$$

For this reason, the estimated parameters do not necessarily converge with the true physical values.

Nevertheless, the estimation algorithm would display improved stability if it considered data over a period of time instead of just the previous iteration. To that end, "population-based" methods [375] have been introduced for calibrating a linear model based on several previous iterates. This can be easily accomplished using a recursive least squares (RLS) algorithm with exponential data weighting that minimises a cost function based on the change in the affine model. This is achieved by adopting the covariance matrix $\boldsymbol{P}(t - dt)$ as the weighting matrix $\boldsymbol{W}(t)$:

$$\boldsymbol{\hat{L}_{\xi,t}} = \boldsymbol{\hat{L}_{\xi,t-dt}} + \frac{(\boldsymbol{\Delta\xi_{low,t}} - \boldsymbol{\hat{L}_{\xi,t-dt}\Delta\theta_t})\ \boldsymbol{\Delta\theta_t}^\top\ \boldsymbol{P_{t-dt}J_\theta^+}}{\varrho + \boldsymbol{\Delta\theta_t}^\top\ \boldsymbol{P_{t-dt}}\ \boldsymbol{\Delta\theta_t}} \tag{3.36}$$

Here, $\boldsymbol{P}(t)$ denotes a covariance matrix:

$$\boldsymbol{P_t} = \frac{1}{\varrho}\left(\boldsymbol{P_{t-dt}} - \frac{\boldsymbol{P_{t-dt}}\ \boldsymbol{\Delta\theta_t}\ \boldsymbol{\Delta\theta_t}^\top\ \boldsymbol{P_{t-dt}}}{\varrho + \boldsymbol{\Delta\theta_t}^\top\ \boldsymbol{P_{t-dt}}\ \boldsymbol{\Delta\theta_t}}\right) \tag{3.37}$$

As shown previously, the behaviour of this method depends on the forgetting parameter ϱ, which can be tuned from 0 to 1 and ponders previous movements. ϱ compromises between information provided by old data from previous movements and new data that is possibly corrupted by noise. This kind of RLS algorithm has a memory approximately equal to $\frac{1}{1-\varrho}$. Strictly speaking, the proposed estimator is valid only when $\boldsymbol{L_\xi}$ is time-invariant, but the proposed forgetting factor ϱ makes this method valid when the system moves slowly.

In [376], a novel approach for uncalibrated visual servoing was presented. This approach uses an RLS algorithm with a modified stabilising term in (3.37) only, which depends linearly on $\boldsymbol{P_{t-dt}}$.

Surprisingly, no previous work has proposed adopting an adaptive forgetting factor in (3.36) and (3.37). Therefore, a memory term $\varrho(\boldsymbol{\dot{\theta}})$ that self-adjusts—exactly as a gain-scheduling technique would do in control theory—depending on the range of camera motion should be considered and set as follows:

- If the camera does not move ($\boldsymbol{J_\theta\dot{\theta}} \simeq 0$), ϱ is set at 1. The new information is averaged with all past data, and the system is not very sensitive and is very stable.

- If the camera moves fast ($\boldsymbol{J_\theta}\dot{\boldsymbol{\theta}} \gg 0$), ϱ is set close to 0. The system only becomes sensitive to observed data.
- Between these two extreme cases, ϱ varies linearly between 1 and 0. The old data are weighed less and less, and the estimator tracks the time-varying interaction matrix.

This method performs a robust estimation of the image interaction matrix with a quite low sensitivity to noise and a relatively high repeatability. This adaptive algorithm demonstrates high stability and improves sensibility to sudden camera movements compared to classic fixed-parameters, Broyden-based methods.

3.1.7 Controller design

The control problem is to determine the torque vector $\boldsymbol{\delta\tau}$ such that the joint rotation vector $\boldsymbol{\theta}$ tracks the desired trajectory $\boldsymbol{\theta_d}$ with a suitable accuracy while $\boldsymbol{\delta e}$ converges to zero as quickly as possible. For this reason, each joint can be regarded as a single-input multiple-output (SIMO) system. A common approach in the control of such systems involves the design of LQR controllers. To that end, the linear state-space representation of the entire flexible arm, including rigid and flexible modes, is used. The following can be deduced from (3.5):

$$\dot{\boldsymbol{x}}(t) = \underbrace{\begin{bmatrix} 0 & \boldsymbol{I} \\ -\boldsymbol{M}^{-1}\boldsymbol{K} & 0 \end{bmatrix}}_{\boldsymbol{A_c}} \boldsymbol{x}(t) + \underbrace{\begin{bmatrix} 0 \\ -\boldsymbol{M}^{-1}\boldsymbol{U} \end{bmatrix}}_{\boldsymbol{B_c}} \boldsymbol{\delta\tau}(t) \tag{3.38}$$

$$\boldsymbol{y_c}(t) = \underbrace{\begin{bmatrix} \boldsymbol{I} & 0 & 0 & 0 \end{bmatrix}}_{\boldsymbol{C_c}} \boldsymbol{x}(t) \tag{3.39}$$

with $x = [\boldsymbol{\theta}\ \boldsymbol{\delta e}\ \dot{\boldsymbol{\theta}}\ \dot{\boldsymbol{\delta e}}]^\top$.

In order to verify the state controllability of the system (3.38–3.39), let us calculate the controllability matrix $\boldsymbol{\mathcal{C}} \in \mathbb{R}^{(2n+2m)\times n(2n+2m)}$ defined by:

$$\begin{aligned} \boldsymbol{\mathcal{C}} &= \begin{bmatrix} \boldsymbol{B_c} & \boldsymbol{A_c}\boldsymbol{B_c} & \boldsymbol{A_c}^2\boldsymbol{B_c} & \dots & \boldsymbol{A_c}^{2n+2m-1}\boldsymbol{B_c} \end{bmatrix} \\ &= \left[\begin{array}{c|c|c|c} 0 & -\boldsymbol{M}^{-1}\boldsymbol{U} & \dots & -(-\boldsymbol{M}^{-1}\boldsymbol{K})^{n+m-1}\boldsymbol{M}^{-1}\boldsymbol{U} \\ -\boldsymbol{M}^{-1}\boldsymbol{U} & 0 & \dots & 0 \end{array}\right] \end{aligned} \tag{3.40}$$

The rank of $\boldsymbol{\mathcal{C}}$ is the size of the largest collection of linearly independent columns or rows. It is clear that $\mathrm{rank}(\boldsymbol{B_c}) = \mathrm{rank}(\boldsymbol{A_c}\boldsymbol{B_c}) = n$. As far as the other columns of $\boldsymbol{\mathcal{C}}$ are concerned, two cases are to be considered:

- if $n \geq m$, then $\mathrm{rank}(\boldsymbol{A_c}^2\boldsymbol{B_c}) = \mathrm{rank}(\boldsymbol{A_c}^3\boldsymbol{B_c}) = m$; consequently, one obtains $\mathrm{rank}(\boldsymbol{\mathcal{C}}) = \mathrm{rank}([\boldsymbol{B_c}\ \boldsymbol{A_c}\boldsymbol{B_c}\ \boldsymbol{A_c}^2\boldsymbol{B_c}\ \boldsymbol{A_c}^3\boldsymbol{B_c}]) = 2n + 2m$; and

- if $n < m$, then $\text{rank}(\boldsymbol{A_c}^k \boldsymbol{B_c}) = n$ for $k \in [2, 2n+2m-1]$; since $n(2n+2m)-2n \geq 2m$ for all positive integers n and m, one obtains $\text{rank}(\boldsymbol{\mathcal{C}}) = 2n + 2m$.

Consequently, $\boldsymbol{\mathcal{C}}$ has full rank $(2n + 2m)$ and the pair $(\boldsymbol{A_c}, \boldsymbol{B_c})$ is controllable.

LQR techniques involve choosing a control law $\boldsymbol{\delta\tau} = \boldsymbol{L_1 y_c} - \boldsymbol{L_2 x}$ that stabilises the controlled output vector $\boldsymbol{y_c}$ to its desired values $\boldsymbol{y_d} = \boldsymbol{\theta_d}$ while minimising the quadratic cost function:

$$\mathcal{J} = \int_0^\infty \left(\boldsymbol{X}(t)^\top \boldsymbol{Q_{LQR}} \boldsymbol{X}(t) + \boldsymbol{\delta\tau}(t)^\top \boldsymbol{R_{LQR}} \boldsymbol{\delta\tau}(t)\right) dt \tag{3.41}$$

where the penalty matrices $\boldsymbol{Q_{LQR}}$ and $\boldsymbol{R_{LQR}}$ are symmetric, positive, semidefinite and symmetric, positive, definite matrices, respectively. The optimisation horizon for the summation is the stopping time step for the cost function.

Due to the coupled dynamics of the arm, the control of the low-dynamic rigid motion subsystem will be made much easier if the fast-dynamic elastic vibration subsystem is controlled as quickly as possible. Consequently, the component of $\boldsymbol{Q_{LQR}}$ related to $\boldsymbol{\delta e}$ (and $\boldsymbol{\delta \dot{e}}$) must be chosen to be large in comparison with those related to $\boldsymbol{\theta}$ (and $\boldsymbol{\dot{\theta}}$).

Finding $\boldsymbol{L_1}$ and $\boldsymbol{L_2}$ that minimise $\mathcal{J}$ involves solving the following Riccati equation [377]:

$$\boldsymbol{Y A_c} + \boldsymbol{A_c}^\top \boldsymbol{Y} - \boldsymbol{Y B_c R_{LQR}}^{-1} \boldsymbol{B_c}^\top \boldsymbol{Y} + \boldsymbol{Q_{LQR}} = 0 \tag{3.42}$$

where $\boldsymbol{Y}$ is the $2(n + m) \times 2(n + m)$ matrix to be determined.

Finally, the feed-forward and feedback matrices $\boldsymbol{L_1}$ and $\boldsymbol{L_2}$ can be set as follows:

$$\boldsymbol{L_2} = \boldsymbol{R_{LQR}}^{-1} \boldsymbol{B_c}^\top \boldsymbol{Y} \tag{3.43}$$

$$\boldsymbol{L_1} = \left(\boldsymbol{C_c}(\boldsymbol{A_c} - \boldsymbol{B_c L_2})^{-1} \boldsymbol{B_c}\right)^{-1} \tag{3.44}$$

Fig. 3.6 illustrates the entire control scheme, including the vibration estimator and the LQR controller.

3.2 Advanced model of a rotating bending beam

An all-in-one method was proposed in the previous section to solve the problem of vibration suppression using visual features without any markers or a priori knowledge of the environment. The tip displacement induced by vibrations is estimated by exploiting a simple physical model of the manipulator. Using a camera mounted in an eye-in-hand configuration, this model is readjusted using direct measurement of the tip oscillations with respect to the static environment. Since the joint torque is the only available input to make the arm follow the desired trajectory while the tip deflection converges to zero,

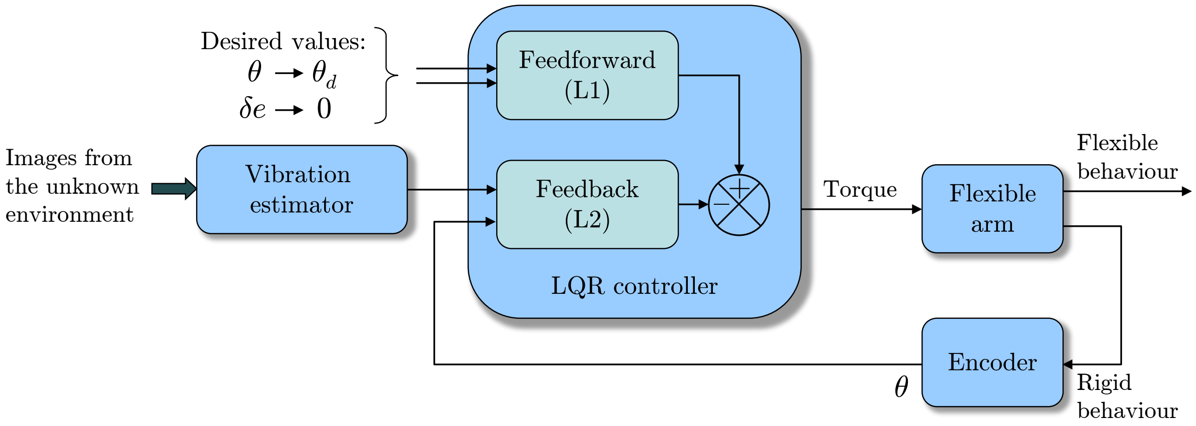

Figure 3.6: Diagram of the control scheme

a LQR has been chosen to address the control problem.

When a vibration occurs, sudden transient articular accelerations are applied to the system to damp the oscillations. However, if the proposed method yields globally satisfactory results (see section 4.2), one unforeseen effect of such a control is the impact on the beam behaviour of previously neglected inertia terms.

The primary objective in this section, which builds on the results of [64], is to remedy that problem by considering these additional terms in the derivation of the dynamic model of the manipulator. This change should make the overall scheme more efficient by decreasing the prediction error.

A considerable amount of theoretical and experimental research has been carried out over the last decade on obtaining exact multimode dynamic models for flexible-link manipulators (see section 2.1.2). Their derivation through energetic considerations often yields a set of non-linear equations that are accurate but not implementable easily in real-time applications. Consequently, this section endeavours to obtain a computationally light model without making any detrimental compromises to its accuracy. Manufacturers now provide industrial viewing systems that can achieve framerates up to 250fps. Even by narrowly respecting the Nyquist–Shannon sampling theorem [378], the vision-based method described previously would allow observation of up to three or four modes within the 0–100 Hz range.

The following sections are organised as follows. Section 3.2.1 derives the equation of motion and boundary conditions of a loaded, flexible beam rotating freely in a vertical plane. The beam's natural frequencies and mode shapes are obtained in section 3.2.2. Section 3.2.3 demonstrates the orthogonality of the mode shapes. Next, 3.2.4 establishes the dynamic response of the rotating flexible beam using the eigenfunction expansion method. In section 3.2.5, the state observer obtained in section 3.1.3 is modified in order to consider this new model.

3.2.1 Equation of motion and boundary conditions

Due to its slender design, the link is modelled by a homogeneous and isotropic rotating beam of length L. Its density and Young's modulus are denoted ρ and E, respectively. Its moment of inertia I and cross-section S are constant. The beam is free to rotate in a vertical plane and bends longitudinally; however, it is considered stiff in lateral bending and in torsion. In addition, the beam is subjected to its own weight and a tip load is attached to its free end. It is assumed to be rigidly attached to a rotating frame subjected to an external torque $\boldsymbol{\tau}(t)$.

One could choose to include $\boldsymbol{\tau}$ as an external force acting on the system. Instead, it is considered that $\boldsymbol{\tau}$ only affects the rotating rigid frame while the beam is only subjected to gravity and inertia forces. This choice, already made in section 3.1.1, is particularly relevant when it is easier to measure $\ddot{\boldsymbol{\theta}}$ as the model input rather than $\boldsymbol{\tau}$.

As in section 2.1.2, $v(t)$ is the transverse displacement away from the straight, undeflected position. In this section, $\boldsymbol{\tau}$, $\ddot{\boldsymbol{\theta}}$ and all the other link or joint variables are one-dimensional. Therefore, normal fonts are adopted instead of bold fonts for these variables for ease of reading.

From Euler-Bernoulli formalism, the governing differential equation of the beam motion is given by:

$$EIv''''(x,t) + \rho S\ddot{v}(x,t) + \rho Sx\ddot{\theta}(t) + \rho Sg\cos\theta = 0 \tag{3.45}$$

where " $'$ " represents the derivative operator regarding space and " $\dot{}$ " represents the derivative operator regarding time.

Without a loss of generality, this differential equation can be expressed around a given steady-state position. Such an equilibrium is characterised by the following equation:

$$EIv_0''''(x) + \rho Sg\cos\theta = 0 \tag{3.46}$$

where $v_0(x)$ represents the static deflection along x for a given joint position θ. The well-known analytic expression of $v_0(x)$ is given by:

$$v_0(x) = -\frac{M_p g\cos\theta x^2}{6EI}(3L - x) - \frac{\rho Sg\cos\theta x^2}{24EI}(x^2 + 6L^2 - 4Lx) \tag{3.47}$$

Let us consider $\delta v(x,t) = v(x,t) - v_0(x)$ as the deviation of v from its static value. Subtracting (3.46) from (3.45) provides the following simpler equation, in which the gravity term no longer appears:

$$EI\delta v''''(x,t) + \rho S\ddot{\delta v}(x,t) + \rho Sx\ddot{\delta\theta}(t) = 0 \tag{3.48}$$

The initial conditions of the problem can be deduced from the static case:

$$\delta v(x,0) = v(x,0) - v_0(x) = 0 \tag{3.49a}$$

$$\dot{\delta v}(x,0) = 0 \tag{3.49b}$$

$$\ddot{\delta v}(x,0) = 0 \tag{3.49c}$$

The boundary conditions to be satisfied by $v(x,t)$ in the dynamic case are mainly the same as those to be satisfied by $v_0(x)$ in the static case. Consequently, most of the boundary conditions regarding $\delta v(x,t)$ are null except the last one, which includes inertia terms:

$$\delta v(0,t) = 0 \tag{3.50a}$$

$$\delta v'(0,t) = 0 \tag{3.50b}$$

$$\delta v''(L,t) = 0 \tag{3.50c}$$

$$EI\delta v'''(L,t) = M_p \left(\ddot{\delta v}(L,t) + L\ddot{\delta\theta}(t)\right) \tag{3.50d}$$

Since condition (3.50d) is non-homogeneous, a new variable $w(x,t)$ is introduced and defined as follows:

$$w(x,t) = \delta v(x,t) + \underbrace{\left(\frac{2x^2}{L} - \frac{4x^3}{3L^2} + \frac{x^4}{3L^3}\right)}_{g(x)} \delta\theta \tag{3.51}$$

where $g(x)$ is chosen so that $g(0) = 0$, $g(L) = L$, $g'(0) = 0$, $g''(L) = 0$ and $g'''(L) = 0$.

This change of variable yields an homogeneous system of boundary conditions:

$$w(0,t) = \delta v(0,t) = 0 \tag{3.52a}$$

$$w'(0,t) = \delta v'(0,t) = 0 \tag{3.52b}$$

$$w''(L,t) = \delta v''(L,t) = 0 \tag{3.52c}$$

$$EIw'''(L,t) = M_p\ddot{w}(L,t) \tag{3.52d}$$

The new differential equation of motion is given by:

$$EIw''''(x,t) + \rho S\ddot{w}(x,t) = f(x,t) \tag{3.53}$$

with

$$f(x,t) = \frac{8EI}{L^3}\delta\theta(t) + \rho S(g(x) - x)\ddot{\delta\theta}(t) \tag{3.54}$$

The initial conditions for this new problem are then:

$$w(x,0) = g(x)\delta\theta_0 \tag{3.55a}$$

$$\dot{w}(x,0) = g(x)\delta\dot{\theta}_0 = 0 \tag{3.55b}$$

$$\ddot{w}(x,0) = g(x)\delta\ddot{\theta}_0 = 0 \tag{3.55c}$$

if one assumes that the beam is initially stationary.

The equation of motion, boundary conditions and initial conditions form an initial-boundary-value problem that can be solved using separation of variables and eigenfunction expansion.

3.2.2 Natural frequencies and mode shapes

Let us consider the homogeneous problem by setting $f(x,t) = 0$ in order to obtain the natural frequencies and the eigenfunctions. By splitting $w(x,t)$ into two functions such that $w(x,t) = W(x)\eta(t)$, the equation of motion (3.53) can be separated into two ordinary differential equations:

$$W''''(x) - k^4 W(x) = 0 \tag{3.56}$$

$$\ddot{\eta}(t) + \omega^2 \eta(t) = 0 \tag{3.57}$$

k is related to the angular frequency ω by the dispersion relation:

$$k^4 = \frac{\rho S}{EI}\omega^2 \tag{3.58}$$

which can be re-written into the expression of ω by introducing the dimensionless parameter λ:

$$\omega = \sqrt{\frac{EI}{\rho S}}\frac{\lambda^2}{L^2} \tag{3.59}$$

Equation (3.59) clearly shows that the natural frequencies in this model are the result of the competition between inertia forces and spring forces. The natural frequencies combine two terms:

- $\sqrt{\frac{E}{\rho}}$, which characterises the intrinsic properties of the material (elasticity E, density ρ), and can be seen as the speed of sound in the beam; and
- $\frac{1}{L^2}\sqrt{\frac{I}{S}}$, which characterises the geometry of the structure (length L, section S, inertia I).

The general solutions of (3.56) and (3.57) can be written using the following equations, respectively:

$$W(x) = a_1 \sin(kx) + a_2 \cos(kx) + a_3 \sinh(kx) + a_4 \cosh(kx) \tag{3.60}$$

$$\eta(t) = b_1 \cos(\omega t) + b_2 \sin(\omega t) \tag{3.61}$$

where a_1, a_2, a_3, a_4, b_1 and b_2 are constant coefficients.

Note that the boundary conditions can be expressed only in terms of the spatial function $W(x)$:

$$W(0) = 0 \tag{3.62a}$$

$$W'(0) = 0 \tag{3.62b}$$

$$W''(L) = 0 \tag{3.62c}$$

$$W'''(L) + \frac{M_p k^4}{\rho S} W(L) = 0 \tag{3.62d}$$

Considering that (3.60) must satisfy this set of boundary conditions, a linear system of four equations is obtained:

$$\begin{bmatrix} 0 & 1 & 0 & 1 \\ 1 & 0 & 1 & 0 \\ -\sin(kL) & -\cos(kL) & sh(kL) & ch(kL) \\ F_{41} & F_{42} & F_{43} & F_{44} \end{bmatrix} \begin{bmatrix} a_1 \\ a_2 \\ a_3 \\ a_4 \end{bmatrix} = \{0\}_{4\times1} \tag{3.63}$$

with

$$\begin{aligned} F_{41} &= -\cos(kL) + \frac{M_p k}{\rho S}\sin(kL) \\ F_{42} &= \sin(kL) \quad + \frac{M_p k}{\rho S}\cos(kL) \\ F_{43} &= ch(kL) \quad + \frac{M_p k}{\rho S} sh(kL) \\ F_{44} &= sh(kL) \quad + \frac{M_p k}{\rho S} ch(kL) \end{aligned}$$

The determinant of the above matrix must be null to avoid the trivial solution $\{0\}_{4\times1}$ for the coefficients to identify. The equation obtained by setting this determinant to 0 is the frequency equation:

$$1 + \cos(kL)ch(kL) + \frac{M_p k}{\rho S}\left(\cos(kL)sh(kL) - \sin(kL)ch(kL)\right) = 0 \tag{3.64}$$

which can only be solved for a discrete set of $\lambda_i = k_i L$. This infinite number of roots are dimensionless wave numbers, which can be translated into natural frequencies using

(3.59):

$$\omega_i = \sqrt{\frac{EI}{\rho S}\frac{\lambda_i^2}{L^2}} \tag{3.65}$$

The frequency equation (3.64) includes the ratio between the tip payload and the beam's own weight. Therefore, this relation could be simplified regarding the specific conditions of the achieved task.

The corresponding spatial solutions $W_i(x)$ are called eigenfunctions or mode shapes. Up to this point, the coefficients a_1, a_2, a_3 and a_4 are unique up to a multiplicative constant. This remaining constant is usually determined by normalising the mode shapes for convenience (see section 3.2.3).

By solving system (3.63) and keeping a_1 as the multiplicative constant, (3.60) becomes:

$$W_i(x) = a_1 \left(\sin(k_i x) - \sinh(k_i x)\right) - a_1 \frac{s_i + sh_i}{c_i + ch_i}\left(\cos(k_i x) - \cosh(k_i x)\right) \tag{3.66}$$

where c_i, s_i, ch_i and sh_i correspond to the constants $\cos(k_i L)$, $\sin(k_i L)$, $\cosh(k_i L)$ and $\sinh(k_i L)$, respectively. W_i denotes the i^{th} eigenfunction, which corresponds to the natural frequency ω_i. Since a_1 is an arbitrary constant, let us choose it so W_i can be written $W_i = \mathcal{A}_i \cdot Y_i$ where $Y_i(0) = 0$ and $Y_i(L) = 1$. This leads to the following:

$$a_1 = \mathcal{A}_i \frac{1}{2}\frac{c_i + ch_i}{sch_i - csh_i} \tag{3.67}$$

where sch_i and cch_i denote the constants $\sin(k_i L)\, ch(k_i L)$ and $\cos(k_i L)\, ch(k_i L)$, respectively.

Therefore, (3.66) becomes the following:

$$W_i(x) = \mathcal{A}_i \cdot Y_i(x) \tag{3.68}$$

with

$$Y_i(x) = \frac{1}{2}\frac{c_i + ch_i}{sch_i - csh_i}\left(\sin(k_i x) - \sinh(k_i x)\right) - \frac{1}{2}\frac{s_i + sh_i}{sch_i - csh_i}\left(\cos(k_i x) - \cosh(k_i x)\right) \tag{3.69}$$

3.2.3 Orthogonality conditions

In order to obtain the forced response of the beam, the eigenfunction expansion method is used. Therefore, the orthogonality conditions of the eigenfunctions must be established.

The spatial equation of the homogeneous problem (3.56) can be written using the operator formalism:

$$\mathcal{K}(W_i) = \omega_i^2 \mathcal{M}(W_i) \tag{3.70}$$

where the operators $\mathcal{K}$ and $\mathcal{M}$ are expressed by:

$$\mathcal{K}(W_i) = EI\frac{d^4W_i}{dx^4} \tag{3.71}$$

$$\mathcal{M}(W_i) = \rho S W_i \tag{3.72}$$

$\mathcal{K}$ and $\mathcal{M}$ are self-adjoint (with corresponding boundary conditions) if:

$$\int_0^L \left[W_i^\top \mathcal{K}(W_j) - W_j^\top \mathcal{K}(W_i)\right] dx = 0 \tag{3.73}$$

$$\int_0^L \left[W_i^\top \mathcal{M}(W_j) - W_j^\top \mathcal{M}(W_i)\right] dx = 0 \tag{3.74}$$

Note that condition (3.74) is automatically satisfied. Using (3.70), (3.73) can be written as:

$$(\omega_j^2 - \omega_i^2) \int_0^L W_i^\top \mathcal{M}(W_j) dx = 0 \tag{3.75}$$

Since $\omega_j^2 \neq \omega_i^2$ for $j \neq i$, the integral part of the above equation must be zero:

$$\int_0^L W_i^\top \mathcal{M}(W_j) dx = 0 \qquad \text{for } j \neq i \tag{3.76}$$

This is the orthogonality condition for the eigenfunctions. When $j = i$, the eigenfunctions can be normalised by setting the integral equal to 1:

$$\int_0^L W_i^\top \mathcal{M}(W_i) dx = 1 \qquad \text{for } i = 1, 2, 3... \tag{3.77}$$

Combining (3.75) and (3.76) leads to the following:

$$\int_0^L W_i^\top \mathcal{M}(W_j) dx = \delta_{ij} \tag{3.78}$$

where δ_{ij} is the Kronecker delta.
Choosing $\mathcal{A}_i$ so $||W_i|| = \int_0^L W_i^\top \mathcal{M}(W_i) dx = 1$ leads to the following:

$$\mathcal{A}_i^2 = \frac{4k\left(csh_i - sch_i\right)^2 / \rho S}{3\left(1 + cch_i\right)\left(csh_i - sch_i\right) + kL\left(s_i + sh_i\right)^2} \tag{3.79}$$

Finally, by substituting the expression for the operator $\mathcal{K}$ into (3.70) and integrating by parts twice, the boundary conditions satisfy the following relation:

$$\left[W_i W_j''' - W_j W_i'''\right]_0^L + \left[W_j' W_i'' - W_i' W_j''\right]_0^L = 0 \tag{3.80}$$

Therefore, in the boundary-value problem considered, $\mathcal{K}$ and $\mathcal{M}$ are self-adjoint operators and the eigenfunctions W_i are orthogonal to each other and define an orthonormal base of functions.

3.2.4 Dynamic response

The eigenfunction expansion method assumes that the solutions of equation (3.53) $w(x,t)$ and the forcing function $f(x,t)$ can both be represented as a summation of eigenfunctions (the spatial solution to the homogeneous problem) multiplied by functions of time that are still to be determined:

$$w(x,t) = \sum_{i=1}^{\infty} \eta_i(t) W_i(x) \tag{3.81}$$

$$f(x,t) = \sum_{i=1}^{\infty} f_i(t) \mathcal{M}(W_i(x)) \tag{3.82}$$

Although the functions $W_i(x)$ are already known, the time-dependent functions $\eta_i(t)$ must be found before solving the dynamic problem. The expressions for $\eta_i(t)$ can be obtained by applying the operator $\mathcal{M}$ to (3.81), multiplying it by $W_j^\top$ and integrating over the domain $(0 \leq x \leq L)$:

$$\int_0^L W_j^\top \mathcal{M}(w(x,t)) dx = \sum_{i=1}^{\infty} \eta_i \int_0^L W_j^\top \mathcal{M}(W_i) dx \tag{3.83}$$

Simplifications can be made using the orthonormality conditions given in (3.78):

$$\eta_i(t) = \int_0^L W_j^\top \mathcal{M}(w(x,t)) dx \tag{3.84}$$

Similarly, $f_i(t)$ can be found by multiplying (3.82) by $W_j^\top$ and integrating over the domain $(0 \leq x \leq L)$:

$$f_i(t) = \int_0^L W_j^\top f(x,t) dx \tag{3.85}$$

Developing $f(x,t)$ leads to the following:

$$f_i(t) = f_i(\delta\theta(t), \delta\ddot{\theta}(t)) = \alpha_i \delta\theta(t) + \beta_i \delta\ddot{\theta}(t) \tag{3.86}$$

with

$$\alpha_i = \int_0^L \frac{8EI}{L^3} W_i dx = \frac{8EI\mathcal{A}_i}{kL^3} \frac{(1 + cch_i - c_i - ch_i)}{(shc_i - sch_i)} \tag{3.87}$$

$$\begin{aligned}\beta_i &= \int_0^L \rho S\left(g(x)-x\right)W_i dx \\ &= \frac{\rho S\mathcal{A}_i}{k^5L^3}\frac{8\left(1+cch_i-c_i-ch_i\right)+k^3L^3\left(s_i+sh_i\right)}{\left(shc_i-sch_i\right)}\end{aligned} \tag{3.88}$$

Substituting the assumed solution (3.81) and the forcing function (3.82) into the equations of motion (3.53) leads to the following:

$$\sum_{i=1}^{\infty}\frac{d^2\eta_i(t)}{dt^2}\mathcal{M}(W_i(x))+\sum_{i=1}^{\infty}\eta_i(t)\mathcal{K}(W_i(x))=\sum_{i=1}^{\infty}f_i(t)\mathcal{M}(W_i(x)) \tag{3.89}$$

Then, using (3.70), multiplying by $W_j^{\top}(x)$ and integrating over the domain ($0 \leq x \leq L$) results in:

$$\frac{d^2\eta_j(t)}{dt^2}+\omega_i^2\eta_j(t)=F_j(t) \tag{3.90}$$

The initial conditions $\eta_i(0)$ and $[d\eta_i/dt]_{t=0}$ are obtained from the initial conditions regarding $w(x,0)$ and $\dot{w}(x,0)$, using (3.55a), (3.55b) and (3.84).

$$\begin{aligned}\eta_i(0) &= \int_0^L W_i^{\top}\mathcal{M}(w(x,0))dx \\ &= \frac{8\rho S\mathcal{A}_i\delta\theta_0\left(1+cch_i-c_i-ch_i\right)}{L^3K^5\left(shc_i-sch_i\right)}+\frac{\rho SL\mathcal{A}_i\delta\theta_0\left(1+cch_i\right)}{K\left(shc_i-sch_i\right)}\end{aligned} \tag{3.91}$$

$$\dot{\eta}_i(0)=\int_0^L W_i^{\top}\mathcal{M}(\dot{w}(x,0))dx=0 \tag{3.92}$$

Solving (3.90) yields:

$$\eta_i(t)=\underbrace{\frac{1}{\omega_i}\int_0^t f_i(\tau)\sin\omega_i(t-\tau)d\tau}_{(f_i(t)*\sin\omega_i t)}+\eta_i(0)\cos\omega_i t+\frac{1}{\omega_i}\left[\frac{d\eta_i}{dt}\right]_{t=0}\sin\omega_i t \tag{3.93}$$

Even though this expression is of no practical use, it is interesting to explicate its physical meaning. $\eta_i(t)$ is composed of two terms:

- the first term corresponds to the filtered generalised forces around the natural frequency ω_i; and
- the second term corresponds to the projection of the initial conditions into the modal base ($\cos\omega_i t$, $\sin\omega_i t$).

3.2.5 Modification of the internal model of the Kalman filter

As in [65], let us consider δe as the deviation of the tip deflection from its static values:

$$\delta e(t)=\delta v(L,t) \tag{3.94}$$

Using (3.51), (3.68) and (3.81), δe can be re-written as:

$$\delta e(t) = \sum_{i=1}^{\infty} \mathcal{A}_i \eta_i(t) - L\delta\theta \tag{3.95}$$

Consequently, the process to be estimated can be expressed as the following continuous state-space model:

$$\begin{aligned} \dot{\boldsymbol{x}}(t) &= \boldsymbol{A}\boldsymbol{x}(t) + \boldsymbol{w}(t) \qquad (3.96) \\ \boldsymbol{z}(t) &= \boldsymbol{C}\boldsymbol{x}(t) + \boldsymbol{w}(t) \qquad (3.97) \end{aligned}$$

where $\boldsymbol{x} = \begin{bmatrix} \delta\theta & \delta\dot{\theta} & \delta\ddot{\theta} & \eta & \dot{\eta} & \delta e \end{bmatrix}^{\top}$ and $\boldsymbol{z} = \begin{bmatrix} \delta\theta_{meas} & \delta\xi_{high} \end{bmatrix}^{\top}$. $\boldsymbol{w}(t)$ and $\boldsymbol{w}(t)$ are the usual white and zero-mean Gaussian noises. The matrices $\boldsymbol{A}$ and $\boldsymbol{C}$ are defined by:

$$\boldsymbol{A} = \left[\begin{array}{ccc|c|c|c} 0 & 1 & 0 & \multicolumn{3}{c}{} \\ 0 & 0 & 1 & \multicolumn{3}{c}{0_{3\times(2p+1)}} \\ 0 & 0 & 0 & \multicolumn{3}{c}{} \\ \hline \multicolumn{4}{c|}{0_{n\times(3+p)}} & \boldsymbol{I}_{p\times p} & 0_{p\times 1} \\ \hline \boldsymbol{\alpha} & 0_{p\times 1} & \boldsymbol{\beta} & -\boldsymbol{\omega^2} & \multicolumn{2}{c}{0_{p\times(p+1)}} \\ \hline 0 & -L & 0 & 0_{1\times p} & \boldsymbol{\mathcal{A}} & 0 \end{array}\right] \qquad \boldsymbol{C} = \left[\begin{array}{c|c} 1 & 0_{1\times(2p+3)} \\ \hline 0_{1\times(2p+3)} & \boldsymbol{L_{\xi}J_{e}} \end{array}\right]$$

In these matrices p is the number of modes to control. $-\boldsymbol{\omega^2}$ represents a $p \times p$ diagonal matrix whose diagonal entries are the $-\omega_i^2$ given by (3.65), $\boldsymbol{\mathcal{A}}$ is the $1 \times p$ vector whose components are the $\mathcal{A}_i$ given by (3.79), $\boldsymbol{\alpha}$ is the $p \times 1$ vector whose components are the α_i given by (3.87), $\boldsymbol{\beta}$ is the $p \times 1$ vector whose components are the β_i given by (3.88), $\boldsymbol{L_{\xi}}$ refers to the interaction matrix relating the velocity of the tip camera to the velocity of the image features and $\boldsymbol{J_e}$ refers to the Jacobian matrice of the end-point with respect to the deflection variable.

3.3 Alternative vibration sensing method based on online sinusoidal regression

Although the method described in section 3.1 and enhanced in section 3.2 provides successful results, it has one main drawback. The Kalman filter used as a vibration estimator is based on a model whose input can be either the joint acceleration or the applied torque. Consequently, the control problem remains unsolved if the vibration is not due to the joint dynamics but to an embedded process or an impact. The camera may perceive a vibration, whereas the internal input-output model still believes the arm is stationary, which is highly detrimental to the accuracy of the estimation.

Following the developments in [67], this section remedies that problem by considering sinusoidal regression instead of a Kalman filter to predict the current deflection from the delayed visual data (see Fig. 3.7). In spite of the great versatility of the solutions it provides, sine regression has not been used extensively to address engineering problems such as vibration control. Since the only assumption made here is that the vibration has a sinusoidal shape—which is verified if one only aspires to damp the fundamental—the proposed method is well-suited for vibrational behaviours of any origin. Two regression methods are put forward and compared based on their complexity and the results they yield. To limit the trade-off between suitable tracking capability and the quality of vibration reconstruction, these algorithms are performed over a variable-length sliding window.

Since the proposed method is no longer based on a physical model of the arm, it is unnecessary to express this deflection in the 3D world to perform an effective control. Consequently, it is no more necessary to estimate the interaction matrix as it was in section 3.1. This greatly simplifies the implementation of the scheme.

Eventually, an estimation of the arm vibration $\hat{\boldsymbol{\delta\xi}}_{\boldsymbol{high}}$ is obtained in pixel units and is projected onto an orthogonal basis. Afterwards, and as in section 3.1, this estimation directly feeds an LQR that makes the end-point follow the desired trajectory using an inverse Jacobian procedure, while $\hat{\boldsymbol{\delta\xi}}_{\boldsymbol{high}}$ is brought to zero as quickly as possible.

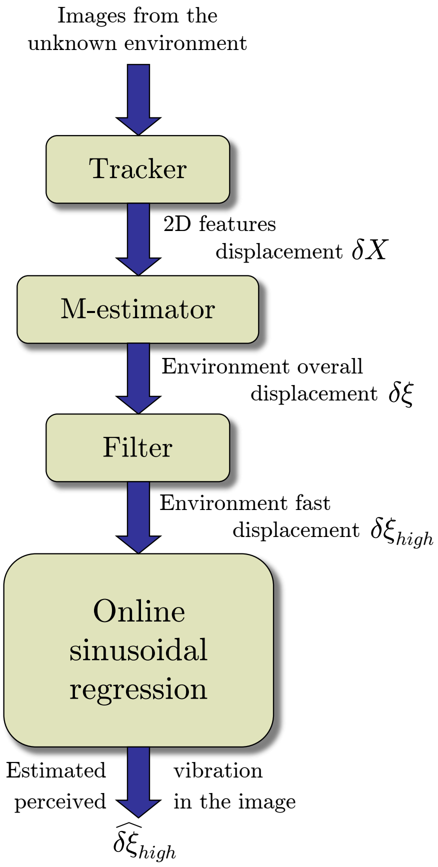

Figure 3.7: Principle of the modified vibration estimator

After a general introduction to sinusoidal regression in section 3.3.1, sections 3.3.2 and 3.3.3 present an exact solution and a simplified method to solve the proposed problem, respectively. Section 3.3.4 describes the principles of the variable-length sliding window and the change detection mechanism used to automatically adjust its length.

3.3.1 Real-time sinusoidal regression

To obtain a robust prediction of the vibration to be rejected, sinusoidal regression is performed using the data (t_i, y_i) received from the feature tracker. The following sinusoidal function is considered:

$$f(t) = a + b\sin(\omega t) + c\cos(\omega t) \tag{3.98}$$

The proposed objective is to determine the values of the parameters a, b, c and ω that cause this function to best fit the observed data provided by the feature tracker.

Many popular parameter estimation algorithms have been proposed, including blockwise or recursive least squares (BLS/RLS), instrumental variables, maximum likelihood and extended Kalman filter. However, to the best of the author's knowledge, none of these algorithms seems perfectly adapted to the vibration suppression problem. The desired algorithm must meet the following requirements:

- it must be an online estimation process;
- it must track time-varying parameters because the amplitude of the oscillation is likely to change over time;
- it must be extremely reactive to enable the controller to damp an abruptly occurring vibration as soon as it appears; and
- it must be fitted to prediction purpose due to visual data's long processing time.

Least-square (LS) regression techniques are preferred to other estimation processes due to their computational effectiveness and completeness. They provide good results with relatively moderate data sets. In addition, out-of-date data should be discarded as new data is collected to facilitate time-varying parameter tracking. This can be achieved by employing a weighting scheme that decreases the effect of old data exponentially, e.g. through variable forgetting factors [379, 380]. However, such algorithms generally provide attractive results in reconstructing signals, but their tracking capability remains limited because old data are never completely discarded. Sliding windows are useful in the sense that they explicitly discard old data. Up to this point, any recursive LS method performed over a fixed-size sliding window is likely to fit most of the requirements above. Nevertheless, the statistical properties of these algorithms, which represent their main advantage in some cases, may not be suitable for estimating abrupt changes in parameters.

The objective of the following sections is to present an optimal, suitable parameter estimation algorithm for highly time-varying systems. The basic idea behind achieving this objective is to use a sliding window BLS algorithm in which the window length is adjusted by a signal change detection algorithm. To this end, a new variable-length sliding window LS scheme has been developed to provide the following:

- reactive parameter tracking during transients to enable quick damping of undesirable vibrations; and
- high-quality estimation accuracy at the steady state to avoid soliciting the actuator during endurable minor oscillations.

Consequently, the proposed scheme involves solving a non-linear LS problem online; the exact solution to this problem will be provided in section 3.3.2. However, accurate RH operations rely on RH tools' appropriate force feedback capabilities, and the servo computational time is generally expected to be within 1 ms for stable and transparent interactions within the environment. Implementing a robust sinusoidal regression algorithm at such a high servo rate is far from trivial. Therefore, a much more easily implementable method is proposed in section 3.3.3.

3.3.2 Exact solution

Since it has been chosen to estimate the set of parameters using LS, the criterion to be minimised is the sum of the squares of the residuals:

$$\begin{aligned}\epsilon_{a,b,c,\omega} &= \sum_{i=1}^{N} \left(y_i - f(t_i)\right)^2 \\ &= \sum_{i=1}^{N} \left(y_i - (a + b\sin(\omega t_i) + c\cos(\omega t_i))\right)^2\end{aligned} \tag{3.99}$$

The best way to solve such a problem is to come down to a linear regression form. To that end, a differential equation can be used; this equation's solution is considered the sinusoidal function:

$$f(t) = a - \frac{1}{\omega^2}\frac{d^2 f(t)}{dt^2} \tag{3.100}$$

The criterion (3.99) yields a linear system where the two unknowns are a and $\nu = 1/\omega^2$:

$$\epsilon_{a,b,c,\omega} = \sum_{i=1}^{N} \left(y_i - a + \nu y_i''\right)^2 \tag{3.101}$$

Unfortunately, this method is practically ineffective because the computation of the second derivative y_i'' from the data (t_i, y_i) usually leads to a large deviation. In contrast, the numerical computing of integrals is far less problematic. Therefore, an integral equation can be used instead of (3.100):

$$f(t) = -\omega^2 G(t) + \mathcal{P}(t) \tag{3.102}$$

where $G(t)$ is the second antiderivative of $f(t)$, such as $G'(t) = g(t) = F(t)$ and $F'(t) = f(t)$. $\mathcal{P}(t)$ is a second-order polynomial depending on the parameters a, b, c and ω and the arbitrary constants of integration C_1 and C_2:

$$\mathcal{P}(t) = \frac{1}{2}a\omega^2t^2 + C_1\omega^2 t + a + C_2\omega^2 = \beta t^2 + \gamma t + \delta \tag{3.103}$$

Thus, by posing $\alpha = -\omega^2$, (3.102) can be re-written as:

$$f(t) = \alpha G(t) + \beta t^2 + \gamma t + \delta \tag{3.104}$$

in which α, β, γ and δ are unknown, but they can be estimated using linear regression. Here, (3.99) yields to:

$$\epsilon_{a,b,c,\omega} = \sum_{i=1}^{N}\left(y_i - \left(\alpha G(t_i) + \beta t_i^2 + \gamma t_i + \delta\right)\right)^2 \tag{3.105}$$

whose minimum can be found by setting its gradient to 0, provided that the vector $G(t_i)$ has previously been computed. This can be achieved by using the usual numerical integration algorithms. From this point, let us assume that $F(t_i)$ and $G(t_i)$ are computed according to the initial conditions $F(0) = 0$ and $G(0) = 0$. The constants of integration C_1 and C_2 are now fully determined and can be related respectively to b and c:

$$C_1 = \frac{b}{\omega} \qquad\qquad C_2 = \frac{c}{\omega^2} \tag{3.106}$$

Minimising (3.105) leads to the linear system:

$$\begin{cases} \left(\dfrac{\partial\epsilon}{\partial\alpha}\right)_{(\alpha_0,\beta_0,\gamma_0,\delta_0)} = -2\displaystyle\sum_{i=1}^{N}\left(y_i - \left(\alpha_0 G(t_i) + \beta_0 t_i^2 + \gamma_0 t_i + \delta_0\right)\right)G(t_i) = 0 \\ \left(\dfrac{\partial\epsilon}{\partial\beta}\right)_{(\alpha_0,\beta_0,\gamma_0,\delta_0)} = -2\displaystyle\sum_{i=1}^{N}\left(y_i - \left(\alpha_0 G(t_i) + \beta_0 t_i^2 + \gamma_0 t_i + \delta_0\right)\right)t_i^2 = 0 \\ \left(\dfrac{\partial\epsilon}{\partial\gamma}\right)_{(\alpha_0,\beta_0,\gamma_0,\delta_0)} = -2\displaystyle\sum_{i=1}^{N}\left(y_i - \left(\alpha_0 G(t_i) + \beta_0 t_i^2 + \gamma_0 t_i + \delta_0\right)\right)t_i = 0 \\ \left(\dfrac{\partial\epsilon}{\partial\delta}\right)_{(\alpha_0,\beta_0,\gamma_0,\delta_0)} = -2\displaystyle\sum_{i=1}^{N}\left(y_i - \left(\alpha_0 G(t_i) + \beta_0 t_i^2 + \gamma_0 t_i + \delta_0\right)\right) = 0 \end{cases} \tag{3.107}$$

Its solution can be written in the matrix form:

$$\underbrace{\begin{bmatrix}\alpha_0\\ \beta_0\\ \gamma_0\\ \delta_0\end{bmatrix}}_{X_0} = \underbrace{\begin{bmatrix}\Sigma G^2(t_i) & \Sigma t_i^2 G(t_i) & \Sigma t_i G(t_i) & \Sigma G(t_i)\\ \Sigma t_i^2 G(t_i) & \Sigma t_i^4 & \Sigma t_i^3 & \Sigma t_i^2\\ \Sigma t_i G(t_i) & \Sigma t_i^3 & \Sigma t_i^2 & \Sigma t_i\\ \Sigma G(t_i) & \Sigma t_i^2 & \Sigma t_i & N\end{bmatrix}^{-1}}_{M_0} \underbrace{\begin{bmatrix}\Sigma y_i G(t_i)\\ \Sigma y_i t_i^2\\ \Sigma y_i t_i\\ \Sigma y_i\end{bmatrix}}_{Y_0} \tag{3.108}$$

where conventionally $\Sigma = \sum\limits_{i=1}^{N}$.

Then, ω_0, a_0, b_0 and c_0 can be deduced:

$$\omega_0 = \sqrt{-\alpha_0} \tag{3.109}$$

$$a_0 = -\frac{2\beta_0}{\alpha_0} \tag{3.110}$$

$$b_0 = \frac{\gamma_0}{\sqrt{-\alpha_0}} \tag{3.111}$$

$$c_0 = \frac{2\beta_0}{\alpha_0} + \delta_0 \tag{3.112}$$

An expression of the sinusoidal function that best fits the data received from the feature tracker over a period of time is now available. From this expression, the tip deflection can readily be predicted between the present time and the next data reception, assuming that only slight changes can affect the frequency and amplitude of the oscillation.

3.3.3 Simplified method based on the M-estimation of the frequency

Since an estimation of the first vibrational modes of the robotic structure is often available, the use of a simplified method with the advantage of a reduced computational cost can also be considered.

When ω can be considered a known parameter, the optimisation only concerns parameters a, b and c and the problem is directly reduced to a linear LS problem. As in section 3.3.2, the minimum of the sum of squares is found by setting its gradient to 0, which leads to the following set of equations:

$$\begin{cases} \sum\limits_{i=1}^{N} (y_i - (a_1 + b_1 s_i + c_1 c_i)) = 0 \\ \sum\limits_{i=1}^{N} (y_i - (a_1 + b_1 s_i + c_1 c_i))\, s_i = 0 \\ \sum\limits_{i=1}^{N} (y_i - (a_1 + b_1 s_i + c_1 c_i))\, c_i = 0 \end{cases} \tag{3.113}$$

where s_i and c_i refer to $\sin(\omega_e t_i)$ and $\cos(\omega_e t_i)$, respectively, for simplicity's sake. ω_e is the estimated value of the vibration angular frequency.

The solution of system (3.113) can be written in the matrix form:

$$\underbrace{\begin{bmatrix} a_1 \\ b_1 \\ c_1 \end{bmatrix}}_{X_1} = \underbrace{\begin{bmatrix} N & \Sigma s_i & \Sigma c_i \\ \Sigma s_i & \Sigma s_i^2 & \Sigma s_i c_i \\ \Sigma c_i & \Sigma s_i c_k & \Sigma c_i^2 \end{bmatrix}^{-1}}_{M_1} \underbrace{\begin{bmatrix} \Sigma y_i \\ \Sigma y_i s_i \\ \Sigma y_i c_i \end{bmatrix}}_{Y_1} \tag{3.114}$$

Equation (3.114) lays the foundations for a simpler implementation of online sinusoidal regression, provided that the parameter ω_e can be evaluated separately. To that end, it is assumed that an initial evaluation of ω_e reasonably close to the real value is known. This can be easily obtained through computer-aided modal analysis performed on the computer-aided design (CAD) representation of the robotic device.

Eventually, an online vibration predictor based on sinusoidal regression is obtained. Its principle is illustrated in Fig. 3.8.

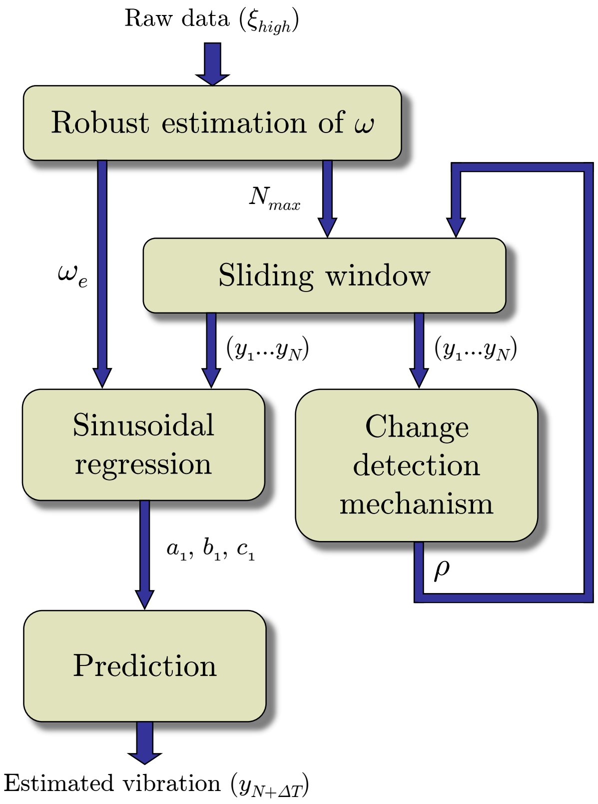

Figure 3.8: Principle of the online sine regression (simplified method)

Since the quality of the vibration reconstruction is heavily based on the accurate evaluation of the vibrational frequency, this estimate ω_e is updated online by detecting the zero-crossing of the $\{y_i\}$ sequence, which is supposed to happen every half-period. However, due to the feature extraction noise and potential temporary disturbances, multiple zero-crossings over short periods of time may corrupt this raw data. To minimise the influence of these outliers, robust statistics can be employed again, which makes it possible to recover the structure that best fits the majority of the computed values of ω_e over a window while identifying and rejecting deviating substructures.

As in the feature tracker (see section 3.1.5) this is achieved by using a robust M-estimator, which can be considered a more general form of an MLE [381] because it permits the use of different minimisation functions not necessarily corresponding to normally distributed data. Such an estimator can be written as:

$$\hat{\omega} = \underset{\omega}{\text{argmin}} \left[\sum_{i=1}^{N} \Lambda(\omega_{ei}, \omega) \right] \tag{3.115}$$

where Λ is an influence function (Tukey's, Huber's, etc.) that can be chosen in such a way to provide the estimator's desirable properties in terms of bias and efficiency.

For this reason, four different M-estimators have been compared to each other in order to obtain the most appropriate estimation of ω_e.

1. The Huber estimator [382] asymptotically reduces the influence of outliers toward zero. Its influence function is given by:

   $$\Lambda(\chi) = \begin{cases} \frac{1}{2}\chi^2 & \text{if } |\chi| \leq h \\ h|\chi| - \frac{1}{2}h^2 & \text{if } |\chi| > h \end{cases} \tag{3.116}$$

   where $\chi = \frac{\omega_e - \omega}{MAD}$. MAD represents the median absolute deviation estimator. With $h = 1.345$, this estimator assumes that all values within the bounds of 95% of the data are 100% correct and gradually reduces the probability of features outside this region.

2. Tukey's estimator [383] completely rejects outliers by giving them a zero weight. Its influence function is:

   $$\Lambda(\chi) = \begin{cases} \frac{1}{6}[1 - (1 - \chi^2)^3] & \text{if } |\chi| \leq 1 \\ \frac{1}{6} & \text{if } |\chi| > 1 \end{cases} \tag{3.117}$$

   where $\chi = \frac{\omega_e - \omega}{h \times MAD}$. MAD still represents the median absolute deviation estimator and h is still a tuning parameter that adjusts the asymptotic efficiency of the obtained M-estimator. The value $h = 4.6851$ gives 95% efficiency on the standard normal distribution.

3. Cauchy's estimator [384] provides a gradual attenuation of the outliers:

   $$\Lambda(\chi) = \frac{h^2}{2} ln[1 + \chi^2] \tag{3.118}$$

   where χ is defined as in the previous estimator. The 95% asymptotic efficiency on the standard normal distribution is obtained with $h = 2.3849$.

4. The Geman-McClure influence function [385] tends to further reduce the effect of large errors:
$$\Lambda(\chi) = \frac{\chi^2/2}{1+\chi^2} \tag{3.119}$$
with χ defined as in Huber's estimator.

In many practical situations, the choice of the influence function is not critical to obtaining a precise and robust estimate, and different choices will give similar results in terms of improvement over classical estimation techniques. Section 4.4 in the next chapter will present an experimental comparison of these four estimators and will show that Tukey's and Cauchy's functions are both suitable.

3.3.4 Variable-length sliding window / change detection mechanism

Sections 3.3.2 and 3.3.3 described two vibration prediction methods based on sinusoidal regression over a sliding window. The performance of these algorithms obviously depends on the window length. When the window length is longer, the estimation accuracy is higher. On the other hand, when the window is shorter, the parameter estimation is more responsive. Therefore, one main feature of the proposed approach lies in its ability to quickly adapt the window length as soon as a change in the system parameters is detected to achieve the best performance in the transient and steady states.

When sudden changes occur, the window will be harshly shrunk to its minimal size. Then, it will progressively expand until it returns to its original length in order to maintain steady-state performance. When a continuous signal change occurs, the window will be shrunk or expanded progressively, depending on the rate of change, until the end of the change is detected. This algorithm is illustrated in Fig. 3.9.

As long as no change is detected, the sliding window keeps a size of N_{max} values. N_{max} is chosen to provide the best estimation accuracy as possible. Based on experience, this implies that the window entails about one period of the vibration, which results in:

$$N_{max} = k_n \left\lfloor \frac{1}{2\pi\omega_e\Delta t} \right\rfloor \tag{3.120}$$

where k_n is an adjusting factor. When a sudden change is detected, the window size is set to N_{min}, which must be adjusted experimentally to obtain the desired responsivity. Finally, when a progressive change is detected, the window size is intermediate and varies linearly with the normalised change rate υ:

$$N = (1-\upsilon)N_{max} + \upsilon N_{min} \tag{3.121}$$

To automatically initiate and complete the window length adjustment, a change detection scheme must be used. This change detection mechanism must also distinguish the sudden emergence of a vibration from the progressive growth of a previously negligible vibration.

Consequently, the following features are vital to this scheme:

- detect the onset of a change;
- distinguish a gradual change from an abrupt one;
- estimate the change rate when a gradual change occurs; and
- detect the termination of a change.

Several different ways exist to detect parameter changes in a system [386]. To be as reactive as possible, a change detection scheme is implemented based on the last received measurement rather than the last estimated set of parameters or the last prediction $f(t_i)$, which are inherently averaged over a window. Assuming that the variations of ω are correctly evaluated by the M-estimator described in section 3.3.3, a change in the arm's vibrational behaviour will only affect the amplitude of the oscillation. Such a change can be detected by monitoring changes in the signal variance.

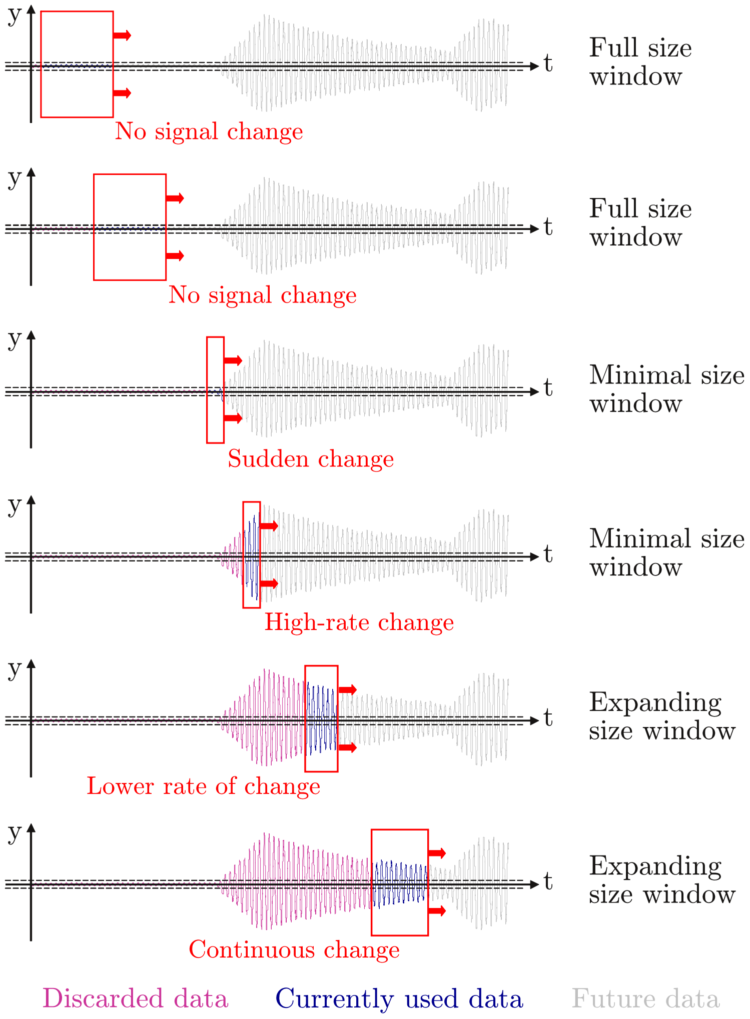

Figure 3.9: Window length adjustment strategy

No time dependence is present between the observations. The objective is to monitor the stability of the variance of the time series (y, t) defined by the independent sequence $\{y_i\}_{i\geq 1}$ of normal random variables with mean $\overline{y}_i$ and variance σ_i^2.

First, let us assume that $\sigma_1^2 \simeq \cdots \simeq \sigma_i^2 \simeq \sigma_0^2$. By observing the data, the goal is to detect if a change occurs in the variance by testing the following hypothesis:

$$H_0 : \sigma_1^2 \simeq \cdots \simeq \sigma_i^2 \simeq \sigma^2 \tag{3.122}$$

against the alternative:

$$H_1 : \sigma_1^2 \simeq \cdots \simeq \sigma_{i-1}^2 \neq \sigma_i^2 = \sigma_*^2 \tag{3.123}$$

In the present case, σ_* is considered unknown whereas σ is assumed to be known and computed at every cycle.

To that end, the statistical test defined as follows can be used:

$$B = \sum_{j=1}^{N} \frac{(j-1)(y_j - \overline{y}_i)^2}{(N-1)\sum_{i=1}^{N}(y_i - \overline{y}_i)^2} \tag{3.124}$$

This is derived from the Bayesian test proposed by [387], which assumes that the initial level of variance and the mean are computed and known under H_0. It yields a value between 0 and 1 that is symmetrically distributed about the mean 0.5.

The type of signal change will be reported if B exceeds conveniently pre-set thresholds:

$$B = \begin{cases} \geq \Gamma_a^+ & \text{abrupt change} \\ \Gamma_g^+ \leq ... < \Gamma_a^+ & \text{gradual change} \\ \Gamma_g^- < ... < \Gamma_g^+ & \text{no change} \\ < \Gamma_a^- ... \leq \Gamma_g^- & \text{abrupt change} \\ \leq \Gamma_a^- & \text{abrupt change} \end{cases} \tag{3.125}$$

The careful choice of Γ_g^-, Γ_g^+, Γ_a^- and Γ_a^+ is imperative because it directly affects the probability of missed detections and false alarms.

3.4 Online estimation of the time-varying capture delay

In previous sections, a vibration sensing method using a vision sensor led to very promising results. The main advantage of this approach is to sidestep problems related to the use of noisy or biased signals from accelerometers or strain gauges. Conversely, vision devices have the disadvantage of a long processing time, which leads not only to delayed measurements but also to low update rates.

The most common method to deal with delay in a control system is to decrease the servo gains to increase damping, thus making the system more robust in the presence of a time delay. In addition to the class of controllers that are robust in relation to time delays, another approach involves accurately estimating the delay itself in order to predict the quantity that must be controlled.

In [60], the controller design is split into two separate problems using a composite control technique; fast feedback stabilises the oscillatory dynamics while a slower visual servo ensures that the current image asymptotically reaches the desired one. With the aim of implementing this fast feedback, a Kalman filter is fed by strain gauge measurements without the camera data being considered at all for vibration control. In such a case, the problem of damping out the vibrations does not suffer from delays or low rates inherent to visual data. Going further, [61] considers camera data in order to improve the system's ability to damp vibrations. A Kalman filter is used to fuse the measurements coming from the different sensors to improve the signal-to-noise ratio. Experimental validation shows that considering the strain gauges and the camera yields smaller residual tip vibrations. However, the authors do not explain how these desynchronised signals are fused together in the state observer.

Only visual data were used in section 3.1 to estimate tip vibration and joint movement. The proposed two-timescale Kalman filter considered the delay due to image processing by extrapolating the measured output to the present time using past and present estimates. To that end, the variable delay ΔN was estimated using timestamps. A timestamp identifies the current time of an event in a given timeframe. If this identifier is chosen to be generated by the servo controller, it may correpond to the servo cycle number and is consequently given with millisecond precision. Such a precision makes the timestamp exchange mechanism suitable for synchronisation purposes between networked computers or applications. In section 3.3, which considered online sinusoidal regression instead of Kalman filtering to reconstruct the vibration, the same timestamp exchange approach was used to predict the current deflection from delayed visual data.

These methods are expected to yield satisfying results. However, ensuring robustness of the controller towards roughly estimated time delays may not always be sufficient, and an accurate online estimation of the delay between the physical phenomenon and the measured signal is likely to be necessary to properly reject the vibration. By estimating the image delay from the exchange of timestamps between the real-time high-sampling-rate controller and the non-real-time supervisor whose sampling rate is aligned to the camera framerate, the uncertainty regarding the camera exposure time is not considered. Including this duration to the estimated delay is expected to improve the vibration reconstruction.

Consequently, the alternative method described in this section involves using a secondary sensor that is synchronous—but potentially noisy and biaised due to its exposure to radiation—in order to properly estimate the delay and enable the correct resynchronisation of the vibration measurement with the physical phenomenon. On one hand, clean but delayed visual data should be used to properly estimate the tip displacement; on the other hand, noisy but synchronous inertial data should be used to readjust this visual data in time.

The primary contribution of this section, which follows the developments in [68], is to propose an online delay estimator. This estimator is based on a cross-correlation technique that explicitly computes the time delay between the two signals cited above. Since the proposed cross-correlation function is partially computed recursively, the computational load of the proposed algorithm is limited.

The following sections are organised as follows. After a short refresher on image capture by vision sensors, section 3.4.1 highlights the main limitation of the delay estimation by timestamp exchange as performed in sections 3.1 and 3.3. Section 3.4.2 describes the method proposed to estimate the time-varying capture delay of a vision sensor performed online and with a high accuracy.

3.4.1 Limitation of the delay estimation by timestamp exchange

Synchronisation between the measured oscillatory signal and the physical vibrational phenomenon is critical to properly suppressing vibrations. Unfortunately, when the visual data processing application runs on a non-real-time OS, the delay can vary substantially. In this section, a description of the delay estimation performed in sections 3.1 and 3.3 is given and the main limitation of this method is discussed.

Delay estimation based on timestamp exchange

An all-in-one method was proposed in section 3.1 to solve the problem of vibration suppression by using visual features acquired by an eye-in-hand-mounted camera in the absence of any markers and a priori knowledge of the environment. In section 3.3, an online sinusoidal regression was performed over a sliding window to analytically identify the measured vibration. Based on the identified function and the estimated capture delay, a prediction step estimates the vibration to reject at the present time.

As with most visual servo control algorithms, these methods are implemented across two systems:

- a controller running a real-time application as quickly as needed to perform a stable and accurate control (constant refresh rate τ_c in the order of 1 ms); and

- a supervisor computer running a non-real-time OS and managing the image acquisition (varying refresh rate τ_s in the order of 14–16 ms).

The two computers can exchange data through various means, such as via the user datagram protocol (UDP).

One simple method to estimate the capture delay relies on the exchange of timestamps. During operations, timestamps are exchanged between the real-time high-sampling rate controller and the non-real-time supervisor, whose sampling rate is aligned to the camera framerate. This principle is illustrated by Fig. 3.10.

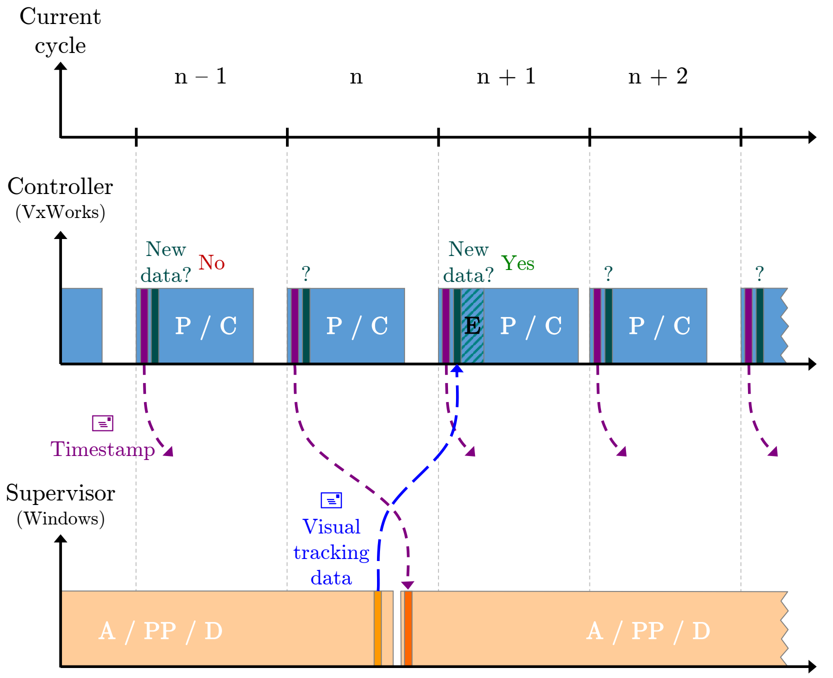

P: Deflection prediction
C: Control
E: Estimation of the sine
A: Acquisition of the image
PP: Post-processing
D: Data transfer

Figure 3.10: Time diagram of communication between the real-time manipulator controller and the non real-time supervisor running the camera driver

Each controller cycle begins with the current timestamp n_c being sent to the supervisor. This timestamp is stored in a buffer and is used only if the application on the supervisor side asks for it. Otherwise, the buffer is overwritten at the next cycle. After the timestamp is sent, a second buffer is read to determine if new visual data is available. If new data is available, a regression is performed. Otherwise, the controller completes the prediction and control steps.

Each supervisor cycle begins by reading the timestamp buffer. Consequently, the time the image capture begins is known with an accuracy of about 1 ms. Let us call the initial timestamp n_i. At the end of the supervisor cycle, the visual data and the initial timestamp feed the data buffer. Therefore, when the controller reads this buffer, the current timestamp n_c and the initial timestamp n_i are available. The capture delay is computed as the difference of these two times:

$$\Delta = (n_c - n_i)\ \tau_c \tag{3.126}$$

Basics on camera capture

To properly justify why the above method is not absolutely satisfying, let us first cover some basics regarding camera capture.

Let us consider either a CCD or a CMOS sensor, which are equipped in most digital cameras today. An image is recorded in this sensor in three phases: reset of the pixel rows to be exposed, exposure of pixel rows and sensor read-out. Several operational modes exist.

- In triggered operation, the sensor is on stand-by and exposes one image immediately after the occurrence of a trigger event. Therefore, the exposure and the image read-out are performed sequentially, and the achievable framerate depends directly on the exposure time.
- In freerun mode, the camera sensor internally exposes one image after another at the set framerate. In this mode, the exposure and the read-out are performed simultaneously, which enables the maximum camera framerate to be achieved.

In freerun, however, the sensor cells must not be exposed during the read-out process. As a result, camera sensors use mechanical or electronic shutters. Depending on the sensor type, either the rolling or global shutter method is used (see Fig. 3.11). CCD sensors use the global shutter method; it is also used in some low-resolution CMOS sensors. On a global shutter sensor, all pixel rows are reset and then exposed simultaneously. At the end of the exposure, all rows are synchronously moved to a darkened area of the sensor. The pixels are then read out row-by-row. Exposing all pixels offers the advantage that fast-moving objects can be captured without geometric distortions. On the other hand, sensors based on global shutters are usually more complex in design and are therefore more expensive than rolling shutter sensors. In the rolling shutter method, the pixel rows are reset and exposed one after the other. At the end of the exposure, the lines are read out sequentially. Unfortunately, this results in a time delay between the exposure of the first and the last rows, and captured images of moving objects are partially distorted. Consequently, the only advantage of such sensors is their reduced price. Rolling shutter sensors offer a higher fill factor compared to global shutter sensors, and they are less expensive to manufacture.

For the purpose of this thesis, a CMOS sensor with an electronic global shutter was used in freemode. The use of this sensor allowed framerates up to 60–70 fps.

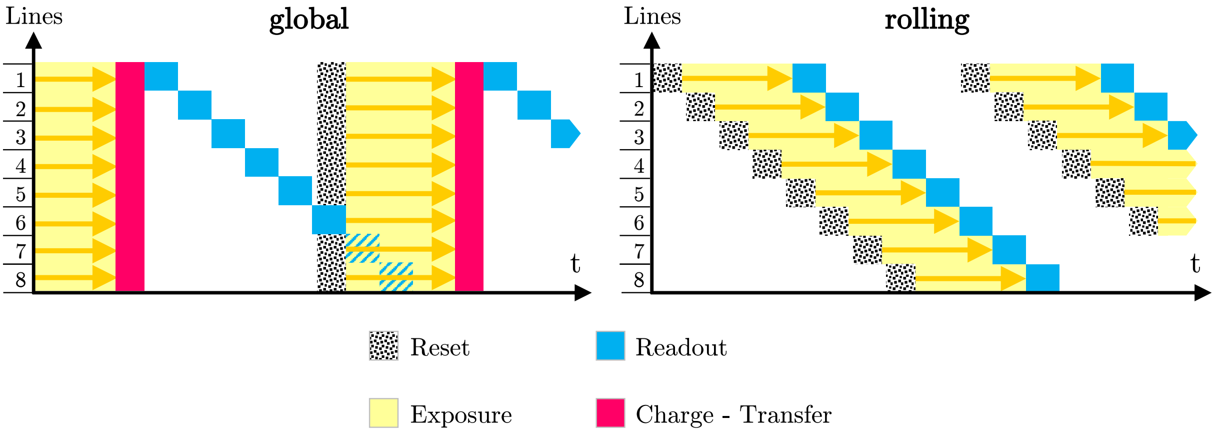

Figure 3.11: Schematic of the global & rolling shutter methods in freerun mode

On the limitation of such a method

In freerun mode, the exposure time is usually set to the reciprocal value of the framerate. As mentioned above, let us consider that the camera achieves a framerate of 60–70 fps. The exposure time is close to 15 ms; there is no way of knowing when, during these 15 ms, the image is taken. In other words, the capture instant is uncertain in the range of ±7 controller cycle and cannot be accurately computed based on the initial timestamp, according to $n_i \times \tau_c$.

For most of visual servoing application, this is not a problem because the main time constants are much larger. In this work, where the goal is to estimate an oscillation whose frequency is in the order of 2–3 Hz, a wrong estimation of this delay of 7 controller samples would lead to an 11.4% error in the signal amplitude. In the worst case scenario, an error in the delay estimation of 15 controller samples would lead to a 24.4% error in the signal amplitude.

What made the online vibration estimation proposed in section 3.3 efficient is that the sinusoidal function parameters were identified over a sliding window of size N $(3 \leq N \leq 20)$. Therefore, it is expected that the vibration control could benefit from a better estimation of the image capture delay. This could be done using a synchronisation sensor, for example.

3.4.2 Delay estimation using a synchronisation sensor and cross-correlation

In this section, an alternative method for estimating the capture delay is described. It involves using a secondary sensor, which is synchronous but prone to noise due to radiation, to synchronise the delayed visual data with the physical oscillation. The proposed approach to estimate the capture delay is based on the concept of cross-correlation.

For two periodic signals $x(n)$ and $y(n)$ having the same period of N_s samples, the cross-correlation is defined as:

$$\mathcal{C}_{xy}(m) = \frac{1}{N_s}\sum_{n=1}^{N_s} x(n)y(n-m) = \frac{1}{N_s}\sum_{n=1}^{N_s} x(n+m)y(n) \tag{3.127}$$

This correlation function also has a period of N_s samples.

Let us consider a periodic signal $z(n)$ and two derived signals $x(n)$ and $y(n)$. $x(n)$ consists of the signal $z(n)$ plus an additive white Gaussian noise $v(n)$, and $y(n)$ corresponds to the signal $z(n)$ delayed by n_0 samples:

$$x(n) = z(n) + v(n) \tag{3.128}$$

$$y(n) = z(n - n_0) \tag{3.129}$$

Now, let us look at the cross-correlation between $y(n)$ and $x(n)$ during M samples (M is much greater than N_s):

$$\mathcal{C}_{yx}(m) = \frac{1}{M}\sum_{n=1}^{M} y(n)x(n-m) \tag{3.130}$$

By replacing the expressions of $x(n)$ and $y(n)$ into (3.130), one obtains:

$$\mathcal{C}_{yx}(m) = \frac{1}{M}\sum_{n=1}^{M} z(n-n_0)[z(n-m) + v(n-m)] \tag{3.131}$$

Developing this relation yields:

$$\mathcal{C}_{yx}(m) = \frac{1}{M}\sum_{n=1}^{M} z(n-n_0)z(n-m) + \frac{1}{M}\sum_{n=1}^{M} z(n-n_0)v(n-m) \tag{3.132}$$

which can be re-written as:

$$\mathcal{C}_{yx}(m) = \frac{1}{M}\sum_{n=1}^{M} z(n-n_0+m)z(n) + \frac{1}{M}\sum_{n=1}^{M} z(n-n_0+m)v(n) \tag{3.133}$$

Finally, the cross-correlation can be expressed by:

$$\mathcal{C}_{yx}(m) = \mathcal{C}_{zz}(m-n_0) + \mathcal{C}_{zv}(m-n_0) \tag{3.134}$$

This result shows that the cross-correlation consists of two terms: the auto-correlation $\mathcal{C}_{zz}(m-n_0)$ of the periodic signal shifted in time and the cross-correlation $\mathcal{C}_{zv}(m-n_0)$ between the periodic signal $z(n)$ and the corrupting noise $v(n)$ also shifted in time. On one hand, $\mathcal{C}_{zv}(m-n_0)$ is usually rather small due to the random nature of noise and the independence of the signal and noise. On the other hand, $\mathcal{C}_{zz}(m-n_0)$ is larger. It is also periodic and has peaks at $m = n_0$, $N_s{+}n_0$, $2N_s{+}n_0$, etc. Thus, by examining $\mathcal{C}_{yx}(m)$, the delay n_0 can be estimated very easily.

Consequently, in order to estimate the capture delay, such a cross-correlation computation can be employed over a fixed-size sliding window on the signals coming from the noisy inertial sensor and the delayed visual data. The size of the window must be large enough to include at least one period of the cross-correlation. Since no new information is received between two consecutive sets of visual data (i.e. for a duration of τ_s), the delay Δ is assumed to be constant during this period. The same value of Δ can be used to predict the vibration until the next data reception from the supervisor. However, one can take advantage of this time to refine the estimation of Δ.

Nevertheless, one last difficulty must be overcome. The capture delay changes for each set of visual data, but the cross-correlation is computed over at least one period of the sinusoidal signals. Consequently, one must consider the P values received after the last supervisor refreshment more highly than previous ones. To do so, let us re-write (3.130) and explicitly consider the last P measured values:

$$\begin{aligned}\mathcal{C}_{yx}(m) &= \frac{1}{M}\sum_{n=1}^{M} y(n)x(n-m)\\ &= \frac{1}{M}\sum_{n=1}^{M-P} y(n)x(n-m) + \frac{1}{M}\sum_{n=M-P+1}^{M} y(n)x(n-m)\\ &= \frac{M-P}{M}\mathcal{C}_{yx}^{old}(m) + \frac{P}{M}\mathcal{C}_{yx}^{new}(m)\\ &= \mathcal{C}_{yx}^{old}(m) + \frac{P}{M}\left(\mathcal{C}_{yx}^{new}(m) - \mathcal{C}_{yx}^{old}(m)\right)\end{aligned} \tag{3.135}$$

where $\mathcal{C}_{yx}^{old}(m)$ represents the cross-correlation computed from the values before the last reception of visual data and $\mathcal{C}_{yx}^{new}(m)$ represents the cross-correlation from the latest values. From (3.135), the new estimate value of $\mathcal{C}_{yx}(m)$ can be regarded as the old estimate $\mathcal{C}_{yx}^{old}(m)$ plus a correction term.

All the measured values throughout (3.135) have the same weight. In the present case, as with any non-stationary system, recently measured values should be weighed more heavily. One method to achieve this is to introduce a forgetting factor ρ:

$$\mathcal{C}_{yx}(m) = \mathcal{C}_{yx}^{old}(m) + \frac{\rho P}{(1{-}\rho)(M{-}P){+}\rho P}\left(\mathcal{C}_{yx}^{new}(m) - \mathcal{C}_{yx}^{old}(m)\right) \tag{3.136}$$

ρ is such that $0 \leq \rho \leq 1$. Note that, for $\rho = \frac{1}{2}$, all the data has the same weight and (3.136) is equivalent to (3.135).

Finally, the capture delay Δ is defined by $n_0{\times}\tau_c$ with n_0 as $\mathcal{C}_{yx}(n_0) = \max\left[\mathcal{C}_{yx}(m)\right]_{0\leq m\leq N_s}$.

3.5 Conclusion on the development of a vision-based vibration control scheme

The scientific contributions of this thesis have been discussed in this chapter.

In section 3.1, a vision-based vibration control was presented for a flexible robot arm. The proposed control scheme entails a vibration estimator that reconstructs the vibrations from visual data without any a priori knowledge of the surroundings. It is based on a robust feature-tracking algorithm that feeds a state observer modified to cope with delayed measurements. This state observer includes a simple dynamic model of the arm, which was then replaced by a more advanced, multimode dynamic model in section 3.2.

Next, section 3.3 described an alternative vibration sensing method using online sinusoidal regression. This approach enables the vision-based control of flexible arms subjected to vibrations of any origin. The proposed method involves performing a regression over a variable-size moving window coupled to a signal change detector, which should yield good tracking capability and estimation accuracy.

Because the performance of the vibration control is expected to increase with the precise synchronisation of the vibration measurement with the physical phenomenon, section 3.4 presented an online estimator of time-varying image-processing delays based on a cross-correlation technique. This algorithm explicitly computes the time delay between the visual data and the output of a synchronisation sensor.

The experimental validation of these various theoretical results will be presented in the next chapter.

4. RESULTS: EXPERIMENTAL VALIDATION

After a short description of the test bed, this chapter successively presents the experimental validation of the theoretical results discussed in sections 3.1 to 3.4 of the previous chapter. First, the vibration is estimated using the proposed two-timescale state observer, in section 4.2. Then, the internal model of the Kalman filter is replaced by the advanced model, which is validated in section 4.3. In section 4.4, the alternative method using sinusoidal regression is assessed. Finally, section 4.5 validates the ability of the cross-correlation technique, described in section 3.4.2, to accurately estimate a time-varying capture delay.

4.1 Description of the experimental set-up

Until the availability of a robotic arm destined for ITER makes the implementation of this scheme on a complete RH system possible, a validation campaign has been carried out on the experimental mock-up shown in Fig. 4.1 [63].

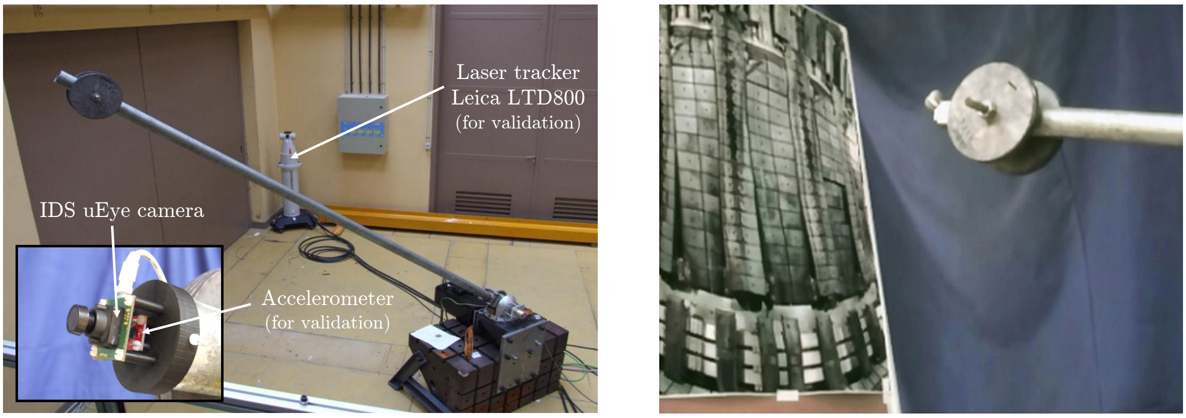

(a) (b)

Figure 4.1: Flexible mock-up at CEA LIST site, in Fontenay-aux-Roses

The mock-up consists of the following materials:

- an actuated joint (capacity ≃ 1000 N.m) driven by a motor through an Harmonic-Drive-based speed reducer;
- a 3 m-long circular beam with a calibrated tip mass (see Table 4.1);
- a 5000 cpr optical encoder to measure the joint position;
- a tip-mounted industrial camera IDS uEye UI-122xLE (resolution 640 × 480);
- a triple-axis accelerometer LIS3LV02DQ; and

- a laser tracker Leica LTD800 to validate the tip position (accuracy = 5.10^{-5} m, frequency $\simeq$ 500 Hz).

A detailed description of the joint and its speed reducer will not be given in the present document since a patent application on their concept is currently being examined. One can simply note the slight flexibility of the joint, which is based on a double Harmonic Drive. Nevertheless, given the dimensions of the attached beam, it will be assumed that most of the system flexibility is distributed along the beam and the joint will therefore be considered rigid.

The circular cross-section beam has been chosen to allow homogenous and easily assessable deformations. Its maximal deflection is 65 mm with a 30 kg load attached at its extremity.

Table 4.1: Parameters of the studied beam

Parameter	**Symbol**	**Value**	**Unit**
Length	L	3	m
Cross-section area	S	4.55×10^{-4}	m^2
Density	ρ	7850	$kg.m^{-3}$
Young's Modulus	E	210×10^9	$N.m^{-2}$
Moment of inertia	I	2.3468×10^{-7}	m^4
Tip mass	M_p	14.1	kg

Establishing the system equations from (3.5) is made clear due to the limited number of freedom:

$$\begin{bmatrix} M_pL^2 & ML \\ ML & M \end{bmatrix} \begin{bmatrix} \ddot{\theta} \\ \ddot{\delta e} \end{bmatrix} + \begin{bmatrix} 0 & 0 \\ 0 & \frac{3EI}{L^3} \end{bmatrix} \begin{bmatrix} \theta \\ \delta e \end{bmatrix} = \begin{bmatrix} I \\ 0 \end{bmatrix} \delta\tau \tag{4.1}$$

Its two first natural frequencies can be measured as 2.44 Hz and 27 Hz, respectively. However, Fig. 4.2 shows that the second mode completely vanishes in approximately one second due to internal damping. Other upper modes can also be neglected.

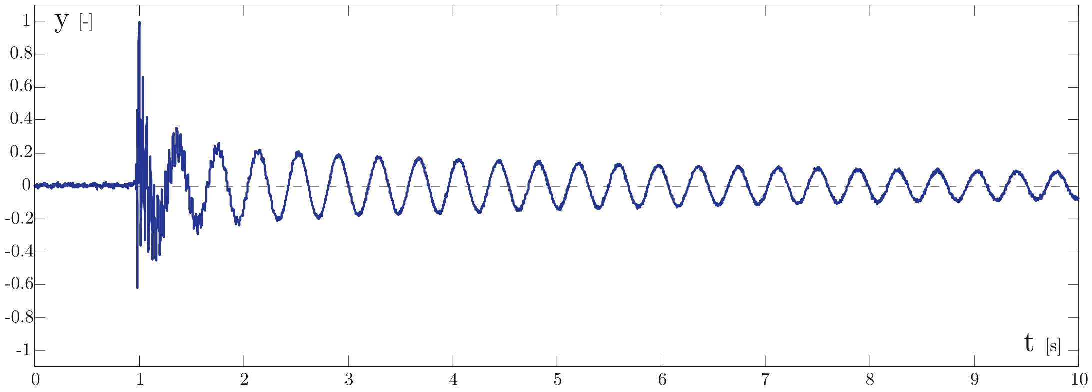

Figure 4.2: Open loop step response of the beam

Therefore, only one mode is considered at first glance since the fundamental oscillation clearly penalises predominantly the performance of the position control. The presence of the second mode will be reconsidered in section 4.3.

Figure 4.3 illustrates the accordance of this simplified model output with experimental data coming from the embarked accelerometer.

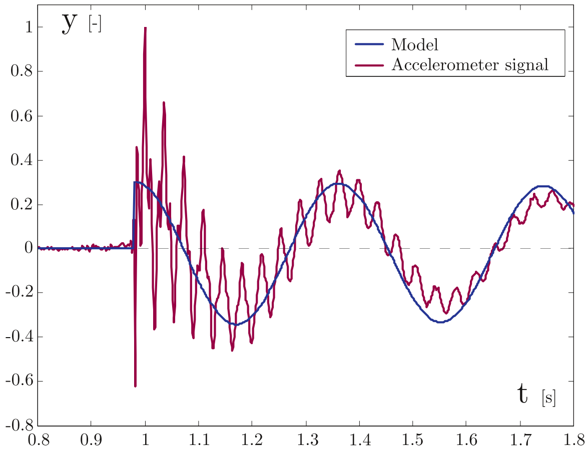

Figure 4.3: Comparaison between model output and experimental data from accelerometers

The joint controller runs the real-time OS VxWorks, whose sampling time has been set to 10 ms first (validation of the overall control scheme) and to 1 ms afterward (validation of the advanced model, the sinusoidal regression algorithm and the capture delay estimator). The overall vision-based application is based on the ViSP software [388]. Its cycle has been monitored around 15 Hz first (section 4.2) and around 60–70 Hz later (sections 4.3, 4.4 and 4.5). The joint friction and gravity torques applied on the beam have been compensated considering measurements from a rigid bar of the same weight. The KLT algorithm has been implemented using the OpenCV implementation, which is computationally the most efficient at the present time. The tracker contains a pool of 20 features, and it considers 10 × 10 windows for each. The minimum distance between features has been set to 30 pixels and the quality factor to 0.01. To avoid the jitter effect on the actuator, the vibration control is only performed if the oscillation amplitude exceeds a threshold set to 5 pixels (camera resolution: 640 × 480).

4.2 Experimental results on vibration control using unknown visual features

This section presents the experimental validation of the vision-based vibration control designed in section 3.1.

Displaying an example of the obtained $\boldsymbol{L_\xi}$ would not make sense because it does not necessarily converge towards values having a physical meaning (see section 3.1.6). Instead, it is quite eloquent to rebuild the low-filtered camera velocity $\widetilde{\dot{\xi}}_{low}$ from the angular velocity and the estimated $\boldsymbol{L_\xi}$, and to compare it to the measured camera velocity. Fig 4.4 validates the benefit of the proposed method. The best results are obtained for $min(\varrho) = 10^{-3}$ and

$\dot{\theta}_{limit}$, which characterises the self-adjustment of ϱ set to 10^{-3} rad/s. The error between the rebuilt and measured velocities is $\approx 14.1\%$; this error increases to 46.5% when ϱ is set at 0.4.

The robustness of the environment displacement estimation is greatly improved by the use of the Tukey M-estimator. For example, the displacement estimation of a static scene disturbed by fleeting partial occlusions yields a temporal standard deviation σ of 0.012979. In comparison, the same estimation made by a classic mean and a trimmed mean yields $\sigma = 1.619542$ and $\sigma = 0.017504$, respectively.

Next, the behaviour of the link with and without the vibration suppression scheme can be compared. As illustrated by Fig. 4.5, the response of the controlled system is very sensitive to the choice of the penalty matrix $\boldsymbol{Q_{LQR}}$. In the case of the 4th curve of Fig. 4.5, priority has been given to the position control. The desired joint position is reached quickly, but a slight overshoot occurs on $\boldsymbol{\delta e}$. Alternatively, priority can be given to the vibration compensation. The 3rd curve of Fig. 4.5 shows that the joint is a bit slower to reach its desired position, but the vibration is damped much better.

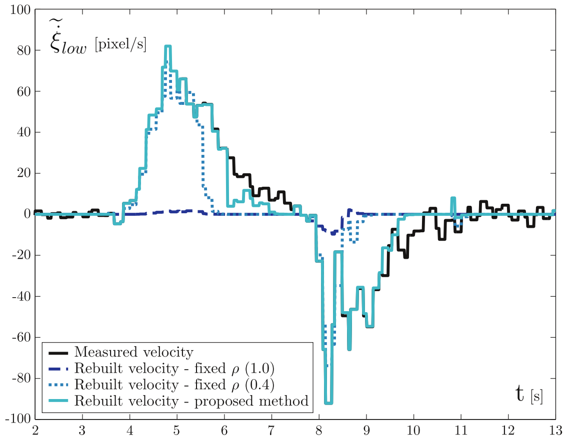

Figure 4.4: Camera velocity rebuilt from different interaction matrix estimators

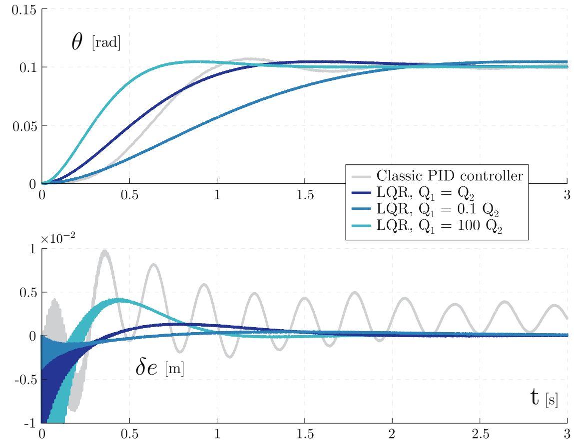

Figure 4.5: Angular step response for different adjustments of the controller

4.3 Experimental validation of the advanced model

This section describes the validation of the advanced model derived in section 3.2.

During these trials, the flexible link has been subjected to stimulating accelerations. Figure 4.6 shows the comparison between the tip position simulated with the proposed model and the one simulated with the model used in section 4.2. They are both compared to the measurements obtained with the accelerometer. This signal has been low-pass filtered in forward and reverse directions during post-processing in order to be representative of the vibration without any delay. Note that the model output is in complete accordance with the experimental data.

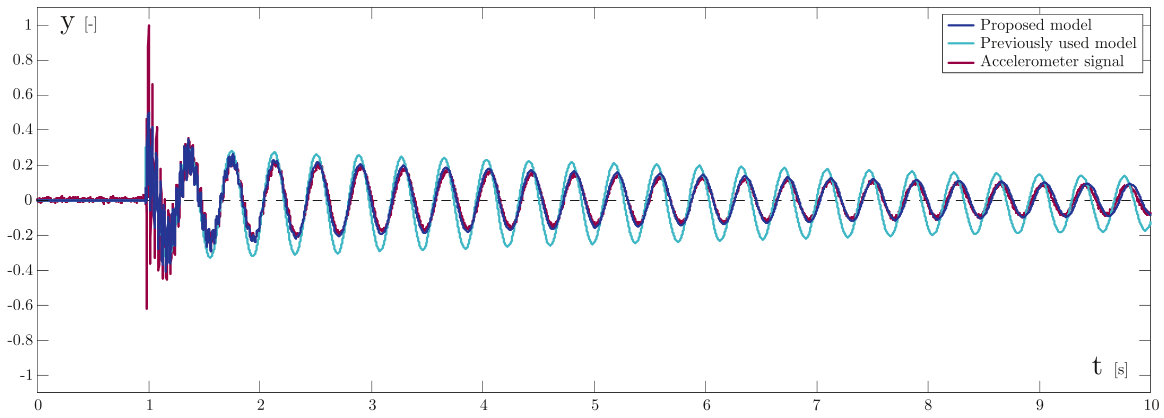

Figure 4.6: Outputs from the proposed model and the former model compared to measurement data

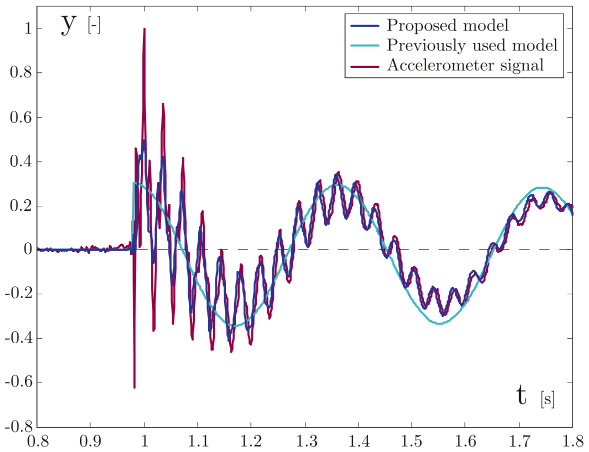

Figure 4.7: Zoom on the vibration emergence

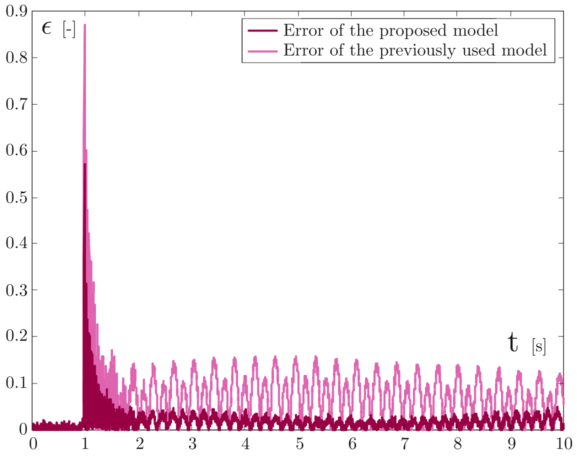

Figure 4.8: Model errors

Figure 4.7 illustrates the increased accuracy of the obtained model during the emergence of a vibration. By considering previously neglected inertia terms, the above-described model more properly weighs the mode shapes corresponding to the upper modes. Model errors are given in Fig. 4.8. To complete this section, Fig. 4.9 illustrates how the proposed model fits the data received from the visual feature tracker.

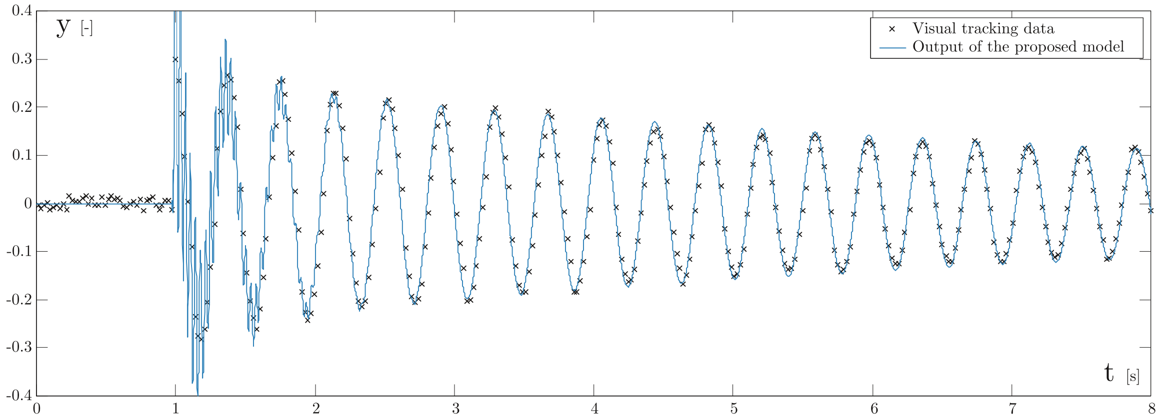

Figure 4.9: Comparison between model output and data from visual tracking

4.4 Experimental results on online sinusoidal regression

This section presents the experimental validation of the developments described in section 3.3 on the proposed vibration-sensing method based on online sinusoidal regression.

Figs. 4.10, 4.11 and 4.12 illustrate the proposed algorithm's ability to predict the vibration with a fairly high accuracy in the presence of sudden and progressive amplitude changes.

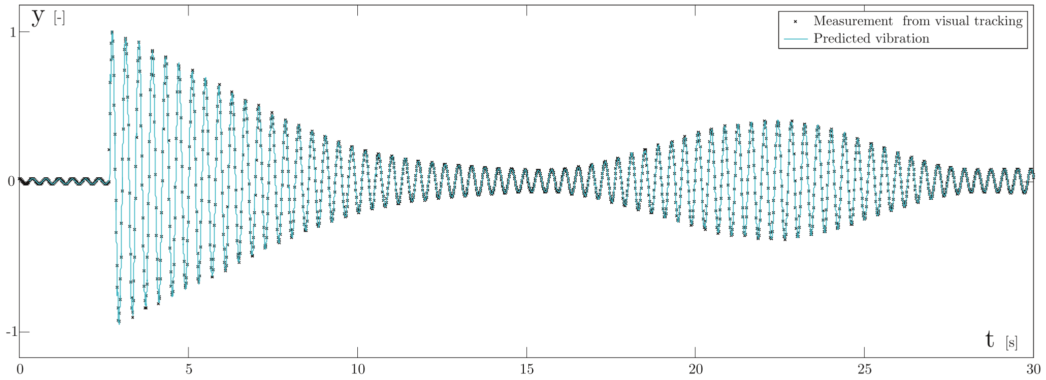

Figure 4.10: Result of the prediction (normalised amplitude)

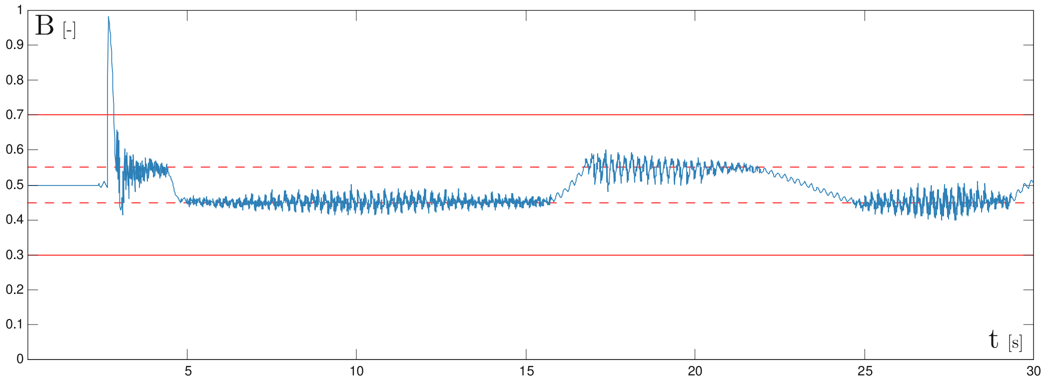

Figure 4.11: Bayesian test B(t)

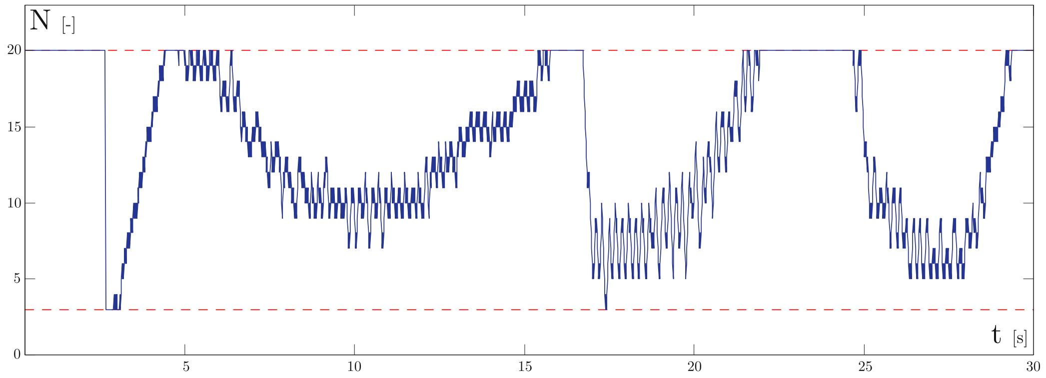

Figure 4.12: Window size N(t)

In this experiment, N_{min} and N_{max} have been set to 3 and 20, respectively. An abrupt variance change is first detected around $t = 2.7$ s. The window size is directly shrunk to N_{min} and then expanded quickly back to N_{max} before the progressive damping of the vibration makes the window size decrease again to approximately $N = 10$. Once this progressive variance change stops, around $t = 12$ s, the window expands stepwise to its full length. To distinguish a gradual change from a sudden one, Γ_g^-, Γ_g^+, Γ_a^- and Γ_a^+ have been set to 0.45, 0.55, 0.3 and 0.7, respectively. The example chosen also illustrates the proposed algorithm's response to two other gradual changes around $t = 17$ s and $t = 25$ s.

Fig. 4.13 highlights the benefit of using a variable-sized window over a fixed-sized window. In cases involving abrupt changes, the vibration prediction is very reactive and yields very accurate results, whereas one period used to be necessary to properly predict the vibration with N fixed to N_{max}.

This quality vibration reconstruction relies on a suitable estimation of the vibrational frequency. Fig. 4.14 compares the frequency evaluation performed with the four robust estimators described in 3.3.3 with both theoretical values and the results obtained by a classical trimmed mean. Around $t = 20$ s, the tip payload suddenly changes to alter the frequency of the oscillation. Whereas the trimmed mean is clearly corrupted by outliers, the M-estimators yields a robust estimation of ω_e. Because it does not completely discard the outliers, Huber's estimator provides results that are less accurate than the others. Since it also decreases the influence of correct data, the Geman-McClure estimator is too sensitive to noise. Tukey's and Cauchy's influence functions provide quite similar and effective results.

The raw frequency estimation based on zero-crossing yields a mean error, a maximum error and a relative standard deviation of $\bar{\epsilon} = 185\%$, $\epsilon_{max} = 1679\%$ and $\sigma = 449\%$, respectively. Using a classic trimmed mean yields $\bar{\epsilon} = 37.76\%$, $\epsilon_{max} = 361.0\%$ and $\sigma = 91.42\%$. In comparison, the same estimation made by the Tukey M-estimator yields $\bar{\epsilon} = 1.59\%$, $\epsilon_{max} = 6.29\%$ and $\sigma = 1.71\%$.

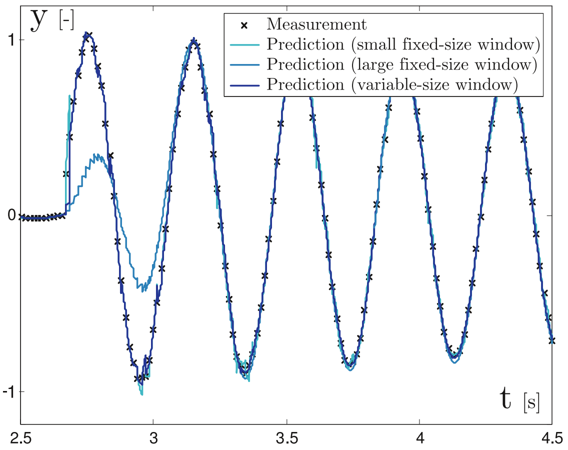

Figure 4.13: Vibration tracking w / wo variable-length sliding window

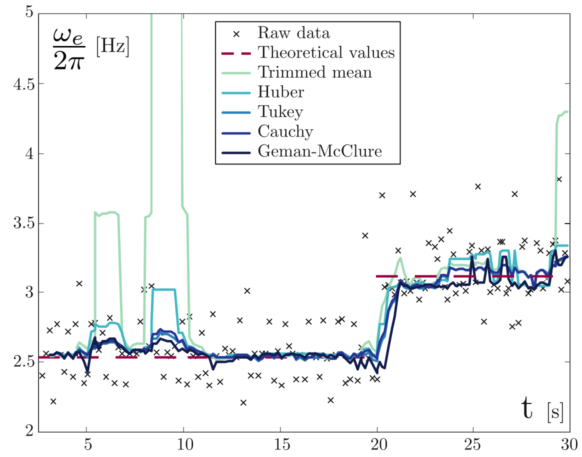

Figure 4.14: Frequency robust estimation

4.5 Experimental results on the online estimation of the capture delay

This section validates the capture delay estimator designed in section 3.4. This experimental work is based on the data collected during the previous work on the test mock-up, which became unavailable while performing the activity described in this section.

As in sections 4.1 and 4.2, only the fundamental, which is situated around 2.5 Hz in the case of this representative experimental setup, is expected to be damped. Fig. 4.15

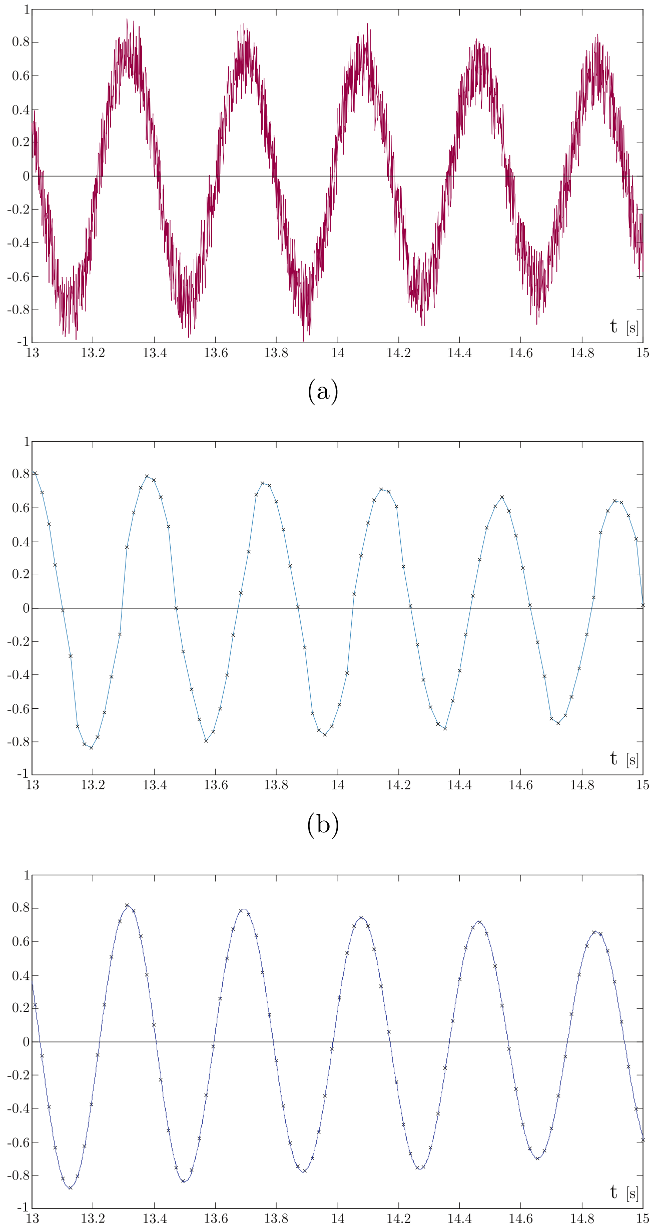

(a)

(b)

(c)

Figure 4.15: Available measurements when the capture delay is estimated using a synchronisation sensor: (a) accelerometer signal (normalised), (b) visual data (normalised), (c) predicted oscillation (normalised)

illustrates the vibration reconstruction when the capture delay is estimated as described in section 3.4.2. Figs. 4.15(a) and 4.15(b) depict the accelerometer signal and the visual data, respectively. Several comments can be made regarding these graphs. First, the accelerometer signal is clearly too noisy to perform a quality vibration rejection, all the more because this signal has been obtained from a non-irradiated sensor. In addition, the signal resulting from the visual tracking is far cleaner. However, note that an important delay (of 1/10 s) exists between these two graphs. That this delay is variable explains why the sinusoidal oscillation seen by the camera is so distorted. Fig. 4.15(c) illustrates the proposed algorithm's ability to properly predict a clean vibration measurement that is synchronised with the physical phenomenon. It is sampled at the controller sampling rate; the crosses indicate only the visual data refreshment times.

The delay time variability is highlighted in Figs. 4.16 and 4.17, which show how the cross-correlation function between the accelerometer signal and visual data enables an accurate estimation of the capture delay. Note that in the selected period of time the capture delay is comprised between 70 ms and 76 ms. During the whole test, its mean value was $\bar{\Delta} = 74$ ms while its standard deviation was $\sigma_{\Delta} = 6.4$ ms. Such a result might partially be explained by the uncertainty of the capture instant, as explained in section 3.4.1. However, the supervisor runs a non-real-time OS; this variability of the capture delay is more likely due to unpredictable changes in the computer load.

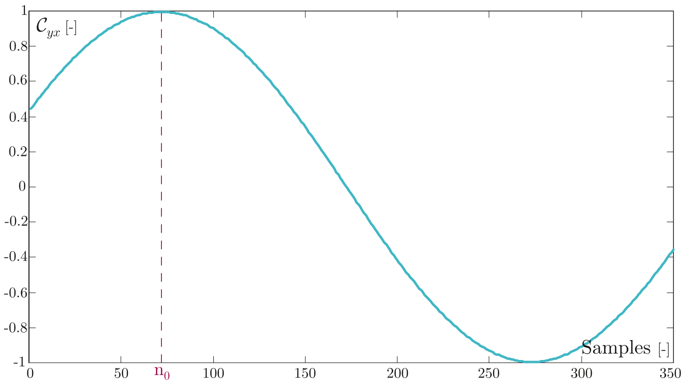

Figure 4.16: Cross-correlation between the two signals at $t = 13$ s

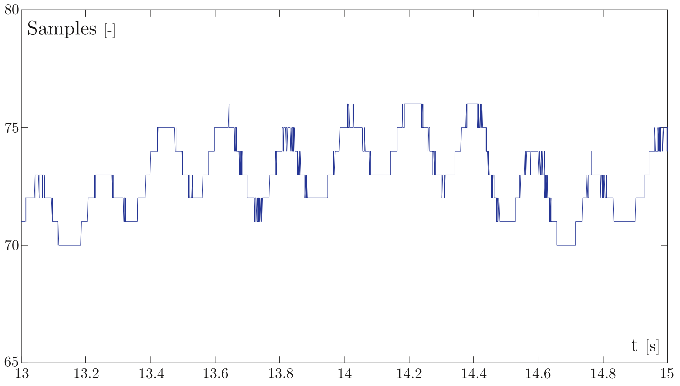

Figure 4.17: Estimated capture delay

Fig. 4.18 compares the two methods described in sections 3.4.1 and 3.4.2, respectively. On one hand, there is no significant difference regarding the general shape of the predicted oscillations obtained with these two methods. In both cases, the sine regression algorithm does its job and the classic Pearson product-moment correlation coefficient (0.9981 and 0.99424, respectively) shows that the reconstructed signals are both very close to decreasing sinusoids. On the other hand, Fig. 4.18(a) also highlights the fact that the deflection estimation is roughly synchronous with the accelerometer signal, i.e. the physical phenomenon, when the capture delay is computed using the correlation method, which is clearly not the case when it is measured using timestamps. Fig. 4.18(b) depicts the errors between the predicted oscillations and the accelerometer signal, which has been cleaned up offline with a zero-phase filter. During the selected period of time, which is reprentative of all the measurements, the mean errors are 15.1% and 2.2% of the sine amplitude using the timestamp method and the correlation method, respectively. In addition, the maximum error on the deflection estimation can add up to one-third of the deflection maximal amplitude using the timestamp method, while it is around 5.7% using the correlation method. In other words, by yielding a better estimation of the camera capture delay, the proposed method enables an average reduction of the sine regression error of 70% to 80%, which is clearly beneficial to the vibration rejection scheme.

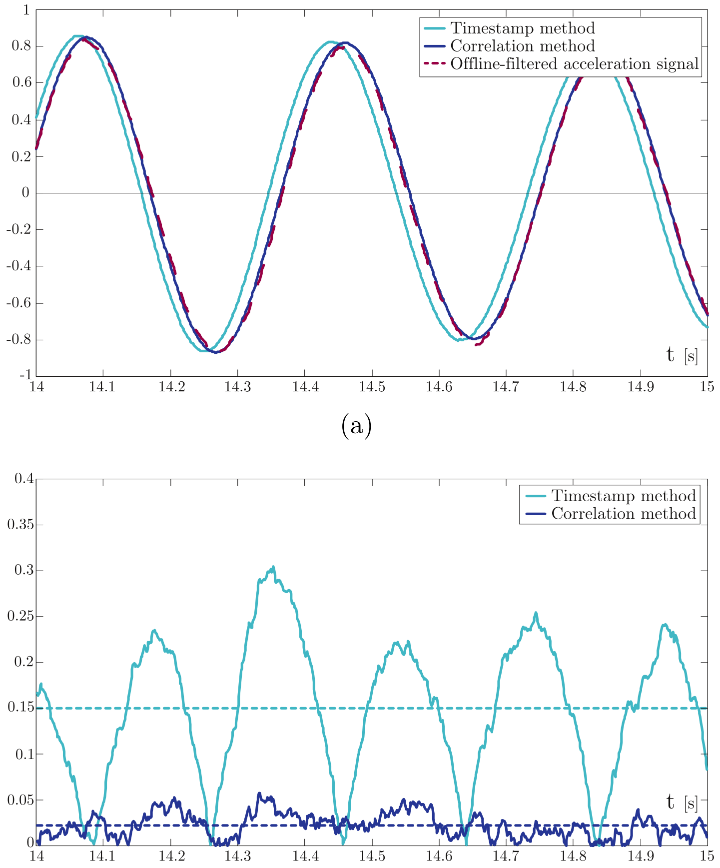

(a)

(b)

Figure 4.18: Comparison between the two methods: (a) predicted oscillations (normalised), (b) error between the prediction and the physically synchronous signal from the accelerometer

5. CONCLUSIONS

The general idea defended within the present thesis is the feasibility of controlling the oscillatory behaviour of remote flexible robotic arms by extracting and exploiting quantitative data from on-board cameras that provide real-time visual feedback to the operators. This makes particular sense in the context of fusion reactor maintenance, for which the higher availability of radiation-tolerant vision sensors compared to suitable high-sensitivity accelerometers has been demonstrated.

The great majority of the results described in this thesis are based on six peer-reviewed publications [63–68]. With the exception of [63], all these articles were published with the author of this thesis as the main author.

In section 3.1, a vision-based vibration control was presented for a flexible inspection arm moving in an unknown and unmarked environment. The proposed control scheme entails a vibration estimator that reconstructs the vibrations from visual data without any a priori knowledge of the surroundings. To that end, a robust tracker based on the KLT algorithm feeds a two-timescale Kalman filter in which some of the measurements are delayed. In other applications, this modified Kalman filter could be extended to multiple-sensor systems with different delays and refresh rates. In addition, the issue of estimating the interaction matrix online was addressed and an adaptive method was proposed to ensure the stability and sensibility of the estimation, no matter what the camera velocity might be. The control scheme was validated on a single-joint flexible mock-up.

In section 3.2, a multimode dynamic model was proposed to implement the vision-based vibration control of a flexible rotating beam. Particular attention was paid to obtaining a computationally light model without making any detrimental compromises regarding its accuracy. The resulting analytic expressions were combined into a new Kalman filter process matrix. The proposed model was also validated on the single-joint mock-up.

An online sinusoidal regression algorithm was described in section 3.3. It enables the vision-based vibration control of long-reach arms that is well-suited for vibrational behaviours of any origin. To obtain good tracking capability and estimation accuracy, the proposed method includes the use of a variable-size window coupled to a signal change detector. This vibration reconstruction algorithm was validated on the same test setup.

Finally, section 3.4 proposed simultaneously using the clean but delayed visual data and the noisy but synchronous inertial data to properly reconstruct the end-effector displacement of a flexible manipulator. Consequently, an online algorithm to estimate time-varying image-processing delays was described. It is based on a cross-correlation technique that explicitly computes the time delay between the visual data and the output of a synchronisation sensor. Because of its recursive formulation, the computational load of this algorithm is quite limited. Synchronisation of the vibration measurement with the physical phenomenon using the proposed method was demonstrated through an experimental example. In addition to allowing the control of flexible manipulators, this method could be extended to monitoring any periodic phenomenon with a vision device.

Out of the two alternatives proposed in this thesis (Kalman filering vs. sinusoidal regression), it is not easy to postulate which is the most promising. On one hand, even though the method described in section 3.1 is particularly robust against visual troubles, such as partial occlusions or camera failure, it is not adapted to cases in which vibrations occur due to contact with the environment or an embedded moving device. On the other hand, the method presented in 3.3 is well-suited no matter the vibration's origin, but it entails no model of the system that could provide the algorithm with particular robustness.

Regarding the level of contribution, one method clearly prevails over the other one. The method based on two-timescale Kalman filtering is an extension of previous works into a more general context; the environment is unknown and absolutely untrimmed. Consequently, the major contribution of this piece of work lies in the all-in-one method in itself. In addition, it entails minor contributions giving more robustness to the whole algorithm (e.g. a self-adjustable memory term). On the other hand, the online sinusoidal regression is an entirely new concept for reconstructing vibrations from low-data-rate sensors.

At this stage, one limitation common to both algorithms is the computation of the environment average displacement from frame to frame. The choice of averaging is purely technical, as it helps to reduce the computational cost of the algorithms and allows to increase the camera framerate. However, when observing a complex environment, object features located at different distances from the camera result in image features moving with different velocities. The displacement of image features corresponding to close objects tends to increase the average, while the displacement of image features corresponding to distant objects tends to decrease it. For this reason, considering the environment overall displacement is by definition an approximation; it is strictly correct if the camera observes a normal plane. Although the proposed algorithms have demonstrated to work efficiently on non-normal planes, an alternative left to future works would consist in considering a field of displacements (including depth-related information) and not only the estimation of an average displacement. This should allow to predict the vibration with higher accuracy.

Another criticism that may be raised against this thesis concerns the legitimacy of the validation process since it involves a single-axis rigid-joint flexible-link mock-up, whereas most of the theoretical developments deal with multi-axes arms. However, the stated goal of the test setup was not to build an entire n-DOF demonstrator but to prove the feasibility of the proposed principles on the simplest device. Now, if one considers a complete, fully actuated, n-DOF robotic arm (e.g. ITER's MPD or Tore Supra's AIA), the control of its end-effector can be seen as a collocated problem. The estimated vibration will thus be projected onto an orthogonal basis and suppressed using only the motion of the relevant module. Of course, this strategy cannot prevent the middle parts of the structure from oscillating. Therefore, one relies upon internal damping to stabilise the entire structure as long as the gripper or the diagnostic tool plugged at the tip does not vibrate.

Finally, another limitation of this work is caused by the experiment not being performed in realistic conditions where the accelerometer would have been seriously affected by the environment. This may be by-passed by using a previously irradiated accelerometer. However, such an experimental setup would have required authorisation from the competent nuclear regulatory authority, which would be far beyond the framework of this study.

As stated in the introduction, this thesis only considers flexible n-DOF manipulators in free space motions. However, in most of the considered applications, it is necessary to control not only the position and vibration of the manipulators but also the force exerted by the end-effector on an object or the environment. Force control of flexible manipulators with a concentrated mass has been extensively studied in recent years [389, 390]. Based on the singular perturbation analysis, which has been widely described in the literature [391], a rigid-joint robot model may be considered for the design of the Cartesian impedance controller. However, force control of flexible link manipulators is essentially still an open problem due to the distributed nature of the models being used. Consequently, the results of this thesis could be extended in future works towards contact dynamics studies or force control following, for instance, the works in [392–394].

The extension to cooperative control of several flexible robots is left for future studies as well. Such works could originate from [395], which considers robust cooperative control of two one-link flexible arms whose bending vibration and torsional vibration are coupled.

These results could eventually be extended to higher-level tasks. Using suitable algorithms would allow the extraction of not only corner features but also more complex geometric shapes (see Fig. 5.1). It would not only make it possible to reject perturbations but also to follow trajectories defined by the in-vessel components themselves, such as the edges between two blanket modules. That would be vision-based trajectory tracking.

In conclusion, let us review the threefold purpose of the present thesis.

The first stated objective of this work was to make a preliminary study available addressing

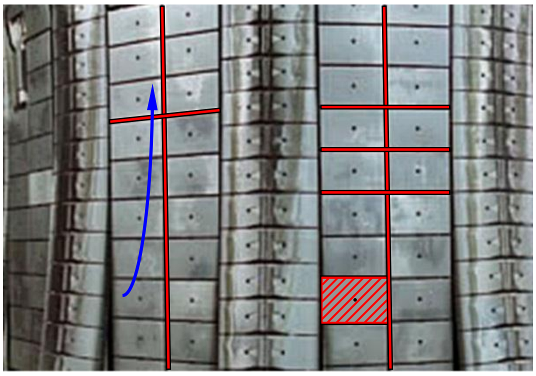

Figure 5.1: Possible prospect: vision-based trajectory tracking using geometric shape recognition

vibration issues during the performance of in-vessel maintenance operations with flexible robotic devices. The second objective was to highlight some promising solutions that could be used as a basis for further developments during the preliminary design of the ITER remote maintenance system. To that end, half of the scientific papers published on the works presented herein were submitted to a journal dedicated to fusion engineering. In addition, the results of this thesis were presented and discussed at several international conferences on fusion, which builds confidence that some key players within the fusion community are aware of this thesis' achievements.

For these reasons, the first two objectives of this thesis are believed to have been met.

The third and last goal of this thesis was to contribute to the already widely explored field of vibration control of flexible robot arms by promoting vision-based techniques made possible by recent improvements in vision sensor performance. With the benefit of hindsight, a short update to the state-of-the-art of vision-based vibration control techniques shows that the works presented in this thesis have already been referenced by a number of publications. Beginning with the developments described in chapter 3, [396] proposed a vision-based vibration control employing radial basis function networks to regulate the control parameters of a PD-controlled flexible manipulator. Still in the robotics domain, [397] and [398] experimentally compared six visual oscillation-sensing approaches for a three-DOF flexible-link robot arm equipped with an eye-in-hand RGB-D camera. Based upon this comparison, the authors proposed a scene-adaptive method for camera motion reconstruction. The proposed scheme adaptively selects the best sensing approach according to the scene texture and depth profile, which is a way of resolving one of the limitations admitted in the above paragraphs. In [399], the same authors compared three predictive signal processing approaches to compensate for the delay inherent in the vision sensor. The results of these last two papers were synthesised in [400].

As a result, the contribution of this work to the overall effort of developing vision-based techniques to control flexible robot arms is acknowledged and, for this reason, it is gladly observed that the third objective of this thesis has been fully achieved.

REFERENCES

[1] World Energy Council, “World energy scenarios: Composing energy futures to 2050”, 2013, http://www.worldenergy.org/wp-content/uploads/2013/09/ World-Energy-Scenarios_Composing-energy-futures-to-2050_Full-report.pdf.

[2] I. Tamm and A. Sakharov, “Plasma physics and the problem of controlled thermonuclear reactions”, in *Proceedings of the 2nd International Conference on the Peaceful Uses of Atomic Energy*, vol. 1. Oxford: Pergamon, 1961, pp. 1–47.

[3] “ITER website – the machine”, http://www.iter.org/mach.

[4] J. Bucalossi, M. Missirlian, P. Moreau, F. Samaille, E. Tsitrone *et al.*, “The WEST project: testing ITER divertor high heat flux component technology in a steady state tokamak environment”, *Fusion Engineering and Design*, vol. 89, no. 7-8, pp. 907–912, 2014.

[5] “Broader approach agreement”, http://fusionforenergy.europa.eu/downloads/aboutf4e/l_24620070921en00340046.pdf.

[6] J. Yeom, K. Kim, Y. Lee, H. Kim, S. Oh *et al.*, “System analysis study for Korean fusion DEMO reactor”, *Fusion Engineering and Design*, vol. 88, no. 6–8, pp. 742–745, 2013.

[7] O. David, A. Loving, J. Palmer, S. Ciattaglia, and J.-P. Friconneau, “Operational experience feedback in JET remote handling”, *Fusion Engineering and Design*, vol. 75–79, no. 0, pp. 519–523, 2005.

[8] A. Rolfe, “Remote handling on fusion experiments”, *Fusion Engineering and Design*, vol. 36, pp. 91–100, 1997.

[9] A. Tesini and A. Rolfe, “The ITER remote maintenance management system”, *Fusion Engineering and Design*, vol. 84, no. 2–6, pp. 236–241, 2009.

[10] L. Gargiulo, P. Bayetti, V. Bruno, J.-J. Cordier, J.-P. Friconneau *et al.*, “Development of an ITER relevant inspection robot”, *Fusion Engineering and Design*, vol. 83, no. 10–12, pp. 1833–1836, 2008.

[11] C. Hernandez, H. Roche, C. Pocheau, C. Grisolia, L. Gargiulo *et al.*, “Development of a Laser Ablation System Kit (LASK) for Tokamak in vessel tritium and dust inventory control”, *Fusion Engineering and Design*, vol. 84, no. 2–6, pp. 939–942, 2009.

[12] D. Keller, J.-P. Friconneau, and Y. Perrot, “An ITER relevant robot for remote handling: On the road to operation on Tore Supra”, *Advances in Service Robotics*, 2008.

[13] Ahlberg, “N35HR datasheet”, 2014, http://www.ahlberg-electronics.com//uploads/up_newsfiles/22_519_PDF.pdf.

[14] Centronic Raditec, “CR2224 datasheet”, 2010, http://www.centronic.co.uk/New%20files/CR2224%20Rad%20Tol %20TV%20Camera%20iss%208%20June%2010.pdf.

[15] Diakont, “D40 datasheet”, 2011, http://www.diakont.com/wp-content/uploads/2011/10/DIAK-Product-D40.pdf.

[16] Diakont, “Star camera datasheet”, 2011, http://www.diakont.com/wp-content/uploads/2011/10/DIAK-Product-Star-Camera.pdf.

[17] Eca Robotics, “VS 370 N datasheet”, 2014, http://www.eca-robotics.com/ftp/ecatalogue/248/VS370N.pdf.

[18] Eca Robotics, “VS 390 N datasheet”, 2014, http://www.eca-robotics.com/ftp/ecatalogue/449/VS390N.pdf.

[19] Mirion, “IST-REES R93 MK3 datasheet”, 2014, https://mirion.box.com/s/jd62bdyacpid5oryfxl6.

[20] Mirion, “IST-REES r985 datasheet”, 2013, https://mirion.box.com/s/s5ivzb9m0u7ya77ww8h8.

[21] Visatec, “VT5065RR datasheet”, 2014, http://www.visatec.net/EN/PDFs/VT_5065.pdf.

[22] K. Leinemann, F. Katz, H. Knüppel, W. Olbrich, and D. Maisonnier, “Synthetic viewing: comprehensive work representation, making remote work clearer to the operator”, *Fusion Engineering and Design*, vol. 29, pp. 317–323, 1995.

[23] P. Garrec, F. Geffard, Y. Perrot, G. Piolain, and A. Freudenreich, “Evaluation tests of the telerobotic system MT200-TAO in AREVA NC La Hague hot cells”, in *Proceedings of the European Nuclear Conference*, Brussels, Belgium, Sep. 2007, pp. 160–166.

[24] A. Borthwick, G. Agarici, A. Davis, P. Dumortier, F. Durodie *et al.*, “Mechanical design features and challenges for the ITER ICRH antenna”, *Fusion Engineering and Design*, vol. 84, no. 2–6, pp. 493–496, 2009.

[25] A. Rolfe, “A perspective on fusion relevant remote handling techniques”, *Fusion Engineering and Design*, vol. 82, no. 15–24, pp. 1917–1923, 2007.

[26] L. Bartolini, A. Coletti, M. Ferri de Collibus, G. Fornetti, C. Neri *et al.*, “Amplitude modulated laser In-Vessel Viewing System (LIVVS) for ITER/JET”, *Fusion Engineering and Design*, vol. 1, pp. 685–688, 1998.

[27] C. Neri, L. Bartolini, A. Coletti, M. Ferri De Collibus, G. Fornetti *et al.*, “The laser In-Vessel Viewing System (IVVS) for ITER: Test results on first wall and divertor samples and new developments”, *Fusion Engineering and Design*, vol. 82, no. 15–24, pp. 2021–2028, 2007.

[28] C. Neri, U. Besi, M. Ferri De Collibus, G. Mugnaini, C. Monti *et al.*, “Status of the design refinement and the characterisation of the In-Vessel Viewing System for ITER”, in *Proceedings of the 25nd IEEE Symposium on Fusion Engineering*, 2013, pp. 1–4.

[29] G. Dubus, A. Puiu, C. Damiani, M. Van Uffelen, A. Lo Bue *et al.*, “Conceptual design finalisation of the ITER In-Vessel Viewing and Metrology System (IVVS)”, *Fusion Engineering and Design*, vol. 88, no. 9–10, pp. 1973–1977, 2013.

[30] G. Dubus, A. Puiu, P. Bates, C. Damiani, R. Reichle *et al.*, “Progress in the design and R&D of the ITER In-Vessel Viewing and Metrology System (IVVS)”, *Fusion Engineering and Design*, vol. 89, no. 9-10, pp. 2398–2403, 2014.

[31] S. Kakudate, K. Oka, T. Yoshimi, K. Taguchi, M. Nakahira *et al.*, “Mechanical characteristics and position control of vehicle/manipulator for ITER blanket remote maintenance”, *Fusion Engineering and Design*, vol. 51–52, pp. 993–999, 2000.

[32] S. Kakudate and K. Shibanuma, “Sensor based control test for remote installation of ITER blanket module”, *Fusion Engineering and Design*, vol. 65, no. 1, pp. 33–38, 2003.

[33] T. Maruyama, A. Aburadani, N. Takeda, S. Kakudate, M. Nakahira *et al.*, “Robot vision system R&D for ITER blanket remote handling system”, *Fusion Engineering and Design*, vol. 89, no. 9-10, pp. 2404–2408, 2014.

[34] Point Grey Research, “Flea2 datasheet”, 2014, http://www.ptgrey.com/support/downloads/documents/Flea2%20Technical%20Reference.pdf.

[35] C. Wagner-Bartak, J. Middleton, and J. Hunter, “Shuttle remote manipulator system hardware test facility”, in *Proceedings of the 11th Space Simulation Conference*, vol. 2150, 1980, p. 79.

[36] S. Greaves, K. Boyle, and N. Doshewnek, “Orbiter boom sensor system and shuttle return to flight: operations analyses”, in *AIAA Guidance, Navigation and Control Conference and Exhibit*, San Francisco, USA, 2005, p. 5986.

[37] D. Hunter, “The space station servicing system”, in *Proceedings of the International Symposium on Artificial Intelligence, Robotics and Automation in Space*, Pasadena, USA, 1994.

[38] R. Boumans and C. Heemskerk, “The European robotic arm for the international space station”, *Robotics and Autonomous Systems*, vol. 23, pp. 17–27, Mar. 1998.

[39] T. Matsueda, K. Kuraoka, K. Goma, T. Sumi, and R. Okamura, “JEMRMS system design and development status”, in *Proceedings of the National Telesystems Conference*, vol. 1, Atlanta, USA, Mar. 1991, pp. 391–395.

[40] S. Doi, Y. Wakabayashi, M. T., and N. Sato, “JEM remote manipulator system”, *Journal of the Japan Society for Aeronautical and Space Science*, vol. 50, pp. 7–14, 2002.

[41] S. Abiko and K. Yoshida, “An effective control strategy of Japanese experimental module remote manipulator system (JEMRMS) using coupled and un-coupled dynamics”, in *Proceedings of the 7th International Symposium on Artificial Intelligence, Robotics and Automation in Space*, Nara, Japan, May 2003.

[42] S. Dubowsky, “Dealing with vibrations in the deployment structures of space robotic systems”, in *Proceedings of the 5th International Conference on Adaptive Structures*, Sendai, Japan, Dec. 1994.

[43] S. Wiedemann and C. Kirk, “Dynamic analysis of flexible space shuttle remote manipulator system with large payloads”, in *Proceedings of the 5th International Conference on Dynamics and Control of Structures and Systems in Space*, 2005.

[44] G. Messenger and M. Ash, *The effects of radiation on electronic systems, 2nd edition.* New York: Van Nostrand Reinhold, 1991.

[45] R. Sharp and D. Garlick, *Radiation effects on electronic equipment, a designers'/users' guide for the nuclear power industry.* AEA-D&W-0691, 1994.

[46] L. Houssay, “Robotics and radiation hardening in the nuclear industry”, Master's thesis, University of Florida, 2000.

[47] H. Shea, “Effects of radiation on MEMS”, *Proc. SPIE*, vol. 7928, p. 79280E, 2011.

[48] Measurement Specialties, “34201A datasheet”, 2014, http://precisionsensors.meas-spec.com/pdfs/DS34201A.pdf.

[49] Silicon Designs, “2430 datasheet”, 2014,
http://www.silicondesigns.com/pdfs/2430.pdf.

[50] Monitran, “MTN/1100-R datasheet”, 2013,
http://www.monitran.co.uk/wp-content/uploads/2013/05/1100-R_DS0254.1-.pdf.

[51] Wilcoxon Research, “793R datasheet”, 2014,
http://www.wilcoxon.com/prodpdf/793R_spec%2898204%29%20A.pdf.

[52] Meggitt, “Endevco 2273A datasheet”, 2014,
http://www.hoskinscientifique.com/uploadpdf/Instrumentation/
Endevco/hoskin_2273A_4a82e226ac955.pdf.

[53] PCB, “357B53 datasheet”, 2014,
http://www.pcb.com/linked_documents/powergen/pg_357b53_357b54_lowres.pdf.

[54] A. Fernandez, H. Ooms, B. Brichard, M. Coeck, S. Coenen *et al.*, “SCK–CEN gamma irradiation facilities for radiation tolerance assessment”, in *IEEE Radiation Effects Data Workshop*, 2002, pp. 171–176.

[55] A. Tzes, M. Englehart, and S. Yurkovich, “Input preshaping with frequency domain information for flexible link manipulators”, in *Proceedings of the AIAA Guidance, Navigation and Control Conference*, Boston, USA, Aug. 1989, pp. 1167–1175.

[56] N. Singer and W. Seering, “Preshaping command inputs to reduce system vibration”, *Artificial intelligence at MIT: expanding frontiers*, pp. 128–147, 1990.

[57] S. Hutchinson, G. Hager, and P. Corke, “A tutorial on visual servo control”, *IEEE Transactions on Robotics and Automation*, vol. 12, no. 5, pp. 651–670, 1996.

[58] P. Tang, H. Wang, and S. Lu, “A vision-based position control system for a one-link flexible arm”, in *Proceedings of the IEEE International Workshop on Intelligent Motion Control*, vol. 2, 1990, pp. 523–528.

[59] K. Hashimoto, T. Kimoto, T. Ebine, and H. Kimura, “Manipulator control with image-based visual servo”, in *Proceedings of the IEEE International Conference on Robotics and Automation*, Sacramento, USA, 1991, pp. 2267–2271.

[60] L. Bascetta and P. Rocco, “Two-time scale visual servoing of eye-in-hand flexible manipulators”, *IEEE Transactions on Robotics*, vol. 22, no. 4, pp. 818–830, 2006.

[61] L. Bascetta and P. Rocco, “End-point vibration sensing of planar flexible manipulators through visual servoing”, *Mechatronics*, vol. 16, no. 3-4, pp. 221–232, 2006.

[62] X. Jiang, Y. Yosuke, A. Konno, and M. Uchiyama, “Vibration suppression control of a flexible arm using image features of unknown objects”, in *Proceedings of the IEEE/RSJ International Conference on Intelligent Robots and Systems*, 2008, pp. 3783–3788.

[63] T. Gagarina-Sasia, O. David, G. Dubus, E. Gabellini, F. Nozais *et al.*, “Remote handling dynamical modelling: assessment of a new approach to enhance positioning accuracy with heavy load manipulation”, *Fusion Engineering and Design*, vol. 83, no. 10–12, pp. 1856–1860, 2008.

[64] G. Dubus, O. David, Y. Measson, and J.-P. Friconneau, “PREFIT project: integration of man-in-the-loop and automation for manipulation of heavy loads and forces in ITER”, *Fusion Engineering and Design*, vol. 84, no. 2–6, pp. 698–702, 2009.

[65] G. Dubus, O. David, and Y. Measson, “Vibration control of a flexible arm for the ITER maintenance using unknown visual features from inside the vessel”, in *Proceedings of the IEEE/RSJ International Conference on Intelligent Robots and Systems*, Saint Louis, USA, Oct. 2009, pp. 5697–5704.

[66] G. Dubus, O. David, and Y. Measson, “Vibration control of the IVVS long-reach deployer using unknown visual features from inside the ITER vessel”, *Fusion Engineering and Design*, vol. 85, no. 10–12, pp. 2027–2032, 2010.

[67] G. Dubus, O. David, and Y. Measson, “A vision-based method for estimating vibrations of a flexible arm using on-line sinusoidal regression”, in *Proceedings of the IEEE International Conference on Robotics and Automation*, Anchorage, USA, May 2010, pp. 4068–4075.

[68] G. Dubus, “On-line estimation of time varying capture delay for vision-based vibration control of flexible manipulators deployed in hostile environments”, in *Proceedings of the IEEE/RSJ International Conference on Intelligent Robots and Systems*, Taipei, Taïwan, Oct. 2010, pp. 3765–3770.

[69] I. Sharf, “Geometrically non-linear beam element for dynamics of multibody systems”, *International Journal for Numerical Methods in Engineering*, vol. 39, pp. 763–786, 1996.

[70] F. Boyer, N. Glandais, and W. Khalil, “Flexible multibody dynamics based on a non-linear euler-bernoulli kinematics”, *International Journal for Numerical Methods in Engineering*, vol. 54, no. 1, pp. 27–59, 2002.

[71] A. Cuce, G. Grasso, G. Sortino, and C. Vinci, “Fuzzy modelling of an experimental flexible arm”, in *Proceedings of the 5th IEEE International Conference on Fuzzy Systems*, vol. 3, New Orleans, USA, Sep. 1996, pp. 1666–1669.

[72] P. Wang and J. Wei, “Feedback control of vibrations in a moving flexible robot arm with rotary and prismatic joints”, in *Proceedings of the IEEE International Conference on Robotics and Automation*, vol. 4, Mar. 1987, pp. 1683–1689.

[73] Y. Pan, R. Scott, and A. Ulsoy, “Dynamic modeling and simulation of flexible robots with prismatic joints”, *Journal of Mechanical Design*, vol. 112, no. 3, pp. 307–314, 1990.

[74] M. Kalyoncu and F. Botsali, “Dynamic modeling of a robot manipulator with a translating and rotating elastic arm”, in *Proceedings of the 3rd International Mechatronics Design and Modeling Workshop*, Ankara, Turkey, 1997, pp. 237–247.

[75] B. Siciliano and O. Khatib, Eds., *Handbook of Robotics.* Berlin/Heidelberg: Springer, 2008.

[76] R. Cannon and E. Schmitz, “Initial experiments on the end-point control of a flexible one-link robot”, *International Journal of Robotics Research*, vol. 3, no. 3, pp. 62–75, 1984.

[77] I. Shung and M. Vidyasagar, “Control of a flexible robot arm with bounded input: Optimum step responses”, in *Proceedings of the IEEE International Conference on Robotics and Automation*, vol. 4, Mar. 1987, pp. 916–922.

[78] G. Hastings and W. Book, “A linear dynamic model for flexible robotic manipulators”, *IEEE Control Systems Magazine*, vol. 7, no. 1, pp. 61–64, Feb. 1987.

[79] D. Meldrum and M. Balas, “Application of model reference adaptive control to a flexible remote manipulator arm”, in *Proceedings of the American Control Conference*, Seattle, USA, Jun. 1986, pp. 825–832.

[80] R. Theodore and A. Ghosal, “Comparison of the assumed modes and finite element models for flexible multilink manipulators”, *Int. J. Rob. Res.*, vol. 14, no. 2, pp. 91–111, 1995.

[81] W. Book, “Analysis of massless elastic chains with servo controlled joints”, *Journal of Dynamic Systems and Measurement Control*, vol. 101, pp. 187–192, 1979.

[82] R. Krauss, “Transfer matrix modeling”, Ph.D. dissertation, School of Mechanical Engineering, Georgia Institute of Technology, 2006.

[83] D. Hutton, *Fundamentals of finite element analysis.* Boston: McGraw-Hill, 2004.

[84] M. Serna and E. Bayo, “A simple and efficient computational approach for the forward dynamics of elastic robots”, *Journal of robotic systems*, vol. 6, no. 44, pp. 363–382, 1989.

[85] M. de Smet, C. Liefooghe, P. Sas, and R. Snoeys, “Dynamic analysis of flexible structures using component mode synthesis”, *Journal of Applied Mechanics*, vol. 56, no. 4, pp. 874–880, 1989.

[86] M. Pereira and P. Proença, “Dynamic analysis of spatial flexible multibody systems using joint coordinates”, *Int. J. Numer. Meth. Engrg.*, vol. 32, pp. 1799–1812, 1991.

[87] P. Chaichanavong and D. Banjerdpongchai, “A case study of robust control experiment on one-link flexible robot arm”, in *Proceedings of the 38th IEEE Conference on Decision and Control*, vol. 5, Phoenix, USA, 1999, pp. 4319–4324.

[88] S. Timoshenko, *History of Strength of Materials.* New York: Dover, 1983.

[89] J. Strutt, *Theory of Sound.* London: Macmillan, 1877.

[90] R. Davis, “The frequency of transverse vibration of a loaded fixed-free bar III: the effect of rotatory inertia of the bar”, *Philosophical Magazine*, vol. 563, 1937.

[91] S. Timoshenko, “On the transverse vibrations of bars of uniform cross-section”, *Philosophical Magazine*, vol. 125, 1922.

[92] E. Kruszewski, “Effects of transverse shear and rotary inertia on the natural frequencies of a uniform beam”, *National Advisory Committee for Aeronautics*, vol. 1909, 1949.

[93] R. Traill-Nash and A. Collar, “The effects of shear flexibility and rotatory inertia on the bending vibrations of beams”, *Quarterly Journal of Mechanics and Applied Mathematics*, vol. 6, pp. 186–213, 1953.

[94] T. Huang, “The effect of rotatory inertia and of shear deformation on the frequency and normal mode equations of uniform beams with simple end conditions”, *Journal of Applied Mechanics*, pp. 579–584, 1961.

[95] N. Stephen and M. Levinson, “A second order beam theory”, *Journal of Sound Vibration*, vol. 67, pp. 293–305, Dec. 1979.

[96] M. Levinson, “Further results of a new beam theory”, *Journal of Sound Vibration*, vol. 77, pp. 440–444, Aug. 1981.

[97] L. Meirovitch, *Principles and techniques of vibrations.* Prentice Hall, 1997.

[98] W. Book, “Recursive Lagrangian dynamics of flexible manipulator arms via transformation matrices”, Robotics Institute, Pittsburgh, USA, Tech. Rep., Dec. 1983.

[99] A. de Luca and B. Siciliano, “Closed-form dynamic model of planar multilink lightweight robots”, *IEEE Transactions on Systems, Man and Cybernetics*, vol. 21, no. 4, pp. 826–839, Jul./Aug. 1991.

[100] S. Cetinkunt and W. Yu, “Accuracy of finite dimensional dynamic models of flexible manipulators for controller design”, *Journal of Robotic Systems*, vol. 9, no. 3, pp. 327–350, 1992.

[101] G. Yang and M. Donath, “Dynamic model of a one-link robot manipulator with both structural and joint flexibility”, in *Proceedings of the IEEE International Conference on Robotics and Automation*, Philadelphia, USA, Apr. 1988, pp. 476–481.

[102] X. Ding, T. Tarn, and A. Bejczy, “A general dynamic model of flexible robot arms for control”, in *Proceedings of the IEEE International Conference on Robotics and Automation*, Scottsdale, USA, May 1989, pp. 1678–1683.

[103] T. Tarn, A. Bejczy, and X. Ding, “On the modelling of flexible robot arms for control”, in *Proceedings of the 8th International Symposium on Mathematical Theory of Networks and Systems*, 1988, pp. 91–104.

[104] R. Judd and D. Falkenburg, “Dynamics of non-rigid articulated robot linkages”, *IEEE Transactions on Automatic Control*, vol. 30, no. 5, pp. 499–502, May 1985.

[105] K. Khorasani and M. Spong, “Invariant manifolds and their application to robot manipulators with flexible joints”, in *Proceedings of the IEEE International Conference on Robotics and Automation*, vol. 2, Mar. 1985, pp. 978–983.

[106] F. Khorrami and U. Ozguner, “Singular perturbation analysis of a distributed parameter model of flexible manipulators”, in *Proceedings of the American Control Conference*, Atlanta, USA, Jun. 1988, pp. 1704–1709.

[107] F. Khorrami, “Analysis of multi-link flexible manipulators via asymptotic expansions”, in *Proceedings of the 28th IEEE Conference on Decision and Control*, Tampa, USA, Dec. 1989, pp. 2089–2094.

[108] N. Creamer, “Deployment of a flexible beam from an oscillating base”, *Journal of Guidance, Control and Dynamics*, vol. 15, no. 2, pp. 527–529, 1987.

[109] J. Wen and R. Buche, “Modeling and control of a rotating flexible beam on a translated base”, in *Proceedings of the 30th IEEE Conference on Decision and Control*, Brighton, UK, Dec. 1991, pp. 1646–1651.

[110] G. Nothmann, “Vibration of a cantilever beam with prescribed end motion”, *Journal of Applied Mechanics*, vol. 16, pp. 327–334, 1948.

[111] T. Yen and S. Kao, “Vibration of beam-mass systems with time-dependent boundary conditions”, *ASME J. Applied Mechanics*, vol. 26, pp. 353–356, 1959.

[112] R. Mindlin and L. Goodman, “Beam vibrations with time-dependent boundary conditions”, *J. appl. mech. ASME*, vol. 17, pp. 377–380, 1950.

[113] D. Grant, “Beam vibrations with time-dependent boundary conditions”, *Journal of Sound and Vibration*, vol. 89, no. 4, pp. 519–522, 1983.

[114] G. Herrmann, “Forced motion of elastic rods”, *Journal of Applied Mechanics*, vol. 21, pp. 221–224, 1954.

[115] G. Anderson and C. Thomas, “A forced vibration problem involving time derivatives in the boundary conditions”, *Journal of Sound and Vibration*, vol. 14, no. 2, pp. 193–214, 1971.

[116] S. Lee and S. Lin, “Non-uniform Timoshenko beams with time-dependent elastic boundary conditions”, *Journal of Sound and Vibration*, vol. 217, no. 2, pp. 223–238, 1998.

[117] K. Sato, “Vibrations of non-homogeneous membranes with time-dependent boundary conditions”, *Journal of Sound Vibration*, vol. 72, pp. 273–278, Sep. 1980.

[118] J. Venkataramana, M. Maiti, and R. Srinivasan, “Vibration of rectangular plates with time-dependent boundary conditions”, *Journal of Sound Vibration*, vol. 62, pp. 327–337, Feb. 1979.

[119] S. Lin, “The closed-form solution for the forced vibration of non-uniform plates with distributed time-dependent boundary conditions”, *Journal of Sound and Vibration*, vol. 232, no. 3, pp. 493–509, 2000.

[120] G. Herrmann, “Forced motions of Timoshenko beams”, *Journal of Applied Mechanics*, vol. 22, p. 53, 1955.

[121] D. Williams, “Displacement of a linear elastic system under a given transient load”, Br. R.A.E., Tech. Rep. Report S.M.E. C/7219/DW/19, 1946.

[122] H. Reismann, “On the forced motion of elastic solids”, *Applied Scientific Research*, vol. 18, no. 1, pp. 156–165, Jan. 1968.

[123] J. Berry and P. Naghdi, “On the vibration of elastic bodies having time dependent boundary conditions”, *Quarterly of Applied Mathematics*, vol. 14, pp. 43–50, 1956.

[124] N. Ölçer, “General solution to the equation of the vibrating membrane”, *Journal of Sound Vibration*, vol. 6, pp. 365–374, Nov. 1967.

[125] H. Reismann, “Forced motion of elastic plates”, *J. Appl. Mech. Series E ASME*, vol. 35, p. 510, 1968.

[126] S. Chandra, “Some comments on the mindlin-goodman method of solving vibrations problems with time dependent boundary conditions”, *Journal of Sound Vibration*, vol. 67, pp. 275–277, Nov. 1979.

[127] S. Wu, “Classical solutions of forced vibration of rod and beam driven by displacement boundary conditions”, *Journal of Sound and Vibration*, vol. 279, no. 1–2, pp. 481–486, 2005.

[128] A. Yigit, R. Scott, and A. Ulsoy, “Flexural motion of a radially rotating beam attached to a rigid body”, *Journal of Sound and Vibration*, vol. 121, no. 2, pp. 201–210, 1988.

[129] G. Naganathan and A. Soni, “Coupling effects of kinematics and flexibility in manipulators”, *Int. J. Rob. Res.*, vol. 6, no. 1, pp. 75–84, 1987.

[130] S. Hanagud and S. Sarkar, “Problem of the dynamics of a cantilever beam attached to a moving base”, *Journal of Guidance, Control and Dynamics*, vol. 12, no. 3, pp. 438–441, 1989.

[131] H. Baruh and S. Tadikonda, “Issues in dynamics and control of flexible robot manipulators”, *Journal of Guidance, Control and Dynamics*, vol. 12, pp. 569–671, 1989.

[132] S. Choura, S. Jayasuriya, and M. Medick, “On the modeling, and open loop control of a rotating thin flexible beam”, *American Society of Mechanical Engineers*, Dec. 1989.

[133] T. Kane and R. Ryan, “Dynamics of a cantilever beam attached to a moving base”, *Journal of Guidance, Control and Dynamics*, vol. 10, pp. 139–151, 1987.

[134] J. Simo and L. Vu-Quoc, “The role of non-linear theories in transient dynamic analysis of flexible structures”, *Journal of Sound and Vibration*, vol. 119, no. 3, pp. 487–508, 1987.

[135] A. Bloch, “Stability analysis of a rotating flexible system”, *Acta Applicandae Mathematicae: An International Survey Journal on Applying Mathematics and Mathematical Applications*, vol. 15, no. 3, pp. 211–234, Jun. 1989.

[136] W. Zhu and C. Mote, “Dynamic modeling and optimal control of rotating Euler-Bernoulli beams”, in *Proceedings of the American Control Conference*, vol. 5, Albuquerque, USA, Jun. 1997, pp. 3110–3114.

[137] K. Yuan and C. Hu, “Nonlinear modeling and partial linearizing control of a slewing Timoshenko-beam”, *Journal of Dynamic Systems, Measurement and Control*, vol. 118, no. 1, pp. 75–83, 1996.

[138] J. Yang, L. Jiang, and D. Chen, “Dynamic modelling and control of a rotating Euler-Bernoulli beam”, *Journal of Sound and Vibration*, vol. 274, no. 3–5, pp. 863–875, 2004.

[139] C. Lee, R. Katz, A. Ulsoy, and R. Scott, “Modal analysis of a distributed parameter rotating shaft”, *Journal of Sound Vibration*, vol. 122, pp. 119–130, Apr. 1988.

[140] A. Argento, H. Morano, and R. Scott, “Accelerating load on a rotating Rayleigh beam”, *ASME Transactions Journal of Vibration Acoustics*, vol. 116, pp. 397–403, Jul. 1994.

[141] A. Argento and H. Morano, “A spinning beam subjected to a moving deflection dependent load, part II: parametric resonance”, *Journal of Sound and Vibration*, vol. 182, no. 4, pp. 617–622, 1995.

[142] R. Katz, C. Lee, A. Ulsoy, and R. Scott, “Dynamic stability and response of a beam subjected to a deflection-dependent moving load”, *ASME Journal of Vibration, Acoustics, Stress and Reliability in Design*, vol. 109, pp. 361–365, 1987.

[143] L. Frýba, “Non-stationary response of a beam to a moving random force”, *Journal of Sound Vibration*, vol. 46, pp. 323–338, Jun. 1976.

[144] H. Zibdeh, “Stochastic vibration of an elastic beam due to random moving loads and deterministic axial forces”, *Engineering Structures*, vol. 17, no. 7, pp. 530–535, 1995.

[145] W. Wang, S. Lu, and C. Hsu, “Experiments on the position control of a one-link flexible robot arm”, *IEEE Transactions on Robotics and Automation*, vol. 5, no. 3, pp. 373–377, Jun. 1989.

[146] D. Russell, “On mathematical models for the elastic beam with frequency-proportional damping”, in *SIAM Control and Estimation in Distributed Parameter Systems*, Philadelphia, USA, 1992, pp. 125–169.

[147] D. Wang and M. Vidyasagar, “Observer-controller stabilization of a class of manipulators with a single flexible link”, in *Proceedings of the IEEE International Conference on Robotics and Automation*, Sacramento, USA, Apr. 1991, pp. 516–521.

[148] O. Wallrapp and R. Schwertassek, “Representation of geometric stiffening in multibody system simulation”, *International Journal for Numerical Methods in Engineering*, vol. 32, no. 8, pp. 1833–1850, 1991.

[149] E. Bakr and A. Shabana, "Geometrically nonlinear analysis of multibody systems", *Computers & Structures*, vol. 23, no. 6, pp. 739–751, 1986.

[150] A. Shabana, *Dynamics of Multibody Systems.* New York: John Wiley & Sons, 1989.

[151] J. Mayo, J. Domínguez, and A. Shabana, "Geometrically nonlinear formulations of beams in flexible multibody dynamics", *J. Vibr. Acoust.*, vol. 117, pp. 501–509, 1995.

[152] H. El-Absy and A. Shabana, "Coupling between rigid body and deformation modes", *Journal of Sound and Vibration*, vol. 198, no. 5, pp. 617–637, 1996.

[153] J. Huang, R. Fung, and C. Tseng, "Dynamic stability of a cantilever beam attached to a translational/rotational base", *Journal of Sound and Vibration*, vol. 224, no. 2, pp. 221–242, 1999.

[154] C. Hsu, "On the parametric excitation of dynamic system having multiple degrees of freedom", *Journal of Applied Mechanics*, pp. 367–372, 1963.

[155] B. Moore, "Principal component analysis in linear systems: controllability, observability, and model reduction", *IEEE Transactions on Automatic Control*, vol. 26, no. 1, pp. 17–32, Feb. 1981.

[156] A. Laub, "Computation of balancing transformations", in *Proceedings of the Joint Automatic Control Conference*, vol. 1, San Francisco, USA, 1980.

[157] J. Sveinsson and F. Fairman, "Minimal balanced realization of transfer function matrices using Markov parameters", *IEEE Transactions on Automatic Control*, vol. 30, no. 10, pp. 1014–1016, Oct. 1985.

[158] J. de Abreu-Garcia and F. Fairman, "Balanced realization of orthogonally symmetric transfer function matrices", *IEEE Transactions on Circuits and Systems*, vol. 34, no. 9, pp. 997–1010, Sep. 1987.

[159] C. Therapos, "Balancing transformations for unstable non-minimal linear systems", *IEEE Transactions on Automatic Control*, vol. 34, no. 4, pp. 455–457, Apr. 1989.

[160] C. Gregory, "Reduction of large flexible spacecraft models using internal balancing theory", *Journal of. Guidance, Control and Dynamics*, vol. 7, pp. 725–732, 1984.

[161] E. Jonckheere, "Principal component analysis of flexible systems–open-loop case", *IEEE Transactions on Automatic Control*, vol. 29, no. 12, pp. 1095–1097, Dec. 1984.

[162] T. Williams, "Closed-form grammians and model reduction for flexible space structures", *IEEE Transactions on Automatic Control*, vol. 35, no. 3, pp. 379–382, Mar. 1990.

[163] L. Ljung, *System identification: Theory for the user, 2nd edition.* Upper Saddle River: Prentice-Hall, 1999.

[164] S. Sheu and M. Walker, "Basis sets for manipulator inertial parameters", in *Proceedings of the IEEE International Conference on Robotics and Automation*, Scottsdale, USA, May 1989, pp. 1517–1522.

[165] H. Mayeda, K. Yoshida, and K. Ohashi, "Base parameters of dynamic models for manipulators with rotational and translational joints", in *Proceedings of the IEEE International Conference on Robotics and Automation*, Scottsdale, USA, May 1989, pp. 1523–1528.

[166] M. Gautier and W. Khalil, "Direct calculation of minimum set of inertial parameters of serial robots", *IEEE Transactions on Robotics and Automation*, vol. 6, no. 3, pp. 368–373, Jun. 1990.

[167] W. El-Maraghy, H. El-Maraghy, A. Zaki, and A. Massoud, “A study on the design and control of robot manipulators with flexibilities”, in *Proceedings of the 4th IFAC symposium on robot control*, Capri, Italy, 1994.

[168] P. Dépincé, “Parameters identification of flexible robots”, in *Proceedings of the IEEE International Conference on Robotics and Automation*, vol. 2, Leuven, Belgium, May 1998, pp. 1116–1121.

[169] D. Nissing and J. Polzer, “Parameter identification of a substitution model for a flexible link”, in *Proceedings of the 12th IFAC Symposium on System Identification*, 2000.

[170] M. Östring, S. Gunnarsson, and M. Norrlöf, “Closed-loop identification of an industrial robot containing flexibilities”, *Control Engineering Practice*, vol. 11, no. 3, pp. 291–300, 2003.

[171] D. Rovner and R. Cannon, “Experiments toward on-line identification and control of a very flexible one-link manipulator”, *International Journal of Robotics Research*, vol. 6, no. 4, pp. 3–19, 1987.

[172] S. Cetinkunt and S. Wu, “Tip position control of a flexible one arm robot with predictive adaptive output feedback implemented with lattice filter parameter identifier”, in *Proceedings of the IEEE International Conference on Robotics and Automation*, Cincinnati, USA, May 1990, pp. 1620–1625.

[173] A. Tzes and S. Yurkovich, “Application and comparison of on-line identification methods for flexible manipulator control”, *International Journal of Robotics Research*, vol. 10, no. 5, pp. 515–527, 1991.

[174] Y. Aoustin, P. Chedmail, and A. Glumineau, “Some simulation results on the robustness of a flexible arm non-linear control law”, *International Journal of Modeling and Simulation*, vol. 12, no. 4, pp. 1–7, Jul. 1992.

[175] T. Parks and H. Pak, “Effect of payload on the dynamics of a flexible manipulator - modeling for control”, *Journal of Dynamic Systems, Measurement, and Control*, vol. 113, no. 3, pp. 409–418, 1991.

[176] P. Dépincé, P. Chedmail, and F. Bennis, “Determination of the minimum set of parameters of flexible robots with rigid solids attached to the links”, in *Proceedings of the International Conference on Systems, Man and Cybernetics*, Le Touquet, France, Oct. 1993, pp. 583–588.

[177] M. Chen and Y. Zheng, “Vibration-free handing of deformable beams by robot end-effectors”, *Journal of Robotic Systems*, vol. 12, no. 5, pp. 331–347, 1995.

[178] W. Singhose, W. Seering, and N. Singer, “Input shaping for vibration reduction with specified insensitivity to modeling errors”, in *Proceedings of the Japan/USA Symposium on Flexible Automation*, vol. 1, 1996, pp. 307–313.

[179] A. Albu-Schaffer and G. Hirzinger, “A globally stable state feedback controller for flexible joint robots”, *Advanced Robotics*, vol. 15, 2001.

[180] Y. Sakawa, F. Matsuno, and S. Fukushima, “Modeling and feedback control of a flexible arm”, *Journal of Robotic Systems*, vol. 2, no. 4, pp. 453–472, 1985.

[181] Z. Luo, “Direct strain feedback control of flexible robot arms: new theoretical and experimental results”, *IEEE Transactions on Automatic Control*, vol. 38, no. 11, pp. 1610–1622, Nov. 1993.

[182] W. Nelson and D. Mitra, “Load estimation and load-adaptive optimal control for a flexible robot arm”, in *Proceedings of the IEEE International Conference on Robotics and Automation*, vol. 3, Apr. 1986, pp. 206–211.

[183] F. Harahima and T. Ueshiba, “Adaptive control of flexible arm using end-point position sensing”, in *Proceedings of the Japan–USA Symposium on Flexible Automation*, Osaka, Japan, Jul. 1986.

[184] V. Feliu, K. Rattan, and H. Brown, “Adaptive control of a single-link flexible manipulator in the presence of joint friction and load changes”, in *Proceedings of the IEEE International Conference on Robotics and Automation*, vol. 2, May 1989, pp. 1036–1041.

[185] C. Damaren, “Adaptive control of flexible manipulators carrying large uncertain payloads”, *Journal of Robotic Systems*, vol. 13, no. 4, pp. 219–228, 1996.

[186] B. Siciliano, B. Yuan, and W. Book, “Model reference adaptive control of a one link flexible arm”, in *Proceedings of the 25th IEEE Conference on Decision and Control*, vol. 25, Dec. 1986, pp. 91–95.

[187] J. Yuh, “Application of discrete-time model reference adaptive control to a flexible single-link robot”, *Journal of Robotic Systems*, vol. 4, no. 5, pp. 621–630, 1987.

[188] A. Koivo and K. Lee, “Self-tuning control of planar two-link manipulator with non-rigid arm”, in *Proceedings of the IEEE International Conference on Robotics and Automation*, Scottsdale, USA, May 1989, pp. 1030–1035.

[189] W. Cheng and J. Wen, “A neural controller for the tracking control of flexible arms”, in *Proceedings of the IEEE International Conference on Neural Networks*, San Francisco, USA, 1993, pp. 749–754.

[190] J. Donne and U. Ozguner, “Neural control of a flexible-link manipulator”, in *Proceedings of the IEEE International Conference on Neural Networks*, vol. 4, Orlando, USA, Jun./Jul. 1994, pp. 2327–2332.

[191] T. Tsuji, B. Xu, and M. Kaneko, “Neuro-based adaptive torque control of a flexible arm”, in *Proceedings of the IEEE International Symposium on Intelligent Control*, Istanbul, Turkey, Jul. 1997, pp. 239–244.

[192] A. Jnifene and W. Andrews, “A fuzzy logic control of the end-point vibration in an experimental flexible beam”, *Journal of Vibration and Control*, vol. 10, pp. 493–506, 2004.

[193] M. Kwak and D. Sciulli, “Fuzzy-logic based vibration suppression control experiments on active structures”, *Journal of Sound and Vibration*, vol. 191, no. 1, pp. 15–28, 1996.

[194] T. Takawa, T. Fukuda, and K. Nakashima, “Technical note: Fuzzy control of vibration of a smart CFRP laminated beam”, *Smart Material Structures*, vol. 9, pp. 215–219, Apr. 2000.

[195] P. Tomei, “A simple PD controller for robots with elastic joints”, *IEEE Transactions on Automatic Control*, vol. 36, no. 10, pp. 1208–1213, Oct. 1991.

[196] A. de Luca, B. Siciliano, and L. Zollo, “PD control with on-line gravity compensation for robots with elastic joints: Theory and experiments”, *Automatica*, vol. 41, no. 10, pp. 1809–1819, 2005.

[197] C. Ott, A. Albu-Schaffer, A. Kugi, S. Stamigioli, and G. Hirzinger, “A passivity based cartesian impedance controller for flexible joint robots - part I: torque feedback and gravity compensation”, in *Proceedings of the IEEE International Conference on Robotics and Automation*, vol. 3, Apr./May 2004, pp. 2659–2665.

[198] M. Spong, “Modeling and control of elastic joint robots”, *Journal of Dynamic Systems, Measurement and Control*, vol. 109, no. 4, pp. 310–318, 1987.

[199] J. Swigert, “Shaped torque techniques”, *Journal of Guidance and Control*, vol. 3, no. 5, pp. 460–467, 1980.

[200] B. Murphy and I. Watanabe, “Digital shaping filters for reducing machine vibration”, *IEEE Transactions on Robotics and Automation*, vol. 8, no. 2, pp. 285–289, Apr. 1992.

[201] P. Meckl and W. Seering, “Reducing residual vibration in systems with uncertain resonances”, *IEEE Control Systems Magazine*, vol. 8, no. 2, pp. 73–76, Apr. 1988.

[202] P. Meckl and W. Seering, “Experimental evaluation of shaped inputs to reduce vibration for a cartesian robot”, *Journal of Dynamic Systems, Measurement and Control*, vol. 112, no. 2, pp. 159–165, 1990.

[203] E. Bayo, P. Papadopoulos, J. Stubbe, and M. Serna, “Inverse dynamics and kinematics of multilink elastic robots: An iterative frequency domain approach”, *The International Journal of Robotics Research*, vol. 8, no. 6, pp. 49–62, 1989.

[204] R. Thompson, J. Junkins, and S. Vadali, “Near-minimum time open-loop slewing of flexible vehicles”, *Journal of Guidance, Control and Dynamics*, vol. 12, pp. 82–88, 1989.

[205] R. Kinceler and P. Meckl, “Input shaping for nonlinear systems”, in *Proceedings of the American Control Conference*, vol. 1, Seattle, USA, Jun. 1995, pp. 914–918.

[206] D. Gorinevsky and G. Vukovich, “Nonlinear input shaping control of flexible spacecraft reorientation maneuver”, *Journal of Guidance, Control and Dynamics*, vol. 21, no. 2, pp. 227–264, 1998.

[207] D. Magee and W. Book, “The application of input shaping to a system with varying parameters”, NASA, Tech. Rep., Nov. 1991.

[208] G. Parker, B. Petterson, C. Dohrmann, and R. Robinett, “Command shaping for residual vibration free crane maneuvers”, in *Proceedings of the American Control Conference*, vol. 1, Seattle, USA, Jun. 1995, pp. 934–938.

[209] A. Tzes and S. Yurkovich, “An adaptive input shaping control scheme for vibration suppression in slewing flexible structures”, *IEEE Transactions on Control Systems Technology*, vol. 1, no. 2, pp. 114–121, Jun. 1993.

[210] S. Jones and A. Ulsoy, “An approach to control input shaping with application to coordinate measuring machines”, *Journal of Dynamic Systems, Measurement and Control*, vol. 121, no. 2, pp. 242–247, 1999.

[211] R. Kress, J. Jansen, and M. Noakes, “Experimental implementation of a robust damped-oscillation control algorithm on a full-sized, two-degree-of-freedom, AC induction motor-driven crane”, in *Proceedings of the 5th International Symposium on Robotics and Manufacturing*, Maui, USA, Aug. 1994, pp. 14–18.

[212] N. Singer, W. Singhose, and E. Kriikku, “An input shaping controller enabling cranes to move without sway”, in *Proceedings of the 7th Topical Meeting on Robotics and Remote Systems*, Augusta, USA, 1997.

[213] G. Parker, K. Groom, J. Hurtado, J. Feddema, R. Robinett *et al.*, “Experimental verification of a command shaping boom crane control system”, in *Proceedings of the American Control Conference*, vol. 1, San Diego, USA, 1999, pp. 86–90.

[214] W. Singhose, W. Seering, and N. Singer, “Time-optimal negative input shapers”, *Journal of Dynamic Systems, Measurement and Control*, vol. 119, no. 2, pp. 198–205, 1997.

[215] L. Pao and W. Singhose, “On the equivalence of minimum time input shaping with traditional time-optimal control”, in *Proceedings of the 4th IEEE Conference on Control Applications*, Albany, USA, Sep. 1995, pp. 1120–1125.

[216] W. Singhose and L. Pao, “A comparison of input shaping and time-optimal flexible-body control”, *Control Engineering Practice*, vol. 5, Apr. 1997.

[217] M. Lau and L. Pao, “Comparison of input shaping and time-optimal control of flexible structures”, in *Proceedings of the American Control Conference*, vol. 2, Arlington, USA, 2001, pp. 1485–1490.

[218] Z. Mohamed, A. Chee, A. Mohd Hashim, M. Tokhi, S. Amin *et al.*, “Techniques for vibration control of a flexible robot manipulator”, *Robotica*, vol. 24, no. 4, pp. 499–511, 2006.

[219] D. Economou, C. Mavroidis, I. Antoniadis, and C. Lee, “Maximally robust input preconditioning for residual vibration suppression using low-pass FIR digital filters”, *Journal of Dynamic Systems, Measurement and Control*, vol. 124, no. 1, pp. 85–97, 2002.

[220] J. Feddema, “Digital filter control of remotely operated flexible robotic structures”, in *Proceedings of the American Control Conference*, San Francisco, USA, Jun. 1993, pp. 2710–2715.

[221] D. Economou, C. Mavroidis, and I. Antoniadis, “Comparison of filter types used for command preconditioning in vibration suppression applications”, in *Proceedings of the American Control Conference*, vol. 3, 2002, pp. 2273–2278.

[222] W. Singhose, N. Singer, and W. Seering, “Comparison of command shaping methods for reducing residual vibration”, in *Proceedings of the 3rd European Control Conference*, vol. 2, 1995, pp. 1126–1131.

[223] D. Economou, C. Mavroidis, and I. Antoniadis, “Robust vibration suppression in flexible systems using infinite impulse response (IIR) digital filters”, *Journal of Guidance, Control and Dynamics*, vol. 27, no. 1, pp. 107–117, 2004.

[224] J. Craig, *Introduction to Robotics: Mechanics and Control, 3rd edition.* Boston, USA: Addison-Wesley Longman, 2004.

[225] P. Khosla and T. Kanade, “Experimental evaluation of nonlinear feedback and feedforward control schemes for manipulators”, *International Journal of Robotics Research*, vol. 7, no. 1, pp. 18–28, 1988.

[226] K. Rattan and V. Feliu, “Feedforward control of flexible manipulators”, in *Proceedings of the IEEE International Conference on Robotics and Automation*, Nice, France, May 1992, pp. 788–793.

[227] E. Rijanto, A. Moran, T. Kurihara, and M. Hayase, “Robust tracking control of flexible arm using inverse dynamics method”, in *Proceedings of the 4th International Workshop on Advanced Motion Control*, vol. 2, Mie, Japan, Mar. 1996, pp. 669–674.

[228] H. Kanoh and H. Lee, “Vibration control of one-link flexible arm”, in *Proceedings of the 24th IEEE Conference on Decision and Control*, vol. 24, Dec. 1985, pp. 1172–1177.

[229] M. Balas, “Feedback control of flexible systems”, *IEEE Transactions on Automatic Control*, vol. 23, no. 4, pp. 673–679, Aug. 1978.

[230] T. Soong and J. Chang, “Active vibration control of large flexible structures”, *Shock Vibration Information Center Shock Vibration Bulletin*, pp. 47–54, May 1982.

[231] D. Luenberger, “Observing the state of a linear system”, *IEEE Transactions on Military Electronics*, vol. 8, no. 2, pp. 74–80, Apr. 1964.

[232] R. Kalman and R. Bucy, “New results in linear filtering and prediction theory”, *Transactions of the ASME - Series D - Journal of Basic Engineering*, vol. 83, pp. 95–107, 1961.

[233] L. Meirovitch and H. Baruh, “The implementation of modal filters for control of structures”, *Journal of Guidance and Control*, vol. 8, pp. 707–716, 1985.

[234] P. Tomei, “An observer for flexible joint robots”, *IEEE Transactions on Automatic Control*, vol. 35, no. 6, pp. 739–743, Jun. 1990.

[235] M. Balas, “Do all linear flexible structures have convergent second-order observers?”, in *Proceedings of the American Control Conference*, vol. 4, Philadelphia, USA, Jun. 1998, pp. 2319–2323.

[236] M. Demetriou, “Natural observers for second order lumped and distributed parameter systems using parameter-dependent lyapunov functions”, in *Proceedings of the American Control Conference*, vol. 3, Arlington, USA, 2001, pp. 2503–2508.

[237] D. Kristiansen, “Modeling of cylinder gyroscopes and observer design for nonlinear oscillations”, Ph.D. dissertation, Norwegian University of Science and Technology, Trondheim, Norway, 2000.

[238] W. Lohmiller and J. Slotine, “On contraction analysis for non-linear systems”, *Automatica*, vol. 34, no. 6, pp. 683–696, 1998.

[239] T. Nguyen and O. Egeland, “Tracking and observer design for a motorized Euler-Bernoulli beam”, in *Proceedings of the 42nd IEEE Conference on Decision and Control*, vol. 4, Dec. 2003, pp. 3325–3330.

[240] Y. Li and X. Chen, “End-point sensing and state observation of a flexible-link robot”, *IEEE/ASME Transactions on Mechatronics*, vol. 6, no. 3, pp. 351–356, Sep. 2001.

[241] W. Book and M. Majette, “Controller design for flexible, distributed parameter mechanical arms via combined state space and frequency domain techniques”, *Journal of Dynamic Systems, Measurement and Control*, vol. 105, pp. 245–254, 1983.

[242] G. Hastings and W. Book, “Experiments in optimal control of a flexible arm”, in *Proceedings of the American Control Conference*, Jun. 1985, pp. 728–729.

[243] T. Fukuda and A. Arakawa, “Optimal control and sensitivity analysis of two links flexible arm with three degrees of freedom”, in *Proceedings of the 28th IEEE Conference on Decision and Control*, Tampa, USA, Dec. 1989, pp. 2101–2106.

[244] A. Arakawa and T. Fukuda, “Vibration control of a flexible robotic arm – experiments and relationship between sensitivity analysis and am control method”, in *Proceedings of the 16th Annual Conference of the IEEE Industrial Electronics Society*, Pacific Grove, USA, Nov. 1990, pp. 273–278.

[245] R. Sutton, G. Halikias, A. Plummer, and D. Wilson, “Modeling and h_∞ control of a single link flexible manipulator”, *Proceedings of the Institution of Mechanical Engineers*, vol. 213, no. 2, pp. 85–104, 1999.

[246] A. Arakawa, T. Fukuda, and F. Hara, "H_{inf} control of a flexible robotic arm, effect of parameter uncertainties on stability", in *Proceedings of the IEEE/RSJ International Conference on Intelligent Robots and Systems*, Osaka, Japan, Nov. 1991, pp. 959–964.

[247] I. Landau, J. Langer, D. Rey, and J. Barnier, "Robust control of a 360° flexible arm using the combined pole placement/sensitivity function shaping method", *IEEE Transactions on Control Systems Technology*, vol. 4, no. 4, pp. 369–383, Jul. 1996.

[248] I. Landau, D. Rey, A. Karimi, A. Voda, and A. Franco, "A flexible transmission system as a benchmark for robust digital control", *European Journal of Control*, vol. 1, no. 2, pp. 77–96, 1995.

[249] M. Safonov and M. Athans, "Gain and phase margin for multi-loop LQG regulators", in *Proceedings of the IEEE Conference on Decision and Control*, vol. 15, Dec. 1976, pp. 361–368.

[250] J. Doyle and G. Stein, "Multivariable feedback design: Concepts for a classical/modern synthesis", *IEEE Transactions on Automatic Control*, vol. 26, no. 1, pp. 4–16, Feb. 1981.

[251] A. Albert and R. Sittler, "A method for computing least-squares estimators that keep up with the data", *SIAM Journal of Control*, vol. 3, pp. 384–417, 1966.

[252] J. Knani, "Dynamic modelling of flexible robotic mechanisms and adaptive robust control of trajectory computer simulation–part I", *Applied Mathematical Modelling*, vol. 26, no. 12, pp. 1113–1124, 2002.

[253] M. Karkoub and K. Tamma, "Modelling and μ-synthesis control of flexible manipulators", *Computers & Structures*, vol. 79, no. 5, pp. 543–551, 2001.

[254] V. Utkin and K. Young, "Methods for constructing discontinuity planes in multidimensional variable structure systems", *Automation and Remote Control*, vol. 39, pp. 1466–1470, 1978.

[255] J. Slotine, "Sliding controller design for nonlinear system", *International Journal of Control*, vol. 40, no. 2, pp. 421–434, 1984.

[256] R. DeCarlo, S. Zak, and G. Matthews, "Variable structure control of nonlinear multivariable systems: a tutorial", *Proceedings of the IEEE*, vol. 76, no. 3, pp. 212–232, Mar. 1988.

[257] K. Yeung and Y. Chen, "Sliding-mode controller design of a single-link flexible manipulator under gravity", *International Journal of Control*, vol. 52, no. 1, pp. 101–117, 1990.

[258] P. Nathan and S. Singh, "Sliding mode control and elastic mode stabilization of a robotic arm with flexible links", *Journal of Dynamic Systems, Measurement and Control*, vol. 113, no. 4, pp. 669–676, 1991.

[259] M. Moallem, K. Khorasani, and R. Patel, "An inverse dynamics sliding mode technique for flexible multi-link manipulators", in *Proceedings of the American control conference*, vol. 3, 1997, pp. 1407–1411.

[260] M. Gokasan, O. Bogosyan, A. Arabyan, and A. Sabanovic, "A sliding mode based controller for a flexible arm with a load", in *Proceedings of the 24th Annual Conference of the IEEE Industrial Electronics Society*, vol. 2, Aachen, Germany, Aug./Sep. 1998, pp. 1083–1087.

[261] A. Sabanovic, K. Jezernik, and K. Wada, "Chattering-free sliding modes in robotic manipulators control", *Robotica*, vol. 14, pp. 17–29, 1996.

[262] X. Chen and G. Zhai, “Sliding mode method based vibration control of flexible arms”, in *Proceedings of the American Control Conference*, vol. 3, 2002, pp. 2374–2379.

[263] A. Arisoy, M. Gokasan, and O. Bogosyan, “Sliding mode based position control of a flexible-link arm”, in *Proceedings of the 12th International Power Electronics and Motion Control Conference*, Aug./Sep. 2006, pp. 402–407.

[264] M. Allen, F. Bernelli-Zazzera, and R. Scattolini, “Sliding mode control of a large flexible space structure”, *Control Engineering Practice*, vol. 8, no. 8, pp. 861–871, 2000.

[265] S. Choi, C. Cheong, and H. Shin, “Sliding mode control of vibration in a single-link flexible arm with parameter variations”, *Journal of Sound and Vibration*, vol. 179, no. 5, pp. 737–748, 1995.

[266] H. Elmali and N. Olgac, “Sliding mode control with perturbation estimation (SMCPE): a new approach”, *International Journal of Control*, vol. 56, no. 4, pp. 923–941, 1992.

[267] J. Moura, R. Ghosh-Roy, and N. Olgac, “Optimum trajectory pre-shaping for sliding mode control”, in *Proceedings of the Japan/USA Symposium on Flexible Automation*, Boston, USA, 1996.

[268] N. Jalili, H. Elmali, J. Moura, and N. Olgac, “Tracking control of a rotating flexible beam using modified frequency-shaped sliding mode control”, in *Proceedings of the American Control Conference*, vol. 4, Albuquerque, USA, Jun. 1997, pp. 2552–2556.

[269] D. Young and U. Özgüner, “Frequency shaping compensator design for sliding mode”, *International Journal of Control*, vol. 57, no. 5, pp. 1005–1019, 1993.

[270] T. Singh, M. Golnaraghi, and R. Dubey, “Sliding-mode/shaped-input control of flexible/rigid link robots”, *Journal of Sound Vibration*, vol. 171, pp. 185–200, Mar. 1994.

[271] S. Choi and J. Cheon, “Vibration control of a single-link flexible arm subjected to disturbances”, *Journal of Sound and Vibration*, vol. 271, no. 3–5, pp. 1147–1156, 2004.

[272] T. Inoue, M. Nakano, and S. Iwai, “High accuracy control of servomechanism for repeated contouring”, in *Proceedings of the 10th Annual Symposium on Incremental Motion Control Systems and Devices*, 1981, pp. 258–292.

[273] S. Hara, Y. Yamamoto, T. Omata, and M. Nakano, “Repetitive control system: a new type servo system for periodic exogenous signals”, *IEEE Transactions on Automatic Control*, vol. 33, no. 7, pp. 659–668, Jul. 1988.

[274] P. Lucibello and S. Panzieri, “End point trajectory control with internal stability of a flexible link by learning”, in *Proceedings of the IEEE International Conference on Robotics and Automation*, vol. 3, Minneapolis, USA, Apr. 1996, pp. 2117–2123.

[275] A. Green and J. Sasiadek, “Inverse dynamics and fuzzy repetitive learning flexible robot control”, in *Proceedings of the 15th IFAC World Congress*, vol. 15, Barcelona, Spain, 2002.

[276] V. Feliu, I. Munoz, P. Roncero, and J. Lopez, “Repetitive control for single link flexible manipulators”, in *Proceedings of the IEEE International Conference on Robotics and Automation*, Apr. 2005, pp. 4303–4308.

[277] N. Hootsmans, S. Dubowsky, and P. Mo, “The experimental performance of a mobile manipulator control algorithm”, in *Proceedings of the IEEE International Conference on Robotics and Automation*, Nice, France, May 1992, pp. 1948–1954.

[278] M. Torres, S. Dubowsky, T. Corrigan, and A. Pisoni, “The coupling map method for path-planning of long reach space robotic systems with experimental evaluation”, 1994.

[279] S. Dubowsky and M. Torres, “Path planning for space manipulators to minimize spacecraft attitude disturbances”, in *Proceedings of the IEEE International Conference on Robotics and Automation*, Sacramento, USA, Apr. 1991, pp. 2522–2528.

[280] B. Siciliano and W. Book, “A singular perturbation approach to control of lightweight flexible manipulators”, *International Journal of Robotics Research*, vol. 7, no. 4, pp. 79–90, 1988.

[281] J. Chow and P. Kokotovic, “Two-time-scale feedback design of a class of nonlinear systems”, *IEEE Transactions on Automatic Control*, vol. 23, no. 3, pp. 438–443, Jun. 1978.

[282] K. Yuan and C. Hu, “Nonlinear modeling and partial linearizing control of a slewing timoshenko-beam”, *Journal of Dynamic Systems, Measurement and Control*, vol. 118, no. 1, pp. 75–83, 1996.

[283] Z. Luo and B. Guo, “Shear force feedback control of a single-link flexible robot with a revolute joint”, *IEEE Transactions on Automatic Control*, vol. 42, no. 1, pp. 53–65, Jan. 1997.

[284] Z. Li and P. Bainum, “Momentum exchange – feedback control of flexible spacecraft maneuvers and vibration”, *Journal of Guidance, Control, and Dynamics*, vol. 15, pp. 1354–1360, Aug. 1992.

[285] C. Goh and T. Caughey, “On the stability problem caused by finite actuator dynamics in the collocated control of large space structures”, *International Journal of Control*, vol. 41, no. 3, pp. 787–802, 1985.

[286] Y. Khulief, “Vibration suppression in rotating beams using active modal control”, *Journal of Sound and Vibration*, vol. 242, no. 4, pp. 681–699, 2001.

[287] D. Zimmerman and H. Cudney, “Practical implementation issues for active control of large flexible structures”, *Journal of vibration, acoustics, stress, and reliability in design*, vol. 111, no. 3, pp. 283–289, 1989.

[288] A. Yousefi-Koma and G. Vukovich, “Vibration suppression of flexible beams with bonded piezo transducers using wave-absorbing controllers”, *Journal of Guidance, Control and Dynamics*, vol. 23, no. 2, pp. 347–354, 2000.

[289] Y. Lee and S. Elliott, “Active position control of flexible smart beam using internal model control”, *Journal of Sound and Vibration*, vol. 242, no. 5, pp. 767–791, 2001.

[290] A. El-Sinawi and M. Hamdan, “Optimal vibration estimation of a non-linear flexible beam mounted on a rotating compliant hub”, *Journal of Sound and Vibration*, vol. 259, no. 4, pp. 857–872, 2003.

[291] B. Al-Bedoor, A. El-Sinawi, and M. Hamdan, “Non-linear dynamic model of an inextensible rotating flexible arm supported on a flexible base”, *Journal of Sound and Vibration*, vol. 251, no. 5, pp. 767–781, 2002.

[292] A. Sharon and D. Hardt, “Enhancement of robot accuracy using end-point feedback and a macro-micro manipulator system”, in *Proceedings of the American Control Conference*, Jun. 1984, pp. 1836–1845.

[293] J. Jansen, S. Babcock, R. Kress, B. Burks, and W. Hamel, “Long reach manipulation for underground storage tank remediation”, in *Proceedings of the ASME Winter Annual Meeting*, Atlanta, USA, 1991, pp. 67–73.

[294] D. Kwon, D. Hwang, S. Babcock, and B. Burks, “Input shaping filter methods for the control of structurally flexible, long-reach manipulators”, in *Proceedings of the IEEE International Conference on Robotics and Automation*, San Diego, USA, May 1994, pp. 3259–3264.

[295] C. Vaillancourt and G. Gosselin, “Compensating for the structural flexibility of the SSRMS with the SPDM”, in *Proceedings of the International Advanced Robotics Program, Second Workshop on Robotics in Space*, 1994.

[296] W. Ballhaus and S. Rock, “End-point control of a two-link flexible robotic manipulator with a mini-manipulator: dynamic coupling issues”, in *Proceedings of the ASME Winter Annual Meeting*, Anaheim, USA, November 1992.

[297] J. Lew and D. Trudnowski, “Vibration control of a micro/macro-manipulator system”, *IEEE Control Systems Magazine*, vol. 16, no. 1, pp. 26–31, Feb. 1996.

[298] I. Sharf, “Active damping of a large flexible manipulator with a short-reach robot”, in *Proceedings of the American Control Conference*, vol. 5, Seattle, USA, Jun. 1995, pp. 3329–3333.

[299] D. Cannon, D. Magee, W. Book, and J. Lew, “Experimental study on micro/macro manipulator vibration control”, in *Proceedings of the IEEE International Conference on Robotics and Automation*, vol. 3, Minneapolis, USA, Apr. 1996, pp. 2549–2554.

[300] C. Mavroidis, “End-point control of long reach manipulator systems”, *Proceedings of the 9th World Congress on the Theory of Machines and Mechanisms*, 1995.

[301] M. Hanson and R. Tolson, “Reducing flexible base vibrations through local redundancy resolution”, *Journal of Robotic Systems*, vol. 12, no. 11, pp. 767–779, 1995.

[302] D. Nenchev, K. Yoshida, P. Vichitkulsawat, and M. Uchiyama, “Reaction null-space control of flexible structure mounted manipulator systems”, *IEEE Transactions on Robotics and Automation*, vol. 15, no. 6, pp. 1011–1023, Dec. 1999.

[303] A. Konno, M. Uchiyama, Y. Kito, and M. Murakami, “Configuration-dependent vibration controllability of flexible-link manipulators”, *International Journal of Robotics Research*, vol. 16, no. 4, pp. 567–576, 1997.

[304] T. Miyazaki and S. Hagihara, “Parallel control method for bilateral master-slave manipulator”, *Journal of the Robotics Society of Japan*, vol. 7, no. 5, pp. 46–52, Oct. 1989.

[305] J. Colgate, “Power and impedance scaling in bilateral manipulation”, in *Proceedings of the IEEE International Conference on Robotics and Automation*, Sacramento, USA, Apr. 1991, pp. 2292–2297.

[306] N. Matsuhira, M. Asakura, and H. Bamba, “Maneuverability of a master-slave manipulator with different configurations and its evaluation tests”, *Advanced Robotics*, vol. 2, 1994.

[307] T. Komatsu and T. Akabane, “Control of a space flexible master-slave manipulator based on parallel compliance models”, in *Proceedings of the IEEE International Conference on Robotics and Automation*, vol. 3, Leuven, Belgium, May 1998, pp. 1932–1937.

[308] Y. Morita, N. Tsukamoto, K. Asai, H. Ukai, H. Kando *et al.*, “Assist control for positioning task by flexible master-slave system”, in *Proceedings of the IEEE International Conference on Industrial Technology*, vol. 2, Dec. 2003, pp. 790–795.

[309] Y. Yokokohji and T. Yoshikawa, “Bilateral control of master-slave manipulators for ideal kinesthetic coupling-formulation and experiment”, *IEEE Transactions on Robotics and Automation*, vol. 10, no. 5, pp. 605–620, Oct. 1994.

[310] K. Kosuge, T. Ito, and T. Fukuda, “Task-oriented control of scaled telemanipulation system”, *Transactions of the IEE of Japan*, vol. 115-C, no. 10, pp. 1121–1127, 1995.

[311] F. Matsuno and T. Endo, “Dynamics based control of two-link flexible arm”, in *Proceedings of the 8th IEEE International Workshop on Advanced Motion Control*, Mar. 2004, pp. 135–140.

[312] K. Osuka and F. Matsuno, “On robustness of passivity of manipulator”, *Journal of the Robotics Society of Japan*, vol. 19, no. 1, pp. 75–80, 1999.

[313] T. Mori, Y. Morita, and H. Ukai, “On the passivity of a one-link rigid master – flexible slave manipulator”, in *Proceedings of the IFAC World Congress*, Prague, Czech Republic, 2005.

[314] W. Levine, *The control handbook.* New York: CRC Press, 1996.

[315] L. Weiss, A. Sanderson, and C. Neuman, “Dynamic sensor-based control of robots with visual feedback”, *IEEE Journal of Robotics and Automation*, vol. RA-3, no. 1, pp. 404–417, Oct. 1987.

[316] W. Wilson, W. C. Hulls, and G. Bell, “Relative end-effector control using Cartesian position based visual servoing”, *IEEE Transactions on Robotics and Automation*, vol. 12, no. 5, pp. 684–696, 1996.

[317] B. Thuilot, P. Martinet, L. Cordesses, and J. Gallice, “Position based visual servoing: Keeping the object in the field of vision”, in *Proceedings of the IEEE International Conference on Robotics and Automation*, 2002, pp. 1624–1629.

[318] G. Hager, “A modular system for robust positioning using feedback from stereo vision”, *IEEE Transactions on Robotics and Automation*, vol. 13, no. 4, pp. 582–595, 1997.

[319] F. Chaumette, “Image moments: a general and useful set of features for visual servoing”, *IEEE Transactions on Robotics*, vol. 20, no. 4, pp. 713–723, 2004.

[320] O. Tahri and F. Chaumette, “Point-based and region-based image moments for visual servoing of planar objects”, *IEEE Transactions on Robotics*, vol. 21, no. 6, pp. 1116–1127, 2005.

[321] F. Chaumette and S. Hutchinson, “Visual servo control I: Basic approaches”, *IEEE Robotics Automation Magazine*, vol. 13, no. 4, pp. 82–90, Dec. 2006.

[322] F. Chaumette and S. Hutchinson, “Visual servo control II: Advanced approaches”, *IEEE Robotics Automation Magazine*, vol. 14, no. 1, pp. 109–118, Mar. 2007.

[323] N. Papanikolopoulos, P. Khosla, and T. Kanade, “Visual tracking of a moving target by a camera mounted on a robot: a combination of control and vision”, *IEEE Transactions on Robotics and Automation*, vol. 9, no. 1, pp. 14–35, Feb. 1993.

[324] K. Hashimoto and H. Kimura, “LQ optimal and nonlinear approaches to visual servoing”, *Visual Servoing, Robotics and Automated Systems*, vol. 7, pp. 165–198, 1993.

[325] B. Nelson and P. Khosla, “Strategies for increasing the tracking region of an eye-in-hand system by singularity and joint limit avoidance”, *Journal of Robotics Research*, vol. 14, pp. 418–423, 1995.

[326] B. Espiau, F. Chaumette, and P. Rives, “A new approach to visual servoing in robotics”, *IEEE Transactions on Robotics and Automation*, vol. 8, no. 3, pp. 313–326, Jun. 1992.

[327] A. Castano and S. Hutchinson, "Visual compliance: task-directed visual servo control", *IEEE Transactions on Robotics and Automation*, vol. 10, no. 3, pp. 334–342, 1994.

[328] Y. Ma, S. Soatto, J. Kosecka, and S. Sastry, *An Invitation to 3-D Vision: From Images to Geometric Models.* Springer Verlag, 2003.

[329] H. Michel and P. Rives, "Singularities in the determination of the situation of a robot effector from the perspective view of 3 points", INRIA, Tech. Rep. RR-1850, 1993.

[330] E. Malis, "Improving vision-based control using efficient second-order minimization techniques", in *Proceedings of the IEEE International Conference on Robotics and Automation*, vol. 2, 2004, pp. 1843–1848.

[331] J.-T. Lapreste, F. Jurie, M. Dhome, and F. Chaumette, "An efficient method to compute the inverse jacobian matrix in visual servoing", in *Proceedings of the IEEE International Conference on Robotics and Automation*, vol. 1, 2004, pp. 727–732.

[332] H. Rowley, S. Baluja, and T. Kanade, "Neural network-based face detection", in *Proceedings of the IEEE Computer Society Conference on Computer Vision and Pattern Recognition*, 1996, pp. 203–208.

[333] G. Wells, C. Venaille, and C. Torras, "Vision-based robot positioning using neural networks", *Image and Vision Computing*, vol. 14, no. 10, pp. 715–732, 1996.

[334] K. Hosoda and M. Asada, "Versatile visual servoing without knowledge of true Jacobian", in *Proceedings of the IEEE/RSJ International Conference on Intelligent Robots and Systems*, 1994, pp. 186–193.

[335] M. Jagersand, O. Fuentes, and R. Nelson, "Experimental evaluation of uncalibrated visual servoing for precision manipulation", in *Proceedings of the IEEE International Conference on Robotics and Automation*, vol. 4, Albuquerque, USA, Apr. 1997, pp. 2874–2880.

[336] J. Piepmeier, G. McMurray, and H. Lipkin, "Uncalibrated dynamic visual servoing", *IEEE Transactions on Robotics and Automation*, vol. 20, no. 1, pp. 143–147, 2004.

[337] K. Mikolajczyk and T. Tuytelaars, "Local image features", in *Encyclopedia of Biometrics*, 2009, pp. 939–943.

[338] V. Caselles, R. Kimmel, and G. Sapiro, "Geodesic active contours", *International Journal of Computer Vision*, vol. 22, no. 1, pp. 61–79, 1997.

[339] C. Papageorgiou, M. Oren, and T. Poggio, "A general framework for object detection", in *Proceedings of the 6th International Conference on Computer Vision*, 1998, pp. 555–562.

[340] J. Shi and J. Malik, "Normalized cuts and image segmentation", *IEEE Transactions on Pattern Analysis and Machine Intelligence*, vol. 22, no. 8, pp. 888–905, 2000.

[341] J. Shi and C. Tomasi, "Good features to track", in *Proceedings of the IEEE Conference on Computer Vision and Pattern Recognition*, Seattle, USA, Jun. 1994, pp. 593–600.

[342] H. Moravec, "Visual mapping by a robot rover", in *Proceedings of the 6th international joint conference on artificial intelligence*, 1979, pp. 598–600.

[343] C. Harris and M. Stephens, "A combined corner and edge detector", in *Proceedings of the 4th Alvey Vision Conference*, 1988, pp. 147–151.

[344] W. Förstner, "A framework for low level feature extraction", in *Proceedings of the 3rd European Conference on Computer Vision*, Stockholm, Sweden, 1994, vol. 801, pp. 383–394.

[345] K. Mikolajczyk and C. Schmid, "Scale & affine invariant interest point detectors", *International Journal of Computer Vision*, vol. 60, no. 1, pp. 63–86, 2004.

[346] D. Lowe, "Distinctive image features from scale-invariant keypoints", *International Journal of Computer Vision*, vol. 60, no. 2, pp. 91–110, Nov. 2004.

[347] T. Tuytelaars and L. Van Gool, "Wide baseline stereo matching based on local, affinely invariant regions", in *Proceedings of the British Machine Vision Conference*, 2000, pp. 412–425.

[348] T. Kadir, A. Zisserman, and M. Brady, "An affine invariant salient region detector", in *Proceedings of the 8th European Conference on Computer Vision*, Prague, Czech Republic, 2004, vol. 3021, pp. 228–241.

[349] K. Mikolajczyk and C. Schmid, "A performance evaluation of local descriptors", *IEEE Transactions on Pattern Analysis and Machine Intelligence*, vol. 27, no. 10, pp. 1615–1630, 2005.

[350] L. Kitchen and A. Rosenfeld, "Gray-level corner detection", *Pattern Recognition Letters*, vol. 1, no. 2, pp. 95–102, 1982.

[351] M. Trajkovic and M. Hedley, "Fast corner detection", *Image and Vision Computing*, vol. 16, no. 2, pp. 75–87, Feb. 1998.

[352] E. Rosten and T. Drummond, "Fusing points and lines for high performance tracking", in *IEEE International Conference on Computer Vision*, vol. 2, Oct. 2005, pp. 1508–1511.

[353] M. Swain and D. Ballard, "Color indexing", *International Journal of Computer Vision*, vol. 7, no. 1, pp. 11–32, Nov. 1991.

[354] M. Stricker and M. Orengo, "Similarity of color images", in *Proceedings of IS&T/SPIE Storage and Retrieval for Image and Video Databases*, 1995, pp. 381–392.

[355] G. Pass, R. Zabih, and J. Miller, "Comparing images using color coherence vectors", in *Proceedings of the 4th ACM International Conference on Multimedia*, 1996, pp. 65–73.

[356] J. Huang, S. Kumar, M. Mitra, W.-J. Zhu, and R. Zabih, "Image indexing using color correlograms", in *Proceedings of the IEEE Computer Society Conference on Computer Vision and Pattern Recognition*, 1997, pp. 762–768.

[357] S. Gauglitz, T. Höllerer, and M. Turk, "Evaluation of interest point detectors and feature descriptors for visual tracking", *International Journal of Computer Vision*, vol. 94, no. 3, pp. 335–360, 2011.

[358] A. Yilmaz, O. Javed, and M. Shah, "Object tracking: a survey", *ACM Computing Surveys*, vol. 38, no. 4, Dec. 2006.

[359] Z. Yin and R. Collins, "Shape constrained figure-ground segmentation and tracking.", in *Proceedings of the IEEE Computer Society Conference on Computer Vision and Pattern Recognition*, 2009, pp. 731–738.

[360] X. Ren and J. Malik, "Tracking as repeated figure/ground segmentation.", in *Proceedings of the IEEE Computer Society Conference on Computer Vision and Pattern Recognition*, 2007, pp. 1–8.

[361] H. Baltzakis and A. Argyros, “Propagation of pixel hypotheses for multiple objects tracking”, in *Proceedings of the 5th International Symposium on Visual Computing*, vol. 5876, Las Vegas, USA, 2009, pp. 140–149.

[362] H. Tao, H. Sawhney, and R. Kumar, “Object tracking with bayesian estimation of dynamic layer representations”, *IEEE Transactions on Pattern Analysis and Machine Intelligence*, vol. 24, no. 1, pp. 75–89, 2002.

[363] D. Comaniciu, V. Ramesh, and P. Meer, “Kernel-based object tracking”, *IEEE Transactions On Pattern Analysis and Machine Intelligence*, vol. 25, no. 5, pp. 564–575, 2003.

[364] A. Jepson, D. Fleet, and T. El-Maraghi, “Robust online appearance models for visual tracking”, *IEEE Transactions on Pattern Analysis and Machine Intelligence*, vol. 25, no. 10, pp. 1296–1311, 2003.

[365] M. Isard and A. Blake, “Condensation: conditional density propagation for visual tracking”, *International Journal of Computer Vision*, vol. 29, no. 1, pp. 5–28, 1998.

[366] N. Paragios and R. Deriche, “Geodesic active contours and level sets for the detection and tracking of moving objects”, *IEEE Transactions on Pattern Analysis and Machine Intelligence*, vol. 22, no. 3, pp. 266–280, 2000.

[367] C. Bibby and I. Reid, “Robust real-time visual tracking using pixel-wise posteriors”, in *Proceedings of the 10th European Conference on Computer Vision*, vol. 5303, Marseille, France, 2008, pp. 831–844.

[368] H. Schweitzer, J. Bell, and F. Wu, “Very fast template matching”, in *Proceedings of the 7th European Conference on Computer Vision*, vol. 2353, Copenhagen, Denmark, 2002, pp. 358–372.

[369] B. Lucas and T. Kanade, “An iterative image registration technique with an application to stereo vision (darpa)”, in *Proceedings of the DARPA Image Understanding Workshop*, Apr. 1981, pp. 121–130.

[370] B. Schunck, “The image flow constraint equation”, *Computer Vision, Graphics and Image Processing*, vol. 35, no. 1, pp. 20–46, 1986.

[371] P. Belanger, “Estimation of angular velocity and acceleration from shaft encoder measurements”, in *Proceedings of the IEEE International Conference on Robotics and Automation*, 1992, pp. 585–592.

[372] T. Larsen, N. Andersen, O. Ravn, and N. Poulsen, “Incorporation of time delayed measurements in a discrete-time Kalman filter”, in *Proceedings of the 37th Conference on Decision and Control*, vol. 4, Tampa, USA, Dec. 1998, pp. 3972–3977.

[373] H. Alexander, “State estimation for distributed systems with sensing delay”, in *Proceedings of SPIE*, vol. 1470, 1991.

[374] C. Broyden, “A class of methods for solving nonlinear simultaneous equations”, *Mathematics of Computation*, vol. 19, pp. 577–593, 1965.

[375] M. Bonkovic, A. Hace, and K. Jezernik, “Population-based uncalibrated visual servoing”, *IEEE / ASME Transactions on Mechatronics*, vol. 13, no. 3, pp. 393–397, Jun. 2008.

[376] K. Miura, K. Hashimoto, J. Gangloff, and M. de Mathelin, “Visual servoing without Jacobian using modified simplex optimization”, in *Proceedings of the IEEE International Conference on Robotics and Automation*, Apr. 2005, pp. 3504–3509.

[377] A. Laub, “A Schur method for solving algebraic Riccati equations”, *IEEE Transactions on Automatic Control*, vol. 17, pp. 60–65, Jan. 1978.

[378] C. Shannon, “Communication in the presence of noise”, *Proceedings of the Institute of Radio Engineers*, vol. 37, no. 1, pp. 10–21, Jan. 1949.

[379] S. Song, J.-S. Lim, S. Baek, and K.-M. Sung, “Gauss Newton variable forgetting factor recursive least squares for time varying parameter tracking”, *Electronic Letters*, vol. 36, pp. 988–990, 2000.

[380] R. Mahony and R. Lozano, “Generalized forgetting functions for on-line least-squares identification of time-varying systems”, *International Journal of Adaptive Control and Signal Processing*, vol. 15, pp. 393–413, 2001.

[381] J. Aldrich, “R.A. Fisher and the making of maximum likelihood 1912–1922”, *Statistical Science*, vol. 12, no. 3, pp. 162–176, Sep. 1997.

[382] P. Huber, “Robust estimation of a location parameter”, *The annals of mathematical statistics*, vol. 35, no. 1, pp. 73–101, Mar. 1964.

[383] D. Andrews, P. Bickel, F. Hampel, P. Huber, W. Rogers *et al.*, *Robust estimates of location: survey and advances.* Princeton, USA: Princeton University Press, 1972.

[384] T. Ferguson, “Maximum likelihood estimates of the parameters of the cauchy distribution for samples of size 3 and 4”, *Journal of the American Statistical Association*, vol. 73, no. 361, pp. 211–213, Mar. 1978.

[385] S. Geman and D. McClure, “Statistical methods for tomographic image reconstruction”, in *Proceedings of the 46th session of the International Statistical Institute*, vol. 52, 1987.

[386] M. Basseville and I. Nikiforov, *Detection of abrupt changes: theory and application.* Prentice-Hall, 1993.

[387] D. Hsu, “Detecting shifts of parameter in gamma sequences, with applications to stock price and air traffic flow analysis”, *Journal of the American Statistical Association*, vol. 74, pp. 31–40, 1979.

[388] E. Marchand, F. Spindler, and F. Chaumette, “Visp for visual servoing: a generic software platform with a wide class of robot control skills”, in *IEEE Robotics and Automation Magazine*, Dec. 2005, pp. 40–52.

[389] T. Yoshikawa, K. Harada, and A. Matsumoto, “Hybrid position / force control of flexible-macro / rigid-micro manipulator systems”, *IEEE Transactions on Robotics and Automation*, vol. 12, no. 4, pp. 633–640, Aug. 1996.

[390] A. Albu-Schaffer and G. Hirzinger, “Cartesian impedance control techniques for torque controlled light-weight robots”, in *Proceedings of the IEEE International Conference on Robotics and Automation*, vol. 1, 2002, pp. 657–663.

[391] P. Kokotovic, J. O’Reilly, and H. Khalil, *Singular perturbation methods in control: analysis and design.* Orlando: Academic Press, 1986.

[392] J. Yang, F. Lian, and L. Fu, “Adaptive hybrid position/force control for robotic manipulators with compliant links”, in *Proceedings of the IEEE International Conference on Robotics and Automation*, vol. 1, Nagoya, Japan, May 1995, pp. 603–608.

[393] A. García and V. Feliu, “Force control of a single-link flexible robot based on a collision detection mechanism”, *IEE Proceedings - Control Theory and Applications*, vol. 147, no. 6, pp. 588–595, 2000.

[394] T. Endo and F. Matsuno, “Dynamics based force control of one-link flexible arm”, in *SICE Annual Conference*, vol. 3, Aug. 2004, pp. 2736–2741.

[395] F. Matsuno, “Modeling and robust cooperative control of two one-link flexible arms considering bending and torsional vibrations”, in *Proceedings of the 37th IEEE Conference on Decision and Control*, vol. 4, Tampa, FL, USA, Dec. 1998, pp. 3611–3616.

[396] Z. Qiu, B. Ma, and X. Zhang, “End edge feedback and RBF neural network based vibration control of flexible manipulator”, in *Proceedings of the IEEE International Conference on Robotics and Biomimetics*, Dec. 2012, pp. 1680–1685.

[397] J. Malzahn, A. Phung, and T. Bertram, “Scene adaptive RGB-D based oscillation sensing for a multi flexible link robot arm in unstructured dynamic environments”, in *Proceedings of the IEEE/RSJ International Conference on Intelligent Robots and Systems*, Oct. 2012, pp. 1017–1022.

[398] J. Malzahn and T. Bertram, “Einsatz eines RGB-D-Sensors zur schwingungsgedämpften Positionierung eines gliedelastischen Roboterarms”, in *Regelungstechnisches Kolloquium*, Boppard, Feb. 2012.

[399] J. Malzahn, A. Phung, and T. Bertram, “Predictive delay compensation for camera based oscillation damping of a multi link flexible robot”, in *Intelligent Robotics and Applications*, 2012, vol. 7508, pp. 93–102.

[400] J. Malzahn, A. Phung, and F. Hoffmann, “Bildbasierte Regelung eines gliedelastischen Roboterarms mit einem RGB-D-Sensor”, *Automatisierungstechnik Methoden und Anwendungen der Steuerungs-, Regelungs- und Informationstechnik*, vol. 60, pp. 246–259, Oct. 2012.

Tampereen teknillinen yliopisto
PL 527
33101 Tampere

Tampere University of Technology
P.O.B. 527
FI-33101 Tampere, Finland

ISBN 978-952-15-3374-7 (printed)
ISBN 978-952-15-3375-4 (PDF)
ISSN 1459-2045